Applications of a novel many-component Lattice Boltzmann simulation

Michael Maurice Dupin

July 2004

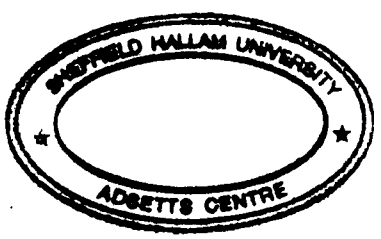

A thesis submitted in partial fulfillment of the requirements of Sheffield Hallam University for the degree of Doctor of Philosophy

Abstract

There are many important systems which involve the flow of dense suspensions of deformable particles; blood is an example. However, the modeling of such materials represents a considerable challenge to established methods such as computational fluid dynamics (CFD). In this PhD project, work has been undertaken to extend the lattice Boltzmann method (LBM), and enable it to represent a large number of mutually immiscible, deformable, droplets (separated by narrow interfaces). The new method imposes a relatively small computational overhead and has been validated against experimental observations. The work has also led to very promising developments in the simulation of micro-fluidic systems, allowing much quicker simulations than traditional CFD methods.

The principal target application of this project is the mesoscale modeling of blood flow, where the typical length is about 10 red blood cells' diameters. We address in here the identified gap in models capable of modeling efficiently, explicitly, many deformable bodies within a surrounding incompressible fluid. We generalised, improved, and extended an existing LBM model for binary fluids. Our $N \gg 2$ non-coalescing fluids (droplets) are defined to represent the different deformable particles of the suspension. Their interactions with the walls as well as their deformability are controlled by local fluid-wall wetting and fluid-fluid surface tensions methods, which we have also been developed and validated.

All interfacial methods suffer from small but spurious flows that disturb the solution. Our model is, unfortunately, no exception when used in a high surface tension and low Reynold's number regime. We describe several steps taken to address this problem which yield a significant reduction in these 'micro-currents' and important improvements in stability and flow field noise reduction. This enabled our model to

access successfully the computationally non-trivial problems of binary fluid microfluidics.

Using our model, we also recover the expected behaviour of deformable and solid particle suspensions with respect to experimental observations on flow of solid and deformable spheres in pressure-driven straight pipe flow. In order to serve as calibration, we measured the macroscopic effect of the droplets' effective deformability against their microscopic properties (surface tension, internal viscosity).

This new model opens very promising and unique grounds of research, by the new capability its offers.

Publications

This thesis contains work published in the following journals:

M. M. Dupin, I. H. Halliday and C. M. Care, *Multi-component lattice Boltzmann equation for mesoscale blood flow*, J. Phys. A, **36**, pages 8517-8534, 2003.

M. M. Dupin, I. H. Halliday and C. M. Care, *A lattice Boltzmann model of flow blunting*, Phil. Trans. Roy. Soc. Lond. A, **362**, pages 1755-1761, 2004.

M. M. Dupin, I. H. Halliday and C. M. Care, *A many component lattice Boltzmann equation for transport of deformable particles*, Phil. Trans. Roy. Soc. Lond. A, **362**, pages 1885-1914, 2004.

Acknowledgments

The body of this work would not have been possible without the help and constant support of those around me, in England and back at home, in France. Firstly, I must thank my parents André and Micheline Dupin for always being there when I needed them, topping up my enthusiasm and providing inevitable financial support throughout my numerous years of study. I am also indebted to my twin brother, Patrick Dupin, for his friendship and for being very supportive, even though we did not have much chance to see each other during the whole of my PhD.

It has been a great pleasure to work with Ian Halliday for three years, and to have been his student for a year in final year of my BSc, here in Sheffield. He increased my confidence significantly and has always been there for me, when my life was not straightforward from time to time, just like my father or a good friend would have done. So, thank you very much Ian, I shall never forget. I would also like to thank Chris Care for his support and kindness.

I am infinitely indebted to Fabien Engel, with whom I started my University career back at home and with whom I came to Sheffield from Geispolsheim in France, in 2000. We discovered the joys of England together, this was certainly one of the best years of my life. Four years later, we are still very good friends. I would also like to thank David Michel (aka *Cabrone*) who has been a very good friend, colleague and house-mate.

I am finally very grateful to all those who have made me feel so welcome in Sheffield, and made my time here very enjoyable. Amongst those is Damien Larroumet, who had been very supportive during some hard times in my PhD. I would like to express all my gratitude to Lucy Smith and her daughter Rosie, with whom I shared 3 years of my life. Sadly we took different paths recently, but both of them will remain

very special to me. I would finally like to thanks Christine Cleaver, who made me feel more than welcome and for being very understanding, patient and supportive during the final rush of a PhD that is the writing-up.

... To Lucy, who did not get the chance to finish her PhD.

Advanced studies

Sept.-Dec. 2001 *Advanced technique in Mathematics*, within the School of Science and Mathematics, Sheffield Hallam University, U.K.

11-13 November 2001 *Fluent's Users Group Meeting*, 2001, Hilton Hotel, Sheffield, U.K.

Jan-June 2002 *Advanced Fluid Dynamics*, within the School of Science and Mathematics, Sheffield Hallam University, U.K.

15-17 April 2002 *Modelling Flow in Oil Reservoirs*, BP Institute, Cambridge, UK.

5-9 August 2002 *11th International Conference on the Discrete Simulation of Fluid Dynamics*, Shanghai, China.

2 July 2003 Presentation at the *Conference on Physical, Mathematical and Numerical Modelling of Blood Flow in Cardiovascular Disease*, York, UK.

25-29 August 2003 Presentation at the *12th International Conference on the Discrete Simulation of Fluid Dynamics: from micro to meso to macro*, Center for Advanced Mathematical Studies, Beirut, Lebanon.

17-19 September 2003 Presentation at the *Computational Modelling in Medicine conference*, Edinburgh, UK.

1 October 2003 *CCP5 Lattice-Boltzmann Workshop*, Daresbury Laboratory, Warrington, UK.

6-8 October 2003 *Fluent's Users Group Meeting 2003*, Courtyard by Marriott Hotel, Rotherham, UK.

18 November 2003 Invited seminar, *Centre for Mathematical Medicine Division of Applied Mathematics School of Mathematical Sciences*, University of Nottingham, Nottingham, UK.

19-23 January 2004 *Towards a Predictive Biology*, Isaac Newton Institute for Mathematical Sciences, Cambridge University, Cambridge, UK.

19 March 2004 Invited seminar, *division of Engineering and applied sciences*, Harvard University, Boston, Boston, Massachusetts, USA.

20 March 2004 Invited seminar, *Steel Laboratory*, Massachusetts General Hospital - Harvard Medical School, Boston, Massachusetts, USA.

29 March - 9 April 2004 *Soft Condensed Matter Physics in Molecular and Cell Biology*, NATO ASI and SUSSP 59, Edinburgh, UK.

Contents

Introduction

Numerical techniques provide, very often, accurate answers to numerous problems that analytical theory cannot address. There exist an endless number of techniques, more or less general with many suited for a very precise application only, or for general configurations. Computational efficiency is always a decisive factor when choosing between techniques, since super-computing is still only available to a few research laboratories. Constant research is needed to ensure that the existing methods are being developed to the full extent of the capability of widely available hardware and also to invent new method where existing models are inadequate.

In recent years, blood flow has been subjected to a high degree of interest by the scientific community, since it is believed that it is often responsible or a consequence of numerous pathologies and complications: from the turbulent heart and artery flow, to the micro-capillary retial flow, improper blood flow is often identified as responsible.
Better understanding of how blood flows and how biological cells interact is therefore needed to assist developing new drugs and surgical techniques. This thesis is concerned in tackling the very complex problem of suspension modeling, especially mesoscopic blood flow, where every biological cell has to be explicitly represented in the surrounding fluid.

The current field of numerical fluid dynamics is heavily dominated by standard techniques: the well established and widely used body of mainstream CFD (Computational Fluid Dynamics). In this thesis, we use the Lattice Boltzmann Method (LBM), which is much more recent than the CFD, but has, already, a very promising future. It is especially designed for fluid-dynamics problems and has (as any other method) associated disadvantages and artifacts, which will be addressed successfully. We identified the Gunstensen LB algorithm extension as being especially well suited for this application, subjected to improvements and generalisation. We addressed numerous of the model's issues, which was necessary for the development, of a final stable, efficient, and hydrodynamically accurate technique for the meso-

scopic modeling of deformable particles.

This is an acknowledged non-trivial problem (and therefore highly rewardable). This thesis sets one of the first mile stone in LB's application, by opening new research opportunities and capabilities.

Aims

The primary aim of this project had been to develop a technique capable of modeling, explicitly, a large number of non-coalescing droplets in solution. As a prime application, the simulation of mesoscale blood flow was obvious, since it is subjected to a large interest in numerous configurations. Other current models can either represent a large number of solid particles in solution or a few deformable particles in solution (and that at high computational cost). There exists therefore, a great challenge for a model that would resolve explicitly and efficiently, a large number of deformable particles in solution.
The secondary aim of this project (which turned out to be as important as the latter) has been to improve the Gunstensen method in Lattice Boltzmann, which is subjected to significant micro-currents, generating a very noisy flow field and reduced stability of the simulations at low Reynolds number and Capillary number. Reducing significantly the micro-currents allowed the efficient simulation of binary fluid microfluidics devices, which grew into an obvious aim while developing and realising the potential and advantage of this method.
It turned out that reducing the micro-currents was necessary anyway, for an eventual simulation of mesoscale blood flow.

Thesis layout

Chapter 1: General Background. This chapter begins by introducing general concepts in Fluid Dynamics, and shows briefly how standard numerical techniques have evolved from it. It then introduces the bases of kinetic theory, and the subsequent Boltzmann approaches, to provide an alternative, self con-

sistent point of view to fluid dynamics. The link between fluid dynamics and Kinetic theory is made explicit. A second part consists of introducing and describing the construction the LBM. It describes in details the steps involved in the algorithm and how it is closely related to the previous Boltzmann Kinetic theory and to fluid dynamics. This chapter contains a literature review of the main, current numerical techniques for fluid dynamics.

Chapter 2: Specific background. This chapter beings by describing the link between a previous LB equation of motion, described in previous chapter, and that of the binary case and the main associated issue: the discontinuity of the equation of motion induced by an interface. It then describes, the generalisation of Gunstensen's LBM, described in the previous chapter. Each step is detailed and the explicit link to LBM is made explicit. Surface tension in the Gunstensen algorithm is then described, showing the original Gunstensen method and the more recent Lishchuk method, which provides a more accurate answer, introducing by the same token, the issue of micro-currents. This chapter finishes by a discussion on stability issues in the binary LB model, mainly centered on the microcurrent issue (omnipresent in this thesis). This chapter also describes a method to implement no-slip solid boundary conditions in LB simulations (moving or static) and a review on the different numerical interfacial methods, in CFD and LB.

Chapter 3: Novel method to reduce the micro-currents. This chapter begins by reviewing the previously introduced micro-currents. It shows that these are not LB related issues only and that most numerical methods have a form of associated unwanted flow. It then describes and investigates their possible origin in the original Gunstensen surface tension method, in an $ab - initio$ discussion. It then describes a new method, addressing this issue, showing significant improvement of the model. A few additional improvements to the method are also described. This chapter finishes by describing a novel method of implementing wall wetting behaviour within the Gunstensen algorithm, and provides a series of proof of capabilities. This chapter contains a review on the micro-currents associated with different LB and CFD numerical techniques.

Chapter 4: The N-component algorithm. This chapter begins by reviewing the current models for the simulation of suspensions, in the blood flow application especially. It demonstrates that current models are unable to simulate realistically and/or efficiently mesoscopic blood flow or deformable particle suspensions. It therefore introduces the main assumption of this thesis: the representation of biological cells as viscous, liquid, non-coalescent droplets in suspension. It then describes how to generalise the previously described Gunstensen LB algorithm to $N \gg 2$ droplets. The generalisations of each step of the algorithm previously described in chapter 1, 2 and 3 are described in details. This chapter finishes by providing proofs of capability for our new model, related to the current application.

Chapter 5: Validation of the N-component method. Previous chapters had shown how to generalise and obtain a new technique for the simulation of the a large number of deformable particles, but only provided proofs of capability. This chapter consists, therefore, in a series of simulations validating the hydrodynamics of our N-component model against experimental observations. It shows that our new model recovers, correctly, some experimental observations of mesoscopic suspensions. It also provides a calibration of the solidity of the droplets in suspension with respect to their parameters (viscosity and surface tension).

Chapter 6: Microfluidic and other applications. This last chapter begins by introducing the other targeted application of this project: the binary microfluidics. The reason why this configuration is acknowledged as computationally non-trivial is made explicit. This chapter describes the 'flow-focusing' configuration that will be our target benchmark for our model. It shows how our model, taken as it stands, does not allow the simulation of micro-fluidic devices and it shows also how to improve further our N-component algorithm, by numerous corrections and the generalisation of the Lishchuk method. It then demonstrated that our new, greatly enhanced model can be applied successfully to binary fluid microfluidic devices. Chapter 6 finishes by describing some proofs of capability of our new model in the blood flow application and

in the simulation of very dense suspension.

Chapter 1

General Background: Classical Fluid Dynamics

Introduction

This section sets the general background necessary for the understanding and referencing of this thesis. Mainly theoretical, it shows how the different approaches to fluid dynamics interlock and how they can be derived from the same general concepts. First, the *fluid dynamics* section derives the Navier-Stokes Equations (NSE), which are a set of highly non linear coupled partial differential equations representing fluid motion. Second, the *Computational Fluid Dynamics* (CFD) section describes traditional techniques to discretise the NSE onto meshes and solve them digitally. Whilst CFD is an immense subject very relevant to put the Lattice Boltzmann Method (LBM) into the digital context, it is not the main subject of this thesis, so it will not be covered in detail. Thirdly, a *Kinetic theory* section sets the basis for the derivation of Lattice Boltzmann Equation. It is essential to do the derivation *ab initio* (i.e. from the atomistic level) to realise the limitations and power of kinetic theory and ultimately LB. And finally, a section on *Lattice Boltzmann* (LB hereafter) describes the derivation of the technique, showing that it can be understood physically from the previous kinetic theory section, which creates its beauty and power compared to other methods: it is designed in essence to resolve fluid dynamics related problems.

1.1 Introduction to Fluid dynamics

It is unavoidable, within the context of this thesis, to describe the derivation of the equations of motion of a fluid (despite being very interesting by themselves). They are the equations that any computer model (including CFD or LBM) has to solve in order to be able to claim that the output post-processed pictures and extracted numbers have any physical meaning. It will be shown first that the macroscopic fluid motion can be derived without any reference to the detailed microscopic atomic structure, only by considering physical fundamentals (which is actually quite fortunate, since it simplifies the task a lot: it would be rather complicated and expensive to consider the individual motion of each individual molecule involved!).

1.1.1 Different points of view

Different fluid flows have common properties. As an illustration, let's consider the flow of the explosion of a supernova. It is believed that when a supernova explodes, a shock wave rushes towards the outer space, inducing a compression zone on its front and depression zone on its tail (standard shock wave). Before exploding, the star had a well defined radial structure, with heavy elements concentrated within its inner layers and lighter elements towards the outside. The negative pressure gradient is directed from the outside to the inside (due to the shock wave), accelerating heavier matter towards lighter matter. It can be shown that acceleration due to a pressure gradient is equivalent to the acceleration due to a force such as gravity, acting towards the centre of the star [209], [63]. This leads to the rather surprising result that the flow of the explosion of a super-nova can be correctly described by the flow of the Rayleigh-Taylor instability (or density fingering), where a heavy fluid sits on the top of a lighter one and both are subjected to the same gravitational field. This is very useful to understand the dynamics of these explosions, since the Rayleigh-Taylor instability is much easier to investigate (analytically, numerically and obviously experimentally).

This analogy is based on the fact that non-relativistic, non-quantum systems obey exactly the same fluid physics, so that explicit detailed resolution of the system is not necessary, only its 'small group behaviour' is enough. As a consequence, the most

commonly used way of imposing numerically a pressure difference in the simulation of a pipe for example, at low Reynolds number, is to set an explicit body force (like gravity) to drive the flow.

1.1.2 Fluid macroscopic continuum motion

This section follows essentially Anderson's second chapter ([2]) and concentrates on setting the general fluid flow equations (that any model must recover), namely the NSE (including the continuity equation).
In obtaining these basic equations of fluid motion, one always begin with the following fundamental principles from the laws of physics:

- Mass is conserved.
- $\mathbf{F} = m\,\mathbf{a}$ (Newton's second law).
- Energy is conserved.

Each of these fundamental principle will be the starting point of an analysis leading to a fluid motion equation.

The continuity equation

The continuity equation is the fluid dynamics analogue of the chemical law by the French Chemist Lavoisier: 'nothing is created, nothing disappears' applied to a set volume of fluid. A control volume, V, represents a finite volume of fluid, where matter is *counted*. It is bounded by its control surface. First, these control volume and surface are considered to move with the flow, expanding or shrinking along any flow velocity streamline. The mass conservation principle implies that the total mass in this control volume has to be constant throughout time, in equation:

$$D_t \iiint_V \rho \, dV = 0 \,. \tag{1.1}$$

Equation 1.1 is refered as the *integral form of the continuity equation*, and because the control volume is moving along with the fluid, it is also designated as the *non-conservation form*. In this equation, the control volume it involves represents, in fact, the volume occupied by a finite and constant (large) number of particles (the

observer is going along or 'advecting' with the particles). Despite being the most fundamental form, the 'material derivative' in equation 1.1 is not easily obtained or very useful in any analysis, and is very often replaced by an expression containing its subsequent set of partial differential operators. They can be obtained by fixing the coordinate of the control volume (the observer now looks at the fluid from above, and is still unable to distinguish any atomic structure) which splits the total derivative D_t into partial derivatives. For quantities depending on time and position only (such as velocity), D_t becomes (from e.g. Batchelor [6]):

$$D_t = \partial_t + \nabla \cdot \mathbf{v} \,. \tag{1.2}$$

D_t is also called the *substantial derivative*, which is physically the rate of change following a moving fluid element, ∂_t is called the *local derivative*, which physically represents the time rate of change at a fixed point and $\nabla \cdot \mathbf{v}$ is the *convective derivative*, which is physically the time rate of change due to the movement of the fluid element from one location to another in the flow, taking spatial difference into account (from e.g. Anderson [2]). The continuity equation (1.1) becomes:

$$\iiint_V [\partial_t \rho + \nabla \cdot (\rho \mathbf{v})] \, dV = 0 \,. \tag{1.3}$$

This form is designated as the *integral conservation.*

The integral in equation 1.3 would make it necessary to make explicit the control volume V, which could be a drawback in the following derivation. This can be avoided by making the control volume infinitesimally small, and equation 1.3 becomes:

$$\partial_t \rho + \nabla \cdot (\rho \, \mathbf{u}) = 0. \tag{1.4}$$

This latter form is the *differential conservation* form of the continuity equation, for compressible fluids. Note that $\mathbf{u}$ denotes the macroscopic velocity and is defined as follow:

$$\mathbf{u} = \iiint_V \mathbf{v} \, dV \,. \tag{1.5}$$

The first form of the continuity equation (equation 1.1) is said to be the most fundamental since its control volume represents in fact the volume occupied by a constant finite number of particles (the observer is going along with the particles).

The last form of the continuity (equation 1.4) is said to be least fundamental since it does not allow for the presence of discontinuities, for it assumes the flow properties to be differentiable, hence continuous. It is therefore not surprising that it leads to significant errors when investigating real flow discontinuities such as shock waves (very local zones of high and low pressures). However, this latter form is just as valid for the type of flow involved in this thesis (incompressible, low Reynolds number). We will consider incompressible fluid only, in which the time derivative the continuity equation vanishes (by definition, no spatial or temporal gradients in density), and from equation 1.4:

$$\nabla \cdot (\rho \mathbf{u}) = 0 \,. \tag{1.6}$$

This is to be the equation referred to as the *continuity equation* throughout this text, even though the three forms of the continuity equation (equations 1.1, 1.3 and 1.4) all represent the same behaviour (conservation of mass), applied under different circumstances.

Momentum equation

In continuing to derive the fluid motion equations, one needs next to consider the second listed law of physics: Newton's second law. This section considers the forces moving and deforming the control volume V considered in the previous section. The control volume experiences two types of forces: *body forces* (represented by $\mathbf{A}$ hereafter), which act on the volumetric mass of the fluid element (gravity, electric and magnetic forces) and *surface forces*, which act on the surface of the fluid element [2]. The surface forces are from two sources only: (a) the pressure distribution acting on the surface by the static surrounding fluid (represented by P) and (b) the shear and normal stresses acting on the surface by the outside fluid *tugging* or *pushing* on the surface by means of friction (represented by $\sigma_{\alpha\beta}$). Within these frames, the total net force per unit volume acting on the moving fluid element in the α direction can be written as:

$$P_\alpha = \partial_\beta \sigma_{\alpha\beta} + \rho A_\alpha \,, \tag{1.7}$$

where $\sigma_{\alpha\beta}$ represents the stresses exerted on the fluid element by the surrounding fluid and relates to its time rate of change of its deformation. The diagonal and non-diagonal components of $\sigma_{\alpha\beta}$ have different physical meanings, yielding to its explicit separation: the diagonal terms are written σ''_α and the non-diagonal terms are written as $\sigma'_{\alpha\beta}$

$$\sigma = \begin{pmatrix} \sigma''_x & \sigma'_{xy} & \sigma'_{xz} \\ \sigma'_{yx} & \sigma''_y & \sigma'_{yz} \\ \sigma'_{zy} & \sigma'_{zy} & \sigma''_z \end{pmatrix} . \tag{1.8}$$

The viscous shear tensor (or shear stress tensor), denoted above by $\sigma'_{\alpha\beta}$ ($\alpha \neq \beta$) relates to the time rate of change of the shearing deformation of the fluid element, responsible for the strains of the elements of the fluid. The normal stress tensor, on the other hand, denoted by σ''_α relates to the time rate of change of volume of the fluid element (pressure). It must be understood as *mechanical* pressure, defined in terms of the mechanical stresses that act on an element of fluid. As a result of equation 1.7, both shear and normal stresses depend on velocity gradients of the flow and the rest of this section consists of describing the relation between $\sigma_{\alpha\beta}$ and $\partial_\alpha u_\beta$.

The normal stress tensor

Let's consider the normal stress tensor first. Pascal's theorem states that stress in a fluid in mechanical equilibrium (no flow) is a scalar quantity (unaffected by changes in the reference frame), completely described by an invariant isotropic pressure P (also called thermodynamic pressure since it is the quantity used in thermodynamics [57] or hydrostatic pressure since it applies to stationary fluids [81]). This means that all three normal components of stress are equal to one another and to P. The normal component of the stress tensor can therefore be written in terms of the fluid pressure only:

$$\sigma''_x = \sigma''_y = \sigma''_z \equiv P ,$$

where P is the thermodynamic pressure. Therefore, in a stationary fluid, the thermodynamic fluid pressure is defined as the average value of the three components of normal stress, i.e.

$$P = \frac{1}{3}\left(\sigma''_x + \sigma''_y + \sigma''_z\right) = \frac{1}{3}\sigma_{\alpha\beta}\,\delta_{\alpha\beta}\,,$$

where $\delta_{\alpha\beta}$ is the Kronecker function.

Stokes, in 1845, obtained that the three normal stresses are unequal in a moving incompressible fluid and defined as [2]:

$$\sigma''_\alpha = P - \mu\, 2\,\partial_\alpha u_\alpha - \zeta\,\nabla\cdot\mathbf{u}\,,$$

where μ is the molecular viscosity coefficient and ζ is the second or bulk viscosity. The term associated to ζ corresponds to the changes in the volume of the fluid due to compression effects (note that $\nabla\cdot\mathbf{u}$ is the left hand side of the continuity equation 1.4) and as a consequence, for incompressible fluids this term vanishes. ζ appears only in measurements of attenuation of sound– the propagation of sound in any fluid (including one which is incompressible) is necessarily accompanied by compressive effects (otherwise the speed of sound would be infinite) [81]. In the case of ordinary fluids, measurements lead to very small value of ζ (or big values of the speed of sound). For incompressible fluids:

$$\sigma''_\alpha = P - 2\,\mu\,\partial_\alpha u_\alpha\,. \tag{1.9}$$

Note that the repeated subscript here is not a sum and that $\frac{1}{3}\sum_\alpha \sigma''_\alpha$ is still the thermodynamic pressure P (through the continuity equation for incompressible fluids $\nabla\cdot\mathbf{u} = 0$). Even with moving fluids, the differences between σ_x, σ_y and σ_z are most often found to be small and they are ignored for most practical purposes [208]. Viscoelastic fluids however are characterised by a significant direction dependance of σ''_α – that is, there are important differences between the normal stresses (i.e. $\sigma''_x \neq \sigma''_y \neq \sigma''_z$).

The shear stress tensor

Let's now consider the shear stress tensor $\sigma'_{\alpha\beta}$. In the late seventeenth century, Isaac Newton stated that shear stress in a fluid is proportional to the time rate of strain,

i.e. velocity gradients. These fluids are therefore called Newtonian fluids and the non diagonal of the stress tensor is written as:

$$\sigma'_{\alpha\beta} = \mu 2 S_{\alpha\beta} , \tag{1.10}$$

where $S_{\alpha\beta}$ is the strain rate tensor defined as follow:

$$S_{\alpha\beta} = \frac{1}{2} \left(\partial_\alpha u_\beta + \partial_\beta u_\alpha \right) . \tag{1.11}$$

Recalling equation 1.7 giving the net force the fluid element is subjected to, together with the definition of the shear stress tensor $\sigma_{\alpha\beta}$ (equations 1.8, 1.9 and 1.10), leads to the following momentum evolution equation of the velocities:

$$\rho D_t u_\alpha = P_\alpha = \rho \partial_t u_\alpha + \rho \left(\mathbf{u} \cdot \nabla \right) u_\alpha = -\partial_\beta \sigma_{\alpha\beta} + \rho A_\alpha ,$$

and after rearrangement, we obtain the momentum equation:

$$\rho \partial_t u_\alpha + \rho \left(u_\beta \partial_\beta \right) u_\alpha = -\partial_\alpha P + \mu \partial_\beta S_{\alpha\beta} + \rho A_\alpha .$$

$S_{\alpha\beta}$ relates to the dissipation in the tangential stresses due to the relative motion of the various layers of fluids (μ is the molecular viscosity coefficient). The shear viscosity of a fluid is therefore the ratio between the rate of strain and the shear:

$$\mu = \frac{Strain}{Shear} , \tag{1.12}$$

and represents the dissipation of local stresses into the fluid. It can be understood as the molecular friction: a non viscous fluid would have its molecules sliding easily next to each other while the molecules of a highly viscous fluid would exchange much more momentum through collision. Accordingly, the density of the fluid obviously plays an important role in the rate of diffusion of momentum and needs to be taken into account for the quantification of the rate of dissipation of stresses. Therefore, the quantity ν defined by:

$$\nu = \frac{\mu}{\rho} \tag{1.13}$$

is called the *Kinematic viscosity* or simply viscosity, where μ is the shear viscosity defined by equation 1.12 and ρ is the density of the fluid.

Colloids or particles embedded in the fluid change the linear relation of equation 1.10 to a non linear relationship. These fluids are called non-Newtonian, blood is

one example as is discussed in chapter 4. If the stress increases faster than the rate of strain (viscosity increasing with the rate of strain), the fluid is said to be *shear-thickening* (wet sand for example), and *shear-thinning* vice-versa (paint, blood, or ink). Other examples of complex behaviours are *Bingham fluids* (no flow is observed until a critical value of the stress: clayey muds, toothpastes and fresh cement are few examples), or *thixotropic fluids* (effective viscosity decreasing with time) such as ketchup or drilling muds.

Energy equation

Following similar steps as previously for the second Newton's law, which lead to the momentum equation, the energy conservation principle leads to the derivation of the energy equation for the fluid. One first states that since energy is conserved: the rate of change of energy inside a fluid element has to be equal to the sum of the net flux of heat into the element and the rate of work done on the fluid element due to body and surface forces. One then obtains an equation which allows the study of temperature diffusion or combustion. This energy equation won't be discussed further since the LB method used in this thesis does not allow any temperature gradients. Moreover, the energy equation does not bring any more information on the flow of an isothermal fluid, the previously described NSE and continuity are sufficient to close the description.

Summary: Equation of motion of the flow of interest

The flow of incompressible ($\partial_t \rho = 0$) non-viscoelastic (isotropic pressure) newtonian (linear relation between strain and stress, or constant viscosity) fluids can be described by two equations: continuity and momentum equations. The *continuity equation* reads as follows:

$$\nabla \cdot \mathbf{u} = 0, \tag{1.14}$$

which ensures that the fluid is incompressible. The momentum equation dictates the effects of external forces and the dissipation of stresses:

$$\rho\, \partial_t u_\alpha + \rho\, (u_\beta \partial_\beta)\, u_\alpha = -\partial_\alpha P + \mu\, \partial_\beta S_{\alpha\beta} + \rho\, A_\alpha, \tag{1.15}$$

The momentum equation is called the *Navier-Stokes equation*, but it is widely understood, however, that the term *Navier-Stokes equations* encompasses the continuity, Navier-Stokes and Energy equation (not described here).
For completeness, it should be noted that Euler had derived the continuity and momentum equation for inviscid flow (null viscosity) but had not derived the energy equation since the science of thermodynamics did not exist at the time. Therefore, a fluid with no dissipation due to viscous stress is identified as a *Eulerian fluid*, obeying the Euler equations (NSE with $\mu = 0$):

$$\partial_t \mathbf{u} + (\mathbf{u} \cdot \nabla)\mathbf{u} = \mathbf{F} - \frac{\nabla P}{\rho}. \tag{1.16}$$

1.1.3 Boundary conditions for fluid flow

General remarks

The NavierStokes equations can take on different forms depending on flow regime:

- Incompressible, steady: Elliptic,
- Incompressible, unsteady: Parabolic,
- Compressible, steady: Elliptic/Hyperbolic,
- Compressible, unsteady: Parabolic/Hyperbolic.

Different numerical methods will succeed in different regimes and therefore different formulations are used to handle compressible and incompressible flow cases.
Mathematical principles on PDEs states that the NSEs should have $\mathbf{u}$ defined over all the boundaries of the flow domain. Therefore, boundaries can't be overlooked and should be subjected to great care. The two main types of boundaries that will be considered are walls and other non-miscible fluid.

Boundary conditions: solid walls

A fluid cannot penetrate into a non-porous wall, which requires that the normal component of the velocity to the boundary of the fluid should be equal to the velocity of the boundary ($\mathbf{u}_{solid} \cdot \mathbf{n} = \mathbf{u}_{liquid} \cdot \mathbf{n}$). In addition to that, in the case of a non-Eulerian fluid (non-zero viscosity), it can be shown that any discontinuity

between the tangential velocity of the fluid and the boundary would lead to infinit energy dissipation at the surface as a result of the non-null viscosity and therefore cannot be allowed. This leads to the non-slip boundary condition:

$$\mathbf{u}_{fluid} \cdot \widehat{\mathbf{t}} = \mathbf{u}_{solid} \cdot \widehat{\mathbf{t}} \tag{1.17}$$

Note that this condition is valid for a solid wall as well as for deformable (moving) walls. Cavitation happens when nearby layers of fluid cannot keep up with the layer of fluid immediately next to the very fast moving wall, due to too small a viscosity, leaving an increasing space between them, leading to low pressure and the formation of bubbles (very often accelerated to supersonic velocities by the very important pressure gradient). On the other hand, in the case of non-moving walls, fluid immediately next to it should have zero velocity.

Boundary conditions: fluid interface

The other type of boundary is the an interface between two fluids. Fluid interfaces can be considered at two levels: the macroscopic (continuum) level and the microscopic (discrete) level. This section concentrates on continuum fluid dynamics and will therefore consider the continuum representation of fluid boundaries. We refer to Rowlinson and Widom [171] for microscopic information about interface structure. In the case of an interface between two fluids ((1) and (2)), the tangential stresses should be continuous through the interface (to avoid any *cavitation* of the two fluids):

$$\left(\sigma^{(1)}_{\alpha\beta} \cdot n_\alpha\right) \cdot t_\alpha = \left(\sigma^{(2)}_{\alpha\beta} \cdot n_\alpha\right) \cdot t_\alpha \,,$$

where n_α and t_α are the normal and tangential unit vector of the interface. It can be understood as the necessity for the interface to have no structure and therefore cannot be the host of any discontinuity (at least from a continuum point of view). Therefore, the condition that the tangential stresses should be continuous leads immediately to the condition (after equation 1.9):

$$\mu_1 \, \partial_y u^{(1)}_\alpha = \mu_2 \, \partial_y u^{(2)}_\alpha \,,$$

where the interface is located in the $x - z$ plane. However, the normal stresses experience a step through the interface due to the effect of surface tension of the

interface of the two fluids. This surface tension if the consequence of the difference of affinity and density of the two fluids in contact. The standard condition on the normal stress at the fluid interface boundary is given by ([116]):

$$\sigma^{(1)}_{\alpha\beta}\,\mathbf{n}_\beta - \sigma^{(2)}_{\alpha\beta}\,\mathbf{n}_\beta = \gamma_{12}\left(\frac{1}{R_1}+\frac{1}{R_2}\right)\mathbf{n}_\alpha\,.$$

As seen previously, normal stresses are closely related to pressure. The normal stress step of the interface corresponds macroscopically to a pressure step from the inside to the outside of the droplet, as defined by the Young-Laplace law:

$$\triangle P = P_1 - P_2 = \gamma_{12}\left(\frac{1}{R_1}+\frac{1}{R_2}\right) \tag{1.18}$$

where γ_{12} is the surface tension coefficient between fluid 1 and fluid 2, and R_1 and R_2 are the local principal radii of curvature. The surface tension parameter is most often positive, indicating that the pressure is higher on the concave side of the interface.

Multi-component(>2) fluid interface

The same approach is taken in the case of an interface between N fluids: a line of contact is subjected to the tensions of the N different surfaces and, since it is without mass (by definition), the vector resultant of the N tensions must have zero component in any direction in which it is free to move. When one of the N media is a solid, the local surface of which will normally be a plane, the line of contact is free to move only in one direction parallel to the solid surface. The following single scalar condition for equilibrium is then given by (in the case of three media, where media 1 is the wall, and 1 and 2 are fluids) by:

$$\gamma_{12} = \gamma_{31} + \gamma_{23}\,cos\theta_c \tag{1.19}$$

which determines and defines the angle of contact θ_c (see figure 1.1).

1.2 Classical Fluid Dynamics modeling techniques

1.2.1 Euler vs Lagrange

A fluid *particle* is defined as an element of fluid V such as its size is very small relative to the length scale that characterises the flow and very large relative to the

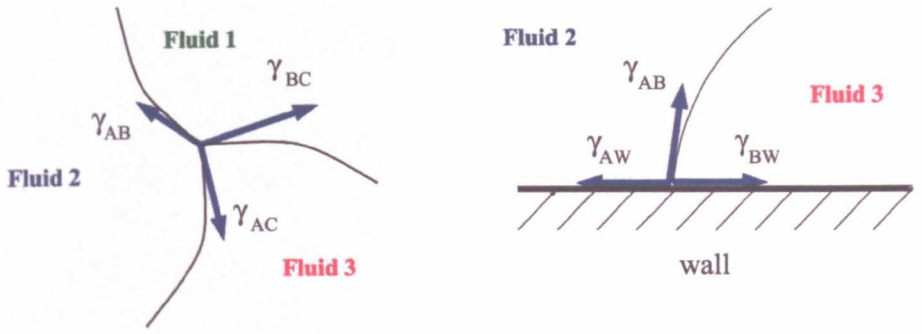

Figure 1.1: Surface tension geometry in the case of three components.

mean free path of a molecule [125]. This is to ensure good statistics of the different quantities within the volume of fluid (particle) and consequently their averages and evolution. When this applies (for most gas problems at normal pressure and for most liquid problems), the fluid can be treated as a *continuous medium* and two distinct alternatives of fluid specification are possible, differing in their reference to the fluid. The first one, the Lagrangian description, considers a fixed volume of fluid V given at a time reference ($t = 0$ generally) advecting with the flow. The flow observables are defined as functions of time and of the choice of material element of fluid, and describe the dynamical history of this selected fluid element (contained in the moving volume V). Useful in certain special contexts, it leads however to rather cumbersome analysis and is at a disadvantage in not giving directly spatial gradients in the fluid ([6]). That is why a rather less complicated approach is used: the Eulerian approach. Here the velocities considered are at a *fixed* point. At each instant of time, the velocity field describes the velocity of different fluid particles (of volume V). Methods describing explicitly each molecule are qualified as Lagrangian while any grid-based approach is therefore qualified as Eulerian. LB is Eulerian.

CFD techniques

The NSE are analytically solvable for only very simple problems where important simplifications, due to the configuration of the flow, can be made. Otherwise, numerical techniques are the only alternative, with the advantage that a solution to the NSE can be obtained, but with the drawbacks of limited accuracy and efficiency. First, some standard techniques to discretise PDEs will be reviewed, since they are very often used to solve the NSE (standard CFD solvers for example). The LBM

will then be described, showing its essential difference: it is restricted and designed to solve the NSE (with additional terms as well such as gravity, surface tension, and other effects if necessary).

Finite difference

The whole idea of discretisation is to replace the (infinitesimal) partial derivatives of the NSE with a suitable (finite) differences quotient (definition of a derivative), i.e. a *finite difference*. This implies a discretisation of the simulational space. Most common finite-difference representations of derivates are based on the Taylor series expansions, where the zeroth order is a first guess (not really good), the first order adds information to capture the slope of the curve and the second order its curvature. It can be shown that partial derivatives can be written as:

$$\partial_x(u) = \frac{u_{i+1,j} - u_{i,j}}{\triangle x} + 0(\triangle x) = \frac{u_{i+1,j} - u_{i-1,j}}{2\triangle x} + 0(\triangle x)^2\,,$$

$$\partial_t(u) = \frac{u_{i,j+1} - u_{i,j}}{\triangle x} + 0(\triangle x) = \frac{u_{i,j+1} - u_{i,j-1}}{2\triangle x} + 0(\triangle x)^2\,,$$

where u_{ij} is the quantity of interest, i is the spacial index and j is the time index. It can be noticed immediately that the accuracy of the solution will depend greatly on the chosen accuracy of the finite difference.

finite volume methods

Finite volume methods do not differ much from the finite-difference technique in that they also involve a discretisation, but now of the integral form of the evolution equation this time. For example, the equation:-

$$\partial_t \int\int\int_V \rho\, dV + \int\int_S \rho\, \mathbf{u}\, dS = 0\,,$$

is the integral form of the continuity equation (where S is the control surface bounding V). Replacing these integrals by finite volumes (which is what an integral represents) enables integral equations to be solved.

These are standard numerical methods for solving non-linear PDE, which can be used for any (including non-fluid dynamics related) problem. Another approach is kinetic theory, which is purposely designed to solve fluid dynamics related problems and described below.

1.3 Kinetic Theory: from Atomistic Dynamics to Thermodynamics

The last section derived the NSE describing the macroscopic fluid flow that fluid dynamics solvers (like LBM) have to recover, it is however necessary to start from the atomistic level (microscopic) to derive the LBM which, as we will see, recovers the NSE to a very good accuracy. This first part follows essentially S. Succi's approach towards LB, from his book *The lattice Boltzmann equation.* [190]. Additional information has been taken from the on line lecture notes by J. R. Graham's from Berkeley University on *Astrophysical Gas Dynamics* [77], from *Statistical Physics and the Atomic Theory of Matter, from Boyle and Newton to Landau and Onsager* by S. G. Brush [21], and from the unavoidable text book by S. Chapman and T. Cowling [28] (*The Mathematical Theory of Non-Uniform Gases*).

1.3.1 Atomistic dynamics

Boltzmann's original concern was to derive the second law of thermodynamics for continuum physics from principles of classical mechanics, and gather more insight on the apparent contradiction on irreversibility of continuum mater (second law of thermodynamics) and reversibility of discrete matter (classical Newtonian mechanics). Through this process, in 1868, he derived a law of velocity distribution for a gas at equilibrium, with an external force field such as gravity present (thus expanding the previous Maxwell's law) [21]. This had been one of the first milestone of kinetic theory, which lead to the description of the motion of a fluid four years latter (still by Boltzmann). In that sense, kinetic theory describes the motion of a fluid by considering a large number of molecules rather than each of their individual motion.

1.3.2 Boltzmann approach

Momentum distribution function

First, the following key quantity has to be defined: *what is the number of molecules in a volume* $(\triangle \mathbf{x})^3$ *with velocities in the range* $\mathbf{v}$ *and* $\mathbf{v} \pm \triangle \mathbf{v}$*?*
The answer is represented the quantity $f(\mathbf{x}, \mathbf{v})$ [28]. This very simple statement is

indeed very powerful since the quantity f does not have to be quantified, precisely its evolution and statistics are enough to derive the laws of fluid motion. Making $\Delta\mathbf{x}$ and $\Delta\mathbf{v}$ infinitesimal, the number f becomes a probability depending on position $\mathbf{x}$ and velocity $\mathbf{v}$. In fact, this *infinitesimal* point of view is from the continuum level, where the number of molecules considered in V is large and V itself is very small compared to the macroscopic length scale (which crosses the definition of fluid's *particle* mentioned previously). This distribution f is the pivotal object in kinetic theory, and will be omnipresent in this thesis.

Macroscopic observables from the momentum distribution function

Integrating the distribution f over $\mathbf{v}$ won't necessarily add up to unity, since f is derived from a *non-normalised* number of molecules, and leads to:

$$\int f(\mathbf{x},\mathbf{v})\, d\mathbf{v} = N_{mol}(\mathbf{x})\,,$$

where $N_{mol}(\mathbf{x})$ is the total number of molecules at V and $\mathbf{x}$. In addition, since f relies to a constant finite volume of fluid (taken to be unity), we have:

$$m \int f(\mathbf{x},\mathbf{v})\, d\mathbf{v} = \rho(\mathbf{x})\,, \tag{1.20}$$

where m is the mass of the fluid particle and $\rho(\mathbf{x})$ is the fluid weight at $\mathbf{x}$, in the volume V: its density. The distribution's total momentum and total energy are simply the sum (or integral) of all the associated momentum and energy of each molecule. They can be computed by 'moments' of f:

$$m \int f(\mathbf{x},\mathbf{v})\, v_\alpha\, d\mathbf{v} = \rho(\mathbf{x})\, u_\alpha(\mathbf{x}) \tag{1.21}$$

$$m \int f(\mathbf{x},\mathbf{v})\, \mathbf{v}^2/2\, d\mathbf{v} = \rho(\mathbf{x})\, e(\mathbf{x}) \tag{1.22}$$

where u_α is the macroscopic flow speed (by convention, v_α is the microscopic molecule's velocity) in the α direction and $\rho(\mathbf{x})\, e(\mathbf{x})$ the energy density. This had been the only way to deal with large numbers of particles whose precise positions and velocities at any instant are unknown. Laplace believed in the deterministic property of the evolution of a gas, and imagined that if a super-intelligence (such as current super-computers) were supplied with complete information about all individual atoms at

one time, it could compute their positions and motions at any other time as well as the macroscopic properties of that gas. Modern quantum physics, however, opposes such an idea through the Heisenberg uncertainty principle, that the accuracy on the position of a quantum particle (such as a gas molecule) and the accuracy on its speed are balanced (there would be no point in wanting to find the precise trajectory of a molecule if its position or velocity were to be subjected to a great uncertainty). Quantum restrictions don't allow a direct bridge to continuum physics, but kinetic theory does!

1.3.3 The Boltzmann equation

In 1872, Boltzmann presented, in a long paper, the evolution equation of the previous quantity f derived from atomistic interaction, which became known as the Boltzmann Equation (BE). It is important to realise the apparent contradiction of the BE: it represents the non-stochastic evolution of an unquantified quantity!

Exact evolution

The first step towards the BE is to find the *rate of change in time* of f. As mentioned previously, f represents a large number of molecules rather than a single particle, and therefore its evolution cannot be represented by a simple time derivative (recall the Eulerian approach). The partial derivative with respect to time $\partial/\partial t$ represents the rate of change of a quantity at a point which is fixed in space and which is occupied by a succession of different fluid particles in turn. The quantity f represents a large number of particles on the move, on the other hand, and therefore these particles occupy a succession of different points (recall the Lagrangian approach). The answer to this paradox is readily found by the Taylor expansion, keeping the first order terms [77]:

$$Df = \frac{\partial f}{\partial t}dt + \frac{\partial f}{\partial x_1}v_1 + \frac{\partial f}{\partial x_2}v_2 + \frac{\partial f}{\partial x_3}v_3 .$$

We will use the following symbol convention:

$$\partial_t = \frac{\partial}{\partial t}, \quad \partial_\alpha = \frac{\partial}{\partial r_\alpha}, \quad \partial_{c\alpha} = \frac{\partial}{\partial c_\alpha} .$$

Following the fluid, the rate of change (or total change during dt) of the quantity f subjected to an external force $\mathbf{F}$ can be re-written as:

$$f(\mathbf{x} + \mathbf{c}\,dt, \mathbf{c} + \mathbf{F}\,dt, t + dt)\,d\mathbf{x}\,d\mathbf{c}\,dt - f(\mathbf{x}, \mathbf{c}, t)\,d\mathbf{x}\,d\mathbf{c}\,dt = \Omega(f)\,d\mathbf{x}\,d\mathbf{c}\,dt\,,$$

where $\Omega(f)$ is the collision operator since $D_t f$ is also equal to the rate of change of the particles undergoing collisions. Letting $dt \to 0$ gives the BE [28]:

$$D_t f = \partial_t f + (u_\alpha \cdot \partial_\alpha)\, f + F_\alpha \cdot \partial_{c\alpha} f = \Omega(f)\,. \tag{1.23}$$

First assumption

The simplest case is to consider the one body distribution f_1 (note that in this chapter, unless otherwise stated, the subscript C on f_C represents the number of bodies of the distribution), and equation 1.23 reads as follow:

$$D_t f_1 = \partial_t f_1 + (u_\alpha \cdot \partial_\alpha)\, f_1 + F_\alpha \cdot \partial_{c\alpha} f_1 = C_2\,, \tag{1.24}$$

where C_2 is the binary collision operator (note that C_1 is absurd) and represents the effect of intermolecular (two-body) collisions taking molecules in/out the streaming trajectory ($C_2 = D_t f_1$). Equation 1.24 is the beginning of the so called BBGKY hierarchy, after Bogoliubov, Born, Green, Kirkwood and Yvon [12] where the dynamic equation for f_2 depends on the three-body distribution function f_3 which in turn depends on f_4 and so on down an endless hierarchy [190].

To close this hierarchy, Boltzmann made few stringent assumptions on the nature of the physical system that was considered: a *dilute gas* of *point-like* and *structureless* molecules was assumed. This assumption has the consequence (unfortunately) of erasing any dependance of the dynamics upon the detailed chemistry of the molecules. However, within this picture, the collision operator of equation 1.24 becomes the (self sufficient) integro-differential function:

$$C_2 = \int [f_2(v_1', v_2') - f_2(v_1, v_2)]\, G(v_1, v_2, v_1', v_2')\, d^3\mathbf{v}\,, \tag{1.25}$$

where the function G depends on the nature of the forces between the molecules, $\{v_1, v_2\}$ are the pre-collisions velocities of the colliding particles (remember that C_2 considerers binary collisions) and $\{v_1', v_2'\}$ are their velocity after collision.

Second assumption

At this point, Boltzmann made another assumption: there is no statistical correlation between the velocities of two molecules before they collide (and therefore after collisions). In other words, they interact via *short-range* two-body potentials. Elementary statistics reminds us that the probability of two uncorrelated events is simply the product of their respective probabilities, which leads to the famous Boltzmann closure assumption, *molecular chaos* or *Stosszahlansatz* [11]:

$$f_2(v_1', v_2') = f_1(v_1) f_1(v_2)\,.$$

This is the main assumption in his theory and is still the subject of active discussions because even-though this assumption is reasonable for dilute gas where molecules spend most of their life traveling alone and being absolutely unaware of their surroundings, it is certainly not so true for liquids. It should also be noted that, even-though it is reasonable to assume no correlation between the molecules before they have ever collided (at the beginning of time say), this lack of correlation for a particle is immediately lost after its first collision, by virtue of mass, momentum and energy conservation.

Summarising, the BE takes the following form ([125]):

$$(\partial_t + \mathbf{u}\cdot\nabla + \mathbf{F}\cdot\partial_{\mathbf{p}}) f_1 = \int \left[f_1(v_1') f_1(v_2') - f_1(v_1) f_1(v_2)\right] G(v_1, v_2, v_1', v_2')\, d^3\mathbf{v}\,.$$

The beauty of this equation is that it links atomistic and continuum behaviour. The left hand side is the faithful microscopic *reversible* Newtonian single-particle dynamics while the right hand side describes continuum intermolecular interactions which, we will see in next section, is *irreversible*. Additional terms can be added to take account of gradient of temperature and fluid velocity, and are known as the *Boltzmann's transport equation*. Boltzmann then showed that collisions always push the distribution f towards the so called *Maxwell-Boltzmann equilibrium distribution function* (note that Maxwell had first given the definition of this distribution [28] by deriving the equilibrium velocity distribution of gases, but without external force).

Dynamical evolution of any fluid velocity distribution: the H-theorem

Although processes are generally reversible at the molecular level, it is known that most macroscopic processes are irreversible. The BE must hold the key. Boltzmann

showed that the following quantity:

$$H = \int f \log(f)\, d\mathbf{v}$$

was always decreasing (a formal derivation can be found in [164] or [125] for example):

$$D_t H \leq 0.$$

In other words, this (H-) theorem states that a uniform gas with a random distribution of velocity will decrease monotonically to an equilibrium state through the effect of collisions. That is, only when $f_1(v_1')\, f_1(v_2') = f_1(v_1) f_1(v_2)$ (hence $D_t H = 0$), which introduces the notion of local equilibrium: when the distribution remains unchanged under the effect of collision (hence time). It should be emphasised that the H-theorem is not in general the same as the principle of monotonic increase of entropy (second law of thermodynamics), in that H is only defined for a uniform gas (see previous Boltzmann's assumptions) while the entropy can be defined for complex systems. Moreover, H is defined for any distribution while entropy is only for system in thermodynamic equilibrium. Therefore, only the special case of a *dilute gas in thermodynamic equilibrium* can H and entropy be defined at the same time. Under these circumstances, the entropy is related to H by $S = -k_B H + K$ where S is the entropy of the system, k_B is the Boltzmann constant and K is a constant [125].

Boltzmann further showed that the collisions are pushing the distribution f towards the equilibrium Maxwell distribution. The H-theorem is equivalent to the generalisation to a dilute gas at non-equilibrium to the statement that the entropy always increases or remains constant (2nd law of thermodynamics) [21].

A first justification could be the general tendency for systems to pass irreversibly towards thermal equilibrium. Boltzmann had another justification, less clear, that the entropy-increasing process corresponds to a transition from less probable to more probable microstates, and entropy itself can be interpreted as a measure of probability. In this view, the Maxwell distribution is therefore the one most likely to be found in thermal equilibrium because it corresponds to the largest number of micro-states. For further reading, see [21] (pages 64-104).

The idea of unavoidable increase of entropy and decrease of the quantity H relate

both ultimately to Clausius' idea of *Heat Death*, namely the universe as a whole evolves in a unique way towards a state of maximum entropy (and minimum H) where all energy is diffused uniformly through space at a temperature very close to absolute zero, so that no mechanical work can be done and life cannot exist. This rather disturbing idea goes along side the idea of unavoidable and unidirectional decay of matter into lead. For further readings, see the section *irreversibility* of D. Levermore's website from the University of Maryland [123].
The next section will concentrate on defining this *equilibrium distribution function* introduced by the H-theorem.

1.3.4 Relaxation to local equilibrium

It is important at this point to distinguish between two different equilibria: the *'state'* or *'macroscopic'* or *'global'* equilibrium and the *'thermodynamical'* or *'microscopic'* or *'local'* equilibrium. The main difference lies in the scale at which they may be represented. Global equilibrium is reached when the macroscopic properties of a system's constituents are not observed to change as further time elapses (density, pressure, temperature, magnetisation, etc) while thermal equilibrium is compatible with rapid spatial variations in the state of the system at the microscopic level of its constituent molecules. Local equilibrium is defined mathematically as a local distribution function f^e, such that gain and loss to the microscopic system are in exact balance [125], so that from equation 1.24:

$$C_2(f^e, f^e) = 0, \tag{1.26}$$

where the subscript *'e'* denotes *'equilibrium'* hereafter. After equation 1.26, this leads to:

$$f_1(v_1')\, f_1(v_2') = f_1(v_1)\, f_1(v_2)\,. \tag{1.27}$$

Following Liboff [125], the logarithm of equation 1.27 gives:

$$ln(f_1(v_1')) + ln(f_1(v_2')) = ln(f_1(v_1)) + ln(f_1(v_2))\,. \tag{1.28}$$

The equality shows that the quantity $ln(f^e)$ does not change under the effect of collisions (remember the left hand side of equation 1.27 represents the pre-collision distributions and the right hand side represents the post-collision distributions). In

addition, at thermodynamic equilibrium, $ln(f)$ must be a linear combination of the three collision invariants defined previously (namely mass, momentum and energy) ([28]):

$$ln(f^e) = A + B_\alpha v_\alpha + C u^2/2,$$

where A, B_α, C are five Lagrangian multipliers defined solely by the macroscopic observables (equation 1.20, 1.21, and 1.22). Elementary quadrature of Gaussian integrals delivers the celebrated Maxwell-Boltzmann equilibrium distribution [190], giving the number of molecules (or probability) with velocity $\mathbf{v}$ with respect to their local density ρ at a temperature T. In D spatial dimensions:

$$f^e(\mathbf{v}, \rho, T) = \rho\,(2\,\pi\,v_T^2)^{-D/2} e^{-\mathbf{c}^2/2v_T^2}\,, \tag{1.29}$$

where $\mathbf{c}$ is the so-called *peculiar velocity*

$$\mathbf{c} = \mathbf{v} - \mathbf{u}\,, \tag{1.30}$$

and

$$v_T = \sqrt{\frac{K_B T}{m}}\,,$$

is the thermal speed associated with the fluid temperature T. It is interesting to note that f^e only depends on the fluid's local macroscopic observables, and is independent of the local neighbouring, chemistry or external fields (it can therefore be greatly different from time to time and from a point in space to another). This infers for this function a notion of absoluteness, which can be viewed as a weakness: it is legitimate to question its applicability and validity when considering the assumptions made to obtain *this equilibrium distribution*, and whether what it represents alongside its dynamics are representative of a real fluid. One could even argue that Boltzmann did everything he could possibly do to get to this result, which shows the limits of this distribution function and demonstrates its paradox: even though it claims to be absolute, it lacks applicability to any real fluid.

These ideas are still highly discussed and argued. To the author's mind, this should not be forgotten, especially when developing a simulation technique that is based on the BE and the Maxwell-Boltzmann equilibrium distribution function (the LBM). The LBM, on the other hand, has been shown to provide (surprisingly maybe?) great results and it has a great advantage to other techniques: locality and 'physicality'.

1.4 From kinetic theory to fluid dynamics

1.4.1 The Boltzmann transport equation

General statements cannot be easily extracted from the BE apart from the H-theorem. A more fruitful approach considers its moments: the one associated with the mass and momentum in particular. Multiplying the BE by some function $Q(\mathbf{x}, \mathbf{v}, t)$ and integrating over all velocities, gives after some algebra:

$$\partial_t \int f_1 Q \, d\mathbf{v} - \int f_1 \, \partial_t Q \, d\mathbf{v} + \partial_\alpha \int Q \, f_1 \, v_\alpha \, d\mathbf{v} - \int f_1 \, v_\alpha \partial_\alpha Q \, d\mathbf{v} + \int F_\alpha \partial_{c\alpha} f_1 \, Q \, d\mathbf{v} = \int Q \, D_t f_2 \, d\mathbf{v} \,. \tag{1.31}$$

Equation 1.31 is the transport equation, and tells us how the volume density $\int f_1 Q \, d\mathbf{v}$ of any quantity that is conserved in binary collisions evolves with time. For a such a quantity Q, the second term $\int f_1 \, \partial_t Q \, d\mathbf{v}$ and the collision integral $\int Q \, D_t f_2 \, d\mathbf{v}$ vanish [77].

First, setting Q to m (the particle's mass), the volume density $\int f_1 \, Q$ gives ρ and any of gradient in Q (spatial or temporal) vanish (because the fluid is considered as incompressible). Therefore, equation 1.31 yields the mass conservation equation seen previously in this chapter (continuity equation 1.6):

$$\partial_t \rho + \partial_\alpha (\rho \, u_\alpha) = 0 \,.$$

Second, setting Q to $m \, u_\alpha$ (the particle's momentum), the volume density $\int f_1 \, Q \, d\mathbf{v}$ gives $\rho \, u_\alpha$ and (after some algebra), $\int v_\alpha f \partial_\alpha m \, u_\beta \, d\mathbf{v}$ gives $\partial_\alpha (P \, \delta_{\alpha\beta} - \sigma'_{\alpha\beta})$, where $\sigma'_{\alpha\beta}$ is the dissipative term of the momentum stress tensor (see equations 1.8 and 1.10). Therefore, equation 1.31 yields also the momentum conservation equation:

$$\partial_t (\rho \, u_\beta) + \partial_\alpha (\rho \, u_\alpha \, u_\beta + P \, \delta_{\alpha\beta} - \sigma'_{\alpha\beta}) + \rho \, F_\beta = 0 \,.$$

This equation can be recognised as the NSE (equation 1.15) and verifies that the (*microscopic*) BE recovers the (*macroscopic*) NSE introduced in previously.

The transport equation is consequently seen as the gateway from the world of microphysics to the world of macrophysics through its moments.

1.4.2 Bhatnagar–Gross–Krook model equation

Since we have defined a (universal) equilibrium distribution function, any distribution can be written in the form:

$$f(\mathbf{x}, \mathbf{v}, t) = f^e(\mathbf{x}, \mathbf{v}, t) + g(\mathbf{x}, \mathbf{v}, t)\,,$$

where f^e is the Maxwellian distribution function (see equation 1.29) and g describes any departure from it. With this definition, in 1954, Bhatnagar, Gross and Krook [9] re-wrote the BE (equation 1.23) in terms of equilibrium and non-equilibrium parts:

$$\Omega(f) = -\nu_c\,(f - f^e)\,, \tag{1.32}$$

therefore,

$$D_t f = -\nu_c\,(f - f^e)\,. \tag{1.33}$$

where ν_c is the collision rate associated with the collision time $\tau_c = 1/\nu_c$. This is the so-called BGK collision operator. Equation 1.33 is named the BGK equation and is much easier to solve than the integro-partial differential equation that is the BE, and most of all, without spoiling the basic physics. Since ν_c can be regarded as independent of f, the BGK equation is linear in f. This allows much easier computation of the transport coefficients and provides a great advantage in subsequent computer models (like LBM) [190].

1.4.3 The Chapman-Enskog procedure

Since the BGK equation provides a simple alternative to the BE, it is interesting to investigate the consequence of the simple collision operator structure on its moments. To do so, a characteristic small parameter needs first to be defined. It is usually taken to be the *Knudsen number* (see J. R. Graham [77] for a justification of this choice), namely the ratio between the molecular mean free path and the shortest scale at which macroscopic variations can be appreciated (note that the bridge between micro and macro becomes explicit here):

$$\epsilon = \frac{l_{mfp}}{l_{Macro}}\,.$$

The Chapman–Enskog procedure is based on a double expansion in the smallness

parameter of both dependent $f(\mathbf{x}, \mathbf{v}, t)$ and independent space-time (x, t) variables (see [125], [28] for a detailed derivation of this expansion). First, the momentum densities are separated between equilibrium ($f^{(0)}$) and non-equilibrium ($f^{(1)}$) parts:

$$f = f^{(0)} + \epsilon f^{(1)} .$$

Note that the major difference between g defined in the BGK equation and $f^{(1)}$ here is that $f^{(1)}$ is assumed $O(1)$ (the smallness of the non–equilibrium part is carried by the pre-factor ϵ) while g carried the smallness and is therefore much smaller than $f^{(1)}$. It should also be understood that $f^{(1)}$ defined as above contains implicitly a whole series of terms: $f = \sum_{n=0}^{\infty} \varepsilon^n f^{(n)}$ (where each f^n is $O(1)$).
Second, time and space are expanded up to the second order:

$$\begin{cases} x &= \epsilon^{-1} x_1 , \\ t &\approx \epsilon^{-1} t_1 + \epsilon^{-2} t_2 , \end{cases}$$

and the differential operators likewise:

$$\begin{cases} \partial_x &= \epsilon \, \partial_{x_1} , \\ \partial_t &\approx \epsilon \, \partial_{t_1} + \epsilon^2 \, \partial_{t_2} , \end{cases}$$

hence the streaming operator becomes:

$$D_t \approx \epsilon \, \partial_{t_1} + \epsilon \, \partial_{t_2} + \epsilon \, u_\alpha \partial_{\alpha_1} + \frac{1}{2} \epsilon^2 \, u_\alpha \, u_\beta \, \partial_{\alpha_1} \, \partial_{\beta_1} .$$

This analysis will be restricted to the second order of the time expansion for reasons that are explained latter. In this analysis, x_1 and t_1 represent the linear (sound wave) fast regime while t_2 represent the long-term (slow) dynamics. This segregation between equilibrium term (fast) and non equilibrium term (slow) is explicit in the moments of the subsequent equations. The zeroth order term of the distributions $f^{(0)}$ is the local Maxwell-Boltzmann distribution function defined in equation 1.29. Similarly as in section 1.4.1, we integrate the BE over $\mathbf{v}$ and take its zeroth and first moments. The first order solutions are found by considering $O(\epsilon)$ in the integrated BE and give (for the zeroth and first order momentum respectively):

$$\partial_{t_1} \rho + \partial_{\alpha_1} \rho u_\alpha = 0 ,$$

$$\partial_{t1}\rho u_\alpha + \partial_{\beta_1}(\rho u_\alpha u_\beta + P\delta_{\alpha\beta}) = 0\,,$$

where $P = \rho T$ is the fluid pressure. These equations are recognised to yield the Euler equations of inviscid flows (equation 1.16). However, although this represents a dynamical evolution of a fluid, the fluid's viscosity is missing in the equation: the distribution of the fluid had been assumed to be the local Maxwellian distribution at all points at all times. Transport phenomena occur when there are large gradients of temperature or velocity, and this should be taken into account in the evolution of f (not only $f^{(0)}$).

It is therefore important to investigate the non-equilibrium moments. The second order solutions are found by considering $O(\epsilon^2)$ in the integrated BE and read as follow:

$$\partial_{t_2}\rho = 0\,,$$
$$\partial_{t_2}\rho u_\alpha + \partial_{\beta_1} m \int \left(f^{(1)} + \partial_\gamma v_\gamma f^{(0)}\right) u_\alpha u_\beta \, d\mathbf{v} = 0\,.$$

In fact, by splitting f into equilibrium ($f^{(0)}$) and non-equilibrium ($f^{(1)}$) components, it can be shown that the two integrals represent the equilibrium and non-equilibrium components of the momentum flux tensor $P_{\alpha\beta}$ defined as follows:

$$P_{\alpha\beta} = m \int f\, v_\alpha\, v_\beta \, d\mathbf{v}\,.$$

Respectively (for an incompressible fluid):

$$\begin{cases} P_{\alpha\beta} \equiv T_{\alpha\beta} + \tau_{\alpha\beta}\,, \\ T_{\alpha\beta} \equiv m \int f^{(0)} v_\alpha v_\beta = \rho\, u_\alpha\, u_\beta + P\delta_{\alpha\beta}\,, \\ \tau_{\alpha\beta} \equiv m \int f^{(1)} v_\alpha v_\beta = 2\,\mu\, S_{\alpha\beta}\,. \end{cases}$$

It is important to notice here that the dissipative term of the momentum flux tensor ($\tau_{\alpha\beta}$) is equal to the viscous stress tensor $\sigma'_{\alpha\beta}$ (equation 1.10) which can therefore be computed purely locally. It provides a great reduction in its computation in the subsequent method (LBM).

Finally, joining the non-equilibrium and equilibrium parts of the zeroth and first moment of the BE order by order gives the NSE.

This demonstrates that a distributions can be explicitly spit into equilibrium and non-equilibrium parts and yet, its evolution still recovers correct continuum viscous

fluid behaviour, despite the assumptions necessary to get to this result. It therefore demonstrates the fact that the NSE contain, implicitly, the same assumptions as Boltzmann's (hidden in its large time and length scale). It can also appear rather surprising that the second order in the truncation of the Knudsen number ϵ does recover the full NSE, but it is fortunate on the other hand, since the Chapman-Enskog treatment of the BE does not converge for higher orders of the Knudsen number: for example, Bobylev [10] has shown that the Burnett and super-Burnett hydrodynamics (from the third and fourth order respectively) violates the basic physics behind the Boltzmann equation (which is now known as the Bobylev instability) and Succi notes that they are exposed to severe numerical instabilities [190]).
In order to recover non-ideal fluid motion (i.e. non Newtonian or visco-elasticity), the 'trick' is to impose additional dependence on the hydrodynamic parameters. This is precisely what CFD solvers do.

1.5 LB: the construction of the algorithm

Historically, U. Frish, B. Hasslacher and Y. Pomeau developed the first simple cellular automaton obeying nothing but conservation laws (see section 1.1.2) at a microscopic level, and were able to reproduce the complexity of real fluid flow [62]: the Lattice Gas Cellular Automaton (LGCA). Then, the earliest example of LBM was essentially an attempt to address statistical noise inherent in LGCA ([137]). With time, the LB technique evolved into a self-standing research subject ([190]). He and Luo [86] showed that, theoretically, the lattice Boltzmann equation (LBE hereafter, equivalent of the BE) is independent of the lattice-gas automaton. Therefore, rather than providing a long genealogical tree (see Succi [190] for more details), this section concentrates on showing how the LBM relates to the continuum and statistical fluid dynamics just described, in a self-consistent matter.

1.5.1 The LBE: a discrete form of the BE

It is interesting to note that other approaches are available to validate the dynamics of LBE. Luo *et al.* for example have shown rigorously that the LBE is a specially discretised form in both space and time of the continuous BE which provides solid

theoretical foundations in order to address several issues inherent to the LBM [85], [86].

First of all, time has to be discretised, decomposing the algorithm into a repetition of two procedures: *collision* and *propagation.* The collision step is taken to be instantaneous (following Boltzmann's assumption), and time evolution is carried by the propagating step. Second, space is discretised, by choosing an adequate lattice element enabling a regular pattern for the nodes and links to be used.

1.5.2 Lattice geometry

Most of LB models deal with a regular lattice, simplifying greatly the algorithm. However, there is nothing preventing one from inventing a complicated geometrical lattice with irregular pattern with appropriate interpolation schemes (multi-grid via recursive sub-division or adaptative meshing) such as the one from [43], [112], [102] for example. The distribution densities f's are transformed into a discrete distributions f_i's that are restricted to exist only on nodes of the lattice and to travel to a neighbouring nodes only (through the links of the lattice). In this way, the *continuous* quantity $f(\mathbf{x}, \mathbf{v}, t)$, described in previous sections, is restricted to exist only on a small number of velocities (equal to the number of neighbouring nodes) and becomes the *discrete* momentum distribution $f_i(\mathbf{x}, t)$: the probability density of the discrete velocity $\mathbf{c}_i$ at position $\mathbf{x}$ and time t. In LB, geometries are commonly designated D_nQ_m, for m discrete speeds and n dimensions (i can take only m different values).

1.5.3 The propagating step

As mentioned previously, in LB densities travel from a node, along the links of the lattice, onto a neighbouring node, spending the amount of time δt. It is important to realise that all the f_i's propagate at the same time, and do not interact doing so (which is consistent with Boltzmann's assumption): 'they fly alone, unaware of each other'.

1.5.4 The collision step

The collision step is the key to the method: this is the step that provides the method with most its hydrodynamics. Recalling the (relatively) simple form of the BE,

$$D_t f = C_2 ,$$

where f is the continuous distribution function and C_2 is the collision operator. It can be shown that the LB scheme has the same evolution:

$$\Delta f_i = C_i(f_i) ,$$

where $C_i(f_i)$ represents the effect of collisions on f_i. Recalling also the BGK equation for continuous distribution (equation 1.33), it can be shown that the complicated discrete collision operator ($C_i(f_i)$) can be replaced by a much simpler form [190]:

$$\Delta f_i = -\omega \left(f_i - f_i^{eq}\right) , \tag{1.34}$$

where ω is the BGK collision time and f_i^{eq} is the discrete form of the Maxwell-Boltzmann equilibrium function.

This equation has appropriately been named *lattice BGK*, *LBGK* for short. ω dictates the rate at which a distribution relaxes towards its corresponding local equilibrium and dictates the rate of transport in the same way: it can be shown that ω relates very simply to the fluid's viscosity [190]:

$$\nu = \frac{1}{6}\left(\frac{2}{\omega} - 1\right) . \tag{1.35}$$

Qian *et al.* [162] note that the physical requirement of positive viscosity (that standard theoretical fluid dynamics requires [81]) gives the condition for numerical stability that the relaxation parameter ω is bound by upper and lower limit:

$$0 < \omega < 2 . \tag{1.36}$$

Due to the simplicity and robustness of this method, the BGK evolution became the most widely used in the LB scheme.

It remains to quantify the discrete equilibrium function f_i^{eq}. It can be shown that

the LBGK equilibrium function takes the form [190]:

$$f_i^{eq} = \rho t_i \left(1 + \frac{c_{i\alpha} u_\alpha}{c_s^2} + \frac{Q_{i\alpha\beta} u_\alpha u_\beta}{2 c_s^4}\right), \tag{1.37}$$

where $Q_{i\alpha\beta} = c_{i\alpha}c_{i\beta} - c_s^2\delta_{\alpha\beta}$ is the kinetic projector and w_i are multiplying weights to take the geometry of the lattice into account. Moments and geometrical restrictions impose a unique set of values to the weights t_i. Following continuum kinetic theory, the discrete equilibrium function has to carry the same density, momentum and energy as the actual distribution function it represents (for these quantities to be conserved over collisions).

The nodal velocity u_α and density ρ can be computed by the following:

$$\begin{cases} \rho(\mathbf{x}) = \sum_i f^{eq}(\mathbf{x}) = \sum_i f(\mathbf{x}) \\ \rho(\mathbf{x})\, u_\alpha(\mathbf{x}) = \sum_i f^{eq}(\mathbf{x})\, c_{i\alpha} = \sum_i f(\mathbf{x})\, c_{i\alpha} \end{cases} \tag{1.38}$$

On the top of that, the geometry of the lattice imposes similar links (i.e. identical associated energy) to have the same weight (isotropy considerations). A whole family of solutions (DnQm, mentioned previously) follow and close the remaining degrees of freedom of equation 1.37. It should be noted that the form of f_i^{eq} is unchanged with the geometry and the number of dimensions. Only the weights vary, depending on the geometry and number of dimensions.

In this project, we use the D2Q9 geometry depicted by figure 1.2.

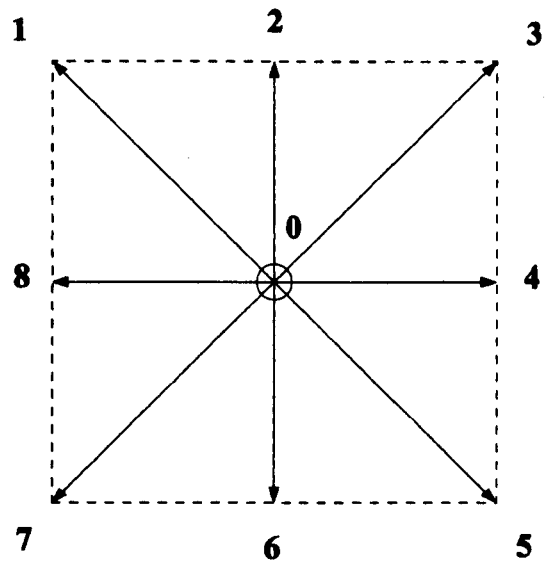

Figure 1.2: D2Q9 Lattice geometry used in this thesis.

The associated equilibrium distribution of the D2Q9 geometry is:

$$f_i^{eq}(\rho, \mathbf{u}) = t_i \rho \left[1 + 3\mathbf{u} \cdot \mathbf{c_i} + \frac{9}{2}(\mathbf{u} \cdot \mathbf{c_i})^2 - \frac{3}{2}\mathbf{u}^2\right]$$

with the associated weights:

$$t_i = \begin{cases} 4/9 & \text{for } i{=}0\,, \\ 1/9 & \text{for } i{=}2{,}4{,}6{,}8\,, \\ 1/36 & \text{for } i{=}1{,}3{,}5{,}7\,. \end{cases}$$

Conclusion

This chapter has set the essential background in continuum fluid dynamics, kinetic theory and LBM for the rest of this thesis. It has introduced the general idea of the BE and shown how Boltzmann reduced a very complex equation to a much simpler form and how it can be simplified even further to give a very elegant method, very well suited to be discretised into the a computer strategy- LBE. This chapter also showed how the Boltzmann approach relates to the continuum fluid dynamics theory and how the LBM can be derived accurately to recover the NSE.

Chapter 2

Specific Background: Binary fluids

Introduction

The previous chapter concentrated on deriving the NSE describing the motion of a continuous fluid. It has also been mentioned that this set of equations is not sufficient when discontinuities occur in the continuum fluid, in which case extra rules have to be implemented. Unfortunately for this project, an interface between two fluids represents a discontinuity for the NSE. Navier-Stokes solvers such as CFD, (see the excellent introduction by Abbot and Bascoe [1]) or LBM, (see the very good description by Succi [190]) inherit this problem, since they are primarily designed to solve the NSE alone, that is for a single fluid. First, some of the most common CFD techniques for interfaces will be described, followed by the current, main interfacial techniques in LB (fluid interface and solid boundaries). We describe the Gunstensen LB interfacial method ([80]) in details since it is the method used in this project. We finish by describing the bounce-back method for implementing LB solid non-slip walls.

2.1 Equations of motion

2.1.1 Illustration

In order to put the problem of simulating binary fluids into context, let's consider the very simple example of a water droplet sitting on a surface, surrounded by air:

- The equations describing the motion of the fluid inside the droplet (water) are the NSE with the parameters of water (viscosity, heat conduction, etc).

- The motion of the surrounding air is described by exactly the same set of equations (NSE), only with different parameters (defining the air properties). Discontinuities in the domain of application of each set of NSE therefore arise at the interface of the two sets of parameters for the NSE and the whole art and idea of any computational method for binary fluids is to bridge *as well as possible* these discontinuities.

- The transition from one domain to another has its own physics (wetting or drying for example here) and it is appropriate to consider the physics of the interfacial region as defining a particular, problematic boundary condition.

2.1.2 General requisites for numerical techniques

Numerical simulations of multiphase flow primarily requires one to locate the interfaces between the different fluids, which shape can vary and become very complex (break-up or coalescence for example). A very good discussion of this problem can be found in reference [179]. In LBM however, as Inamuro *et al.* point out ([99]), (i) LBM models have great advantages over conventional methods for multiphase flow, in that they do not track interfaces, rather they can maintain spontaneous, sharp, interfaces without any additional 'artificial' treatments, and (ii) the LBM conserves accurately the mass of each component. The issue of interface location leads to the separation of interfacial methods into two distinct categories: *Front Tracking* (FT), Lagrangian approach, and *Front Capturing* (FC), Eulerian approach (as explained for example by S. Succi in [190]). FT technics consist of following the fluid interface from the mean position of tracers embedded over the simulational fluid domain, moving and imposing forces on the flow as they deform. Methods based on this approach are robust for fairly smooth and continuous interfaces but they face major difficulties when the interface becomes tortuous, breaks-up or coalesces (as Sethian points out in reference [178]). FC based methods on the other hand overcome this problem by defining a data structure within the computational domain: the interface is defined where explicit colour discontinuities occur. However, compared to

FT techniques, they suffer from much more pronounced numerical diffusion effects which tend to smear out the interface [190].

The Laplace law (equation 1.18) indicates that a droplet at rest exhibits an inner pressure higher than its surrounding fluid, proportional to the ratio of its interfacial pressure step and its radius– defining the interfacial surface tension. As a consequence, there exist two main numerical approaches to impose surface tension on an interface: (i) imposing a pressure step directly on the interface, which defines the surface tension and (ii), imposing directly the surface tension and verifying the pressure step. Both approaches give numerical results which are equally as valid (the old argument of the chicken or the egg), but have subtle differences by design, leading to differences in applications and accuracies.

2.1.3 Binary interfaces with CFD

CFD models are especially well suited for the modeling of single component fluids. However, since their very essence is to not retain locality, they inherit difficulties in handling (sharp) discontinuities. Solid walls are not much of a problem as long as they do not move. Principally, two methods imposed themselves for multicomponent CFD methods: the Volume of Fluid (VOF) and the Set Level Method (LSM).

The VOF method

The VOF ([144], [93]) was developed in the 1960's and is still widely used by CFD solvers, mostly for liquid-gas interfaces. It consists of three ingredients: (i) a scheme to locate the surface (interface), (ii) an algorithm to treat this surface as a sharp interface moving through a computational grid and (iii) a means of applying boundary conditions at the surface. A number of VOF programs have claimed a VOF capability when in reality, they were only implementing one or two of the three VOF ingredients, giving incorrect results, as described by Hirt in [92]. Most pseudo-VOF methods use a fluid volume fraction to locate surfaces, but they then attempt to compute flow in both liquids by a boundary condition, which produces an incor-

rect motion of the surface since the boundary is assumed to move with the average velocity of both liquids. In reality, the two fluids generally move independently of one another except for a thin boundary layer. Other pseudo-VOF practices include representing the interface by a rapid spatial change in density. However, such schemes result in smoothed transition regions between gas and liquids that cover several control volumes rather than sharp interfaces localised in one control volume as the original VOF method [92]. This is especially important when computational resources are limited.

The surface tension on a VOF interface is imposed mainly by two distinct methods. The first consists of a body-force acting perpendicularly to the interface and proportional to the curvature: the continuous surface force method, CSF ([16], [39], [167], [7]). The second consists of representing the surface tension as the divergence of a stress tensor : the continuous surface stress method, CSS ([115], [176]). However, both techniques have spurious or parasite currents described by [176] as *'vortices in the neighbourhood of interface despite the absence of any external forcing. They are observed with many surface tension simulation methods, including the CSF method, the CSS method and the LB method, in which they were first discovered'.* It is interesting to note that the pattern of the micro-currents obtained in VOF methods (pattern pictured in [165] and analysed by Brackbill *et al.* [16]) is qualitatively the same as with most LB models (pattern pictured by Halliday *et al.* [82] for the Gunstensen model, by Wagner [211] for the free energy approach, by Hou *et al.* for the potential approach [95]). Reynardy *et al.* derived PROST (Parabolic Reconstruction of Surface Tension) to eliminate these micro-currents for the VOF method by interpolating the interface (see [165] and chapter 4 for more details).

Despite the very appealing properties of the VOF method, its significant drawbacks lead to the development of other interfacial methods in CFD, such as the LSM (described below).

The LSM

The LSM is much more recent that the VOF method: it was developed mainly by Osher and Sethian around the 1990's (introduced in Osher, S. and Sethian, J.A. [149], based on Sethian's earlier work [179]). The main idea of the level set method is

to consider the original interface and add an extra dimension to the problem, rather than following the interface itself: in other words, treating the problem of a moving interfacial curve (in 2D) as a moving surface. Usually, more dimensions usually mean more work but the trick of embedding the front in a higher dimensional function (the set level function) is apparently well worth the added cost, and in fact, with some work, that cost can be made the same as that of FT techniques (according to Sethian in [178]). The zero level set of a variable Φ (representing the high dimensional interface) is used to determine the position of the interface. Φ must be continuous, smooth and monotonic in the direction normal to the interface. A calculated velocity field can then be used to advect Φ. The 2D technique can be summarised as follow (from [178]): first, the evolving interface is embedded in one higher dimension, using a time-dependant function $\Phi(x, y, z, t = 0)$ in four dimensional space. And then, adjust this higher dimensional function corresponding to the motion of the interface, and compute the "zero" level set to find the position of the propagating interface. It should be noted that the LSM is not naturally conservative (because has not been designed for fluid dynamics problems initially) unlike the VOF method, and an extra mass conservation condition is required. One of the first attempt at using the LSM to address fluid problems was by Sussman *et al.* ([193] and more recently [192]) for large viscosity and density ratios problems. Chang *et al.* showed the derivation of the volume source for surface tension and implemented a mass conserving condition dependent on curvature ([27]). The LSM has even been combined with the VOF method to bring the advantages of both techniques: the LSM is used as a predicate and the VOF for mass conservation (as claimed by Bourlioux [15] and others [196], [5]). Other (non fluid related) applications, include the computation of optimal robot paths around obstacles, the extraction of clinically useful features from noisy output of medical images and the manufacturing steps of transferring a street-map of circuitry onto a small piece of silicon (more applications, information and links can be found in J. A. Sethian's website at Berkeley University [180]).

2.1.4 The main LB interfaces methods

This section details the main competing models in LB for binary fluid flow, showing their strengths, weaknesses, and where they apply best (see [95], [130], [131] for

detailed theoretical and numerical comparisons). A comparison of two-phase LB and VOF methods is available in [177]. Extensive literature on the LB multiphase and multi-component models can be found in [31], [84], [131], [170] and [169]. All of the existing LB multiphase models make full use of one of the main advantages of LBM over other numerical methods: *locality*, removing the task of tracking the interface.

Pseudo-potential approach

This approach derives directly form microscopic considerations of what is happening at the interface between two fluids: molecules sitting at the interface experience a net force driven by the different values of the average intermolecular distance and affinity in the two fluids. This difference is obviously more important for heavy/light fluid interfaces. This approach was introduced by X. Shan and H. Chen ([29], [182]) hence known as the Shan-Chen, S-C, model within the LB community. It was further improved and characterised by the same authors and G. D. Doolen ([183], [184], [185]). In this technique, both phases follow the standard LBGK evolution (equation 1.34) as a mixture, with a source term S_i^α (for the colour α) to distinguish their behaviour:

$$\left.\begin{aligned} \triangle R_i &= -\omega_s \left(R_i - R_i^e\right) + S_i^R \,, \\ \triangle B_i &= -\omega_s \left(B_i - B_i^e\right) + S_i^B \,. \end{aligned}\right\}$$

where R_i and B_i are the *red* and *blue* momentum distribution functions associated with the *red* and *blue* fluid in the lattice.

This source term represents the mesoscopic interactions between the two fluids and relates to surface tension and phase separation. It is represented by a force following pairwise interaction, namely the sum of the momentum exchanges with particles of all other species in the direct neighbourhood. Shan and Chen simplified their model, to use a single species to simulate binary fluids, by noting that the interface between two fluids could be captured by their density: a site with high density belongs to the one fluid and a site with a low density belongs to the other fluid. The transition between light and heavy fluids is controlled by a function $\chi(\rho(\mathbf{x}))$ [183] and taken to provide a sharp transition between the two phases. Sankaranarayanan and Sundaresan ([174]) and Sankaranarayanan *et al.* ([173], [172]) modified this

pseudo-potential approach for the analysis of drag, lift and virtual mass forces in bubbly suspension. Very recently, they derived a multiscale approach based on this technique for the extraction of continuum-level (coarse stability) information directly from LB simulations, applied to the computation of coarse bifurcation diagrams in bubbly flow [201].

The main drawback of this technique however is that the surface tension parameter depends on the phase's separation parameter. This leads to either well separated very stiff droplets or weakly separated sloppy droplets. Another drawback of this method is the width of its interface per se: whilst it is possible to have a very stiff interface of width about one lattice node, the most practical applications of the S-C model seem to require structured interfaces of thickness $\gtrsim 4$ lattice nodes. This considerably broad interface must have some impact on the length scales accessible with this technique (requires a very large number of grid points to down scale the effect of the interfacial width). It should again be noted that this model is subjected, as is any LB model, to micro-currents flow as depicted by Hou ([95]) and addressed by Teng ([200], [41]) for example.

This model is however very popular and especially well suited for the simulation of important differences of fluid's density, such as liquid-gas interfaces ([215] for example).

Free energy approach

A step towards thermodynamic consistency was taken by Swift *et al.* [195], structuring the fluid to reach the right thermodynamic equilibrium directly under the effect of an appropriate equation of state, for a Van der Waals fluid (which exhibits spontaneous separation) which is isothermal. The pressure, P, may be shown to be given by:

$$P = \rho \frac{\partial \Psi}{\partial \rho} - \Psi - \kappa \rho \nabla^2 \rho^2 - \frac{1}{2} \kappa \, |\nabla \rho|^2 \tag{2.1}$$

where Ψ is represents the free energy density functional and κ is related to the surface tension. This leads to a modified equilibrium function and pressure tensor for the model [195]. The advantage of this approach over the previous S-C approach is that the surface tension appears directly in the pressure tensor, avoiding dependance upon segregation. Swift *et al.* obtained good agreement against the Laplace

law ([194]). This model is also very well suited for imposing wetting behaviour as a result of including a suitable external chemical potential, whose gradients act as an effective thermodynamic force and can be directly added to the RHS of the LBE. The local property of the LBE (or BE) makes it possible to tune this force depending on the fluid and whether it is in contact with any wall ([148]). Recently, Dupuis *et al.* obtained very convincing wetting behaviour in several configurations ([122], [49] and [50]). Inamuro *et al.* have designed a method based on this model, and proposed an LBM for multicomponent immiscible fluids with the same density [97], [100] based on the previous work by Inamuro *et al.* [96]. Inamuro *et al.* studied the miscibility of their model and its application to a heat-transfer problem [101]. They improved this method for density ratios up to 1000 and obtained very good agreement with standard bubble shape diagrams as well as experimental comparison of coalescence and break up (original method in [99] and [98]).

Swift's approach, however, does not separate fluids very efficiently and has a wide interfacial width (again, whilst it is possible to have a very stiff interface of width about one lattice node, most practical applications of the S-C model seem to require structured interfaces of thickness $\gtrsim 4$ lattice nodes). This model is therefore not really well suited to simulate large differences of viscosity between the two phases separated fluids or to be used with small lattices.

Finite density models

All multiphase models described so far include temperature only as a static parameter and do not allow self-consistent thermodynamics: the equilibrium state in these models cannot be described by thermodynamics (see Swift *et al.* [195], [194] and Luo [130]). Moreover, the original BE does not apply to dense gases or liquids, it only describes rarefied gases where molecules are considered as point like particles (recall Boltzmann's assumptions discussed in the previous chapter).

In the Boltzmann gas limit (see chapter 1):

$$\left.\begin{array}{l} N \rightarrow \infty, \\ m \rightarrow 0, \\ r \rightarrow 0, \end{array}\right\}$$

where N, m and r are the particle number, particle mass, and interaction range, respectivelly, and $Nm \rightarrow$ finite, $Nr^2 \rightarrow$ finite, and $Nr^3 \rightarrow 0$. Thus, in this limit, the mean free path $l \sim 1/Nr^2$ remains constant, while the total interaction volume Nr^3 goes to zero (from [130]). Therefore, in the strict thermodynamic sense, (i) the Boltzmann equation retains only the thermodynamic properties of a perfect gas, (ii) the finite size of the molecules are being totally overlooked, (iii) any molecular finite size effect such as volume exclusion (term (V-b) in the Van der Vaals equation) are impossible. This calls for finite density corrections to the BE, and involves the two body radial distribution function $\rho_{12} = \int f_{12} d\mathbf{v}$ (which has been replaced by $f_1 f_2$ under the assumption of molecular chaos) and binary collisions only (dilute gas) in the derivation of the BE in last chapter. Luo's idea ([130]) had been precisely to go back to the BE and apply the method he had developed with He [86] to analyse the LBE for multiphase fluids with a non-ideal gas equation of state. This equation is known as the Enskog equation for dense gas [28]. Luo ([84]) then obtained a LBE for isothermal multiphase fluids, which had the required thermodynamic consistency. This neat approach provides a more realistic method for non-dilute gases (i.e. towards liquids) but is still subjected to some approximations (hard spheres, instantaneous collisions) and is believed to be less robust than the standard BKG model ([190]).

Chromodynamic models

These models provide two completely immiscible fluids distinguished by their colour. The original method dates back to the immiscible lattice gas model (ancestor of the LB, see Frisch *et al.* [62] by Rothman and Keller in 1988 ([168]), applied to the LBM by Gunstensen *et al.* in 1991 ([80]) for two spatial dimensions and extended to three by Gunstensen and Rothman ([79]), and subsequently improved by Grunau *et al.* ([78]). Note that in the latter paper, the immiscible lattice BGK was generalising to two components the ideas of Chen *et al.* [30] and Qian *et al.* [162]. Not very popular

within the LB community, it has however decisive advantages against the other models described previously: it is the only LB technique that allows the separation of the treatment of surface tension from the interface tracking (it is a drawback of the interacting potential method and free energy approach that they are unable to fix explicitly the coefficient of surface tension *a priori* [105]). Furthermore, it is the only LB technique able fully to segregate two fluids (i.e. exactly immiscible fluids). A detailed description of this model can be found in section 2.2 (below) since this is the model we based our N-component algorithm upon. Briefly, it consists of fully separating species within a mixed colour node by a process which can be regarded as a brutal segregation of colour lacking proper thermodynamical evolution equation (hence less popular than the free energy or potential approaches). It is subjected (as any other LB and CFD models) to non-zero micro-currents emerging from the interface, affecting the dynamics of the interface in a certain regime of flow and, creating un-physical velocities to the bulk of fluid and a noisy flow field. In reaching large capillary number applications (surface tension and interface dominated flows), reducing these unwanted flows has been a constant motivation. Some results in this application are shown in next chapter.

2.1.5 Large scale LB simulation projects

The great advantages of LB compared to other numerical methods for fluid flow (locality, efficiency, highly parallelisable, wide applicability, etc.) make it very attractive for numerous projects involving real engineering issues. These applications only really took off recently, since LB is considerably younger and rather more immature than standard CFD techniques (massively used for a long time for large scale projects). In these LB projects, fundamental science is not the main issue, they concentrate mainly on technical and computational issues inherent to the large scale simulations. A few examples of these computationally impressive LB projects appropriate at the time of writing are given below.

Ludwig

Kendon and co-workers have developed *Ludwig* in the late 1990's, a general purpose parallel LB code capable of simulating the hydrodynamics of complex fluids in 3-D (a detailed description can be found in [45]). The aim of Ludwig is to simulate multicomponent fluids, amphifilic systems, flow in porous media, colloidal particles and polymers. Desplat *et al.* note that the modular structure of *Ludwig* is its strength and should facilitate its extension to many other problems. So far, *Ludwig* has been used numerically to study the late-stage demixing following spinodal decomposition of a three-dimensional symmetric binary fluid mixture [107], but no further applications have been reported to the best knowledge of the author. It did however demonstrate the feasibility of large numerical LB simulations.

VirtualFluids_real

Following the concept of *Ludwig*, Krafczyk *et al.* ([112], [42]) are developing a LBM-CFD based software, VirtualFluids_real, to compute, very efficiently, transient and steady state flows, the ultimate aim being to provide a very flexible analysis of complex flow phenomena. Doing so, they integrate the three interdependent steps of computational engineering studies (main difference with *Ludwig*): (i) preprocessing, (ii) computation and (ii) postprocessing, and report that their LB-CFD kernel provides major advantages in terms of integrating them [111]. They also note that LBM through its locality, provides considerable numerical and algorithmic advantages. The current application of this project is the interactive analyse of indoor air flow for HVAC systems (Heating, Ventilation and Air Conditioning), with up to one million discrete grid points, at realistic Reynolds numbers and with an updated result every 10 seconds [111]. In VirtualFluids_real, the flow is computed in 'real time' accordingly to the user's inputs: a new computational grid is automatically generated after each user's modification to the computational geometry. The bilateral interaction between the simulation and the flow visualisation is done by Virtual Reality. This project is apparently very successful and gave already very promising results.

RealityGrid

More recently, a more ambitious project sponsored by a major EPSRC (Engineering and Physical Sciences Research Council, the UK Governments leading funding agency for research and training in engineering and the physical sciences) grant to a consortium of universities and collaborating institutions aims to grid-enable the realistic modeling and simulation of complex condensed matter structures at the mesoscale and nanoscale levels as well as to facilitate the discovery of new materials. Called *RealityGrid*, the project is an ambitious and exciting global effort to develop an environment in which individual users can access computers, databases and experimental facilities 'simply and transparently' , without having to consider where those facilities are located. RealityGrid proposes to extend the concept of a Virtual Reality centre across the grid and links it to massive computational resources at high performance computing centres and experimental facilities (a computing environment built around the UK's most advanced computing technology and infrastructure). The Principal Investigator of this grant is P.V. Coveney from University College London, and more details can be found on the *RealityGrid* website [163]. Further details on the art of steering simulations can be found in [136], [33], [20], [32], and some impressive applications using this technology can be found in [76], [83], [75].

Exa Corporation and PowerFLOW

A description of the LBM would not be complete without mentioning that K. Molvig, while on sabbatical from the Massachusetts Institute of Technology (MIT), founded *Exa* (in 1991). *Exa* Corporation is in charge of developing and marketing *PowerFLOW*, the only commercial LB based fluid flow software, for engineers to analyse complex fluid flow problems. *Exa PowerFLOW* claims to be dramatically faster than currently available solutions (CFD) and to deliver unprecedented accuracy. Its applications include automotive, aerospace, petroleum, chemical process-

ing, environmental engineering, material processing, power generation, and HVAC (linked to the project VirtualityFluid_Real described previously). More details can be found on the Exa website [56].

2.2 The Gunstensen method for diphasic LB fluid

2.2.1 Introduction

As with any model, the Gunstensen algorithm is design to address discontinuities occurring in the NSEs in a physical way. Its great advantage over its competitors (LB or CFD) is that it remains very local, segregates fully two fluids, and permits one to set *a priori* the surface tension parameter; enableling explicit assignment of parameters for both fluids, as well as the interface. Together these are the key to a simple and efficient algorithm for our problem here. D. Kehrwald provided a very detailed (numerical and theoretical) analysis of this two-phase incompressible Navier-Stokes model, with several approaches to improving the two dimensional model. Unfortunately, all of them turned out to yield no substantial improvement [105]. In reference [106], he analysed the Gunstensen model's physical consistency, but no attention was paid however to the interface motion or maintenance of immiscibility.

This work had set-out acknowledged difficulties around this model, which we assessed during this project.

As seen with previous multiphase models, the standard LB algorithm (repetitive collision / propagation steps) is not enough to simulate polychromatic fluids. Gunstensen's original idea was inspired by the immiscible lattice gas method of Rothmann and Keller ([168]). It was to keep the core LB algorithm, generalising the "colourblind" densities f_i to r_i and b_i (denoting *red* and *blue*), and adding an extra step between the collision step and propagation step to, (i) segregate colour and, (ii) impose surface tension. This extra step is defined as the recolouring step. Ginzburg and Steiner ([68], [67]) proposed a modified Gunstensen model to simulate free-surface flows and obtained very convincing filling process simulations. Tölke *et al.* ([205]) modified the algorithm slightly for the simulation of variable viscosity and

density ratios (and applied their model convincingly to the flow in porous media).

2.2.2 The collision step

Let's see first the evolution of pure nodes (i.e. containing only one colour, typically in the bulk of either fluids). They undergo exactly the monochromatic collision step from the standard LBGK relaxation algorithm:

$$\left.\begin{aligned} r_i^+ &= r_i - \omega_r \left(r_i - r_i^{eq}\right) \quad \text{for red pure nodes}, \\ b_i^+ &= b_i - \omega_b \left(b_i - b_i^{eq}\right) \quad \text{for blue pure nodes}, \end{aligned}\right\}$$

where the equilibrium distribution functions are defined the usual way:

$$\begin{aligned} r_i^{eq}(\rho, \mathbf{u}) &= t_i \rho^R \left[1 + 3\mathbf{u}\cdot\mathbf{c}_i + \frac{9}{2}(\mathbf{u}\cdot\mathbf{c}_i)^2 - \frac{3}{2}\mathbf{u}^2\right] \text{ for red pure nodes}, \\ b_i^{eq}(\rho, \mathbf{u}) &= t_i \rho^B \left[1 + 3\mathbf{u}\cdot\mathbf{c}_i + \frac{9}{2}(\mathbf{u}\cdot\mathbf{c}_i)^2 - \frac{3}{2}\mathbf{u}^2\right] \text{ for blue pure nodes}. \end{aligned} \tag{2.2}$$

It should be noted that ω_r and ω_b still carry the viscosity information of the fluid considered (see equation 1.35), ensuring that pure nodes evolve consistently to the corresponding NSE. $\mathbf{u}$ and ρ^α (α here denotes either colour) are the macroscopic nodal velocity and density respectively defined as follow:

$$\left.\begin{aligned} \rho^R = \textstyle\sum_i r_i \text{ and } \rho^R u_\alpha = \sum_i r_i c_{i\alpha} \quad \text{for red pure nodes}, \\ \rho^B = \textstyle\sum_i b_i \text{ and } \rho^B u_\alpha = \sum_i b_i c_{i\alpha} \quad \text{for blue pure nodes}. \end{aligned}\right\}$$

Mixed nodes on the other hand have to manufacture a lattice a 'smooth' discontinuity in the parameters of the two adjacent NSE, as well as imbedding the interface's own physics. In this case, the algorithm considers the colourblind densities (similar to the original LBGK note):

$$f_i = r_i + b_i,$$

evolving in the usual way:

$$f_i^+ = f_i - \omega_e \left(f_i - f_i^{eq}\right),$$

where the equilibrium distribution function and the macroscopic observables are

defined as usual:

$$\left.\begin{aligned} f_i^{eq} &= \rho t_i \left[1 + 3\mathbf{u}\cdot\mathbf{c}_i + \tfrac{9}{2}(\mathbf{u}\cdot\mathbf{c}_i)^2 + \tfrac{3}{2}\mathbf{u}^2\right] , \\ \rho &= \textstyle\sum_i (r_i + b_i) = \sum_i f_i , \\ \rho u_\alpha &= \textstyle\sum_i (r_i\, c_{i\alpha} + b_i\, c_{i\alpha}) = \sum_i f_i\, c_{i\alpha} . \end{aligned}\right\}$$

A smooth transition of the kinematic viscosity from one fluid to another through the finite interfacial width, is ensured by the effective BGK relaxation parameter:

$$\omega_e = \frac{\rho}{\rho^R/\omega^R + \rho^B/\omega^B} ,$$

leading to an effective interfacial viscosity:

$$\nu_e = \frac{\rho^R \nu^R + \rho^B \nu^B}{\rho} .$$

The location of the interface emerges from the mixed nodes, very easily tractable: it lies where nodes contain both colours ($\rho^R \neq 0$ *and* $\rho^B \neq 0$).

2.2.3 Recolouring step

The lack of an additional step to the standard LBM, in which the propagation step follows immediately the collide step, would lead to the rapid and nearly total diffusion of all the dynamic links form mixed nodes into surrounding nodes leading to a uniform *soup* of colour. To avoid this, the Gunstensen algorithm segregates colour at every mixed node, at every time step, ensuring that colour, as far as possible, *goes back* where it came from (following microscopic observations of non-miscibility or differential attraction). The aim of the segregation step is therefore to achieve a nodal distribution of colour in which each colour is propagated back as much as possible to its corresponding bulk colour, that is, each side of the interface. To achieve segregation, the technique maximises the work done by the colour-flux $\mathbf{q}^\alpha$ of each colour (measure of the net momentum difference at a site) resulting from the nodal post-segregation distribution, against the colour-field $\mathbf{P}^\alpha$. We define the

colour-flux $\mathbf{q}^\alpha$ and the colour-field $\mathbf{P}^\alpha$ as follow:

$$\begin{aligned}
\mathbf{q}^\alpha(\mathbf{x},t) &= \sum_i \mathbf{c}_i \left[\alpha_i - \overline{\alpha}_i\right] , \\
P^\alpha_\beta(\mathbf{r},t) &= \sum_{ij} \left[\alpha_j(\mathbf{x}+\mathbf{c}_i,t) - \overline{\alpha}_j(\mathbf{r}+\mathbf{c}_i,t)\right] c_{i\beta} \\
&= \sum_i \left[\rho^\alpha(\mathbf{x}+\mathbf{c}_i,t) - \rho^{\overline{\alpha}}(\mathbf{r}+\mathbf{c}_i,t)\right] c_{i\beta} . \qquad (2.3)
\end{aligned}$$

where α is the colour considered and $\overline{\alpha}$ the other colour (i.e. if α is red then $\overline{\alpha}$ is blue), with the associated momentum densities α_i and $\overline{\alpha_i}$ (i.e. if α_i is r_i then $\overline{\alpha}$ is b_i).

Note that $P^\alpha_\beta(\mathbf{x},t)$ stay unchanged by any nodal rearrangement of colour. Maximising the work of the colour-field against the colour-flux for one colour is enough to ensure maximum de-mixing of mixed nodes since there is a maximum of two colours only and that the two corresponding colour-fields and colour-flux are opposite:

$$\left.\begin{aligned}
q^\alpha_\beta(\mathbf{x},t) &= -q^{\overline{\alpha}}_\beta(\mathbf{x},t) , \\
P^\alpha_\beta(\mathbf{x},t) &= -P^{\overline{\alpha}}_\beta(\mathbf{x},t) .
\end{aligned}\right\} \qquad (2.4)$$

Throughout this thesis, any angle in the simulation has been chosen to be measured with respect to direction 4 in the $D2Q9$ geometry (see figure 1.2), which leads to the following formula for the angle of $\mathbf{P}^\alpha$:

$$\theta^\alpha_P = tan^{-1}\left(\frac{P^\alpha_\beta}{P^{\overline{\alpha}}_\beta}\right) \qquad (2.5)$$

This technique makes the assumption that the direction of $\mathbf{P}$ represents the direction of the interface normal. This has been subjected to some discussions but no valid arguments or convincing measurements could be found to refute this essential assumption: no significant difference between the normal of the fitted interface of a closed drop and the computed local colour-field was found (the difference was typically less than a degree), which leads to the conclusion that the previous assumption is valid to a high order of accuracy.

Then, each nodal colour density, ρ^α, is distributed numerically onto the colourblind post-collided dynamical links f_i's by the order of decreasing link/colour-field work $(\mathbf{c}_i \cdot \widehat{\mathbf{P}})$ until ρ^α is exhausted. Figure 2.1 illustrates the way to find the order of recolouring, O_{re} hereafter, for $\theta^B_P = 10^o$.

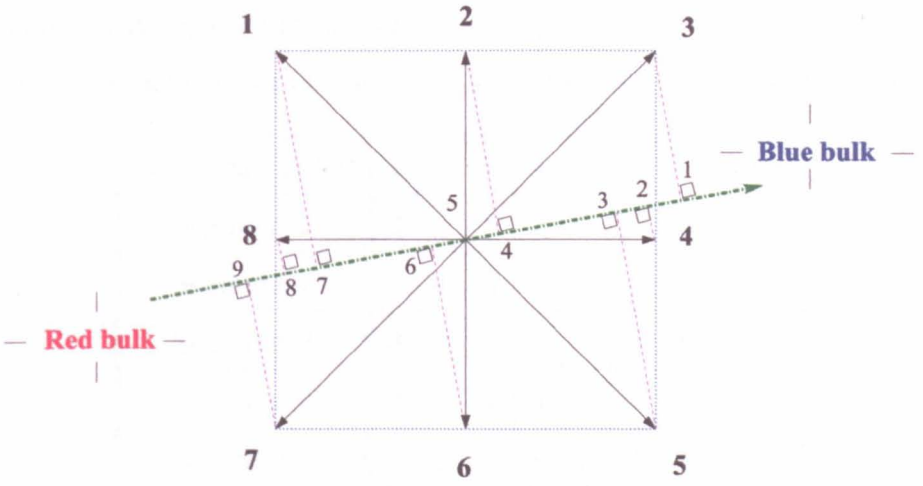

Figure 2.1: Finding the reallocation order of colour. In this example, θ_P^B is 10^o corresponding to an order of recolouring of $[3, 4, 5, 2, 0, 6, 1, 8, 7]$.

Working out the order of recolouring of each link of each node at each time step is very computationally ineffective. This is addressed by noticing that there are only 16 possible different O_{re}. It is therefore possible to resolve the infinite number of θ_P^α into 16 different ranges, defining 16 orders of recolouring (see figure 2.2).

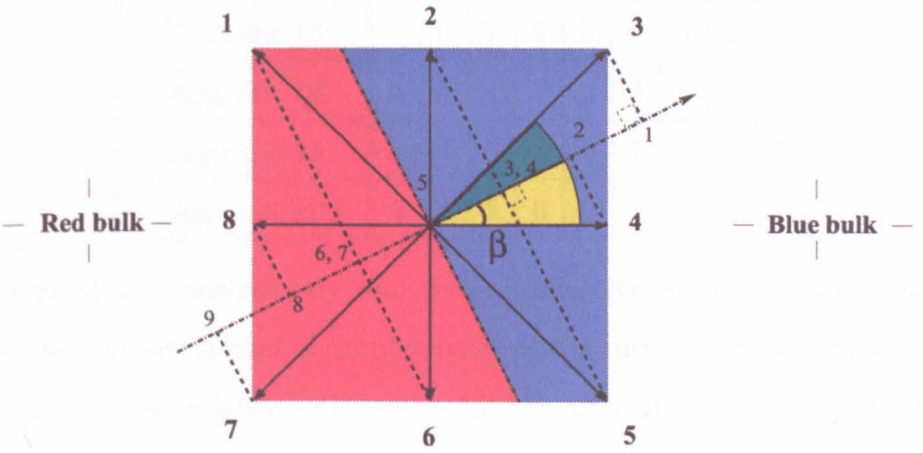

Figure 2.2: In this case, the colour-field direction lies exactly at the boundary where link 2 and 5 have equal priority (as well as 1 and 6 note). The two shaded zones indicates zones of identical reallocating order.

β in figure 2.3 can be easily calculated to be:

$$\beta = tan^{-1}\frac{1}{2} \approx 26,56^o\,.$$

The rest of the orders and angular limits can be easily found by symmetry. This

leads to configuration of figure 2.3 and the following corresponding table of colour reallocation order which can be used as a look up table in the programme:

Hierarchy order	1	2	3	4	5	6	7	8	9
Segment 1	3	4	5	2	0	6	1	8	7
Segment 2	3	4	2	5	0	1	6	8	7
Segment 3	3	2	4	1	0	5	8	6	7
Segment 4	3	2	1	4	0	8	5	6	7
Segment 5	1	2	3	8	0	4	7	6	5
Segment 6	1	2	8	3	0	7	4	6	5
Segment 7	1	8	2	7	0	3	6	4	5
Segment 8	1	8	7	2	0	6	3	4	5
Segment 9	7	8	1	6	0	2	5	4	3
Segment 10	7	8	6	1	0	5	2	4	3
Segment 11	7	6	8	5	0	1	4	2	3
Segment 12	7	6	5	8	0	4	1	2	3
Segment 13	5	6	7	4	0	8	3	2	1
Segment 14	5	6	4	7	0	3	8	2	1
Segment 15	5	4	6	3	0	7	2	8	1
Segment 16	5	4	3	6	0	2	7	8	1

This numerical step ensures very efficient and effective recolouring and segregation of colour: we measured that a droplet retained its integrity (total mass within its closed boundary) to a level better than $10^{-2}\,\%$ after 10^6 steps (steady step). For many, this points out the great advantage to fully recolouring, as it implies stable segregation in time. However, the recolouring step is relatively crude: each colour is forced back without direct reference to the hydrodynamics, disabling any possibility of phase segregation investigation. At the time of writing, the dynamics of the colour is only approximately understood. However, it appears essential to 'counter-diffuse', at least on short time and (of course) length scales.

It should be noted that according to equation 2.4, the interface normal can be considered as lying along either of the red or blue fluid's colour-field. This property is used as a short cut when recolouring colours: say r_i is recoloured first, then

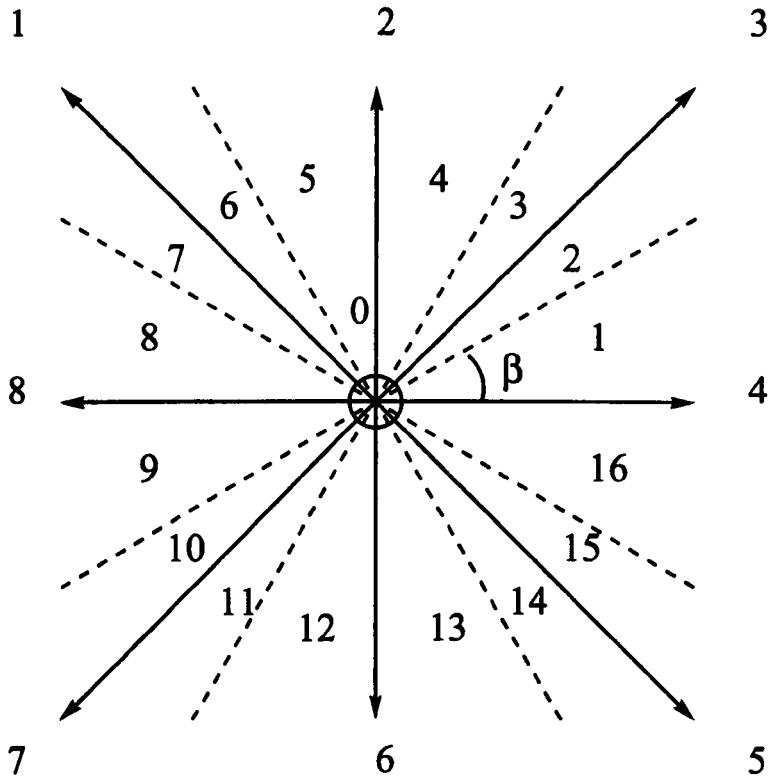

Figure 2.3: D2Q9 segmentation of the colour-field direction into 16 ranges giving identical recolouring order

it is legitimate to state that $b_i = f_i - r_i$ (which would be obtained by applying the recolouring to the blue fluid). Only half of the re-allocation needs to be done which, as well as reducing the execution time of the recolouring process, halves the classification noise added to the r_i's and b_i's (output of the recolouring step).

This section finishes with an example to illustrate this complicated step. Let's say that $\theta_P^R = 10^o$ (recall picture 2.1). It therefore lies in segment number 1 of the above look up table (with figure 2.3), and the recolouring order of the red fluid onto the links within the node is directly found to be $T_r = [3, 4, 5, 2, 0, 6, 1, 8, 7]$. As we saw previously, the blue fluid colour-field will be directed opposite, that is $\theta_P^B = 190^o$, and lies in the segment 9. The blue reallocation table is $T_b = [7, 8, 1, 6, 0, 2, 5, 4, 3]$ (through the colour reallocation look up table), but can be omitted by recalling that $b_i = f_i - r_i$.

2.2.4 Original Gunstensen surface tension

Throughout this thesis, we shall make the explicit distinction between the *Gunstensen algorithm* and the *Gunstensen method*, referring to the general method to tackle the interface in LB and the original method to impose surface tension, respectively.

Halliday *et al.* developed and characterised a Gunstensen type method to impose surface tension on a Gunstensen-type interface ([82]). It should be noted that the description of this method (described further later in this section) is the starting point of significant improvements, and is therefore important.

This approach is based on imposing the surface tension (in opposition to imposing a pressure step). It is inspired by physical observations: the surface tension is, by definition, a tension, i.e. a tendency of the interface to shrink. The method consists therefore in reducing the simulational interfacial length, by removing an amount $\triangle f_i$ of mass density along the surface and adding it to the post collided densities $f_i^+(\mathbf{x}, t)$ and is defined by the mass and momentum conservative perturbation:

$$\triangle f_i(\mathbf{x}, t) = \sigma(\mathbf{x}) \cos\left[2\ (\theta_P(\mathbf{r}) - \theta_i)\right]. \tag{2.6}$$

$\sigma(\mathbf{x})$ is the surface tension parameter set by the user, θ_P is the angle of the interface normal (either $\theta_{\mathbf{P}}^r$ or $\theta_{\mathbf{P}}^b$), and θ_i is the angle of the link i.

It should be noticed that the interface is effectively broader when lying along diagonal links of the lattice (long links, *ll*) than along the longitudinal links (short links, *sl*). Since the perturbation 2.6 is applied to any mixed node, the interface along the *ll* will be subjected to more forcing. This anisotropy was not addressed until the introduction of the λ factor (see next chapter for more details). This difference creates a local anisotropic surface tension. The activation of surface tension is limited to mixed sites by inclusion of a concentration factor CC to the perturbation 2.6 ensuring similar effective surface tension radially throughout the interface of the droplet. It is defined by:

$$CC(\mathbf{r}, t) = 1 - \left|\frac{\rho^R - \rho^B}{\rho^R + \rho^B}\right|. \tag{2.7}$$

It can be shown that these perturbations (equations 2.6 and 2.7) do not change the momentum or velocity of the site.

2.2.5 The Lishchuk method to impose surface tension

In an attempt to reduce the micro-currents, Lishchuk decided not to try to refine the Gunstensen method further but to invent another way of imposing surface tension [127]. His strategy had been to impose the pressure step across the interface via the stress condition, at multi-coloured nodes, giving an effective surface tension (in fact, reverse engineering from the previous original Gunstensen method). This method consists therefore in adding a body force acting towards the droplet, along the normal to the interface, proportional to the expected surface tension and the local radius of curvature (note the great similarity with the continuous surface force method in the VOF model in CFD ([16]). It is in a sense, applying the Laplace law (equation 1.18), locally , inspired from CFD techniques (section 2.1.3). This is achieved by adding the following step (instead of the Gunstensen's perturbation, equations 2.6 and 2.7) to the Gunstensen algorithm, still at the mixed nodes only:

$$\triangle f_i(\mathbf{x}) = \sigma(\mathbf{x})\, t_i\, K(\mathbf{x})\, c_{i\alpha}\, \partial_\alpha \left(\frac{\rho^r - \rho^b}{2\rho} \right) ,$$

where $\sigma(\mathbf{x})$ is the surface tension parameter, K is the local curvature of the interface and t_i are the usual lattice dependant weights. First, the curvature of the red-blue interface at a mixed node $\mathbf{x}$ is calculated from an identity generalised from the result $K = \nabla_S : \hat{n}$ [127]:

$$K(\mathbf{r}) = n_x\, n_y\, (\partial_x\, n_y + \partial_y\, n_x) - n_x^2\, \partial_x\, n_x - n_x^2\, \partial_y\, n_y\, , \tag{2.8}$$

where n_x and n_y are the x and y component of the interface normal. Spatial gradients can be calculated as follow to the $O(4)$ accuracy [127]:

$$\partial_\beta n_\alpha(\mathbf{x}) = \frac{1}{3} \sum_i n_\alpha(\mathbf{x} + \mathbf{c_i})\, c_{i\beta}\, .$$

There are no valid arguments why the direction of the interface normal direction could not be represented again by the colour-field's direction. However, the colour-field vector P_α has to be normalised, since it contains also density gradient information, unwanted for the surface gradient computation (so far, only its angle is of interest):

$$\partial_\beta n_\alpha(\mathbf{x}) = \frac{1}{3} \sum_i \frac{P_\alpha(\mathbf{x} + \mathbf{c_i})}{|\mathbf{P}(\mathbf{x} + \mathbf{c_i})|}\, c_{i\beta}.$$

Lishchuk *et al.* [127] found that, surprisingly, the micro-currents activity μ_a (see equation 3.2) is forty times reduced with this method for a neutrally buoyant drop at rest) compared to the standard Gunstensen method. The isotropy of the droplet was found to be much better as well. These points will be discussed further in next chapter. More details on this method can be found in [127].

2.2.6 Remark on the Gunstensen algorithm

The Gunstensen algorithm consists of a generalisation to two component of the standard repetition of collide and propagate steps in the LB method (see figure 2.4). It can be modified very easily since all procedures are inter-independent. For example, the collision step can, in principle, be any LB evolution developed for other methods.

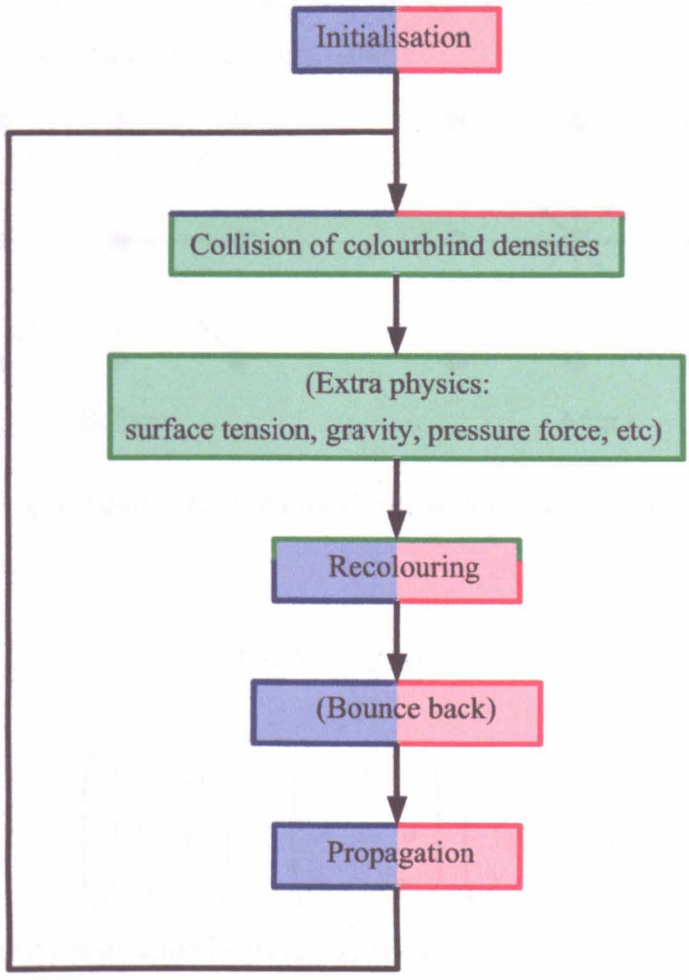

Figure 2.4: Gunstensen algorithm.

2.3 Solid boundary lattice closure with LB

Key applications in this thesis rely upon accurate representations of the boundary.

2.3.1 Bounce back

We use LB's most common and robust way of imposing no-slip boundary condition to our simulation: the bounce back method. There are however two ways of implementing this technique: "on grid" or "mid-grid"[190].

On-grid bounce-back method

The on-grid method consists, crudely, in reversing all density populations sitting on a boundary node (the wall is East-West), splitting the densities into two different groups (North and South). Figure 2.5 and equations 2.10, 2.9 illustrate the on-grid bounce back method (taken from Succi, [190]).

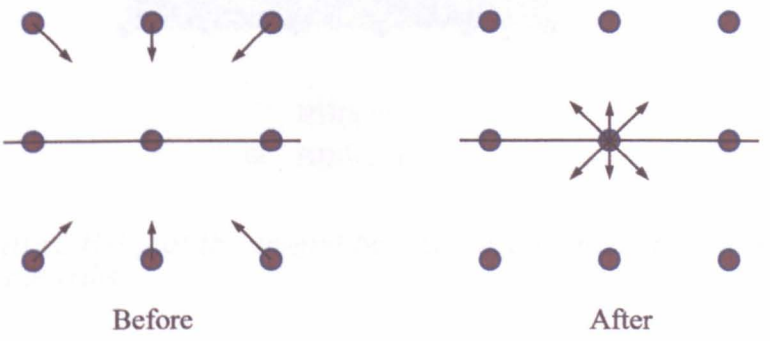

Figure 2.5: On grid bounce back method, the wall is represented by the solid line.

$$f_{in}(N) = f_{out}(S) \tag{2.9}$$

$$\begin{pmatrix} f_6(x,y) \\ f_7(x,y) \\ f_8(x,y) \end{pmatrix} = \begin{pmatrix} 1 & 0 & 0 \\ 0 & 1 & 0 \\ 0 & 0 & 1 \end{pmatrix} \begin{pmatrix} f_2(x,y) \\ f_3(x,y) \\ f_4(x,y) \end{pmatrix} \tag{2.10}$$

The zero slip velocity is obtained exactly on the node location, the physical boundary lies exactly on the grid's line. However, on-grid bounce back is generally credited to be only first-order accurate because the densities at the boundary node do collide

and therefore are modified by what is happening on the other side of the wall (which is obviously unphysical for a non-deformable and non-moving wall).

At a practical level, the position of the walls is defined by a boolean-type array of the same size as the LB lattice: $BB_{on}(\mathbf{x})$. Each element of $BB_{on}(\mathbf{x})$ defines whether there is a wall or not at the position $\mathbf{x}$ (we chose arbitrarily to set $BB_{on}(\mathbf{x}) = 1$ for the presence of a wall and $BB_{on}(\mathbf{x} = 0)$ for the absence of a wall). See figure 2.6 for an illustration.

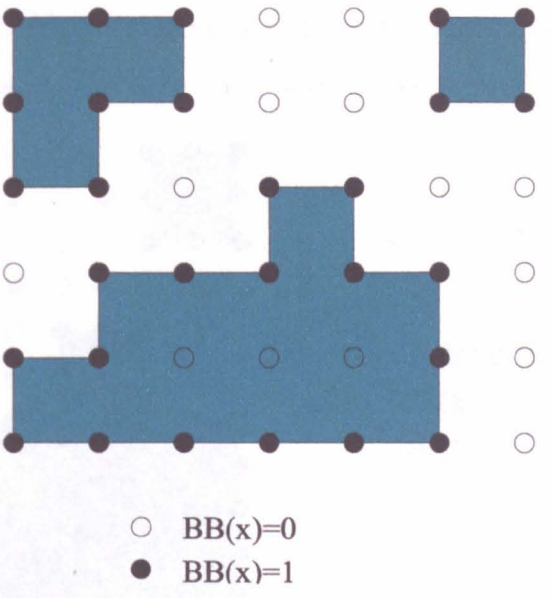

Figure 2.6: Lattice BB_{on} of the on-grid bounce back method determining the position of the walls

Mid-grid bounce back method

The remedy to the accuracy of the on-grid bounce back problem (only first-order accuracy) is to change slightly the method by reflecting densities back. Taking the same example than previously, where a wall is East-West:

$$\begin{pmatrix} f_6(x,y) \\ f_7(x,y) \\ f_8(x,y) \end{pmatrix} = \begin{pmatrix} 1 & 0 & 0 \\ 0 & 1 & 0 \\ 0 & 0 & 1 \end{pmatrix} \begin{pmatrix} f_2(x-1,y-1) \\ f_3(x,y-1) \\ f_4(x+1,y-1) \end{pmatrix} \tag{2.11}$$

The position of the walls is defined effectively by a similar boolean-type array than $BB_{on}(\mathbf{x})$ for the on-link bounce back, but of double size as the LB lattice: $BB_{mid}(\mathbf{x})$ (see figure 2.8) for illustration. It should be noted that a node cannot be the host of

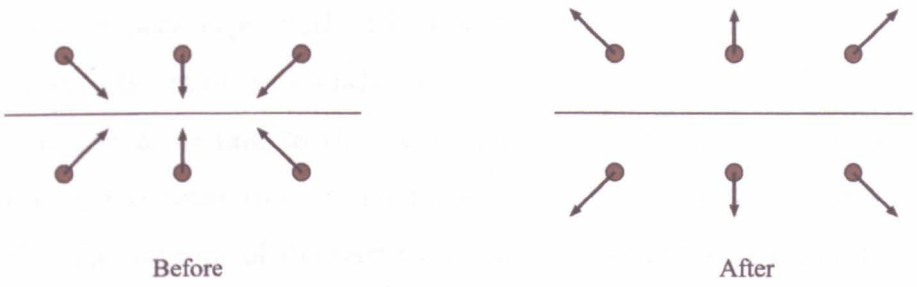

Figure 2.7: Mid-link bounce back method, the wall is represented by the solid line.

a mid-link bounce back (that just does not make any sense) and that $BB_{mid}(\mathbf{x})$ must contain continuous boundaries only (failing to do so induces leakage of velocities).

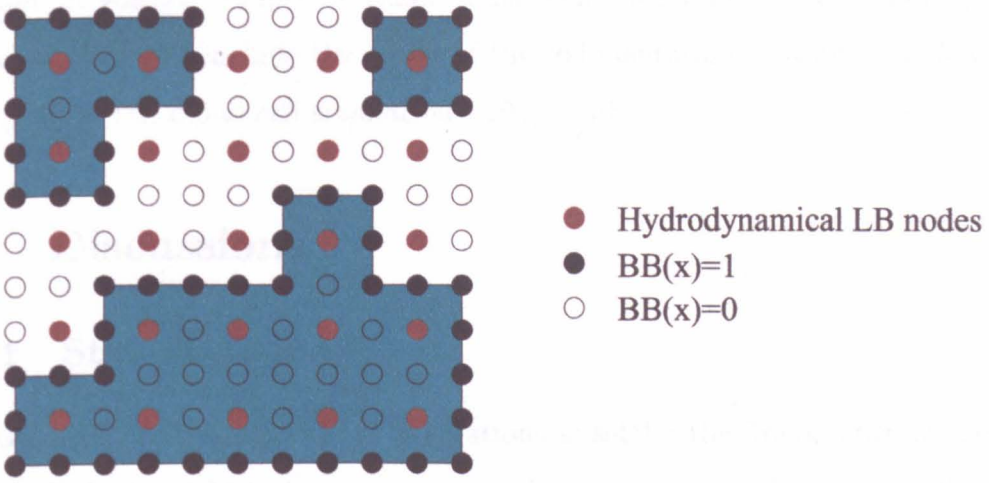

Figure 2.8: Lattice BB_{mid} of the mid-grid bounce back method determining the position of the walls

We used the mid-link bounce back method in this project, but however, as Succi notes, the distinction between mid-grid and on-grid bounce back is not very important since the on-grid method can also be made second order accurate. For more detailed discussion of the treatment of no-slip boundary conditions in LBGK, consult for example Ginzburg and Adler [65] and Ginzburg I. and D'Humières [66], He *et al.* [87], Mei *et al.* [138], [139] or Succi [190].

2.3.2 Moving particles, multicomponent LB: the Ladd method

Solid particles can be added into the LB situational domain by the mean of a technique developed by Ladd *et al.* in 1994 ([113], [114]). Each particle is represented by a closed surface S which is replaced by the set of lattice links cut by S. A

mid-link bounce back type method is used for the *solid* $\rightarrow$ *fluid* interaction. The *fluid* $\rightarrow$ *solid* interaction is slightly more complicated. The solid particle should move and rotate according to the surrounding flow's stresses. This is addressed by integrating the total torque and force acting on the particle, and moving it accordingly. The interior of the particle is filled with fluid which quickly relaxes to a rigid-body motion of the same mass [114]. Ladd also included some lubrication force correction to the particles suspensions for more accurate representation of high volume fraction suspensions [143]. Some applications of this technique range from particle re-suspension problems by Feng *et al.* ([59], [58]) to the modeling of the dynamic of volcanic eruptions [129]. This technique easily address non-spherical particles, examples include the study of the sedimentation of a fiber in Newtonian fluid [103] or red blood cell simulations [191], [140].

2.4 Discussions

2.4.1 Stability issues

The overall stability of most LB simulations is set by the appearance of 'negative densities', $f_i < 0$, which do not have any physical meaning (how does a density of probability be negative?). These negative densities appear mainly for two reasons: (i) the total forcing applied (sum of body force, velocity forcing, surface tension, pressure difference, etc) is too high and fully depletes a link ($f_i < \sum \Delta f_i$), or (ii) the relaxation parameter setting the viscosity of the fluid over-do the relaxation to equilibrium (the relaxation parameter has to be between 0 and 2 (see equation 1.36) and ideally, between 0.1 and 1.9 for most configurations). In the case of binary fluids, instability can rise when the viscosity ratio between two fluids is too high, leading to a too important gradients and discontinuities (ideally the ratio of the viscosities should not be greater than 100).

Stability issues are therefore important and great care has been given to the surface tension methods to provide adequate stability. The Lishchuk method has been found to be much more stable than the original Gunstensen method [127], even though the reasons are not really understood at the time of writing.

2.4.2 Open discussion

It is important to note that most of the current LBM models for multiphase and multicomponent fluid flows do not connect directly to kinetic theory. However, as we mentioned, Luo ([130], [131]) and Luo and Girimaji ([132], [133]) have rigorously derived LBM models for multiphase fluid flows from the Enskog equation (non-ideal gases) from which is the corresponding kinetic equation, and provided a unified framework to treat the LBM models for multiphase and multicomponent fluids ([99]). It would be interesting to analyse methods for a Gunstensen-type algorithm, since it provides easy implementation and does not depend any evolution equation can easily be implemented in this technique (contrary to other LB algorithms).

Conclusion

This chapter provided the reader with the necessary background for the discussions and improvement for the following of this thesis. It showed that the Gunstensen algorithm for handling binary fluid interfaces is different from all the other interfacial LB techniques, in that the latter is the only one to provide well separated fluids, to the expense of the thermodynamics of the colour flux. Micro-currents have also been mentioned as a cause of reduced stability of the model. Next chapter addresses the later issue.

Chapter 3

Binary fluid: reduction of micro-currents and possibility of wetting properties

Introduction

The previous chapters were to set the necessary background information in fluid dynamics and LB theory (monochromatic and binary fluid with the Gunstensen algorithm) to support this and the following chapters. Here, we shall first review work on micro-currents with other binary models such as CFD and LB methods, then qualify and quantify the micro-currents activity and seek their origin in the case of the original LB Gunstensen algorithm and interfacial surface tension method. From that, we then show how to reduce the micro-currents by more than an order of magnitude and, by the same token, improve significantly the circularity of a suspended droplet shape. Finally, we show a method for imposing wetting properties on a Gunstensen interface, followed by simple applications. This provides the first result chapter of this thesis and has been published in [46].

3.1 Literature review and introduction to the micro currents

3.1.1 Did you say micro-currents, spurious flow or artificial velocities?

This section aims to qualify and describe what is meant by what are most commonly known as *'spurious velocities'* in multiphase modeling. It should be noted straight away that there is no difference between the phenomena to which the terms *'micro-currents'*, *'spurious velocities'* or *'artificial flow'* refer to, except authors' habit. At Sheffield Hallam University, we prefer to qualify any unwanted flow artifact attributable to the presence of an interface as *micro-currents*. R. Scardovelli and S. Zaleski [176] describe them as *'vortices in the neighbourhood of an interface, despite the absence of any external forcing'*. Here, the term *micro* is more historical than meaningful since, as we will see in this chapter and in chapter 6, some micro-currents are not so 'micro' and, under certain conditions, the *hydrodynamic* flow can even be overwhelmed. Micro-currents are, by definition, unwanted and are the cause of key limitations in the capability hence applicability, and of most multi-component methods (LB or CFD). It is therefore important to reduce them.
Interestingly enough, the patterns of the micro-currents flow around a stationary droplet are qualitatively the same for the VOF methods (pattern pictured in [165]) and LB binary models (pattern crudely pictured by Halliday *et al.* [82] and Kehrwald [105] for the Gunstensen model, by Wagner [211] and Nourgaliev *et al.* [146] for the free energy approach, and by Hou *et al.* for the potential approach [95]).

3.1.2 Literature review on micro-currents

'Parasite' flow in the VOF methods

The existence of spurious currents in the simulation of a spherical drop with zero initial velocity is a well-known limiting case of the VOF technique [176]. Recall that

the surface tension in the VOF method is mainly imposed by two techniques: the CSF and the CSS.

In 1994, Lafaurie [115] identified and compared these 'parasite' currents emerging from the CSF method with the one obtained with the Rothman-Keller lattice gas model (the 'ancestor' of the Gunstensen model). They found that in both techniques, the surface tension algorithm induced pathological effects, especially at high values of the surface tension.

In 1998, some alternative implementations of the CSF method ameliorated the flow, by smoothing the colour function before calculating its derivatives [108].

In 2001, Ginzburg *et al.* [69] also found that in both the CSS and CFS methods, anomalous currents originate from an approximation issue of the surface tension term due, to discretisation methods. They used a cubic spline aligned grid to represent the surface tension more accurately (based on the original idea of Popinet and Zaleski [159]). The amplitude of the spurious currents was reduced by a factor $4 - 500$, depending on the coarsening of the grids. They found that, generally, the current strength decreases with the spatial resolution.

In 2002, Renardy *et al.* [165] showed that the spurious flow in both the CSF and CSS models in CFD were caused by a lack of spatial/temporal convergence (also shown in a different way by Brackbill *et al.* in [16] and [7]): apparently (i) temporal discretisation error causes drops to stretch rapidly, (ii) while spatial discretisation error causes them to stretch too slowly. They designed a more accurate representation of the body force that imposes the surface tension, consisting in (i) a new body force algorithm, (ii) some improvements in the projection method for the Navier-Stokes solver, and (iii) a higher order interface advection scheme, which effectively eliminates the spurious currents. In this model, the curvature of the interface was calculated from an optimal fit for a quadratic approximation of the interface over surrounding groups of cells. The authors consequently called this algorithm *PROST*: *Parabolic Reconstruction Of Surface Tension* [165].

It should however be noted that all these improved methods are generally elaborate and non-local, against which the Gunstensen method (as well as other LB methods) has an advantage.

'Spurious velocities' in the Free Energy approach

In 2002, Nurgaliev *et al.* [146] derived a model based on this FE technique and shown that the interface spurious velocities were orders of magnitude lower than that for existing LBE models of non-ideal fluids. They were able significantly to improve the stability of the thechnique, particularly when used in the modeling of stiff droplets (high surface tension).

In 2003, Wagner demonstrated that the spurious velocities in diphasic LB models using this method are caused and driven by a non-compatible discretisation of the driving forces for the order-parameter Ψ (see equation 2.1) dictating the colour evolution and the momentum densities f_i [211]. Wagner claims that the same arguments holds for all other LB methods that exhibit spurious velocities but has not published any similar method for any other LB interfacial methods since (to the author's best knowledge) nor have the author and collaborators managed to gain the same order of improvement by applying similar ideas to the Gunstensen interfacial method. Moreover, Wagner's paper is not really clear on the origin of the reduced overall stability of this modified model (nor is it on the proposed, corresponding fix) and the need to input a correction term into the definition of the momentum (to insure invariance).

Teng *et al.* concluded that the existence of the spurious velocities is due to the errors of the discreteness of space and time inherent in any numerical simulations (LB and other macroscopic finite-difference simulations) [200].

It is interesting to note that Nourgaliev, in his previous paper ([146]), argued that since this model conserves local momentum, the interface spurious velocities are significantly smaller than that one for non-local inter-particle interaction potential models (which do not). However, to the author's mind this implication is suspect, since the Guntensen's method conserves local momenta but shows higher micro-currents activity than the Lishchuk method [127], which does not.

'Artefact velocities' in the pseudo-potential approach

As just mentioned, this model does not conserve local net momentum at each site (note that the total momentum of the system is however exactly conserved [183]).

Nourgaliev *et al.* deduced that this is the origin of significant interface spurious velocities, claimed to be caused by the local violation of the momentum conservation [146] (which, again appears to be suspect to the author's mind).

In 1997, Zou *et al.* described this method's micro-currents in details (while comparing this approach with the Gunstensen approach) [95] and observed that the spurious currents can be directly reduced by reducing the value of the interaction potential (determining the surface tension and miscibility), but generating higher miscibility and lower surface tension. We return to this point in next section.

Kato *et al.* [104] studied the thermodynamics of phase transition using a similar approach, but Nourgaliev *et al.* [146] reported that kato's model was still subjected to non-negligible spurious velocities at the interface as well as strong anisotropic effects, even for a static bubble. Cristea *et al.* [41] also addressed this issue of spurious velocities but no convincing remedies has yet been found to the author's best knowledge.

It is interesting to note that the conclusions of all these authors highlight what we consider as a general problem (deriving from the Gunstensen method): the need to maintain (i) narrow interface and (ii) isotropic drops conflicts with the need to reduce the micro-currents.

Micro-currents in the Gunstensen model

In 1997, Hou *et al.* [95] noted that in the Rothman–Keller model [168] (ancestor of the Gunstensen model), the spurious currents are closely related to the value of the surface tension parameter σ and can be reduced by using smaller values of σ, but the surface tension decreases accordingly. They believed that this could be explained in the way the particle-particle interaction is microscopically modeled: interactions between particles exist only in an arbitrarily defined interfacial zone and their strength is calculated through a maximisation process (the recolouring scheme, see section 2.2.3 for details).

In 1998, Halliday *et al.* [82] derived an analytical expression for the Gunstensen surface tension method and suggested that an orientational-dependent anisotropy in the model's surface tension was responsible, at least in part, for the micro-currents. However, they noted that any attempt quantitatively to access the theory of micro-

currents will require substantial work, but would certainly help understanding this phenomenon and provide a chance to eliminate them [82]. To the author's best knowledge, such an analysis has still not been done yet. In 1999, Thompson *et al.* ([203]) provided a more thorough investigation on the drop's isotropy but did not push the analysis of their micro-currents further.

More recently (late 2003), Kehrwald ([105]) studied, analytically, the Gunstensen technique in great detail. He applied equivalent moment analysis and local differential geometry to examine how the interface motion is determined and how the surface tension step can be included such that consistency to the two-phase incompressible NSE can be expected (validating his theoretical analysis by numerical experiments). He also found that the Gunstensen method can be closely connected to the conservative volume tracking method (for determining interface motion) and consequently coupled both methods together. Applied to simple flow fields, this coupled method yields much better results than the plain Gunstensen model. He also observed some spurious currents and assigned their origins to the discretisation of the surface tension formula. This work was certainly very promising and more attention should be paid. Unfortunately, we only discovered this work late in this project and did not have the time to apply any of these ideas to our model. It could be the base for future work in the current application.

3.1.3 Tests on micro-currents: from *ab-initio*

We shall now concentrate on the micro-currents originating from the Gunstensen surface tension approach (see previous chapter for a description of the method).

As we saw in the last section, the micro-currents in the standard Gunstensen model have, as yet, no certain origins unlike most other models (although discretisation error remains the most likely cause). Previous studies have shown that one contribution to the general trend on the interfacial origin of the micro-currents was a mismatch in the surface tension forcing. This section consequently describes the symptoms associated with the micro-currents in the original Gunstensen model, and their assumed origin from the surface tension perturbation through three tests which lead to the development of an improved Gunstensen-type surface tension method. This comprise the first results of this thesis and has been published in July 2003 in

[46].

Test 1– No surface tension: testing the algorithm

The first test consists of describing the conditions under which the micro-currents appear. It is widely acknowledged that a monochromatic LB simulation without forcing does not exhibit any flow (to the extent of the computer's finite accuracy). This suggests that the interfacial method is responsible for the generation of the micro-currents (everybody agrees on that, as last section showed): to test this hypothesis, a droplet (number 1 say) is initialised in a rest fluid, and not subjected to any forcing (surface tension, gravity or pressure gradient).

The velocity field in this simulation has been measured to be uniformly zero (to a similar level than similar monochromatic simulations). We measured that the droplet 'diffuses' into the surrounding fluid at a rate of only 10^{-5} % of its total mass every 10^6 time steps, which demonstrates the very good de-mixing efficiency (immiscibility) of this algorithm.

This information on the velocity field and diffusion confirmed, as expected, that the Gunstensen algorithm does conserve local and total mass, and momentum while de-mixing very efficiently (unlike other models such as the potential approach).

Micro-currents appear when the surface tension parameter is non-zero ($\sigma \neq 0$, from equation 2.6), identifying the surface tension perturbation as one cause (if not the major) of the micro-currents in this technique.

Test 2:– Add surface tension: characterisation of the micro–currents

The second test was to add surface tension to the previous drop with the original Gunstensen method, and investigate the time evolution and dependance of the micro-currents on different parameters of the simulation.

In order to gain consistency within the results of the different tests, it is important to note that σ alone (equations 2.6) is not appropriate to quantify the interfacial surface tension: we use the *macroscopic* (or *effective*) surface tension Σ defined as follow (c.f. the Laplace law, equation 1.18):

$$\Sigma = \frac{\triangle P}{R}. \tag{3.1}$$

where $\triangle P$ is the pressure step inside the drop and R is its radius.

We define also the *normalised* micro-currents activity, μ_a namely the ratio of the overall flow to the measured macroscopic surface tension Σ (from equation 3.1) as:

$$\mu_a(t) = \frac{\sum_{\mathbf{x}} |\mathbf{u}(\mathbf{x}, t)|}{\Sigma}, \tag{3.2}$$

where $\mathbf{u}(\mathbf{x}, t)$ is the calculated nodal velocity (see equation 1.38).

The steady state drop's relative anisotropy (in other words, its general shape) and micro-currents pattern do not depend significantly on the simulation parameters (drop's viscosity, surrounding fluid's viscosity, droplet's surface tension and radius). Figures 3.1-3.3 shows the typical steady state shape (the colour represents the pressure) and associated velocity field of a droplet at 'rest'. The simulation parameters for this data were: 200×200 nodes, $\omega^R = \omega^B = 1.7$, $\rho^0 = 1.8$, $\sigma = 0.001$, $R_{drop} = 33$, periodic boundary conditions top/bottom and left-right.

It is interesting to note that the depletion of the interfacial nodes is clearly noticeable in figure 3.2, where the blue represents low nodal density and corresponds to the position of the interface. This is caused by the surface tension method which effectively depletes links parallel to the interface and feeds those perpendicular, leading to a nodal depletion of the interface (through the propagation step).

We quantify the *total anisotropy* of the droplet by the standard deviation of the distance of the mixed nodes to the averaged radius of the drop:

$$A_T = \sqrt{\frac{\sum_N \left(|\mathbf{x}_{mixed} - \mathbf{x}_{gra}| - \overline{Ra}\right)^2}{N}}, \tag{3.3}$$

where N is the number of mixed nodes in the simulation, $\mathbf{x}_{mixed}$ is the position of the mixed nodes, $\mathbf{x}_{gra}$ is the position of the centre of gravity of the droplet and $\overline{Ra}$ is the drop's average radius defined by the average distance of all mixed nodes to the centre of gravity:

$$\overline{Ra} = \frac{\sum_N |\mathbf{x}_{mixed} - \mathbf{x}_{gra}|}{N}.$$

We define also the drop's *local* anisotropy for a segment (typically 4^o) of the droplet around position $\mathbf{x}$ by the distance of the *neighbouring* mixed nodes to the average

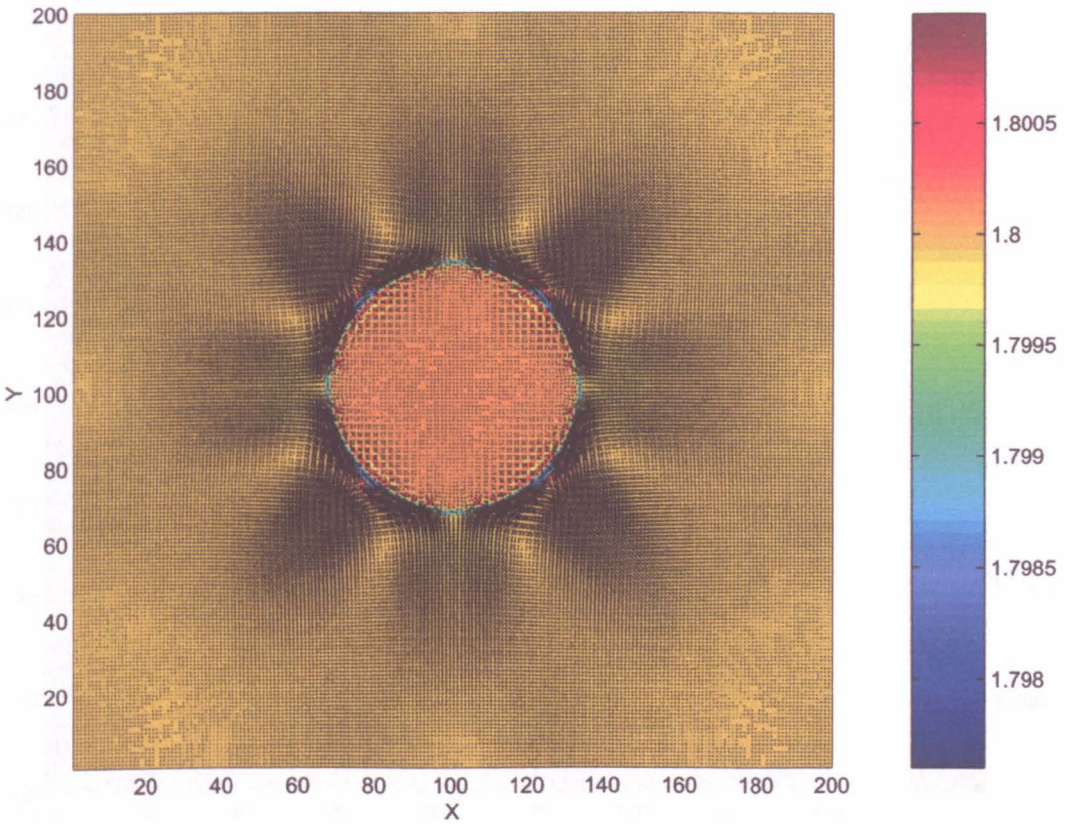

Figure 3.1: Steady state shape and velocity field of a drop with the original Gunstensen method. The colour represents the fluid's pressure.

radius:

$$A_L(\mathbf{x}) = \sum_n \left[|\mathbf{x}_{mixed}(n) - \mathbf{x}_{gra}| - \overline{Ra} \right] \tag{3.4}$$

where n is a neighbouring node within the bounded segment of the droplet interface (containing typically between two and five mixed nodes).

We found that a droplet initialised as a circle (hence isotropic), subjected to a surface tension imposed by a the Gunstensen method, exhibits a high degree of anisotropy during the early development of the flow field and relaxes back to an isotropic configuration.

Figure 3.4 shows this isotropic–anisotropic–isotropic time development. The simulation parameters for this data were: 100×100 nodes, $\omega^R = \omega^B = 1.7$, $\rho^0 = 1.8$, $\sigma = 0.0001$, $R_{drop} = 25$, periodic boundary conditions top/bottom and left-right. This time-dependant local (and total) anisotropy is characterised by the time evolution of quantities A_L (and A_T) shown in figure 3.5 and 3.6 respectively.

It is important to note that an isotropy such as the one obtained with a drop at

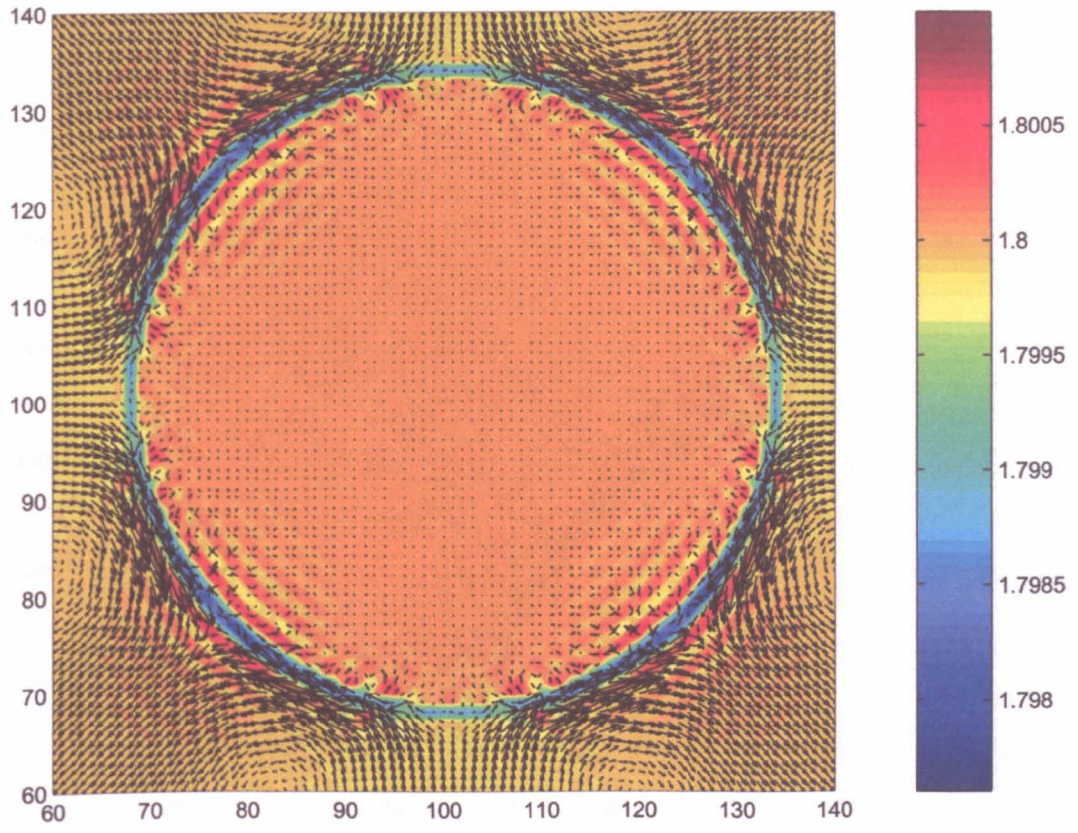

Figure 3.2: Steady state of the internal flow field with the original Gunstensen method. The colour represents the fluid's pressure.

steady state with the Gunstensen method ($A_T \approx 0.4$, see figure 3.6) means that the typical distance of mixed nodes to the continuum interface is less that half a node. Discretisation or resolution constraints require that a A_T below 0.5 is quantitatively meaningless, and that any droplet where $A_T < 0.5$ can be considered as as isotropic as measurable when projected onto a square lattice of the size used (note that this value of 0.5 is be radius and lattice size dependant). We can therefore conclude that an initial isotropic droplet ($A_T(t = 0) < 0.5$), subjected to a Gunstensen type surface tension, reaches a peak of anisotropy ($A_T(t = 1000) \approx 0.8 > 0.5$) during its relaxation to isotropic a final steady state configuration ($A_T(t = \infty) < 0.5$). In between, it acts like a damped oscillator initialised with a non-zero velocity, which can be seen by the alternance of colour in figure 3.5 and the two peaks in figure 3.6.

The corresponding micro-currents, on the other hand, build-up slowly and reach a steady state configuration (μ_a and pattern). Figure 3.7 shows the time evolution of

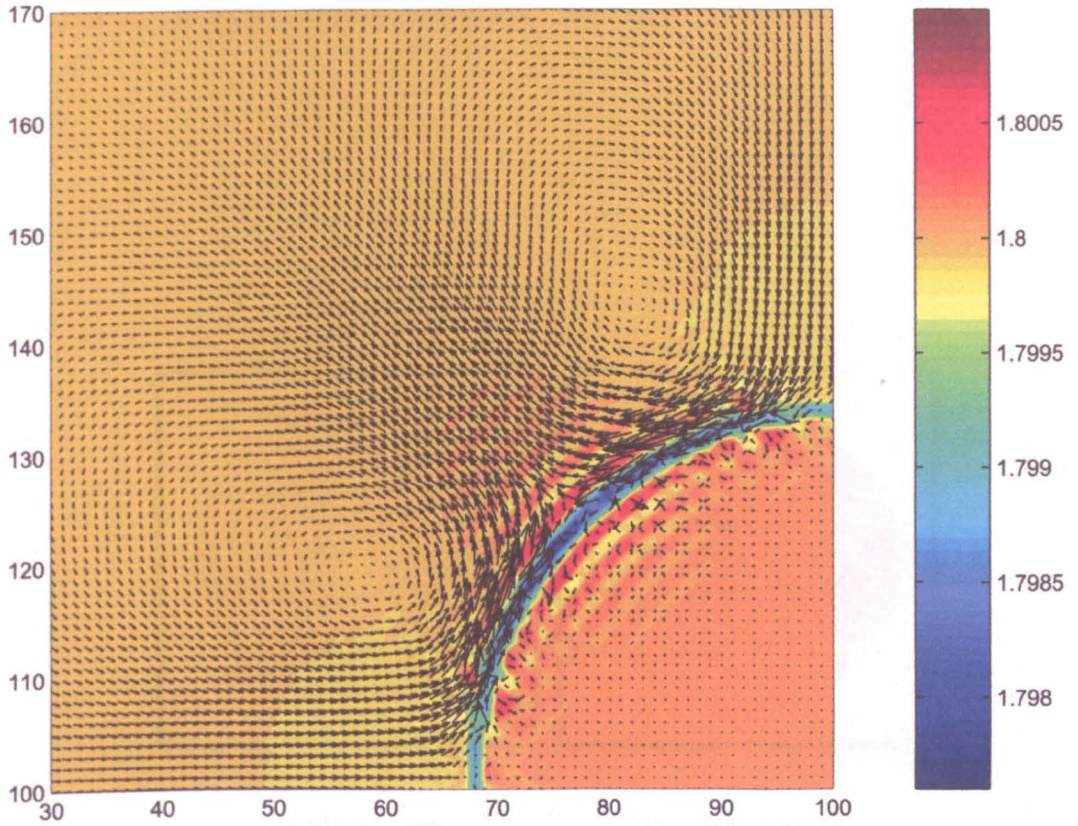

Figure 3.3: Steady state of the external flow field with the original Gunstensen method. The colour represents the fluid's pressure.

μ_a.

It should be noted that μ_a, unlike the micro-currents' pattern and the drop's qualitative anisotropy was found to be directly proportional to Σ (hence σ when every other parameters are kept constant), which points (again) to the surface tension perturbation step as the origin of the micro-currents.

The conclusion of this test on a simple Gunstensen droplet is that the surface tension step defined by equation 2.6 contains, implicitly, a high degree on anisotropy, which we addressed and correct subsequently (see section 3.2 below).

Test 3: Monochromatic droplet

A last test needed to be done to address the claim by Hou *et al.* [95] (see section 3.1.2). They suggested that the Gunstensen micro-currents are due to a mismatch of the colour-field and the interface normal, inducing a missed aligned colour-flux originating from the 'brutal' recolouring step. To assess the validity of this theory,

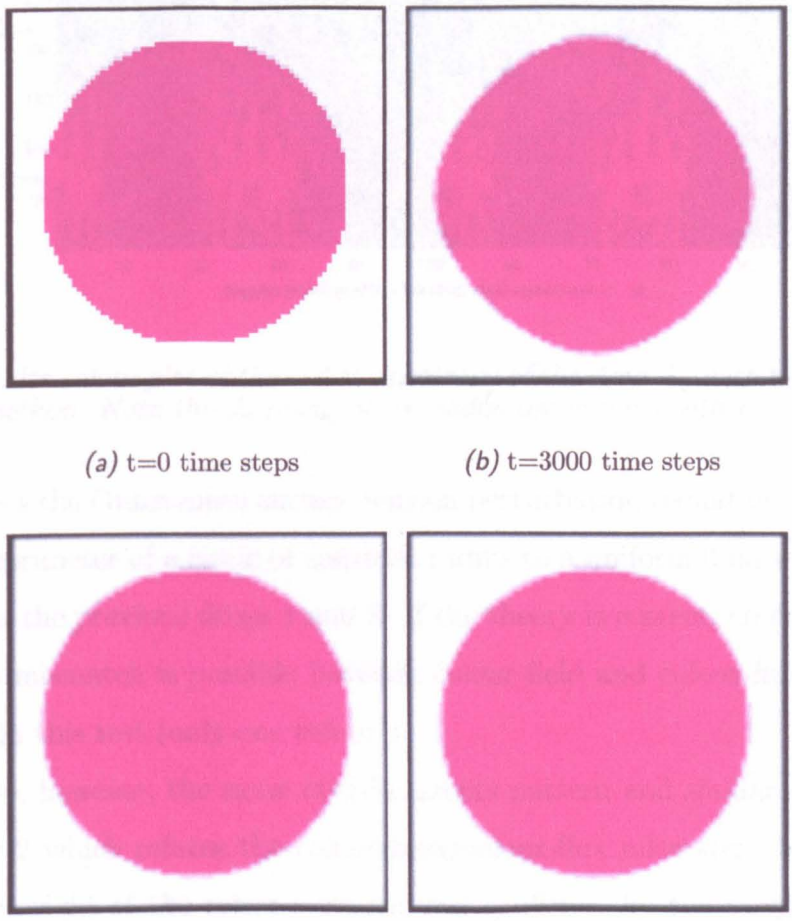

(a) t=0 time steps *(b)* t=3000 time steps

(c) t=10000 time steps *(d)* t=80000 time steps

Figure 3.4: Snap shots of a drop subjected to the Gunstensen method. The isotropic-anisotropic-isotropic sequence is clearly visible.

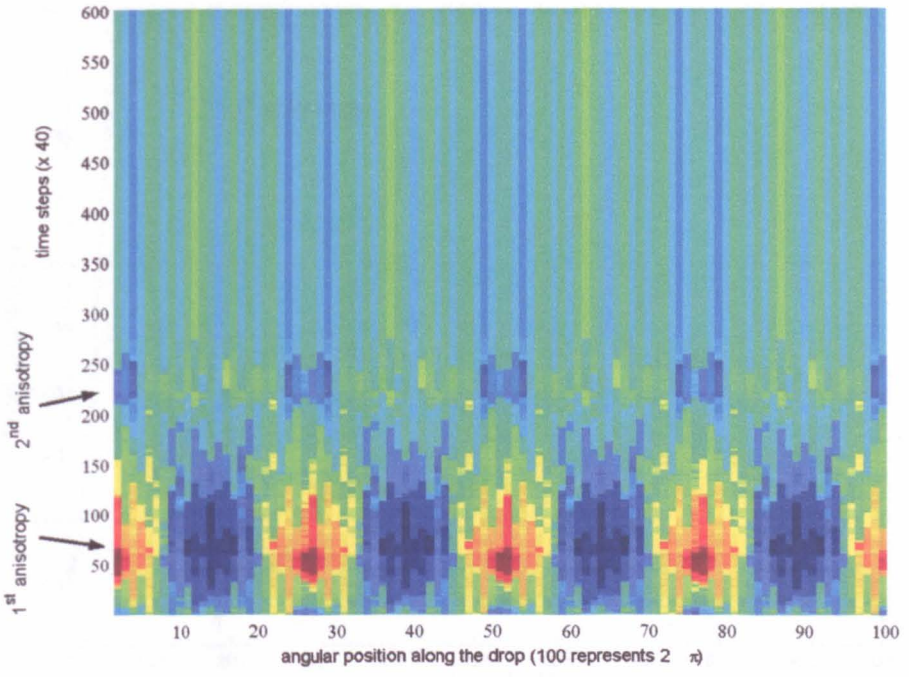

Figure 3.5: False colour plot of the radial anisotropy of the drop A_L with the Gunstensen method. Note the damping of the radial oscillations with time.

the test applies the Gunstensen surface tension perturbation (equation 2.6) to nodes close to the perimeter of a circle of constant radius to a uniform fluid with the same parameters as the previous drops 1 and 2. If the theory is correct, no flow should be observed: no mismatch is possible between colour-field and colour-flux, since they do not exist in this test (only one colour).

This test gave, however, the same micro-currents pattern and similar μ_a as that of drop number 2 which refutes the colour-field/colour-flux mismatch theory of *Hou et al.* for the origin of the micro-currents and confirms, by the same token, that the micro-currents in the Gunstensen method are certainly due to a surface tension perturbation's anisotropy over the length of the interface, rather than any colour related issues.

Similar dependance of the micro-currents in other models

It is interesting to realise that other models (LB and CFD) reported very similar dependance of the micro-currents pattern and activity on the parameters described above. For example, Lafaurie reported that the 'parasite' currents in his CFD model were directly dependant on the applied surface tension [115]. Inamuro reported

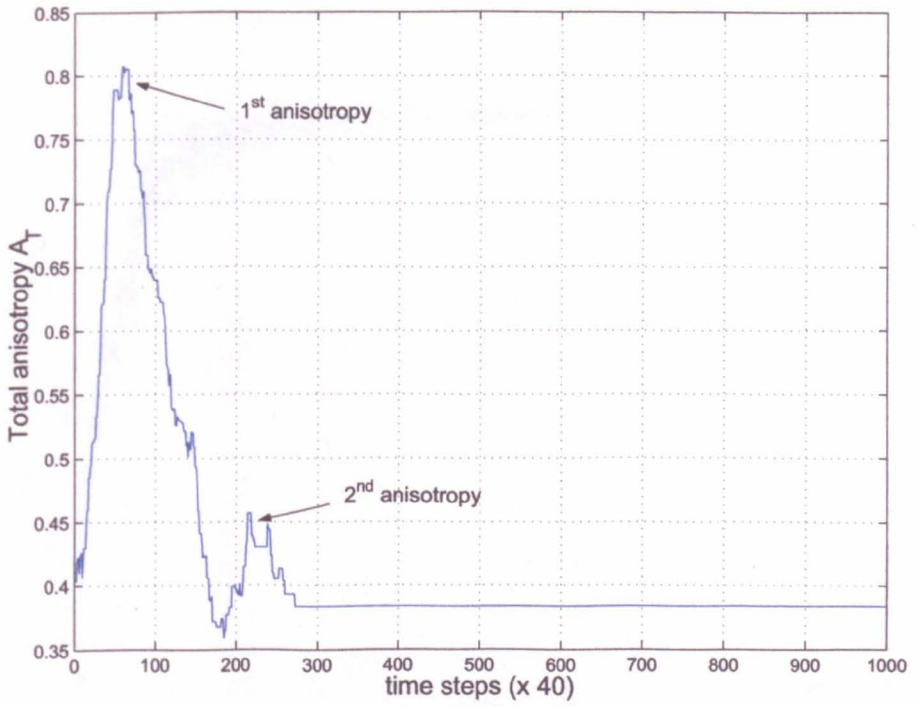

Figure 3.6: Total anisotropy A_T with the Gunstensen method. Note the 'kick' of anisotropy at the beginning of the simulation, subsequent damping, and final isotropic steady state.

the same dependance of the micro-currents activity on these parameters with his potential approach: his μ_a decreases with decreasing surface tension or increasing interfacial width (the study of the accuracy concerning these parameters has been set as future work in this paper) [99]. And Teng *et al.* noticed similar behaviour in the free energy approach [200].

3.2 The 'λ' method: a successful attempt to reduce the micro-currents

Previous sections showed that most fluid interface methods are subjected to some type of micro-currents (essentially due to discretisation issues in the surface tension step), and that LB methods are no exception. Reducing or eliminating them is therefore a great interest for current research, since it would advance further applications where the micro-currents are still blocking progresses.

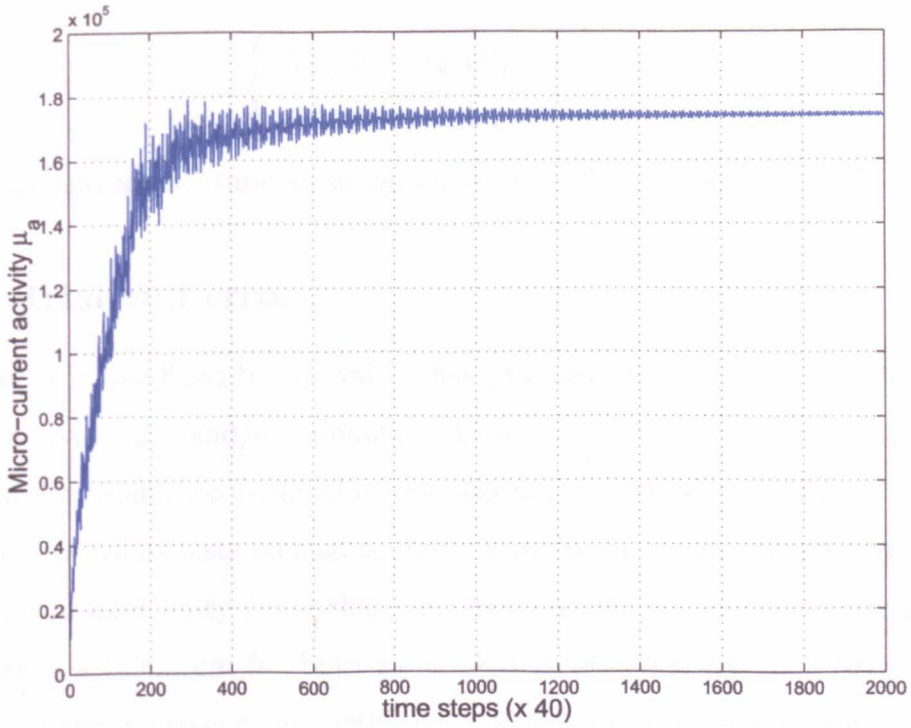

Figure 3.7: Micro-currents activity μ_a 3.2 with the Gunstensen method

3.2.1 The λ correction

We saw in section 3.1.3 that the micro-currents in the Gunstensen method are due to an imbalance within the interface forcing technique, despite the introduction of the concentration factor $CC(\rho^R, \rho^B)$ to the perturbation step. The Gunstensen interfacial perturbation is purely local (equation 2.6) and, in order to retain this main advantage over other techniques, any additional step or modification to the method should also be local.

The underlying D2Q9 lattice (see figure 1.2) can clearly be seen in the shape of the micro-currents (see figure 3.1), and it is therefore natural to impose an imbalance within the perturbation between the different links of the lattice, to counterbalance the observed anisotropy in the velocity field of a drop at rest. As a consequence, the original perturbation parameter σ (equation 2.6) has been added a link dependence:

$$\sigma \rightarrow \sigma_i \, .$$

This new σ_i must retain the basic properties of the original perturbation: nodal mass and momentum conservation. This is achieved by introducing a parameter λ to the new perturbation parameter σ_i as follow (recall the lattice geometry, figure

1.2):

$$\sigma_i = \begin{cases} \lambda\sigma & \text{for } i\text{=2,4,6,8 (short links)}, \\ \sigma & \text{for } i\text{=1,3,5,7 (long links)}. \end{cases}$$

Nodal mass and momentum conservation are easily verifiable.

3.2.2 Trial and error

The value of λ was fixed by the value that provided minimum steady state micro-currents activity (μ_a) and/or minimum anisotropy 'kick' (see figure 3.6) at the beginning of the simulation (defined as the maximum value of A_T in time) for a given λ, since the previous tests seemed to imply that the two artifacts are correlated. Scanning λ around unity (note that the basic Gunstensen method corresponds to $\lambda = 1$) gave a minimum for both μ_a as well as A_T. Figure 3.2.2 (a) shows the evolution of the micro-currents activity μ_a of a drop initialised at rest, varying λ. μ_a is clearly minimum when $\lambda \approx 2.1$ for both the transient and steady state. Figure 3.2.2 (b) shows the evolution of the corresponding total anisotropy $A_T(t)$. Again, the minimum is clearly when $\lambda \approx 2.1$ for both the transient and steady state. The simulation parameters for this data were: 100×100 nodes, $\omega^R = \omega^B = 1.7$, $\rho^0 = 1.8$, $\sigma = 0.001$, $R_{drop} = 25$, periodic boundary conditions top/bottom and left-right.

3.2.3 Improved model with $\lambda \approx 2.1$

According to these measurements, $\lambda \approx 2.1$ ensures minimum micro-currents activity and maximum transient isotropy of a rest droplet. Figure 3.9, 3.10 and 3.11 show that, with this correction, the micro-currents are concentrated much more at the interface, leaving a significantly reduced internal and external flow field. Note that a residual 'checker-board' pattern appears more explicitly with the λ correction, which was probably overwhelmed by the main pattern of the micro-currents in the original method. Such checker-boarding is common noise in numerical methods. We also noticed that this checker board pattern can be removed by time averaging over two time steps the nodal velocity. This suggests that the micro-currents activity and pattern are, in fact, a superposition of multiple effects and gives hope to the possibility of reducing them even further. The simulation parameters for this data

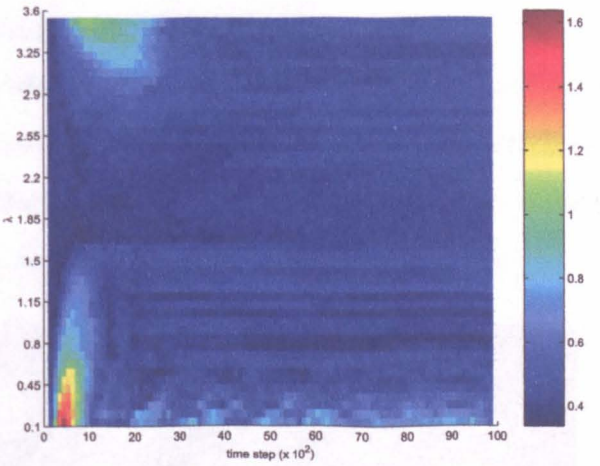

(a) Evolution of $\max(A_T)$ VS $\{\lambda, t\}$

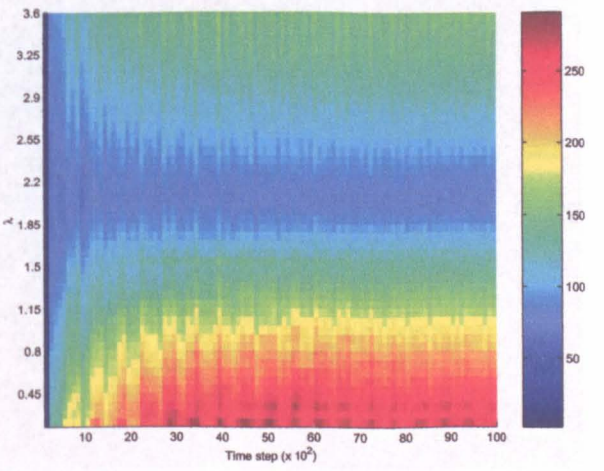

(b) Evolution of μ_a VS $\{\lambda, t\}$

Figure 3.8: False colour plots of micro-currents activity in time. A minimum at $\lambda \approx 2.1$ is clearly visible in both the kick of anisotropy of the drop and the transient and steady-state of the micro-currents activity.

were those of figure 3.1 (original Gunstensen equivalent simulation): 200×200 nodes, $\omega^R = \omega^B = 1.7$, $\rho^0 = 1.8$, $\sigma = 0.001$, $R_{drop} = 33$, periodic boundary conditions top/bottom and left-right.

It should be however noted that the micro-currents' pattern remains approximately the 'same as' with the Gunstensen method (even thought the overall micro-currents are reduced considerably. Figure 3.12 shows this more explicitly, by comparing the modulus of the nodal velocities for the Gunstensen method and the λ method. Note that (i) the micro-currents are mainly concentrated at the interface with the λ method and (ii) the difference in the velocity scale, gives an estimate of the reduction in micro-currents of a factor 4 overall and 6–7 in the bulk.

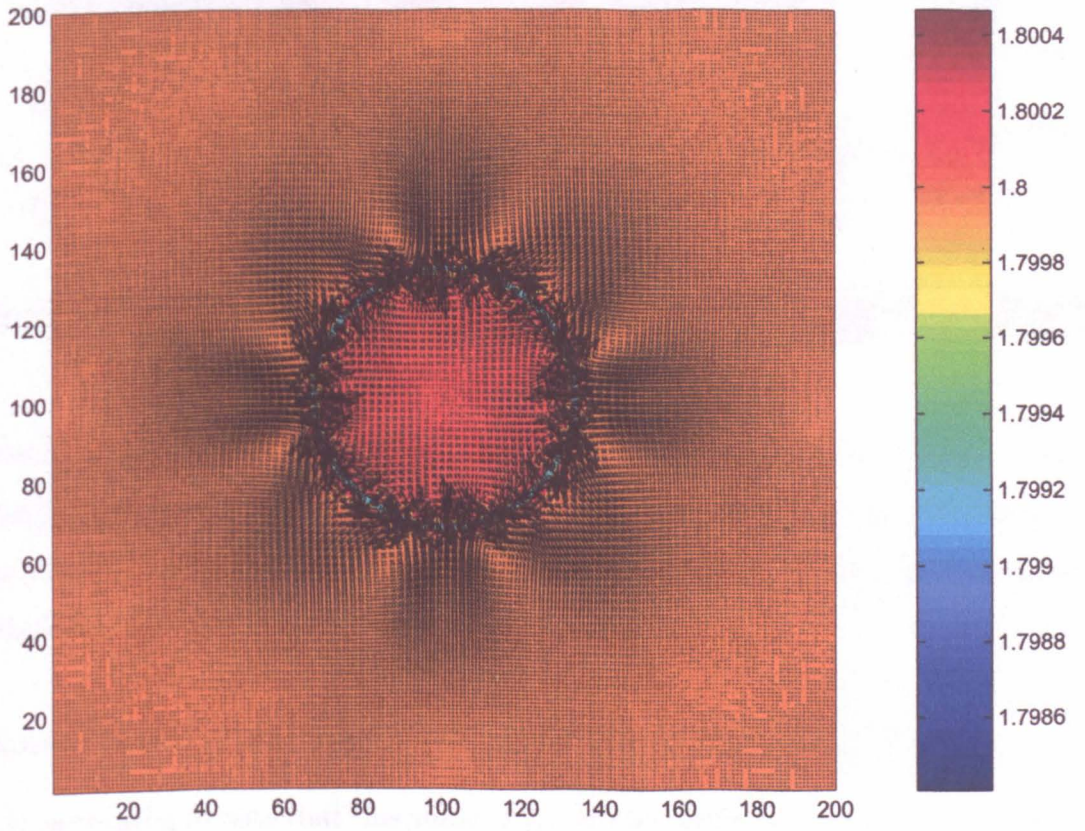

Figure 3.9: Overall micro-currents flow field with the $\lambda = 2.1$ correction. It should be noted that this pattern is qualitatively very similar from the one obtained with the original Gunstensen method.

Quantitatively, figure 3.13 shows that the 'kick' of the isotropy is non-existing, and figure 3.14 shows that μ_a is 5 times reduced.

We investigated the gain of stability of the λ method though the Laplace law (equation 1.18). We define the limit of stability of a method (original Gunstensen or λ)

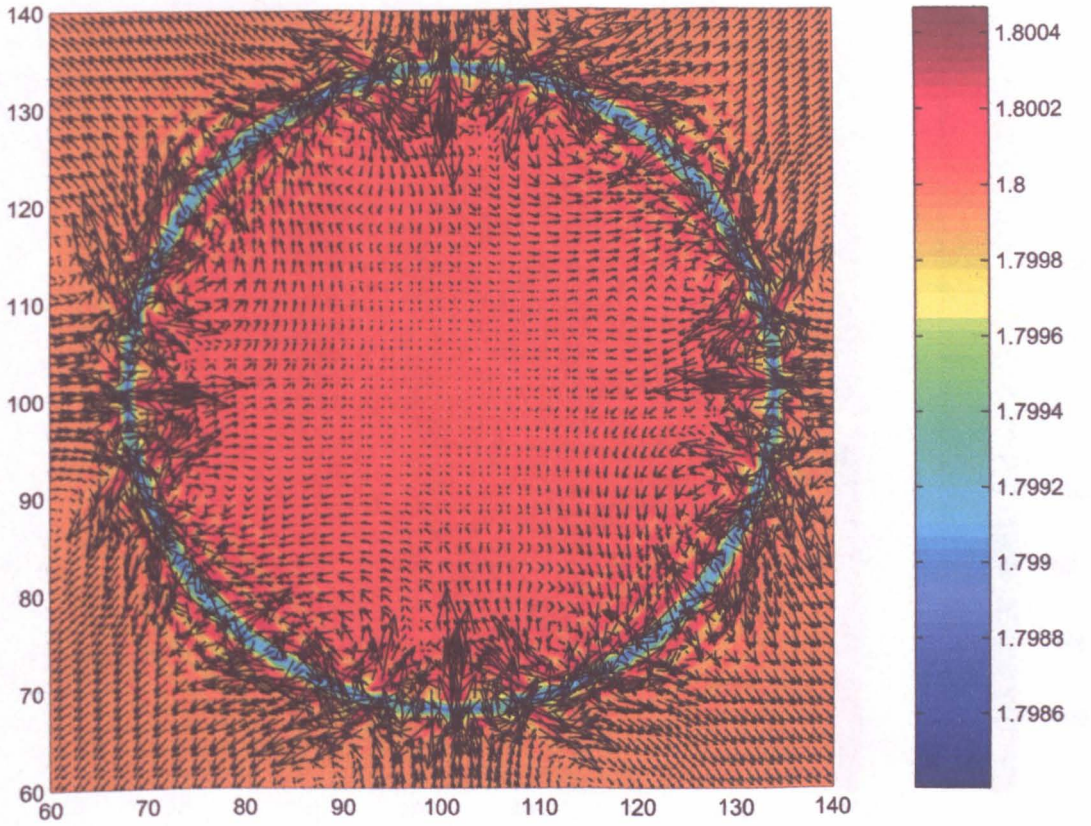

Figure 3.10: Internal micro-currents flow field with the $\lambda = 2.1$ correction. Note the explicit checker board pattern and the peak activity at the poles and equator of the drop.

by the σ parameter, taken as the maximum value of σ giving a difference of pressure ($\triangle P$) which remains in the linear part of the Laplace Law. Figure 3.15 shows that the stability and the linear response over the σ parameter are enhanced by a factor 4 with the λ correction.

3.2.4 Analytical verification of the value of λ

It is interesting to note that this value of 2.1 can be verified analytically. The original Gunstensen surface tension method (equation 2.6) can be adjusted independently in D2Q9 as, for horizontal(diagonal) links, surface tension is produced by perturbating on the short(long) links only. Consequently, Halliday *et al.* [82] showed that the effective surface tension obtained by the Gunstensen algorithm depends indeed on the orientation of a planar interface with respect to the lattice:

$$\Sigma = \begin{cases} 4\sigma \,/\, 3\omega \approx 1.33\,\sigma/\omega & \text{for horizontal interfaces}, \\ 4\sigma \,/\, \sqrt{2}\omega \approx 2.83\,\sigma/\omega & \text{for diagonal interfaces}. \end{cases} \tag{3.5}$$

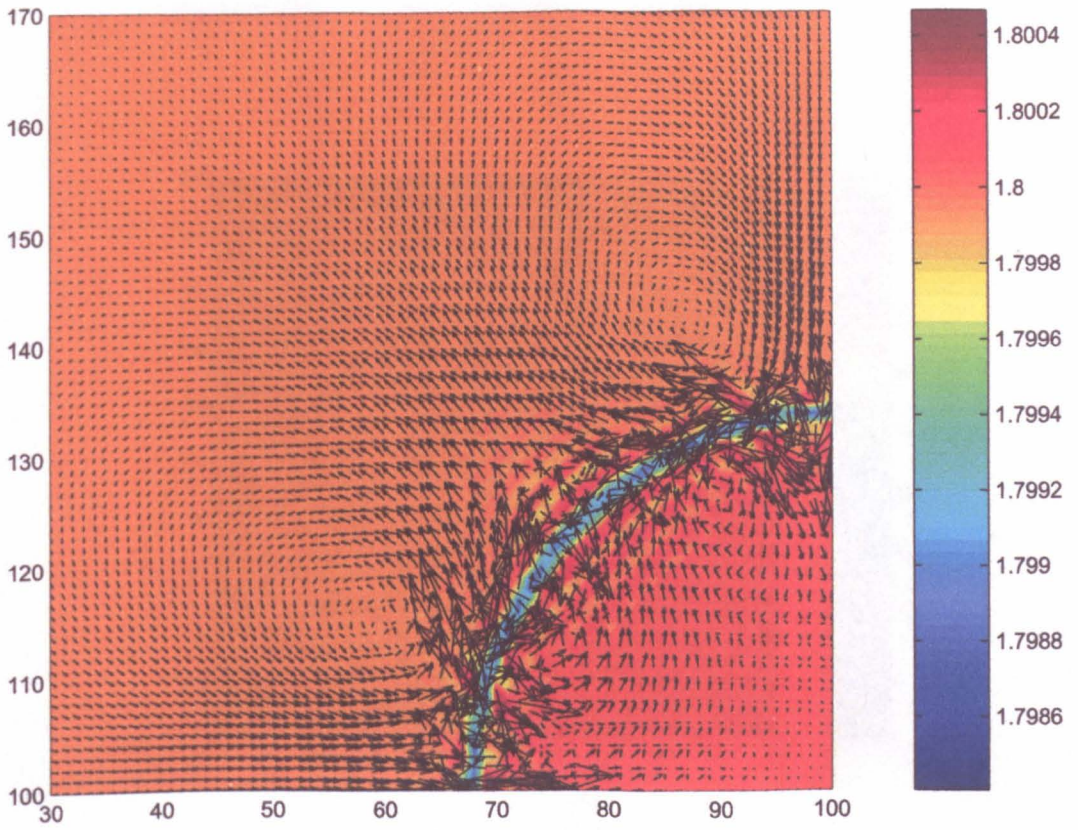

Figure 3.11: External micro-currents flow field with the $\lambda = 2.1$ correction. the External recirculation is similar in shape to the one of the original Gunstensen method.

Note that these formula assume that both fluids have the same viscosity. In the case of a (closed) droplet, the interface lies along all possible directions and the droplet experiences smaller surface tension on its poles and equator (short links) than on its north-east, north west, south-east and south-west faces (long links), since the σ and ω parameters are constant. This explains why, the droplet acquires the shape of figure 3.4 at an early stage but does not explain why the droplet relaxes towards an isotropic shape at steady state. The author does not have an explanation for the later. Figure 3.16 illustrates this point: at t=0, the droplet experiences stronger surface tension when the interface is diagonal than longitudinal.

This imbalance is quantified by the ratio of the effective surface tension along the short and long links and dividing the two equations of equation 3.5, gives the dimensionless ratio:

$$\lambda_0 = \frac{3}{\sqrt{2}} \approx 2.1 \tag{3.6}$$

which corresponds to the value obtained by experiment. The modification of the

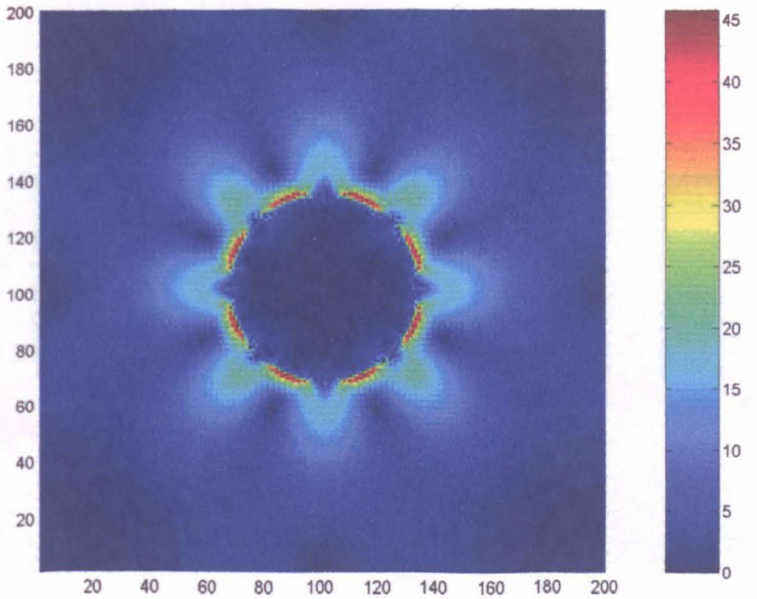

(a) Gunstensen method

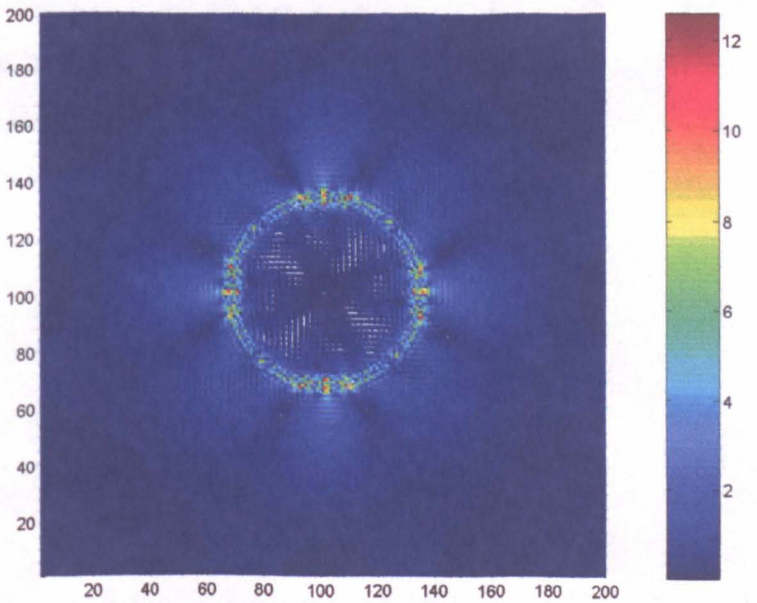

(b) Lambda method

Figure 3.12: Steady state nodal velocity modulus

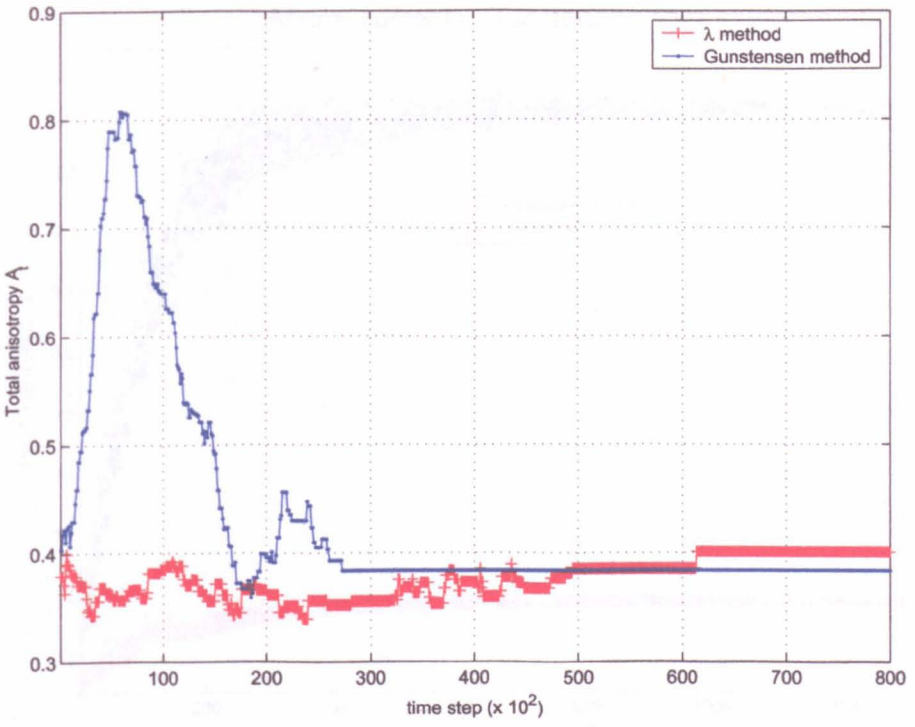

Figure 3.13: Total anisotropy $A_T(t)$. Note that $A_T(t) < 0.5$ for all t, implying that the drop stays isotropic through its relaxation to steady state.

surface tension with $\lambda \approx 2.1$ as the consequence, to erase this imbalance ensures a smooth surface tension along all interfacial directions. This confirms the measurements and the fact that this very simple modification to the Gunstensen's interface is enough to 're-balance' the surface tension perturbation.

3.2.5 Conclusion of the λ correction

We define $\lambda_0 = 2.1415$ the value of the 'counterbalancing' parameter λ providing a minimum A_T and minimum μ_a. We found that this simple correction improves considerably the way a drop relaxes to steady state and reduces the micro-currents activity by a factor 5 (ratio between the total micro-currents with $\lambda = \lambda_0$ and $\lambda = 1$, corresponding to the Gunstensen method). This provides consequently a better flow field at low Re and high Σ (small capillary number regime) [46], by concentrating the micro-currents at the interface.

The reader should note that, in all the remainder of this thesis, the use of the λ correction (with $\lambda_0 = 2.1415$) is implicit when mentioning the use of the 'Gunstensen'

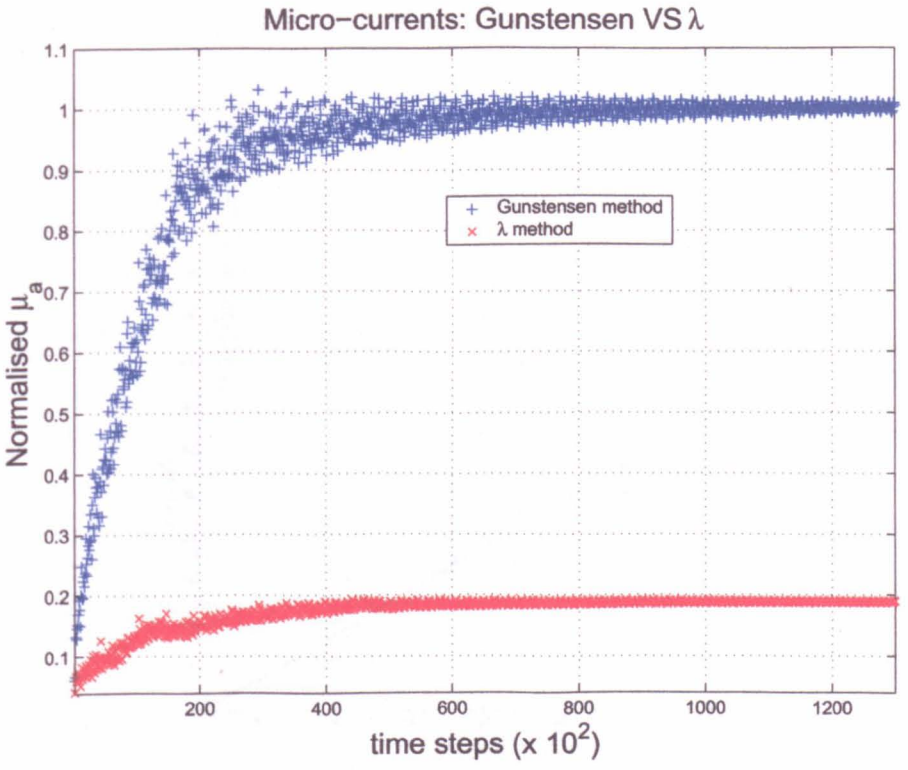

Figure 3.14: Micro-currents activity μ_a

method.

3.3 Further refinements to the Gunstensen algorithm

Driven by the need to reduce μ_a even further in order to reach lower capillary number (for the micro-fluidic applications), few improvements to the Gunstensen method have been necessary, especially in respect of the behaviour of the system near to solid walls, usually at rest.

3.3.1 Redefinition of the colour-field next to the walls

The symptoms

Our first improvement has been to redefine the colour-field at nodes in contact to a wall. We realised that the current definition of the colour-field (equation 2.3) carries

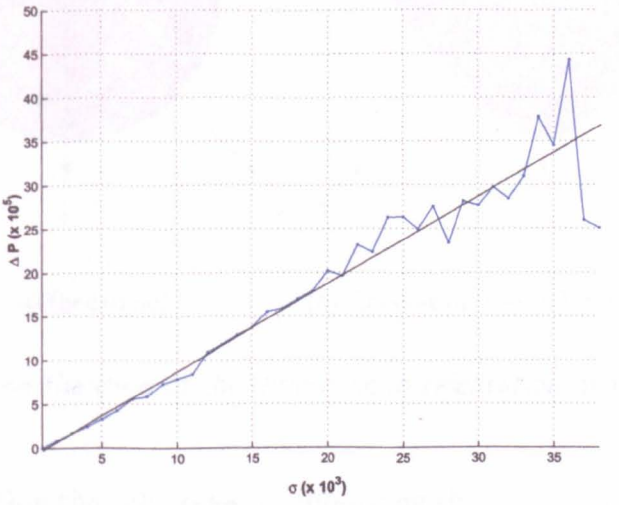

(a) Gunstensen method

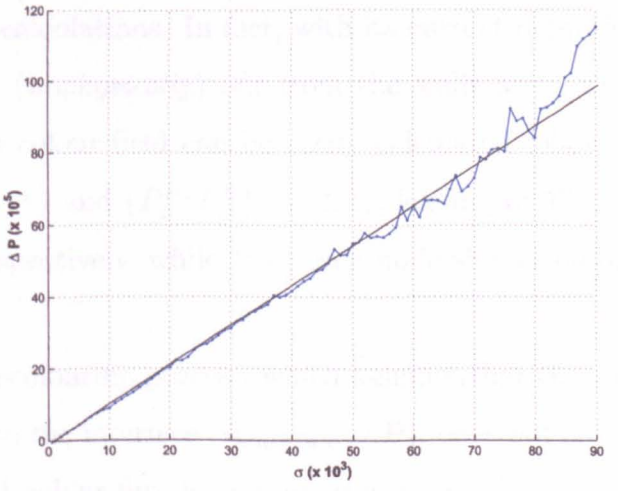

(b) Lambda method

Figure 3.15: Stability over σ. Note that the overall hydrodynamics cannot be guarantied beyond the linear part of these curves, defining the limit of stability.

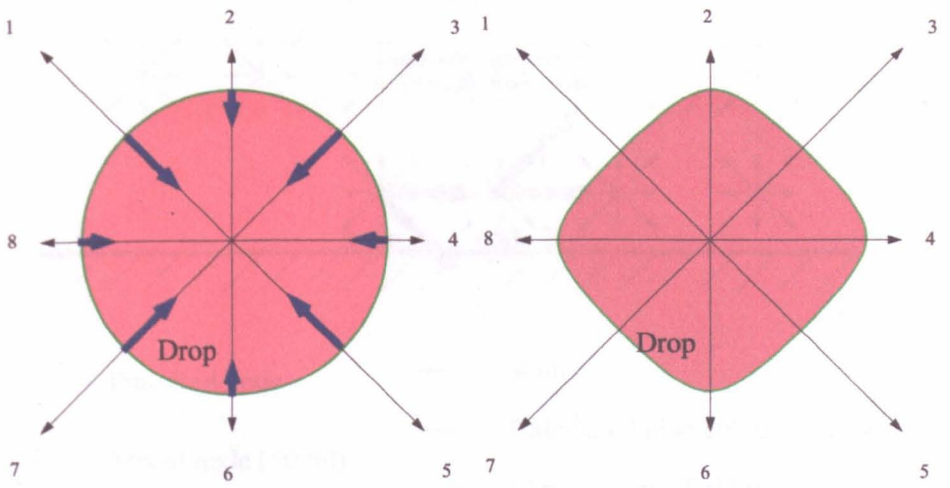

(a) t=0 (isotropic) *(b)* Relaxation through highly anisotropic stage

Figure 3.16: Effect on the drop of the difference in orientation of the effective surface tension.

the implicit assumption that all nodes neighbouring the site are populated. The very presence of a wall near a node (in the mid-link bounce back method, see previous chapter for details) breaks immediately this assumption and leads to subsequent asymmetries in the calculations. In fact, with its current definition, the colour-field would always point (*unphysically*) out from the walls as figure 3.17 explains. In this figure, the blue colour-field can be easily calculated following equation 2.3 to be $\{P_x^B; P_y^B\} = \{2; -1\}$ and $\{P_x^B; P_y^B\} = \{2; 1\}$, leading to $\theta_P^B = 135^o$ and $\theta_P^B = 45^o$ for node 1 and 2 respectively, while $\mathbf{P}$ at each node should be both equal to $\{2, 0\}$ and $\theta_P^B = 0$.

Consequently, the recolouring process, which assumes that the colour-field direction defines the normal to the interface ($\hat{\mathbf{n}}_{interface} = \hat{\mathbf{P}}$), does not reallocate colour properly: an un-physical colour-flux is created and pushed back towards neighbouring nodes (through propagation and bounce back), generating significant micro-currents next to walls.

The solution

To address this problem, the origin of the colour-field vector $\mathbf{P}$ of the previous formula is shifted half a node away from the wall as figure 3.18 explains.

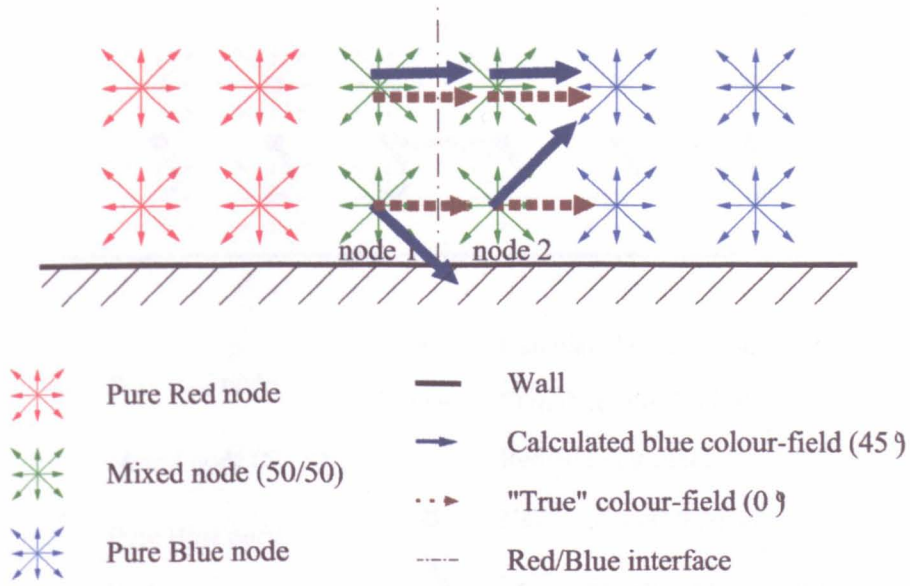

Figure 3.17: This configuration is the typical case of a red/blue fluid interface next to a wall (that can be found in the case of a drop sitting on a wall). The difference of calculated and true colour-field is explicit.

The corrected definition for the colour-field next to walls reads as follow:

$$P_\alpha(\mathbf{x})|_{wall} = \sum_i \left[\rho^R(\mathbf{x}+\mathbf{c_i}-W_\alpha(\mathbf{x})) - \rho^B(\mathbf{x}+\mathbf{c_i}-W_\alpha(\mathbf{x}))\right] c_{i\alpha}\,, \tag{3.7}$$

where W_α represents the relative coordinate of the wall to the node at $\mathbf{x}$, defined as follow:

$$W_\alpha(\mathbf{x}) = \sum_i BB(\mathbf{x}+\mathbf{c_i})\, c_{i\alpha}\,, \tag{3.8}$$

This simple modification reduces the micro-currents activity by a factor 3 when using the Gunstensen method on drops in contact with a solid boundary.

Additional benefit

Small but non-zero sticking of droplet material on walls went unnoticed at first, but became an issue when dealing with a large number of non-coalescing droplets in confined geometry, in our N-component algorithm (see chapter 4).

The original definition of the colour-field has the consequence of generating a 'tail' of drop fluid onto the wall. Figure 3.19 shows the sticking of density (tail) of the drop onto the wall, and the result with the corrected formula. It should be noted

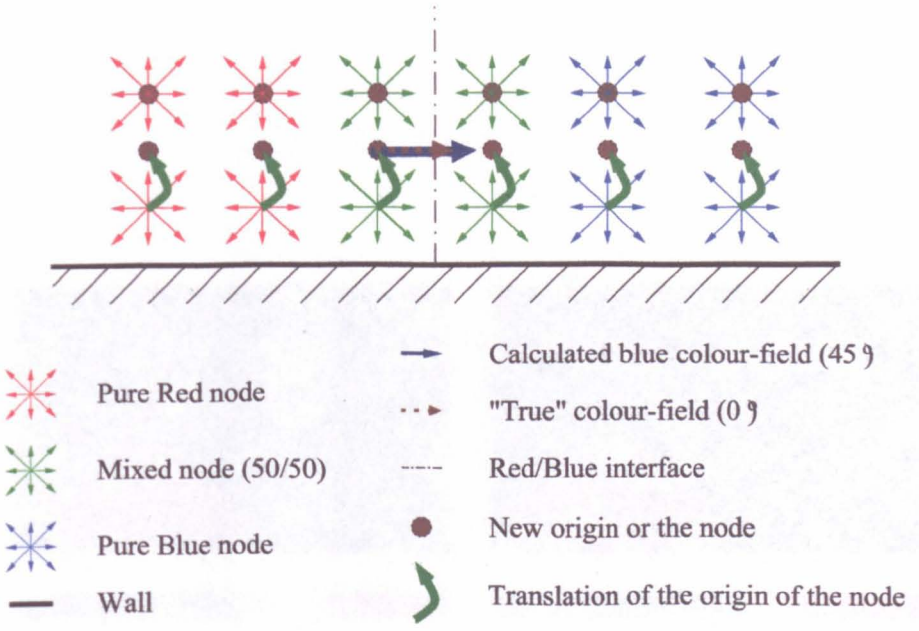

Figure 3.18: Shifting the origin of nodes next to walls of 1/2 a node away from the wall refines the balance of the colour-field definition and solves the problem of calculating the colour-field near a no-slip boundary.

that this loss of density is not very large as the two pictures of the second raw of figure 3.19 *d* demonstrate which show the $\rho^N \equiv \rho^R - \rho^B$ function in the lattice and nothing unusual is to be reported. The only way to picture this tail of sticking density has been to image the mixed nodes, as the row of figure 3.19 demonstrates. The simulation parameters of this data were: 200×50 nodes, $\omega^R = \omega^B = 1.7$, $\rho^0 = 1.8$, $\sigma = 0.001$, $R_{drop} = 20$ initialised on half a circle, periodic boundary conditions top/bottom and left-right, $g = 0.00001$ acting horizontally (body-force mimicking gravity to set the drop into motion, see section 3.4.6).

This new definition of the colour-field consequently ensures that the drops retain their integrity when moving onto a solid surface. This had significant consequence on the stability of the N-component model (see next chapter).

3.3.2 Redefinition of the recolouring order

The symptoms

The accepted recolouring algorithm (discussion above) introduces an asymmetry to the colourflux when the colour-field lies around a lattice direction. In this situation, it seems to be particularly important that the recolouring order should take account

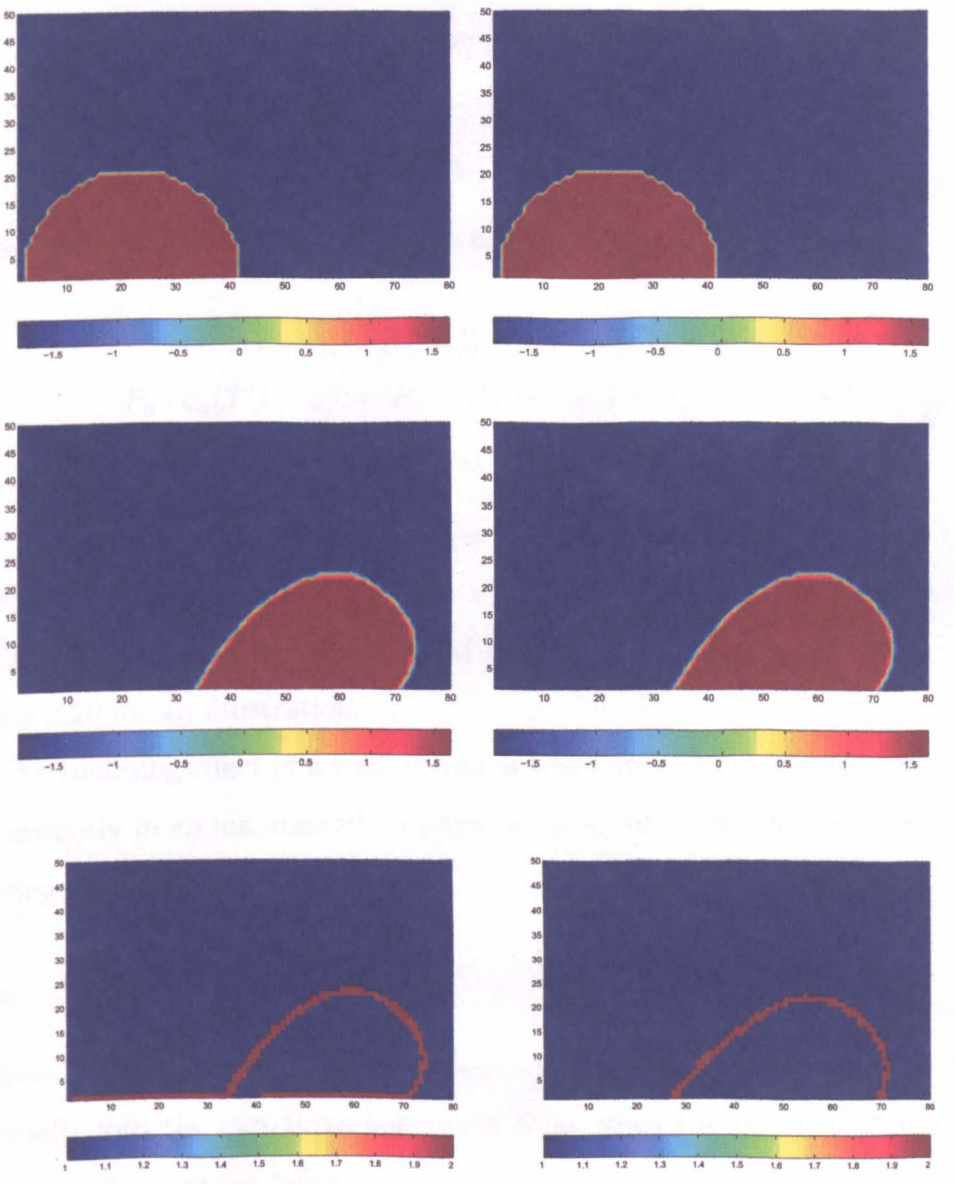

Figure 3.19: First/second column: the original colour-field definition/enhanced definition. First row: initial configuration. Second row: ρ^N function (note that the tail of density cannot be seen). Third row: number of colours at a site.

of the fact that some links produce the same degree or segregation (i.e. same work of the colour field against the link $\mathbf{c_i} \cdot \hat{\mathbf{P}} = \mathbf{c_j} \cdot \hat{\mathbf{P}}$).
This situation can be grouped into two cases:

- When **P** is along a short link, we have:

$$\left.\begin{aligned} P_\alpha \cdot c_\alpha(T(i)) = P_\alpha \cdot c_\alpha(T(i+1)) = P_\alpha \cdot c_\alpha(T(i+2)), \\ P_\alpha \cdot c_\alpha(T(i+3)) = P_\alpha \cdot c_\alpha(T(i+4)) = P_\alpha \cdot c_\alpha(T(i+5)), \\ P_\alpha \cdot c_\alpha(T(i+6)) = P_\alpha \cdot c_\alpha(T(i+7)) = P_\alpha \cdot c_\alpha(T(i+8)), \end{aligned}\right\}$$

- and when **f** is along a long link, we have:

$$\left.\begin{aligned} P_\alpha \cdot c_\alpha(T(i+1)) = P_\alpha \cdot c_\alpha(T(i+2)), \\ P_\alpha \cdot c_\alpha(T(i+3)) = P_\alpha \cdot c_\alpha(T(i+4)) = P_\alpha \cdot c_\alpha(T(i+5)), \\ P_\alpha \cdot c_\alpha(T(i+6)) = P_\alpha \cdot c_\alpha(T(i+7)), \end{aligned}\right\}$$

where $i + n$ represents the n^{th} link after the link i on a base 9 (see the D2Q9 geometry, figure 1.2), T(i) represents the i^{th} link in the order of the look-up table T and $c_\alpha(T(i+n))$ represents its associated velocity in the direction α.
See figure 3.20 for an illustration.
Due to the confining effect of a wall, colour is therefore pushed (via the propagation step) constantly in an maintained un-physical direction, since the incorrect order of recolouring is constant.

The fix

To address this issue, the recoulouring algorithm has been modified to re-allocate mass equally into the two/three equivalent links when the colour-field lies around the direction of a node as follow:

- When **P** lies parallel to a short lattice link the first three directions in the look-up table, T, are taken to be degenerate for colour re-allocation priority. The fourth to the sixth links are likewise taken to be degenerate, as are the seventh to the ninth links. That is, for an upward vertical colour field (along link direction 2), links in the subsets $\{1, 2, 3\}$, $\{4, 5, 6\}$, and $\{7, 8, 9\}$ are recoloured equally amongst themselves.

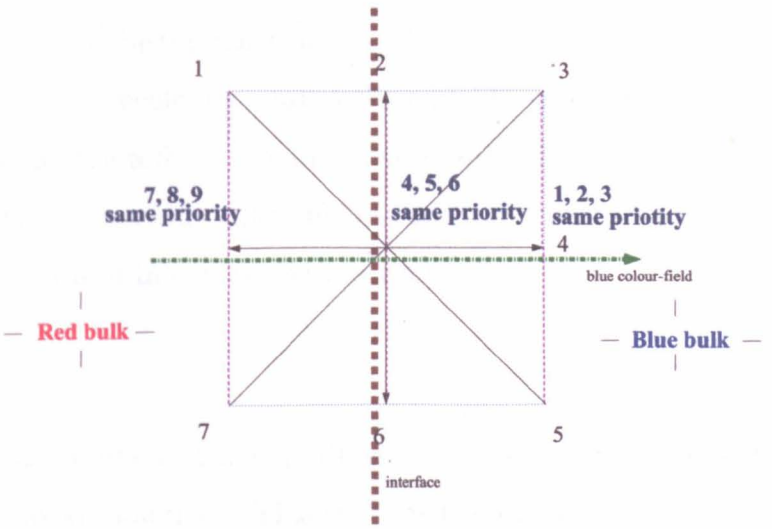

(a) When the colour-field is along the short links

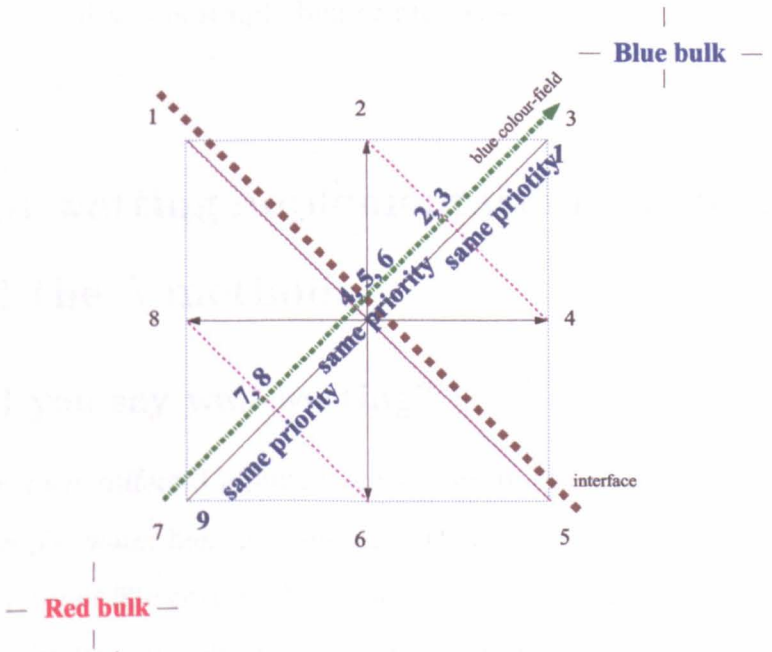

(b) When the colour-field is along the long links

Figure 3.20: Sets of links providing equal segregation with the given colour-field.

- And when **P** is along a long link, the sets of links $\{2,3\}$, $\{4,5,6\}$, and $\{7,8\}$ in the order of the look-up table T should be recoloured equally if there is not enough density to fill the set completely.

We defined arbitrarily the tolerance of $+/-5^o$ for the limit between normal and modified recolouring: the recolouring takes the equality into account when the colour-field's direction is within 5^o of the direction of a lattice link.
We measured that this reduced the micro-currents activity by a factor 2 when the drop is in the bulk *and* in contact with a wall.

Consequences

In the case of two component flow (1 drop, 1 interface), this issue seldom raises and had therefore stayed unnoticed. This enhanced recolouring scheme had more consequences in the case of N–component simulations since the probability of having this recolouring asymmetry is multiplied by N_t (where N_t denotes the number of fluids at a node) compared to the simple binary fluid case.

3.4 Wall-wetting implementation for the Lishchuk and the λ methods

3.4.1 Did you say wall-wetting?

Different fluids have different affinities with other fluids, but also with different surfaces. For example, water has much less affinity with a material such as $Gore-Tex^{®}$ than with a material like cotton. Macroscopically, chemical interactions, often due to hydrophobic-hydrophilic effects, are at the source of this affinity. Mesoscopically and macroscopically, one can overlook these considerations and concentrate on their phenomenological effect: the macroscopic contact angle that interface does on a given surface [94], see figure 3.21.
The angle of contact (θ_c) is very often known experimentally to a great accuracy [81] (e.g. by microscopical indirect measurements [40]), and very often refers to an

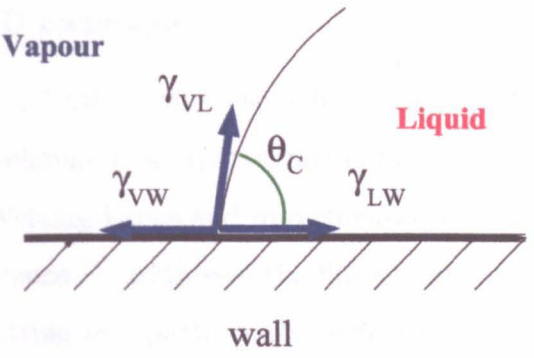

Figure 3.21: Wall wetting diagram of a fluid interface in contact with a wall. θ_C is the contact angle.

interface between a liquid and a vapour. Contrary to the sign of the surface tension between a liquid and a vapour (which can be assumed positive), no assumptions can be made on its sign [81]. This is because the difference of affinity between the two fluids with the surface can easily overcome the interfacial surface tension to give the contact angle a positive value.

In the case of figure 3.21, the contact angle is related to the surface tension and different wettings by the Taylor-Laplace law [6]:

$$cos(\theta_c) = \frac{\gamma_{LW} - \gamma_{VW}}{\gamma_{LV}}, \tag{3.9}$$

where γ_{LW} is the surface tension between the solid and the liquid, γ_{VW} is the surface tension between the vapour phase and the solid, and γ_{LV} is the surface tension of the liquid-vapour interface. Note that this equation is also known as Young's equation, after [216].

Control of wall-wetting behaviour is a requisite for any numerical method modeling confined systems, as explained by Anna *et al.* in [3].

3.4.2 Literature on the implementation of wall-wetting

In order to impose a wall-wetting property alongside a given interfacial technique, it is natural to use an interfacial method which complements the one used to impose surface tension.

Wall-wetting in CFD techniques

Following this principle, VOF solvers use a body force acting parallel to the wall to impose a wetting behaviour, as Hirt explains in a technical report of his VOF solver *Flow3D* [94]. Wetting issues and implementation with the CSF method can be found in [38]. Reference [7] addresses the finite element modelling and issues of surface tension and wetting in a particularly clear way.

Wall-wetting the LB Free Energy model

The Free–Energy LB method uses the gradient of an external chemical potential as a thermodynamic force at the interface [190]. In 1988, Langass *et al.* ([117], [118]) used this approach to implement wetting behaviour and applied this model to the study of the flow in porous media.

Desplat *et al.* had implemented wetting properties into LUDWIG, designed originally for the study of the flow through porous media (but actually never did it to the author's best knowledge). They presented however a scheme for the thermodynamically consistent simulation of wetting phenomena, in the case of static and moving solid boundaries (see Desplat *et al.* [45]).

In a recent paper, Léopoldès *et al.* reported close quantitative match to experimental results, investigating the behaviour of micron-scale fluid droplets jetted onto surfaces patterned with lyophobic and lyophilic stripes (providing accurate predictions of fluid droplet behaviour for a wide range of surfaces) [122]. More recently, Dupuis *et al.* applied this model to describe (i) the spreading of droplets on topologically patterned substrates and (ii) the super-hydrophobic behaviour of a droplet sitting on surfaces covered by an array of micron-scale posts [49] (more information can also be found in [50]).

And very recently, Briant *et al.* have implemented a thermodynamically consistent boundary condition in this free energy model, allowing them to fix the static contact angle θ_c in the simulations. They investigated the applicability of this model to the problem of the motion of the contact line in liquid-gas systems [17] and binary systems [18].

Wall-wetting the LB Potential approach

In 1996, Martys *et al.* compared (favourably) with experiment the relative permeability of different wetting fluid saturations through a microtomography-generated image of sandstone. In addition, they show a three dimensional first-order phase transition, demonstrating, by the same token, the potential of this model for the modeling of phase transitions and the modeling of multiphase flow through porous media [135].

Very recently, Pan *et al.* derived a method based on [135], consisting of a two stage method: a sparse domain decomposition stage and a simulation stage. This avoids the need to store and operate lattice points located within a solid phase [152]. They found that this technique was very efficient to model the flow in porous media, idealised there by a large number of spheres [151].

So far, most of applications using this technique consisted of the study of the flow through porous media, and all find satisfying comparison with experiment. It should not be forgotten, however, that this model does not separate efficiently the two fluids in contact, and one could wonder about the dynamics of these simulations, especially when a different wetting behaviour is applied to each fluid (which requires a sharp interface to be consistent with the length scale of continuum LB).

Wall-wetting in the LB immiscible model

To summary, most numerical models had been implemented with wall-wetting but the Gunstensen model had mostly been left aside. Tölke mentions wall-wetting very briefly [205] (concentrating mostly on the flow of droplets with explicit difference of densities) and addresses it by adding a body–force to the interface. To the best author's knowledge, it is therefore fair to say that the Gunstensen method required an extension to enable differential wall-wetting.

3.4.3 Wall-wetting implementation in the λ method

The wetting behaviour of an interface is strongly linked to the surface tension, since surface spreading is a form of surface tension itself (see equation 3.9). As a consequence, the step of imposing a wetting behaviour to an interface was designed

to be consistent with the step of imposing surface tension, as mentioned for other methods.

Following equation 2.6, which has the effect of imposing a pressure step through the interface, we implement wall-wetting for the λ method following the same approach:

$$\triangle f_i(\mathbf{x}) = \left[\rho^R(\mathbf{x})\,\sigma^R_{wall} + \rho^B(\mathbf{x})\,\sigma^B_{wall}\right]\, cos(2\,(\theta_w(\mathbf{x}) - \theta_i))\,\lambda_i\,, \tag{3.10}$$

where σ^R_{wall} and σ^B_{wall} are wall-wetting parameters for the *red* fluid and *blue* fluid respectively (positive/negative values give drying/wetting behaviours to the fluids), and θ_i is the (usual) angle of the link number i (see D2Q9 lattice, figure 1.2). θ_w is the angle of the vector pointing towards the wall from the nodal position $\mathbf{x}$, and is defined as follows:

$$\theta_w(\mathbf{x}) = tan^{-1}\left(\frac{W_y(\mathbf{x})}{W_x(\mathbf{x})}\right) \tag{3.11}$$

where $W(\mathbf{x})$ is defined as in equation 3.8. Note that we apply this perturbation to any node in contact with walls.

3.4.4 Wall-wetting results

We obtained different wall-wetting behaviours (wetting and drying) by tuning σ^R_{wall} with respect to σ^B_{wall} in equation 3.10. Figure 3.22 demonstrates this capability. The simulation parameters for this data were: 100×50 nodes (200×50 for the two last, high wetting), $\omega^R = \omega^B = 1.7$, $\rho^0 = 1.8$, $\sigma = 0.0002$, $\sigma^R - \sigma^B = 0.001$ to 0.0001, $R_{drop} = 20$ initialised as half a circle onto the wall, periodic boundary left-right and bounce back top and bottom.

Continuum fluid dynamics indicates that the shape of a droplet on a wall should be a segment of a circle, the droplet retaining a constant radius of curvature all around the interface, due to constant surface tension. This feature is clearly visible in figure 3.22.

3.4.5 Discussions of the wall-wetting implementations

Stability of the method

It has been mentioned in last chapter that the overall stability of the system depends on each driving effect: the surface tension has been identified as being one, which

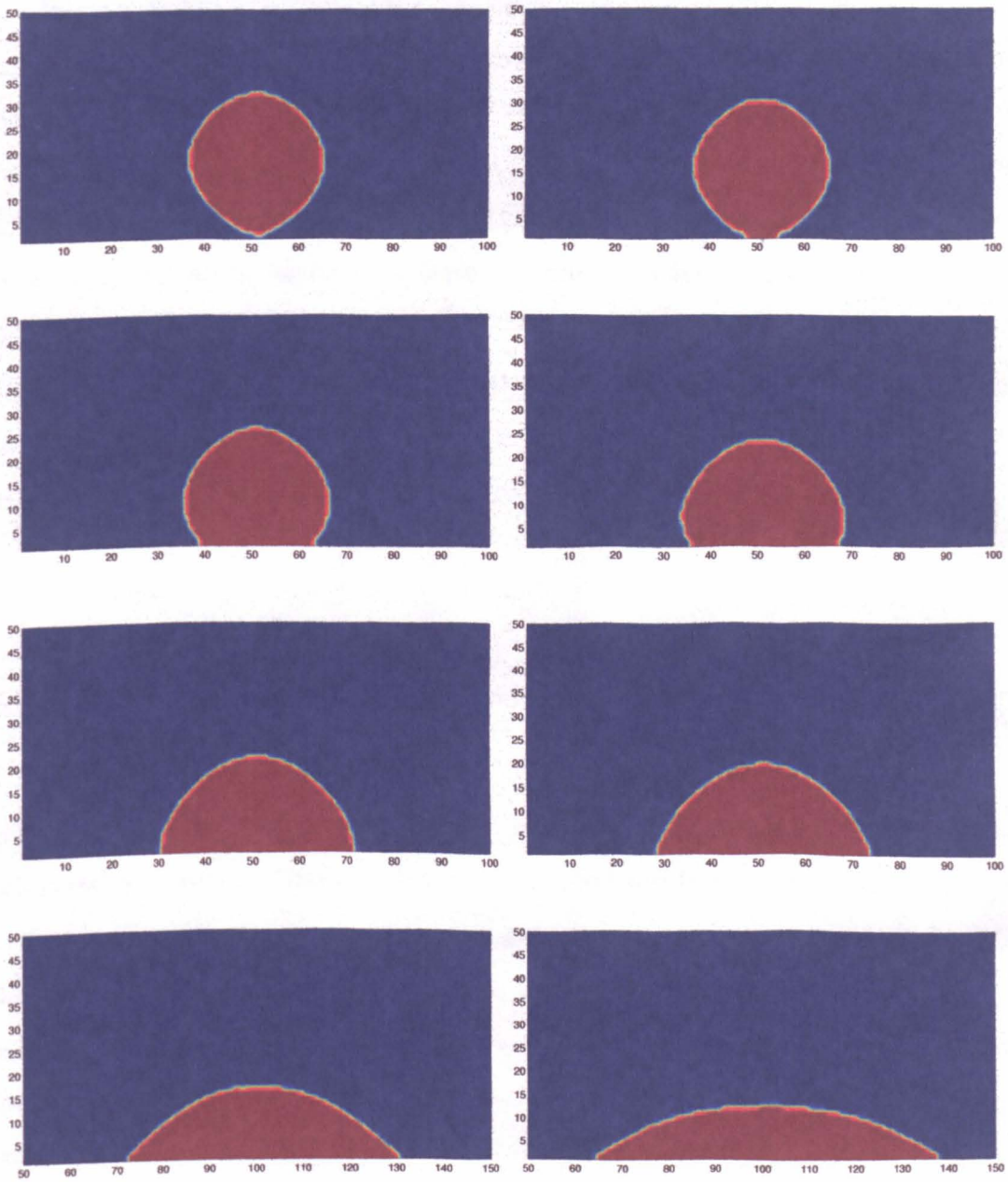

Figure 3.22: Different wall wetting balance between the two fluids in contact with the wall. Note that the droplets are 'isotropic'

could lead to very unstable simulations (in the case of high surface tension, low Taylor number). Similarly, the (otherwise useful) contact angle affects the stability of the algorithm. The wetting parameter σ_{wall} is bounded by an upper limit in exactly the same way as the surface tension parameter is. This is due, again, to the action of a forcing on the finite interfacial region and the key failure is the appearance of negative densities ($f_i < 0$). σ_{wall}'s upper limit depends (like the surface tension parameter) on the viscosity of the drop, the viscosity of the surrounding fluid and the ratio of these viscosities and additional forcing such as surface tension or gravity. The parameter space for the stability is therefore very large and should not be put aside. Unfortunately, we had not have the time to assess it during this thesis, but would certainly be worth pursuing.

We did however observe good stability over the range of wall-wetting parameters we used so far in our target blood flow and micro–fluidic applications, which require strongly non-wetting properties, so that instabilities would have shown up.

Spontaneous wall-wetting of the technique

Recall, the λ method acts essentially by reducing the interfacial length of the contact between two fluids. Without imposing any wall-wetting ($\sigma^R_{wall} = \sigma^B_{wall}$), a droplet subjected to a surface tension with the λ method has been observed to relax into a perfect half circle (contact angle of 90 degrees). This can be understood by recalling that the λ method consists primarily in imposing a tension to the interface. The only stable configuration of the interface in contact with a wall is therefore when the tangential component of the tension is directly null, in other words, when the interface is perpendicular to the wall, giving $\theta_C = 90^o$. See figure 3.23 for an illustration.

This also illustrates that the wetting properties are intrinsically limited, which is constraining if one wants to impose them, as we do here.

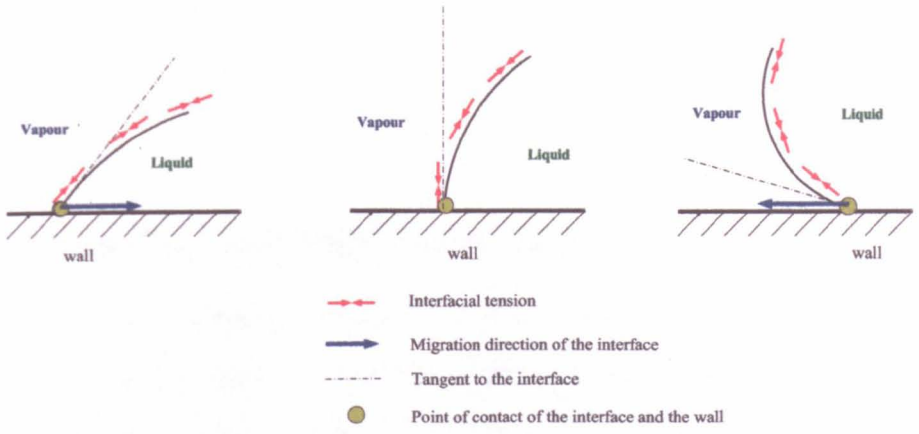

Figure 3.23: Spontaneous wetting of by fluid-fluid interface

3.4.6 Proof of concept: adjusting walls and gravity

Since the contact angle is set at each node and each time step, it allows the wetting parameter to be set locally and dynamically, which can be very useful in certain configurations as this section demonstrates.

Effect of gravity

At low Re, a gravitational force can be accurately added to the simulations by the approximation of a colour-dependant body force acting in the chosen direction. In the case of a heavy drop in a light fluid it could be represented by a larger body-force density acting on the drop. However, the reader should be aware of the validity of this technique: it only truly represents gravity if applied at all sites, at all time, uniformly within the simulation at low Re. It consequently fails very quickly with increasing difference of density. In this case an explicit difference of nodal density is required but the author noticed that unfortunately the problem is not trivial at all if one wants to maintain proper hydrodynamics.
We restricted our investigations to low difference of densities or static cases (where the assumption is valid).

The droplets in figure 3.22 were not subjected to gravity and were therefore circular. Gravity, however, flattens the top of the droplet [81]. Figure 3.24 demonstrate that our λ model does facilitate the modeling of gravity. The simulation parameters for this data were: 100×50 nodes (200×50 for the two last, high wetting), $\omega^R = \omega^B =$

1.7, $\rho^0 = 1.8$, $\sigma = 0.002$, $\sigma^R = \sigma^B = 0$, $R_{drop} = 20$, initialised as half a circle onto the wall, $g = 10^{-6}$ to 10^{-5}, periodic boundary left-right and bounce back top and bottom.

Effect of advancing/receeding contact angle

As mentioned and observed for example by Temperley and Trevena [199], the contact angle depends on the fluid velocity (modulus and orientation with respect to the interface). We did not investigate the dynamical wetting angles qualitatively, but good preliminary agreement with theory and experiment was observed qualitatively as figure 3.25 shows.
The parameters we used for this data were: 100×50 nodes (200×100), $\omega^R = 1.7$, $\omega^B = 0.4$, $\rho^0 = 1.8$, $\sigma = 0.002$, $\sigma^R = \sigma^B = 0$, $R_{drop} = 40$, initialised as half a circle onto the wall, $g = 10^-4$, periodic boundary left-right and bounce back top and bottom.

Conclusion

This first chapter of results is the starting point of our model for the venule scale blood flow. We solved two major obstacles inherent in Gunstensen original method: (i) micro-current activity and (ii) wall wetting considerations. These improved considerably the Gunstensen model and has been used in the generalisation to N-component of this model, in next chapter.

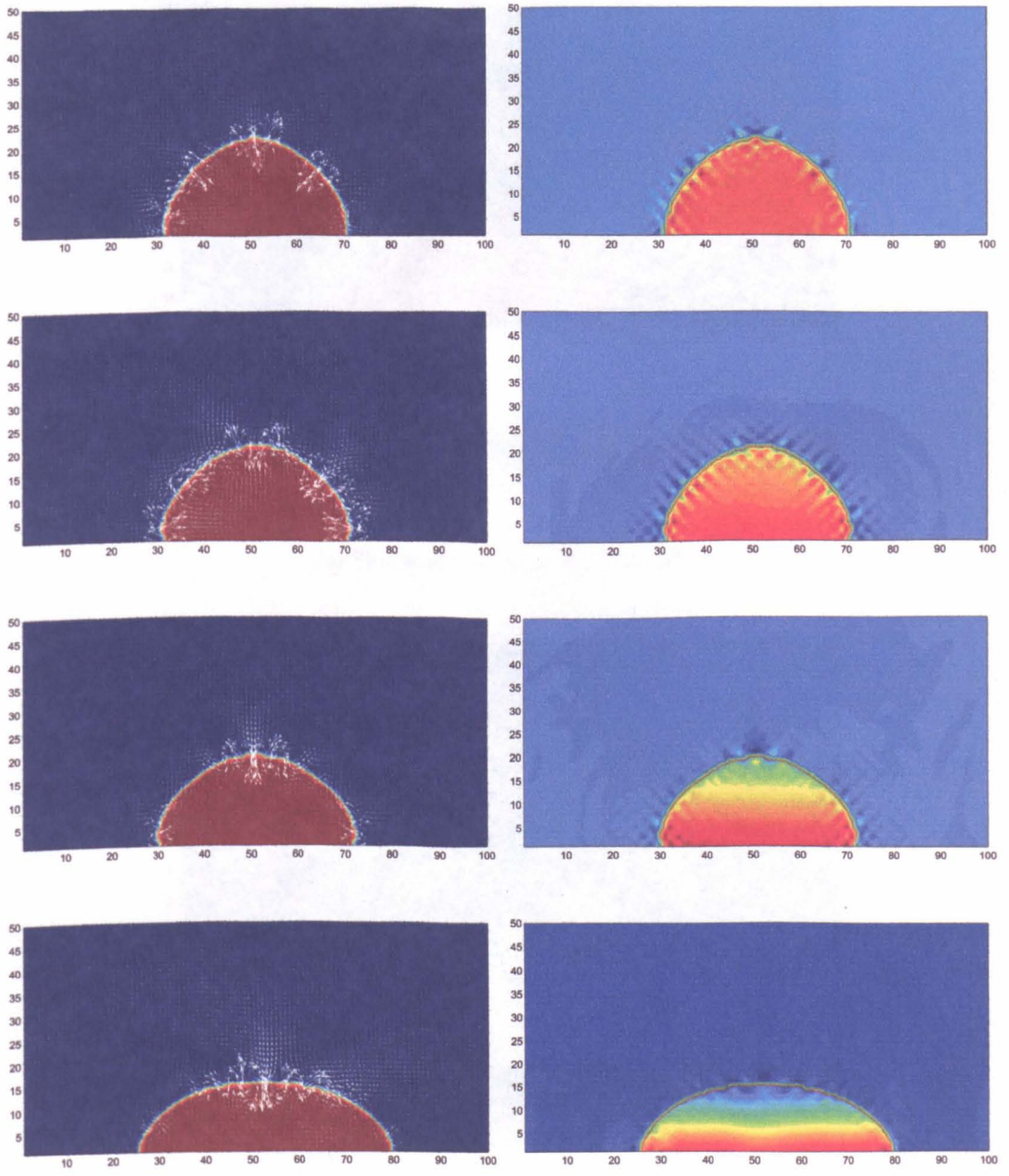

Figure 3.24: Effect of a gravitational force on the shape of the drop. Shape and velocity field, and pressure field.

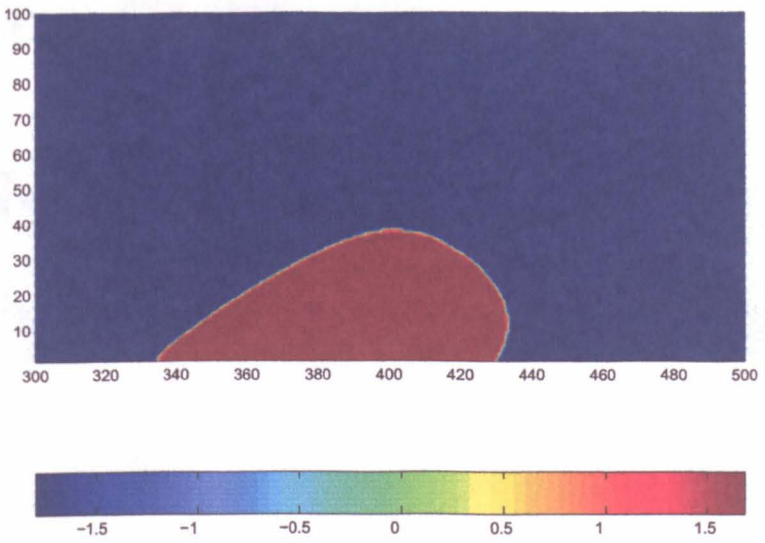

(a) Shape of the drop, function ρ^N

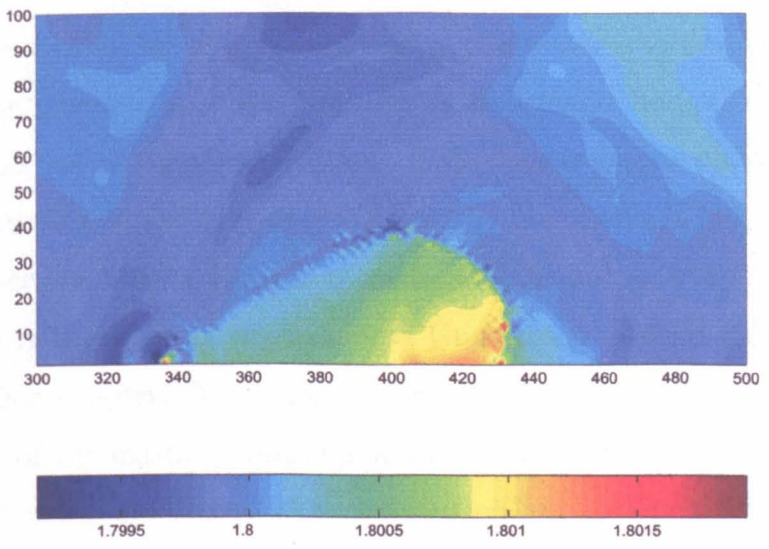

(b) pressure field

Figure 3.25: Drop moving along a solid inclined surface

Chapter 4

The N-component model: construction from the Gunstensen model

Introduction

The author recalls that the main motivation of this thesis is to develop a numerical method for the modeling of a large number of deformable bodies, with mesocopic models of blood flow as target applications. This chapter begins whilst detailing the current literature on blood flow modeling and, by identifying a lack in the current literature, describes how to develop a model able to access a very large number of deformable particles, from the enhanced Gunstensen method (the 'λ method') described in last chapter. This chapter consists of the second set of results: the generalisation of the existing Gunstensen algorithm, surface tension, and wetting methods to $N \gg 2$ components. This new method has been published in [46].

4.1 Literature review on Blood flow modeling

4.1.1 Blood flow composition

Blood flow modeling includes a very wide variety of applications due to the very high complexity, variety, length, time and velocity scales of possible investigations.

This is due in part to the very composition of blood: it is a mixture of plasma and cells. There are four main blood constituents:

- The red blood cells (RBCs hereafter) or erythrocytes: they constitute approximately 40% of the blood composition, have a typical biconcave shape and a size of approximately 8×2 μm. They are the blood cells that can deform most, due to a low surface tension and have a high viscosity (approximately 1000 times higher than the plasma). They are very often referred to 'bag of haemoglobin' or 'deflated bubble'.

- The white blood cells (WBC hereafter) or leukocytes: they constitute approximately 1% of the blood composition. When advecting in the blood stream, they most often have a spherical shape and low deformability. They are slightly bigger than the RBC's and very often omitted when studying blood.

- The platelets (or thrombocytes): they represents less than 1% of the blood composition. Much smaller than the RBC's (about a quarter of the size of the RBC's), they are very often neglected when studying blood flow.

- The plasma: it represents approximately 60% of the blood composition, it is made up mainly of water (92%) and proteins (7%), is used to transport the three previous constituents and platelets around the body to the locations where they are required.

Blood is modeled at several scales: (i) the *macroscopic scale* (hundreds of cells diameter as typical length scale) where blood is considered as a uniform viscoelastic continuous fluid (the presence of cells is ignored but a variety of viscosity models are used to reflect the composition), (ii) the *mesoscopic level* (tens of cells diameter as typical length scale) where each cells are represented explicitly within the surrounding fluid (plasma), and (iii) the *microscopical scale* (one cell's diameter as typical length scale) where the cell's explicit deformation and inner structure are resolved.

4.1.2 Macroscopic Blood flow modeling: very popular

The macroscopic scale considers blood as uniform and is applied at length scales involving 10^4–10^5 cells at the same time, and high Re most often (note that turbulence models are very often required).

Even though the plasma, which is the major constituent of blood, is a Newtonian fluid (see chapter 1), the presence of the cells gives blood a non-Newtonian macroscopic behaviour. As a consequence, it is very common that CFD solvers represent blood as a uniform Non-Newtonian fluid. The current literature does not lack papers on the subject. Most common 'hemodynamics' investigations include, for example, the turbulent artery flow : [25], [141], [197], [128], [4], [8]. The flow of blood in stenosed artery is also widely published (for example [120], [181], [134]) : great concern is expressed by the current medical community, especially in western countries over our diets and food habits leading to weight problems, as demonstrated by the 2002 report of the World Health Organisation [214]. Related to the later concern, modeling heart blood flow is also currently fashionable (for example [158], [60]).

These are issues of great financial and public health interest, and even though standard CFD solvers dominate the domain, LB has been successfully applied to numerous continuum blood flow studies, concentrating mainly on the same area as the previously mentioned CFD applications. A few recent applications can be found in [109], [90], [91], [89], [124], [110] with a recent review on the arterial flows modeling with LB [22].

4.1.3 Microscopic blood flow modeling: deformation of single cells only

Microscopic blood flow modeling can be understood as the detailed study of the deformation of the RBC's (its main constituent). The physics is imposed by very local shear stresses and velocity fields, and the deformation of a single cell is imposed only by its local environment. The complex study of cells' deformation is very relevant to mesocopic and ultimately macroscopic models, since it provides parametrisation and behaviour properties that can be feed into these models. For example, the mechanism involved in RBC's deformation is not fully understood for the moment, and is

the subject of numerous (experimental, analytical and computational) studies (for example, [55], [160], [119] and [121]). The RBC's deformation properties influence the viscosity of the whole blood and hence feed into calculations at the continuum scale. RBC's are reported to have a very unusual dynamical response to shear: their deformability varies with (i) their age, (ii) the frequency of the shear rate and (iii) their environmental chemistry. Detailed simulations of single red blood cell deformations can be found in [161], [147], [53], [13], [14].

These techniques provide a very accurate answer to the study of RBC's deformation (microscopic scale) but they are very computationally expensive and usually restricted to one biological cell only. They are consequently unable to provide much insight on blood flow (requiring a large number of cells).

4.1.4 Current Mesoscopic blood flow modeling: mostly rigid biological cell modeling

The mesoscopic modeling of blood involves typically 10-100 cells, at the scale of several cell's radii. This implies that the overall flow is significantly influenced by (i) the explicit deformation of each cell (which does not matter at the macroscopic level as Goldsmith demonstrated in [71]), and (ii) the mechanical interactions between the cells (which does not matter at the microscopic cells as far as deformation is concerned). This scale is therefore influenced by both scales it lies in between, which is the cause of its computational and analytical challenge and consequently this fact makes it accessible to only few methods. The remainder of this section describes few numerical approaches to suspensions modeling, and demonstrates the central computational challenge of this thesis.

'dry' solid particles modeling technique

A first model of mesoscopic blood flow could be to simulate a large number of solid particles in a tube. Although (very) crude, this represents already a challenge in numerical methods, and only a few techniques are available for this purpose. The Discrete Element Method (DEM) for example provides a 'relatively' computation-

ally accessible alternative to the modeling of a large number of solid bodies (most commonly spheres for simplicity). It consists of resolving, explicitly, each particle of the suspension, and evolving their trajectory through their inter-particle mechanical collisions and hydro-dynamically mediated interactions. The algorithms involved are very complicated and subtle, since the number of possible interactions between the different spheres of the simulation is enormous (most simulations consider no less than a million particles). CSIRO *Inc.* for example applies very successfully this method for a very wide range of industrial problems, such as rotating mills, land slides, or egg distributors (see [44], ref [35] and [36] for more details).

Suspension of solid particles, more expensive

Mesoscopic blood flow simulation requires the Newtonian dynamics of the plasma, as well as the representation of the cells as Dzwinel *et al.* note [53]: 'Blood in the [microscale] must be regarded as a two-phase, nonhomogeneous fluid consisting of a liquid plasma phase and a deformable solid phase of blood cells'. He also notes that 'this situation cannot be modeled by classical computational fluid dynamics'.
It is therefore natural to link previous DEM approaches to a standard NS solver. The major difficulty, however, is to model the interaction force between the particles and the fluid. The most common of these techniques is the Direct Numerical Simulation (DNS). Examples of DNS can be found in [156] and applications include the study of shear-induced migration of single particles (also known as lift-off) by Patankar *et al.* [155] and the simulations of suspension dynamics by Joseph *et al.* [153], [154], [70].
These techniques are generally highly computationally intensive and, consequently, systems are usually greatly simplified (one- or two- dimensional, axisymmetric etc.) as Llewellin notes in [129].
The LBM provides therefore a great advantage over these techniques through its highier computational efficiency. We recall that Ladd *et al.* [113] have developed a technique to embed solid particles in a LB fluid (see chapter 2 for a concise literature). In the blood flow application, Munn *et al.* employed this method for simulating RBC's in capillaries and deduced their unexpected role in WBC rolling

([191], [140]). They, however, restricted their study to a handful RBC's in 2D, and while the relative importance between 2D and 3D can be discussed, the importance of the volume fraction cannot be underestimated in this application. Also, the Ladd method remains a computationally expensive technique and is not without drawbacks in this application (the restriction to solid particles). Recovering a volume fraction of cells high enough in the simulation consists, therefore, of the largest part of the computational problem for the simulation of mesoscopic blood flow.

Deformable particles, most expensive

Just as important as the volume fraction of the suspension or blood, the RBC's deformation cannot be overlooked. Goldsmith ([71]) has shown experimentally that the mesoscopic flow of deformable particles (and red blood cells) is quantitatively different from the mesoscopic flow of rigid particles, demonstrating that deformability has still significant effects on the flow, even at this scale and with a large number of cells.

In the direction of addressing this issue of explicit deformability and large number of cells, one of the only studies is available by K. Boryczko *et al.* [53] where a discrete particle dynamics method is used to model blood flow in microscopic capillaries (100 μm long and with diameters on order of 10 μm). In this technique, the plasma is considered as a 'fluid particles' containing fibrin monomers interacting with each other with a short-ranged, repulsive dissipative force. The red blood cells and capillary walls are modeled using elastic mesh of 'solid' particles. See [53], [13] for similar work. It should however be noted that these numerical simulations involved large computational resources and accounted for only a handful of red blood cells, not a number adequate for our target applications.

This leads to the conclusion that, at this scale, computational model are of great help, providing a much more accurate and detailed analysis of the key problem than experimental or analytical work but they are computationally very expensive (they typically require teraflop multi-processors capabilities that only a very limited number of centres are capable of for the moment [24], [186]).

No models as far (as the author is aware) are therefore able explicitly to simulate a large number of deformable bodies in solution. Models only have the capability to address a large number of solid particles or a few deformable ones. This is the gap in current computational model's capabilities that this thesis addresses, and it is the aim to model blood flow by:

- simplifying the explicit definition of the cells (whilst retaining their deformability) but,
- allowing the model to handle thousands of them,
- in an computationally effective way.

The ultimate assumption: modeling RBC's as incompressible drops

The next step towards biological cell representation, after the just-described solid particle in a Newtonian Navier-Stokes fluid approach, is a deformable immiscible, incompressible droplet with surface tension and (more importantly), high internal viscosity (recall that RBC's have low surface tension but very high viscosity).
However, the assumption of representing biological cells with liquid drops is not without limitations. For simplicity, this approach does not recover the restrictions of constant surface area (or length in two dimensions) for the moment. It is, however, the author's opinion that the modeling of biological cells using immiscible incompressible viscous drops is valid as long as the typical length scale of the system is no less than a few (typically >5) cells diameters. This is based on the assumption that, at this scale, deformation and volume exclusion effects have much more importance on the overall flow than the restriction of constant surface area, especially at relatively low deformation regimes. But most of all, some representation of deformability is a significant improvement upon no representation at all.
This model finds sufficient scope for applications in the venule scale: applications that no other model can tackle efficiently and realistically. Thus for example, this model would find great advantages in drug delivery related problems, or when micro-sized particles have to be injected in the blood stream. It would also provide an appropriate tool for the simulation of larger systems where the size of the particles is comparable to the typical length scale such as the transport of deformable particles.

In some cases, these particles are reacting chemically when in contact with each other, requiring any numerical model to represent them explicitly.
This model, to the author's knowledge, would be the only one capable of modeling such problems and providing an obvious, unique, vehicle of research. Previous developments in LB and studies using binary models settled the appropriate basis and starting points for the development of such a model. The remainder of this chapter explains its development from the corrected and enhanced Gunstensen model described in the two last chapters.

4.2 Towards the modeling of mesoscopic blood flow: the N-component model

Having shown the motivations and needs of a N-component model, this section describes its construction and its subsequent generalisation, after the binary Gunstensen model that spawns it. It should be noted that H. Niimura [145] developed a LB N-component model using the Shan-Chen method for binary fluids [182], and demonstrated non-coalescence and liquid-wetting behaviour with up to 9 components. However, to the author's best knowledge, Niimura has not extended his model to more than 9 different non-coalescing fluids, implying that this model was not designed to consider more fluids. Also, thickness of the interface must impact on length scale and/or computational resources required.

4.2.1 The immiscible N-component LBM:*novel ideas*

Previous chapters have demonstrated (i) the validity of the Gunstensen algorithm, (ii) some improvements (recolouring and colour-field definition) and (iii) an improved surface tension method (λ method).
The N-component model consists of a generalisation of the Gunstensen algorithm and the λ method. Each step of the generalisation to the N-component method is explained in detail by starting with a reminder of the corresponding step in the original Gunstensen method algorithm. It should be noted that, despite all the

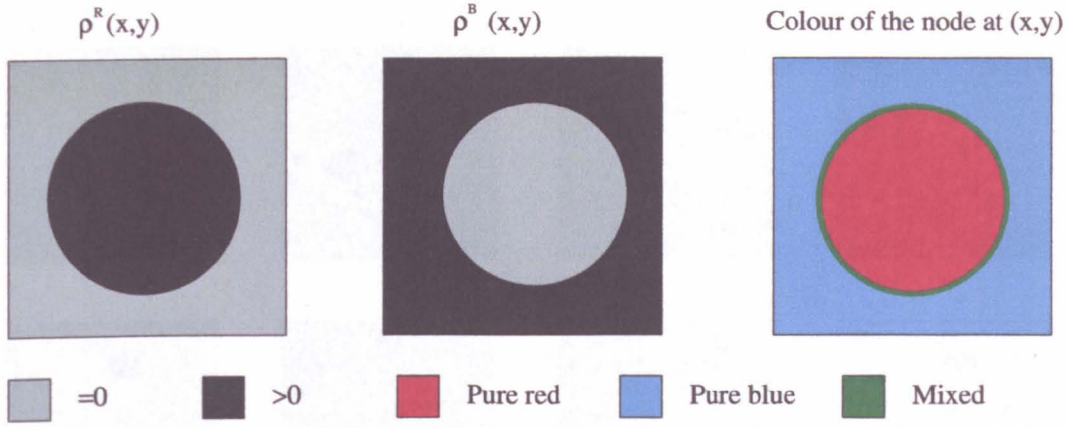

Figure 4.1: Schematic typical configuration of the nodal colour in the immiscible algorithm. The relative nodal density of the red ($\rho^R(x,y,i)$) and blue ($\rho^B(x,y,i)$) matrix determine the colour of the node.

explanations provided for its implementation, very careful programming is required to maintain efficiency and accuracy.

This new method consists of the second result of this thesis. The amount of effort (and frustration) to get to a stable algorithm should not be underestimated.

Efficiency, a necessary *leitmotif*

Let's first put the generalisation into context. As we saw in previous chapters, monochromatic LB models involve the densities of probability f_i's evolving though a repetitive sequence of collide and propagate steps. The mid-link bounce back method can be added to the algorithm to simulate solid, non-moving, walls. The Gunstensen method splits these momentum densities f_i's into two different colour momentum densities r_i (for red) and b_i (for blue). A node is called 'pure' red(blue) when containing only red(blue) densities, and its evolution is similar to monochromatic LB case, with the appropriate relaxation parameter $\omega_R(\omega_B)$. When this node contains two colours however, segregation and surface tension (which can be set to zero) are added to the dynamics of the node to give rise to the interface. The Gunstensen algorithm can therefore be understood as a generalisation, to two components, of the monochromatic LB model. From a computational point of view, it consists of dealing with two real-type matrices $r(x,y,i)$ and $b(x,y,i)$ whose occupancy sets the node's colour as figure 4.1 illustrates.

Generalising this idea to N different colours could be done in the same way, where

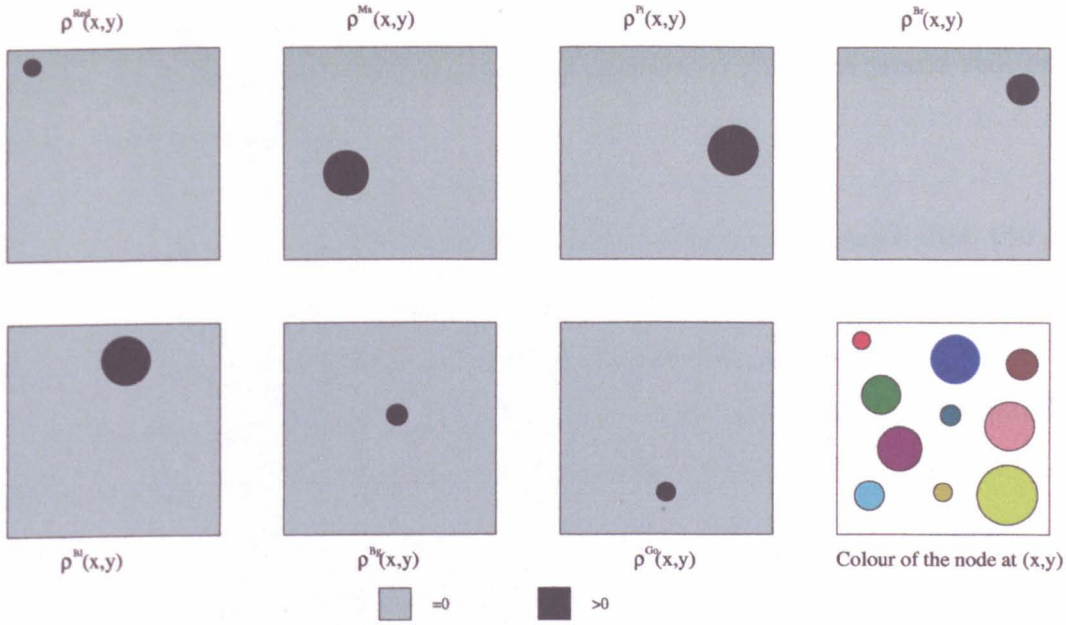

Figure 4.2: Schematic representation of a crude N-component model. The occupancy of the colour matrices are very sparse, leading to a very inefficient management of the computational resources.

instead of having only red and blue, one could have pink, green, blue, red, yellow... with the corresponding real-type matrices accounting for corresponding the momentum densities: p_i, g_i, b_i, r_i, y_i... However, this crude approach highlights two numerical difficulties: (i) the number of possible names for the different colours would be quickly limiting and, (ii) this approach would not be very computationally efficient since each colour matrices would be very sparse (especially when interfaces are narrow), as figure 4.2 illustrates.

Moreover, memory and time requirements would scale linearly with the total number of fluids, N hereafter, limiting the model to only a small number of fluids depending on the available computational resources (which is probably why Niimura [145] did not apply his multiphase model to more than 9 fluids).

Four dimensional momentum density

Let us begin with the first identified issue: the labeling of colour in the programme. To address this problem, we order colour as an extra dimension of the momentum matrices: $r(\mathbf{x}, i, \alpha)$, where the last dimension accounts for colour information. Colour is therefore not identified by its 'common' name but rather by a superscript, α hereafter, corresponding to its position in the last dimension of the matrix. Note

that even though this would solve the issue of naming the colours in the code and make the programme able to access a large number of fluids, it would still not be efficient in term of storage.

The second identified issue is efficiency: it is necessary to recall that the Gunstensen algorithm provides sharp interfaces and very low diffusion between fluids. Using this method therefore provides a much reduced number of mixed nodes, as well as a reduced number of colours at a mixed node compared to other interfacial LB method. In addition, the matrix of momentum densities is very sparse in its last dimension (see figure 4.2), leading to the idea that the momentum density matrix described previously can be concatenated into a matrix much smaller in its colour dimension: the last ('colour') dimension could have a reduced size, representing the maximum number of fluids allowed at a node. We define this number by N_q. We generalised:

$$r(x, y, , i) \text{ and } b(x, y, i) \Rightarrow r(x, y, i, n)\,.$$

This momentum density matrix therefore has the following limits:

$$r(x,y,i,n): \begin{cases} 0 < x < \text{LENGTH} & \text{for the } x\text{-dimension}\,, \\ 0 < y < \text{WIDTH} & \text{for the } y\text{-dimension}\,, \\ 0 < i < Q & \text{for the velocity dimension}\,, \\ 0 < n < N_q & \text{for the 'colour within the node'-dimension}\,. \end{cases} \tag{4.1}$$

For simplicity, we consider that N_q does not depend on position. It therefore represents the maximum number of fluids at *any* node in the simulation. On the other hand, the number of different colours at a node (defined $N_t(\mathbf{x}, t) < N_q$) does change from node to node or time to time, and is bounded by N_q:

$$N_t(t, \mathbf{x}) < N_q \quad \forall \{t, \mathbf{x}\}\,.$$

Colour map for absolute colour

No colour information can be deduced from the matrix $r(x, y, i, n)$ only, we therefore draw a parallel with the allocation of memory in a computer: bytes are stored

in a 'random' way and their 'identity' is stored through their memory 'address' location. Colour can be dealt in the same way: an additional matrix, a colour map, $lb(x, y, i, n)$, is used to provide the necessary colour information to identify the colour of the momentum densities stored in $r(x, y, i, n)$. This colour map has to have exactly the same dimension as the matrix r it refers to:

$$\begin{cases} r(x, y, i, n) & \textit{float} \text{ array for the momentum density}, \\ lb(x, y, i, n) & \textit{integer} \text{ array for the colour}, \end{cases}$$

and consequently with the limits defined by equation 4.1. In this way, each momentum density (element) of the matrix r has a colour stored in the label table lb, at the same coordinate *(x,y,i,n)*. The main implementation issue with this model is to ensure that colour labels stream or propagate in exactly the same way as the momentum density they represent. Failing to do so could induce colour to disappear or to be generated artificially, in an uncontrolled way.

Now the reader is familiar with this new notions of a generalised, compressed, momentum density matrix and its corresponding colour label matrix, it is necessary to review how the main steps of the Gunstensen algorithm are generalised in order to cope with such changes.

4.2.2 The N-component generalised procedures

The description of the implementation of each generalised procedure of the Gunstensen model begins by a brief review of the binary model, necessary to set each generalisation in context.

The generalised collide step

In our generalisation, the colour blind density f_i's are still represented by the sum of the momentum distributions r_i of the link i. In the place of the diphasic assignment $f_i(\mathbf{x}, t) = r_i(\mathbf{x}, t) + b_i(\mathbf{x}, t)$, we have:

$$f_i(\mathbf{x}, t) = \sum_{n=0}^{N_i} r_i(\mathbf{x}, t, n).$$

It should be noted that this sum is only rarely a sum, in that N_t for most of the simulational domain is 1 (in the bulk of the different fluids). The nodal macroscopic observables can be deduced in exactly the same way as in the basic Gunstensen model:

$$\left.\begin{aligned} \rho(\mathbf{x},t) &= \textstyle\sum_i^Q f_i(\mathbf{x},t)\,, \\ u_\alpha &= \textstyle\sum_i^Q f_i(\mathbf{x},t) c_{i\alpha}\,. \end{aligned}\right\}$$

Once the f_i's and the macroscopic observables are calculated, the collide step can be applied in exactly the same way as in the single component LB method, by the standard LBGK evolution formula:

$$f_i^+(\mathbf{x},t) = f_i(\mathbf{x},t) - \omega_e \left[f_i(\mathbf{x},t) - f_i^{eq}(\mathbf{x},t)\right],$$

where the subscript '+' still denotes post-collided total density, with the usual identity for the equilibrium distribution function:

$$f_i^{eq} = \rho t_i \left[1 + 3\mathbf{u}\cdot\mathbf{c}_\mathrm{i} + \frac{9}{2}(\mathbf{u}\cdot\mathbf{c}_\mathrm{i})^2 + \frac{3}{2}\mathbf{u}^2\right],$$

The value of the relaxation parameter ω has still to set according to the different fluids present at the node, and we generalise it to read:

$$\omega_e = \frac{\rho}{\sum_\alpha^{N_t} \frac{\rho^\alpha}{\omega^\alpha}}, \tag{4.2}$$

where ω^α is the relaxation parameter of the fluid α and ρ^α is the colour nodal density of fluid α, defined as follows:

$$\rho^\alpha(\mathbf{x}) = \sum_i^Q \sum_n^{N_t(\mathbf{x})} r(\mathbf{x},i,n)\,\delta^\alpha(\mathbf{x},i,n)\,, \tag{4.3}$$

where we define the function $\delta^\alpha(\mathbf{x},i,n)$ to denote the colour match of a given momentum density to the colour α:

$$\delta^\alpha(\mathbf{x},i,n) = \begin{cases} 1 & \text{if lb(x,i,n)} = \alpha\,, \\ 0 & \text{otherwise}\,. \end{cases}$$

Equation 4.2 entails a smooth transition of the effective kinematic viscosity through the fluid interface (as the original Gunstensen model does):

$$\nu = \frac{\sum_\alpha^{N_t} \rho^\alpha \nu^\alpha}{\rho}.$$

This procedure ensures, as for the Gunstensen model, correct hydrodynamics for the evolution of the colourblind momentum densities. The remaining of the algorithm ensures non-diffusion between fluids and imposes additional physics (interfacial boundary conditions). Still following the Gunstensen algorithm, the next step is to 'recolour' these post-collided colourblind densities f_i^+.

Generalised recolour step

In the basic Gunstensen algorithm, numerical recolouring is achieved by reflecting colour flux back along the direction of the colour-field, ensuring that the work done by the subsequent colour-flux against the colour-field is maximised. In the generalised model, the idea is essentially the same. The main difference, however, is that in the case of a binary fluid model, there is only one possible interface, and colour-field of the two colours are necessarily opposed by 180 degrees (see equation 2.4). This assumption cannot be made when a node contains more than two fluids and the extended method had to be based on new arguments: the colour-field represents the direction of the imbalance of one given colour with respect to the rest of the colours at the node). Therefore, a colour-field has to be defined for each colour α of a mixed node, and the colourblind colour field $P_\beta(\mathbf{x})$ is generalised by:

$$P_\beta^\alpha(\mathbf{x}) = \sum_i^Q (\rho^\alpha(\mathbf{x}+\mathbf{c_i}) - \rho^{\overline{\alpha}}(\mathbf{x}+\mathbf{c_i}))\, c_{i\beta}\,,$$

where $\rho^{\overline{\alpha}}$ is the nodal density of all colours at the node but colour α, and is defined as follows:

$$\begin{aligned}\rho^{\overline{\alpha}} &= \textstyle\sum_i^Q \sum_n^{N_t(\mathbf{x})} r(\mathbf{x},i,n)\ (1-\delta^\alpha(\mathbf{x},i,n))\ ,\\ &= \rho(\mathbf{x}) - \rho^\alpha(\mathbf{x})\,.\end{aligned}$$

We note that the definition of the colour-field of the colour α is therefore simplified as follows:

$$P_\beta^\alpha(\mathbf{x}) = \sum_i^Q (2\,\rho^\alpha(\mathbf{x}+\mathbf{c_i}) - \rho(\mathbf{x}+\mathbf{c_i}))\, c_{i\beta}\,.$$

We define the angle of the colour-field of colour α as:

$$\theta_P^\alpha = tan^{-1}\left(\frac{P_y^\alpha}{P_x^\alpha}\right)\,,$$

in two dimensions (x and y), to determine the reallocation order of colour β, exactly the same way as the basic Gunstensen model.

It is important to note that this operation has to be repeated for each of the $N_t(\mathbf{x})$ colours of the node at $\mathbf{x}$. We deduce from it N_t reallocation priority tables (T_1, T_2, ..., T_{N_t}) for the reallocation of each N_t colours. The order by which these N_t allocation tables are addressed is important for the overall stability of the simulation: it has to be in order of increasing colour nodal density (defined in equation 4.3).
Let's illustrate this important point through an example: suppose we have, at $\mathbf{x}$, 4 different fluids (1, 2, 3 and 4) in the following quantity: $\rho^1 >> \rho^2 \approx \rho^3 \approx \rho^4$. Colour 1 is therefore in majority (in the node) and colours 2, 3 and 4 in minority. Reallocating colour 1 first means that the probability that the recolouring step totally fills a link corresponding to the first priority of colour 2, 3 or 4 is not negligible. Here, this induces minority colour to be *fully* reallocated (because in minority) in a way in which the work of its colour-flux against its colour-field is not maximised, leading to the minority colour's diffusion or evaporation. However, beginning by reallocating the minority species ensures that minority species get recoloured according to their reallocation priority table, the majority colour 'does not even notice'. This could be summarised by: 'the improper recolouring of the majority colour has a major effect on the recolouring of the minority colours while the improper recolouring of the minority colours has only minor effect of the recolouring of majority colour', as figure 4.3 illustrates.

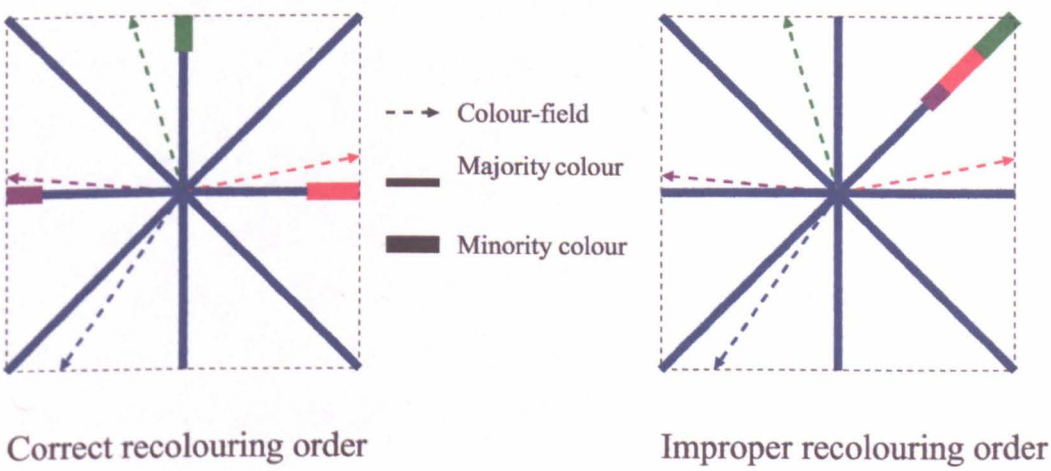

Figure 4.3: The order of recolouring between the majority colour (blue here) and the other minority colour (magenta, red and green) is crucial to ensure proper reallocation. The majority colour should be recoloured last to allow minority colours to be optimally recoloured as they should.

Improper recolouring order induces droplets in contact to stick to each other and some mass of each droplet to stick onto the surface of the other when they separate, as figure 4.4 illustrates. The simulation parameters for this data were 100×200 nodes, $\omega^{\alpha} = 1.7 \ \forall \ \alpha$, $\sigma^{\alpha\beta} = 0.001 \ \forall \ \{\alpha, \beta\}_{\alpha \neq \beta}$ (see next section of the surface tension implementation).

Generalise propagation step

The basic Gunstensen algorithm propagates reallocated colour in the following way (for red and blue fluid):

$$\left.\begin{aligned} r_i(\mathbf{x} + \mathbf{c_i}\Delta t, t + \Delta t) &= r_i(\mathbf{x}, t)\,, \\ b_i(\mathbf{x} + \mathbf{c_i}\Delta t, t + \Delta t) &= b_i(\mathbf{x}, t)\,, \end{aligned}\right\}$$

where $r_i(\mathbf{x} + \mathbf{c_i}\Delta t, t + \Delta t)$ and $b_i(\mathbf{x} + \mathbf{c_i}\Delta t, t + \Delta t)$ are the post-propagated *red* and *blue* colour respectively. Two destination matrices are therefore required to accommodate the two post-recoloured matrices.

This propagation step gets rather more complicated when dealing with the 'coloured' matrix $r(\mathbf{x}, i, n)$ in the N-component algorithm, but a one-to-one propagation from origin to destination lattices (within the n dimension) is still possible since the model assumes a constant maximum number of colour at any site, N_Q (generally 5). An error is returned in the code if there is more than N_Q colours to be propagated into a given node, to avoid overwriting densities and colour label. The labels $lb(\mathbf{x}, i, n)$'s are propagated in exactly the same way. This consists of the main idea of the propagation algorithm, but it should be noted that this method does not provide very tidy momentum and colour matrices.

Colour is therefore ordered within the momentum and colour matrices so that the momentum densities of a given colour index n have the same colour label. As an illustration, let's consider a mixed node where colour 2 is in majority with colours 1, 3 and 4 in minority. The ordering of the colours within the *lb* matrix might be:

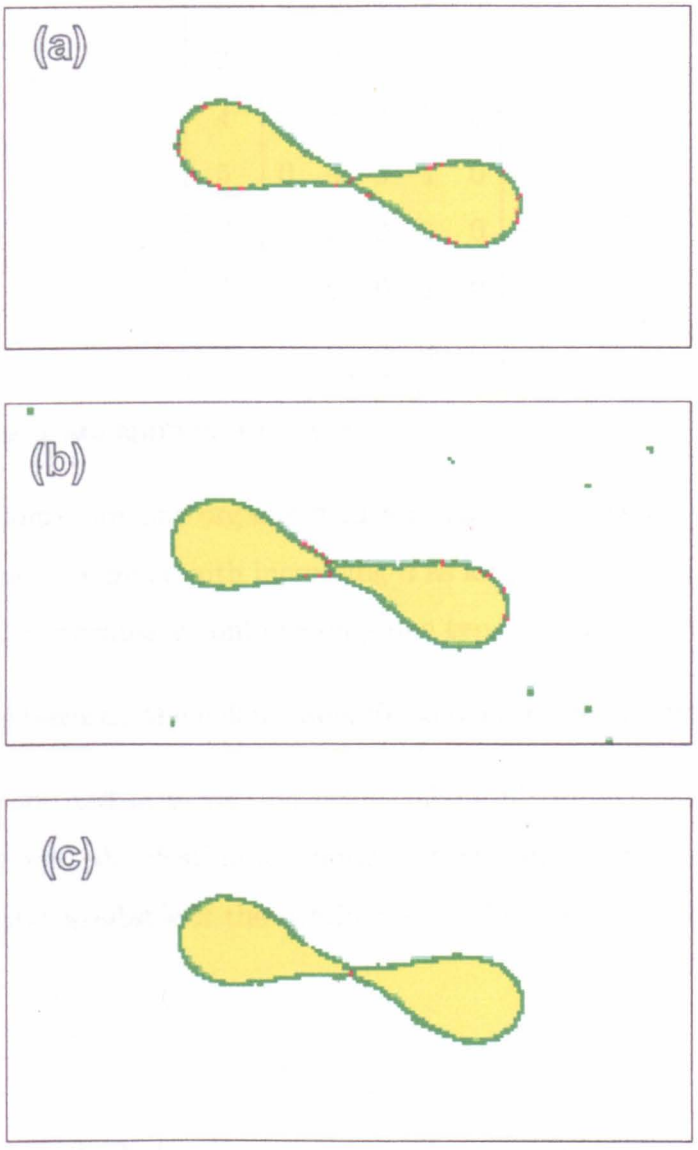

Figure 4.4: Two droplet, originally in contact, pulled apart by a body-force. Colour represents the number of nodes (white and yellow:1, green:2, red:3). Small surface tension between the two droplets ensures that they 'stick' to each other. Case (a) is when the order of recolouring is not addressed, case (b) is when the order of recolouring is done by decreasing colour nodal density (ρ^{α}) and case (c) is when the recolouring is done by increasing nodal density. It is visible that the case (c) should be adopted (maximising segregation of fluids but retaining each fluid's identity).

$i\backslash n$	0	1	2	3	4
0	2	0	0	1	0
1	0	0	0	1	0
2	0	0	4	1	0
3	0	0	0	1	0
4	0	3	0	1	0
5	0	0	0	1	0
6	0	0	0	1	0
7	0	0	0	1	0
8	0	0	0	1	0

A couple of remarks are appropriated here:

- The N_t colours are not organised in any specific order of nodal density or absolute colour number with increasing n as long as each column of the colour dimension at coordinate contains only one type of colour.
- We chose arbitrarily the colour label '0' to denote the absence of colour.
- Colour is allocated in increasing values of the n^{th} index: colour densities are propagated into the destination node in their corresponding colour column, or in the next available if the destination node does not already contain the colour.

Initialisation

Referring to the standard Gunstensen algorithm (figure 2.4), both the initialisation step and the collide step feed the collide step. The arrangement of the densities $r(\mathbf{x}, i, n)$ and colour $lb(\mathbf{x}, i, n)$ after the initialisation step has therefore to be identical to the arrangement after the propagation step. We saw in last section that the different colours of a node are identified by the colour matrix $lb(\mathbf{x}, i, n)$, and they are ordered within the elements of dimension n. Following the remarks of last section, only the first column of lb is initialised to the index chosen for the colour α for a site. We initialise the fluid β (red say) in the original Gunstensen algorithm by:

$$\begin{cases} r(\mathbf{x},i) = t_i\,\rho^0 \\ b(\mathbf{x},i) = 0 \end{cases}.$$

Here we generalise this step and use:

$$\begin{cases} r(\mathbf{x},i,n) = \begin{cases} t_i\,\rho^0 & \text{for n=0}, \\ -1 & \text{otherwise}, \end{cases} \\ \\ lb(\mathbf{x},i,n) = \begin{cases} \beta & \text{for n=0}, \\ -1 & \text{otherwise}, \end{cases} \end{cases}.$$

We set '-1' as a trap for subsequent checking points in the programme (recall that a negative density of probability is not physical and that the programme stops and return an error message in this case).

Generalised mid-link bounce back method

Again, the assumption that a node can only contain a maximum of N_q number of different colours at the same time plays an important role in the simplification and efficiency of the algorithm: when a wall is present between two nodes, each colour labels $lb(\mathbf{x},i,n)$ and densities $r(\mathbf{x},i,n)$ are bounced back in the usual way since the colour acceptance capability of the destination node is the same as the colour acceptance capability of the original node ($=N_q$), which is the same argument as the one used in the generalisation of the propagate step. Instead of bouncing two densities back (r_i and b_i), the generalised mid link bounce back method bounces N_t densities and N_t colours. Note that the remaining $N_Q - N_t$ yet unaddressed densities and colours at a node have to be bounced back as well, to retain the integrity of the bounce back method and to avoid generating colour mass:

$$\left\{ \begin{array}{ll} f_i^+(\mathbf{x},n) = f_{\bar{i}}^+(\mathbf{x}-\mathbf{c_i},n) & \forall\,\{\mathbf{x};i;n\}\,, \\ lb(\mathbf{x},i,n) = lb(\mathbf{x}-\mathbf{c_i},\bar{i},n) & \forall\,\{\mathbf{x};i;n\}\,. \end{array} \right\}$$

where $\bar{i}$ represents the 8 conjugate to i.

This description is enough to obtain non-coalescence of $N >> 2$-components as next section demonstrates.

4.2.3 Proof of concept: non-coalescence of N>2 fluids

This section demonstrates the non-coalescence capability of the N-component model with the information described so far, through the demonstration of 'phase segregation' (term borrowed from [145]). In figure 4.5, a rectangular box is initialised uniformly with a square pattern of 4 different (mutually non-coalescing) fluids with a layer top and bottom of a fifth fluid. A shear is imposed top and bottom (with velocity U_0 and $-U_0$). Note that a small uniform surface tension has been added to ensure phase segregation (see next section for the implementation of the surface tension). The simulation parameters for this data were 100×200 nodes, $\omega^\alpha = 1.7 \; \forall \; \alpha$, $\sigma^{\alpha\beta} = 0.001 \; \forall \; \{\alpha, \beta\}_{\alpha \neq \beta}$ (see next section of the surface tension implementation), $U_0 = 0.05$. Periodic boundary conditions were implemented left and right.

4.3 Generalisation of the surface tension method

So far, this chapter has described how to implement the N-component Gunstensen LB algorithm for many component, walls, and the main hydrodynamics of the model. The previous chapter described how surface tensions in the original Gunstensen algorithm induces instabilities and flow artifacts, leading to the λ correction. This section describes now how to generalise these ideas into our N-component model.

4.3.1 N-component Gunstensen surface tension with the λ correction

background, the λ method

Recall that the λ method imposes the surface tension on an interface via a perturbation step which consists of reducing the interfacial length by adding the following in the LBE:

$$\triangle f_i(\mathbf{x}) = \sigma_i \, CC \, cos(2(\theta_P(\mathbf{x}) - \theta_i)) \,, \tag{4.4}$$

where σ_i is the surface tension including the λ correction, CC is the concentration factor, θ_P is the angle of the colour-field (either red or blue colour-field, recall) and θ_i is the angle of the i^{th} link (see D2Q9 lattice geometry, figure 1.2).

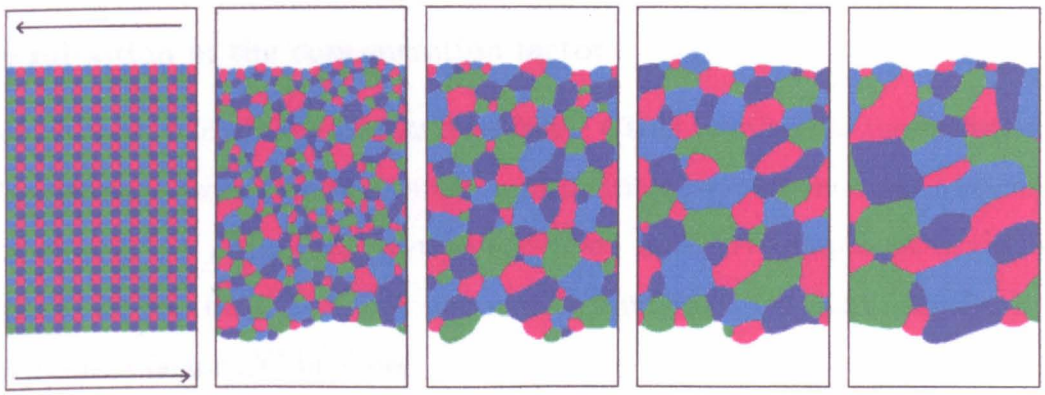

(a) t=0 (b) t=6000 (c) t=12000 (d) t=18000 (e) t=24000

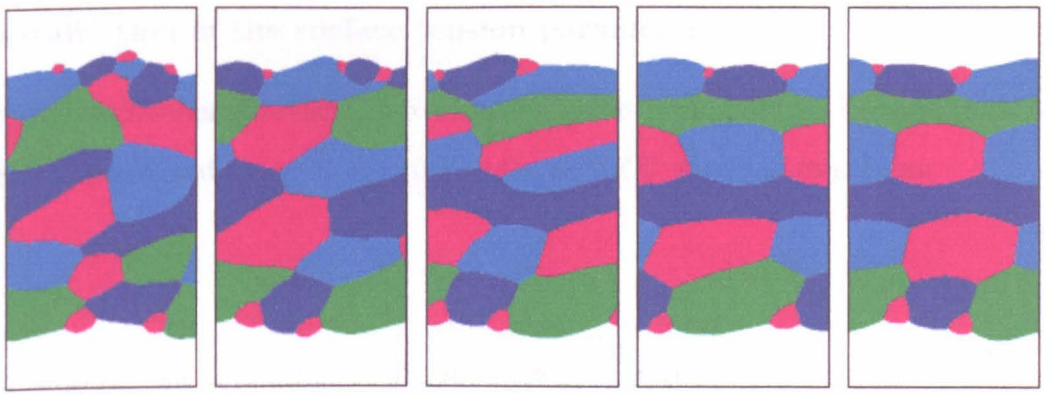

(f) t=30000 (g) t=36000 (h) t=42000 (i) t=48000 (j) t=54000

Figure 4.5: Demonstration of non-coalescence capability of our N-component model. The five fluids in the simulation are mutually non-coalescent. A shear and a small surface tension force induce phase segregation.

It should be noted that equation 4.4 accounts for the interface between *red* and *blue* fluids, and contains explicit reference to each of the colours. Generalising equation 4.4 to N-components therefore means to generalise it to $C_2^{N_t}$ possible interfaces at a node containing N_t interfaces (where each fluid of each possible pair of fluids must have explicit representation in the final formula).
The remainder of this section explains how to generalise each term of equation 4.4.

Generalisation of the concentration factor

Recall that the role of the concentration factor CC is to minimise the activation of surface tension, away from the purely mathematical *red-blue* interface (defined by the contour $\rho^R = \rho^B$). This must be conserved in the N-component model, and therefore, for the fluid α–β fluid interface ($\alpha\beta$ interface for short hereafter), the concentration factor CC becomes:

$$CC^{\alpha\beta} = 1 - \left| \frac{\rho^\alpha - \rho^\beta}{\rho^\alpha + \rho^\beta} \right| .$$

Generalisation of the surface tension parameter

In the N-component method, the surface tension parameter σ_i becomes a $N \times N$ surface tension matrix, $\sigma^{\alpha\beta}$, accounting for each C_2^N possible interfaces:

$$\sigma^{\alpha\beta} = \begin{bmatrix} \sigma^{11} & \sigma^{12} & \dots & \sigma^{1N} \\ \sigma^{21} & \sigma^{22} & \dots & \sigma^{2N} \\ \dots & \dots & \dots & \dots \\ \sigma^{N1} & \sigma^{N2} & \dots & \sigma^{NN} \end{bmatrix} .$$

Few remarks on $\sigma^{\alpha\beta}$:

- $\sigma^{\alpha\beta}$ is symmetric: the surface tension of fluid α with fluid β is the same as the surface tension of fluid β with fluid α ($\gamma_{\alpha\beta} = \gamma_{\beta\alpha}$) since they have the same interface,

- say that the surrounding fluid is represented by natural number n, the n^{th} row and n^{th} column of $\sigma^{\alpha\beta}$ ($\sigma^{n\alpha}$ and $\sigma^{\alpha n}$) correspond to the surface tension of the droplets with the surrounding fluid,
- diagonal elements ($\sigma^{\alpha\alpha}$) are never addressed since they correspond to the surface tension of a fluid with itself (which is absurd),
- the remaining of the elements not listed above (i.e. $\sigma^{\alpha\beta}$ where $\alpha \neq \beta$ and $\alpha \neq n$ and $\beta \neq n$) accounts for the droplet's liquid-wetting properties (wetting between fluid α and fluid β).

Generalisation of the colour-field

In the Gunstensen method, the colour-field represents the direction of the $red-blue$ interface. In N-component generalisation, there are no arguments for not continuing to represent the $\alpha\beta$ interface normal by the $\alpha\beta$ colour-field defined as follow:

$$P_\gamma^{\alpha\beta}(\mathbf{x}) = \sum_i [\rho^\alpha(\mathbf{r}+\mathbf{c_i}) - \rho^\beta(\mathbf{r}+\mathbf{c_i})]c_{i\gamma}\,.$$

And therefore, the angle of the colour-field of the $\alpha\beta$ interface is taken as:

$$\theta_P^{\alpha\beta} = tan^{-1}\left(\frac{P_y^{\alpha\beta}}{P_x^{\alpha\beta}}\right)\,.$$

Summary of the surface tension perturbation N-component model

The final formula of the surface tension with the N-component λ method reads:

$$\triangle f_i(\mathbf{x}) = \sum_{\alpha,\beta} \sigma^{\alpha\beta}\left(1 - \left|\frac{\rho^\alpha - \rho^\beta}{\rho^\alpha + \rho^\beta}\right|\right) cos(2(\theta_P^{\alpha\beta}(\mathbf{x}) - \theta_i))\,.$$

To summarise, the implementation of the surface tension with the λ method is straightforward from the binary method as long as very carefully implemented. The micro-currents and isotropy have been measured to match the micro-currents obtained with the binary model, as one might expect.
This method enables the explicit representation of surface tensions between each possible pair of fluids, through the surface tension matrix $\sigma_{\alpha\beta}$.

4.3.2 Wetting methods in the Gunstensen method

Liquid-wetting in the generalised λ method

The implementation of the liquid-wetting is straightforward from $\sigma^{\alpha\beta}$: tuning $\sigma^{\alpha\beta}$ gives the required liquid-wetting behaviour. No additional step is required to accommodate liquid-wetting between the different droplets in the simulation.

In figure 4.6, a rectangular box is initialised with two fluids (A and B) split horizontally with a round droplet (C) lying in the middle of the interface of fluid 1 and 2. The droplet is subjected to a constant surface tension (equal surface tension between the droplet and the surrounding fluids). We vary the surface tension of the two surrounding fluids (A and B). The simulation parameters for this data were 350×100 nodes, $\omega^{\alpha} = 1.7 \; \forall \; \alpha$, $\sigma^{AC} = \sigma^{BC} = 0.001$ and $\sigma^{AB} = \{$ 0.003, 0.002, 0.0015, 0.001, 0.0005, 0.0001 $\}$.

The droplet in the middle of the interface of fluid 1 and 2 is deformed by the only influence of the surface tension between 1 and 2. Note that this is a standard configuration to test a N-component model.

4.3.3 Spontaneous liquid-wetting behaviour of the λ method for N-components

The spontaneous *liquid*-wetting is assessed here by the final steady state configuration of different fluids into contact, where all the surface tensions are equal.

In figure 4.7), the surface tensions between the surrounding fluid (S) and the droplets (D) are the same, and the surface tension between the droplet is set to zero. The simulation parameters for this data were 200×200 nodes, $\omega^{\alpha} = 1.7 \; \forall \; \alpha$, $\sigma_{SD} = 0.001$ and $\sigma_{DD} = 0$.

These steady state super-ball configurations of figure 4.7 can be understood by considering the purely local property of the λ method: the two droplets have exactly the same surface tension with the surrounding fluid, and none between themselves. So, as far as the surface tension is concerned, they are the same fluid, leading to a spherical droplet made out of the different fluids, with arbitrary internal structure.

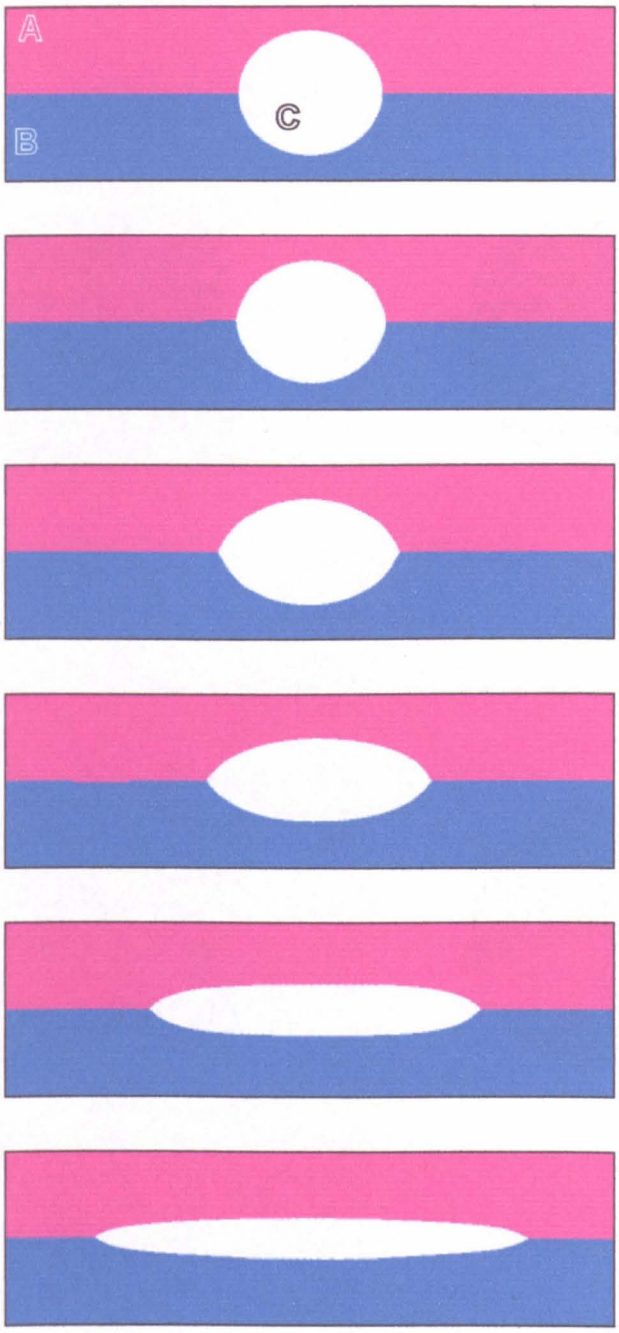

Figure 4.6: Demonstration of liquid-wetting capability of our N-component model. The droplet (C) in the centre is elongated by the increasing surface tension of the blue-magenta (A-B) interface.

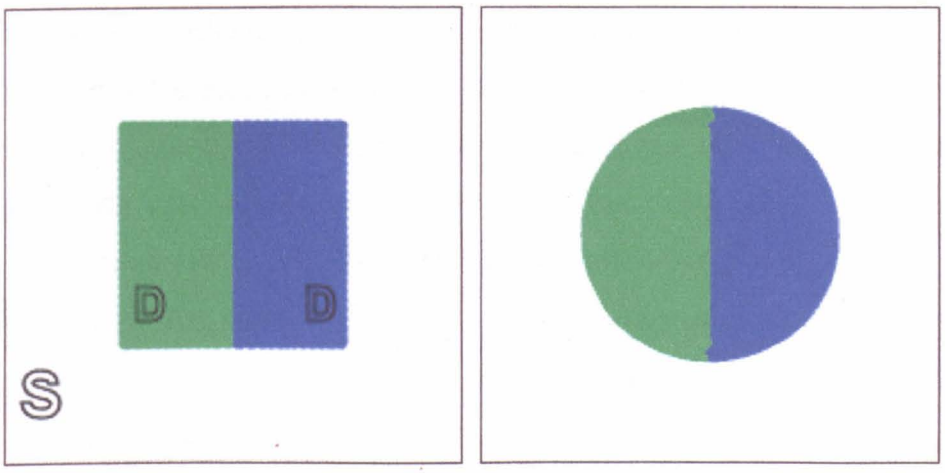

(a) Initial state

(b) Steady state

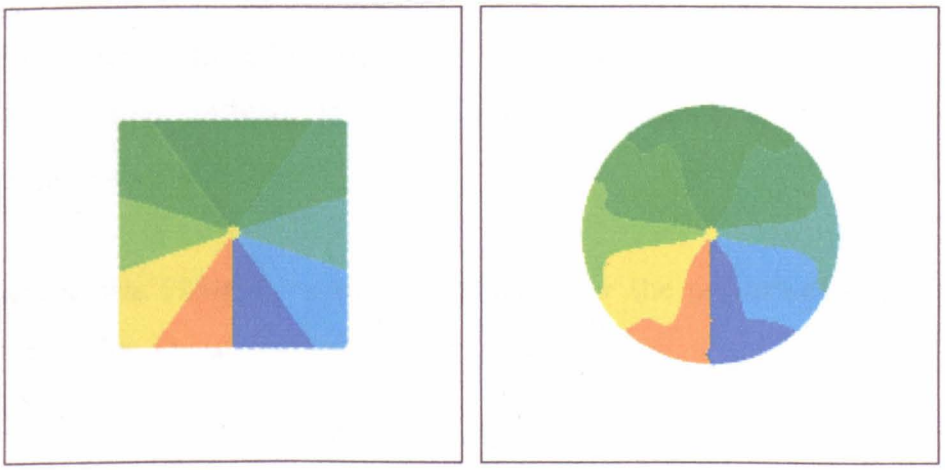

(c) Initial state

(d) Steady state

Figure 4.7: Liquid-wetting spontaneous behaviour. Case when all surface tensions are equal.

Wall-wetting in the generalised λ method

We saw in the first chapter that each liquid had its own wall-wetting behaviour, that is affinity with a given surface. Insignificant in the hydrodynamics when only one fluid is in contact with the walls, it becomes a key factor when more than one fluid is present (see chapter 1). The contact angle of the interface between two fluids and the wall depends on each fluid's wetting as well as their surface tension (recall the Taylor-Laplace law, equation 3.9). The reduction of both wettings to a unique forcing (equal to the difference of wetting of the two fluids) has therefore been possible for the binary case, but is clearly not applicable in N-component. Each fluid's affinity has to be taken into account individually.
Recall that the wetting method for the binary fluid λ method is to impress wetting by imposing a perturbation step similar to the surface tension perturbation step, parallel to the direction of the wall:

$$\triangle f_i = \sigma_{wall}\, \rho\, cos[2(\theta_i - \theta_w)]\,,$$

where σ_{wall} is the wall wetting parameter of the two fluids and θ_w is the wall direction with respect to the node, defined by equation 3.11.
Again, in N-component fluids, the σ_{wall} parameter is defined for each of the N_t fluids α, and σ_{wall} is generalised to σ^{α}_{wall}.

This leads to the following formula accounting for the perturbation of the post-collided densities, to include wall-wetting behaviour:

$$\triangle f_i = \sigma^{\alpha}_{wall}\, \rho^{\alpha}\, cos(2(\theta_i - \theta_w))\,.$$

This operation is repeated N_t times for each (N_t) fluid at the node, giving the following final perturbation:

$$\triangle f_i = cos(2(\theta_i - \theta_w)) \sum_{\alpha}^{N_t} \sigma^{\alpha}_{wall}\, \rho^{\alpha}$$

4.4 Proof of capability of our N-component method

Since the primary objective of this thesis is explicitly to model venule scale blood flow, figures 4.8, 4.9, and 4.10 illustrate the case of two non-coalescing droplets with

high/medium/low surface tension and high viscosity, subjected to body-forces in opposite direction. The liquid-wetting matrix $\sigma^{\alpha\beta}$ has been tuned such that the surface tension between the two droplets is much higher than between the droplets and the surrounding fluid. This ensures that an explicit layer of surrounding fluid is mostly always surrounding or wetting the droplets. The two droplets can be regarded as two vesicles. Deformation and non-coalescence is readily visible.
The simulation parameters for this data were 200×200 nodes, $\omega^S = 1.7$, $\omega^D = 0.5$. We also had, (i) in figure 4.8, $\sigma^{DD} = 0.005$, $\sigma^{SD} = 0.0025$, g=2×10^{-5}, frames were taken every 5000 steps (ii) in figure 4.9, $\sigma^{DD} = 0.005$, $\sigma^{SD} = 0.0025$, g=5×10^{-5}, frames were taken every 5000 steps and (iii) in figure 4.10, $\sigma^{DD} = 0.002$, $\sigma^{SD} = 0.001$, g=5×10^{-5}, frames were taken every 5000 steps.

4.5 How efficient is this new model?

Computational efficiency is a major issue and aim of this project, since we showed that some other numerical models where able to simulate similar application but were rather computationally inefficient. It is therefore important to assess the efficiency of our model to demonstrate the major advantage it has against other related numerical techniques.
We assess efficiency by measuring the time and memory requirements of our model in a standard configuration (square box), with respect to the system size, the number of simulated non-coalescing droplets (N), and the number of possible different fluids at a node (N_Q).

4.5.1 Computational efficiency against the system size

We first needed to verify that our model was applicable to relatively large systems, there would have been only a limited number of possible applications otherwise. Figure 4.11 shows the memory and time requirement of our model with the total number of nodes (note that the explicit configuration does not affect these requirements).
This demonstrates that our new N-component model for non-coalescing droplets scales linearly with the number of nodes, which is, as far as the author is aware, as

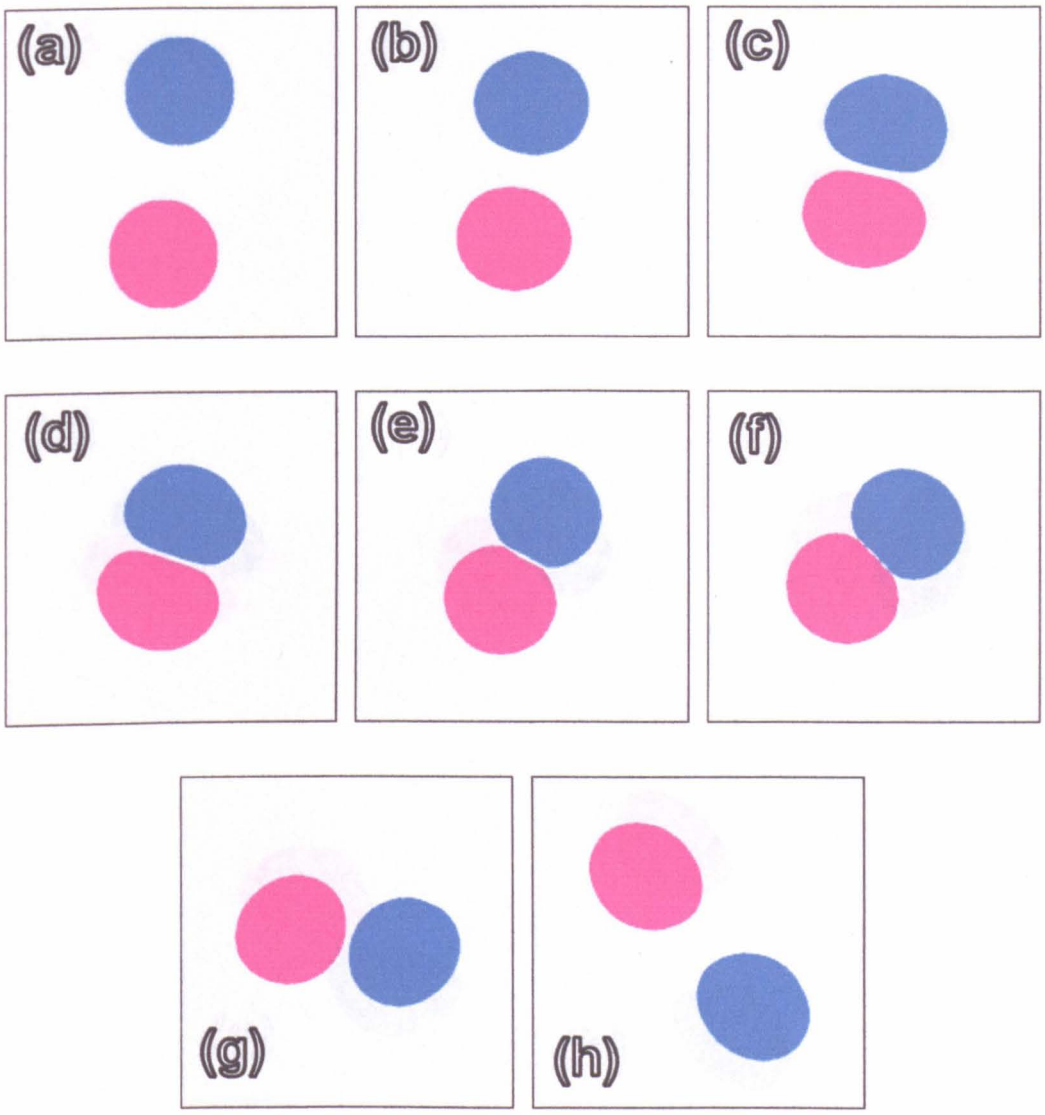

Figure 4.8: Proof of capability of our N-component model. Both droplets have high surface tension and high viscosity.

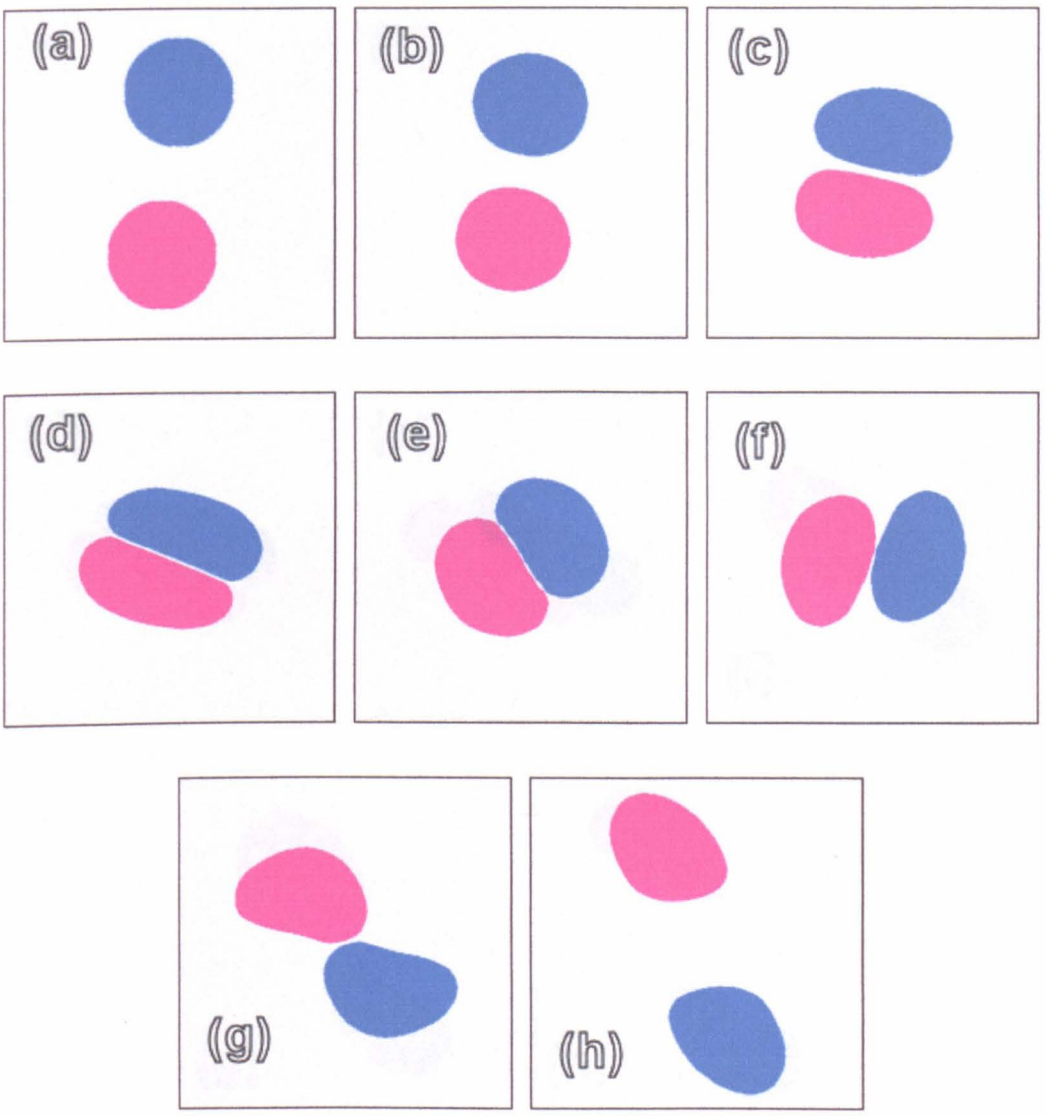

Figure 4.9: Proof of capability of our N-component model. Both droplets have medium surface tension and high viscosity.

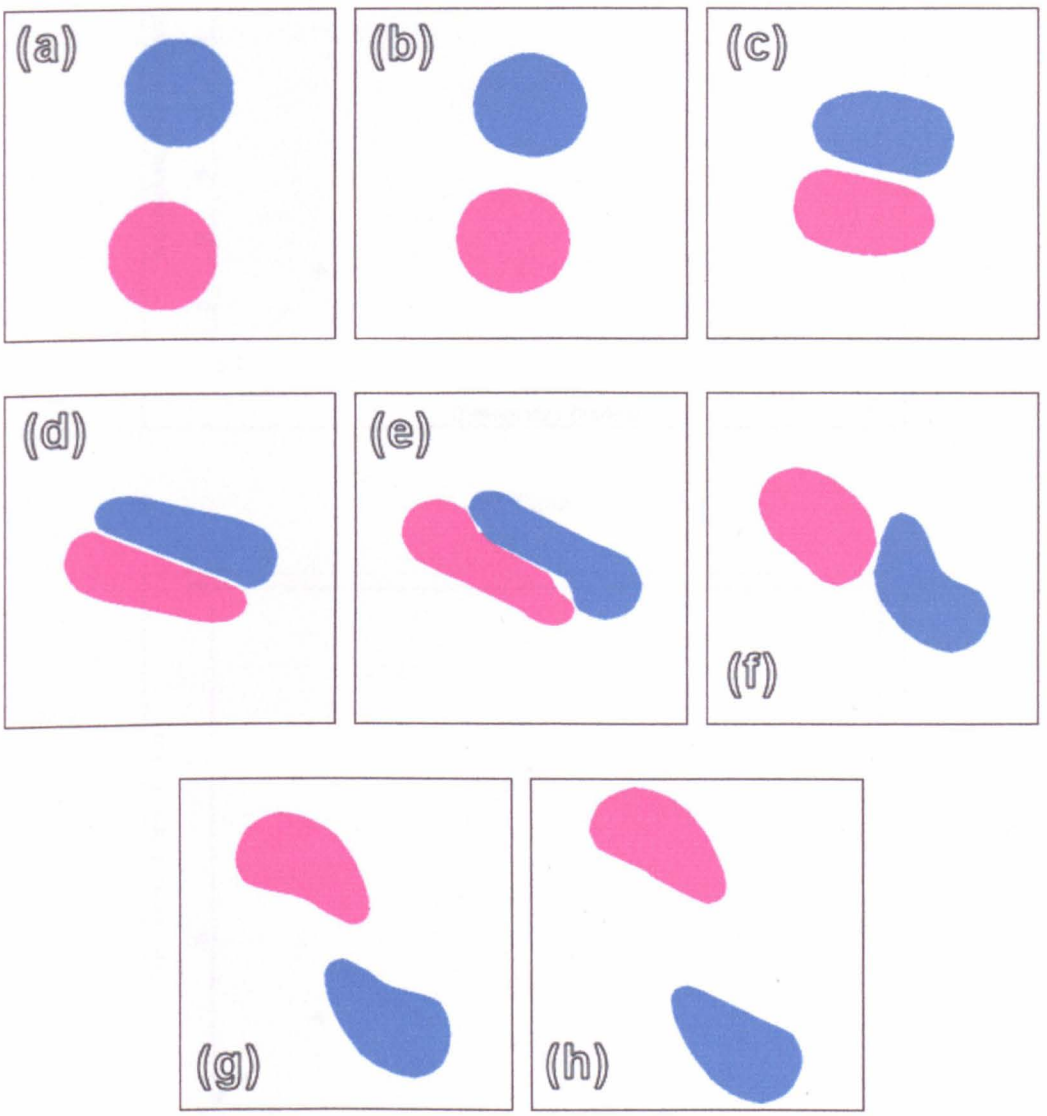

Figure 4.10: Proof of capability of our N-component model. Both droplets have low surface tension and high viscosity.

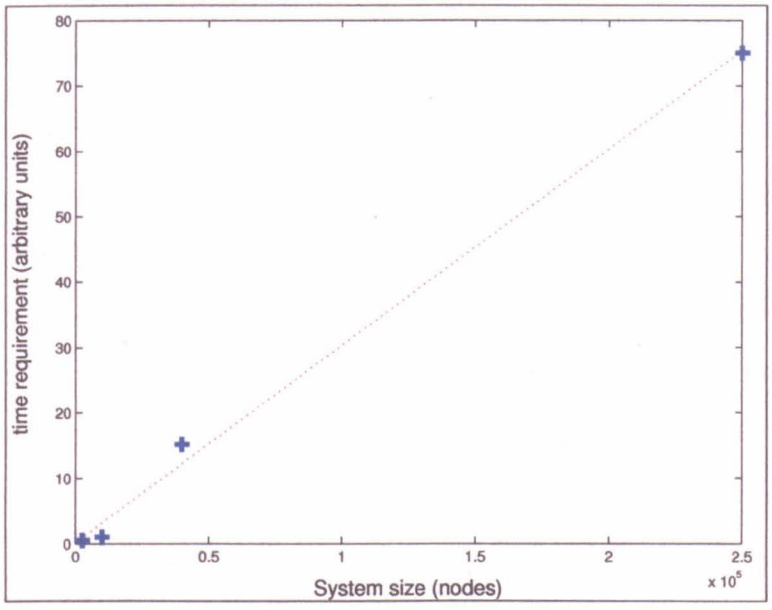

(a) Time

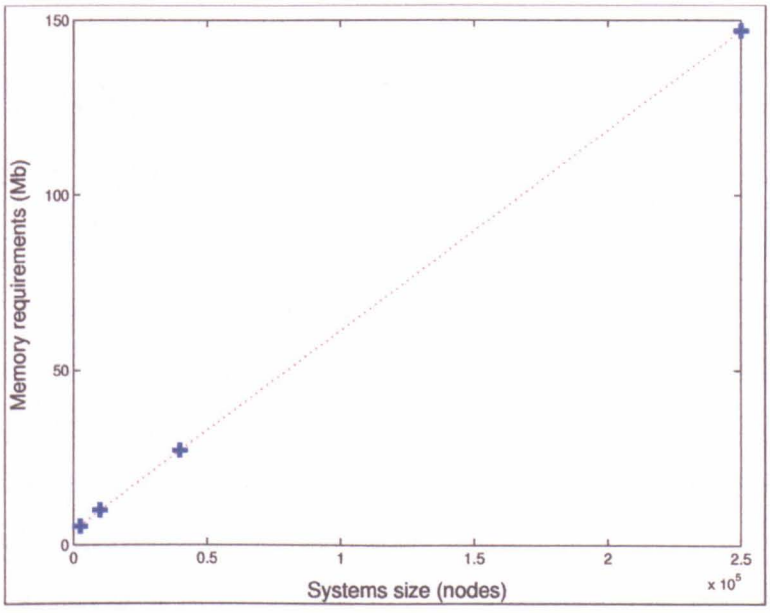

(b) Memory

Figure 4.11: Computational requirement of our new N-component model for non-coalescing droplet with respect to the system size. The linear dependance for both time and memory is as good as any model can get.

good as any other model. In other words, the system size is not a limiting factor in this model.

4.5.2 Computational efficiency against the maximum number of fluids allowed at one node

As described previously, the maximum number of fluids at one node (N_Q) is a major parameter for the stability of the simulation. We usually choose $N_Q = 5$, which has been found to be appropriate for most of our applications so far. However, it has been mentioned that in the case of the simulation of highly poly-dispersed suspension, N_Q might have to be increased, so that nodes can accommodate more fluids at one time. Figure 4.12 shows the memory and time dependance of our N-component model against N_Q.

It demonstrates that both time and memory requirements are linear in N_Q, which means that N_Q should be minimised since it is an 'expensive' parameter. It is also the author's belief that a linear dependance with N_Q is acceptable.

4.5.3 Computational efficiency against the number of simulated droplets

Most importantly in the current applications of simulating large number of droplets (N), the efficiency of the model should be focused on the number of droplets. It otherwise would be as any other model and not providing advantage. Recall that the target application of this model is to simulate (efficiently) more than 100 non-coalescing droplets. Figure 4.13 shows the dependance the memory and time requirements with respect to the total number of simulated droplets.

This shows that the time requirements of our model scales only weakly with N (it takes only half more time to simulate 1000 droplets than 200), and that the memory requirements are independent of the number of droplets, keeping the simulational domain constant. This demonstrates that our model can simulate efficiently a very large number of droplets, which was the aim or this thesis.

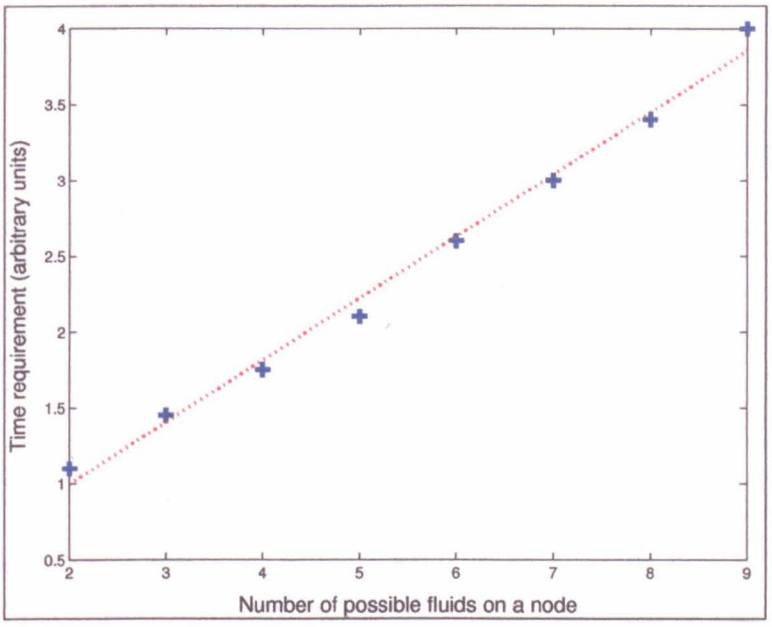

(a) Time

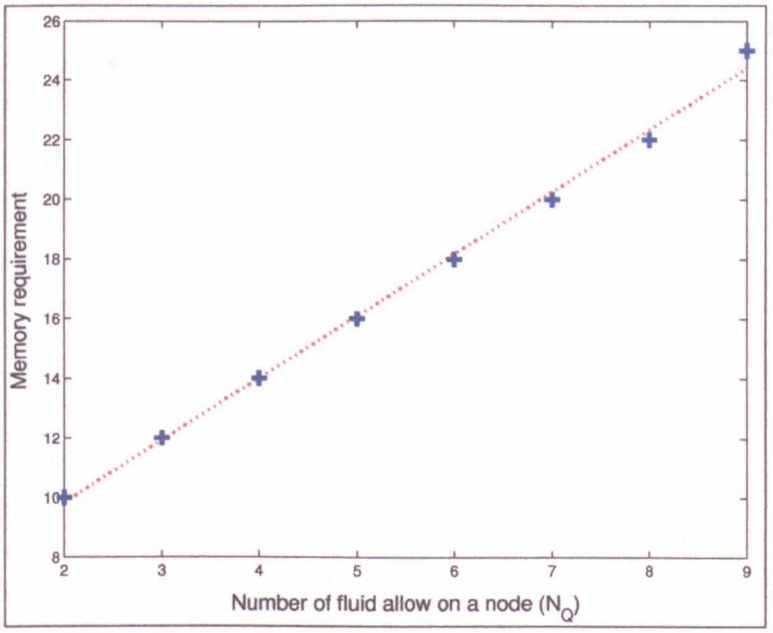

(b) Memory

Figure 4.12: Computational requirement of our new N-component model for non-coalescing droplet with respect to the number of fluids allowed at one node (N_Q). The linear dependance for both time and memory shows that N_Q should be minimised since it is an 'expensive' parameter.

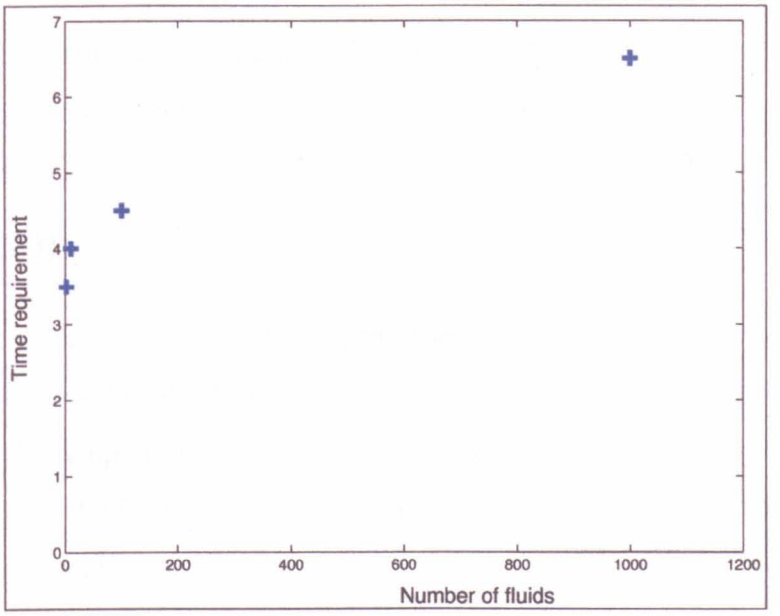

(a) Time

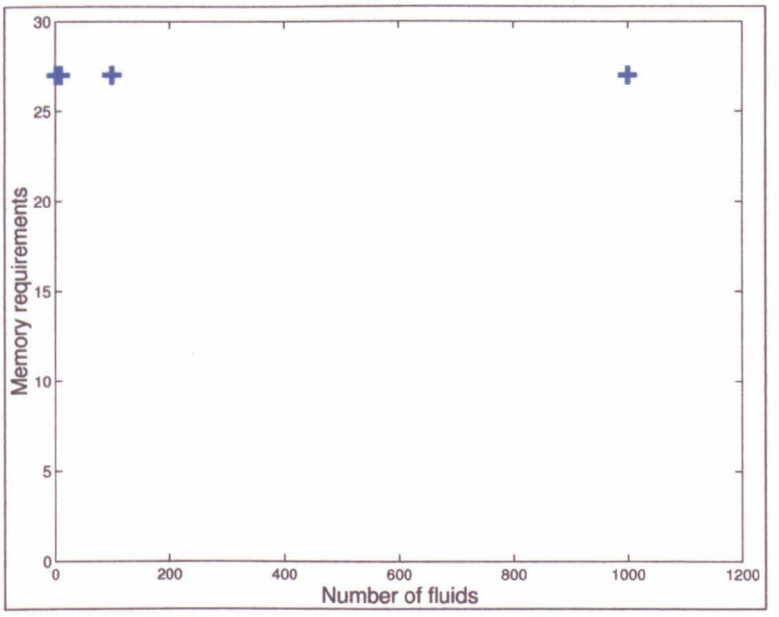

(b) Memory

Figure 4.13: Computational requirement of our new N-component model for non-coalescing droplets with respect to the total number of simulated droplets (N). The very weak dependance of the time requirement and the non-dependance of the memory requirements demonstrate the high efficiency of our model, and its ability to simulate efficiently large number of particles.

4.5.4 Conclusion on efficiency

The previous series of tests, shown in figures 4.11, 4.12 and 4.13, demonstrates that large simulations with large number of non-coalescing droplets are possible with limited computational resources.

Conclusion

We described in this chapter how to generalise the original Gunstensen model for binary LB. We showed that our model was required explicitly to model large numbers of non-coalescing droplet: no other model (as far as the author is aware) is capable of such efficiency. We have shown how to generalise the surface tension method and liquid wetting, providing the first account of mesoscopic blood flow simulation. Only proofs of concept have been shown so far, the next chapter consists of a validation of the dynamics of our new N-component model.

Chapter 5

N-component validation: comparison with experimental behaviour

Introduction

The previous chapter has show how to implement our new N-component LB model to the flow of many droplets in suspension, for example. However, this model needed to be validated through comparison with well-established results. This validation comprises the third set of results of this thesis, and is due to appear in the press late this summer in [48] and [47].

We chose to compare our model against the work of Goldsmith [71], [72], [73], [74] on the flow of RBC's, and solid and deformable particles at the capillary scale (10 cells in diameter).

5.1 Experimental observations

As we saw previously in this chapter, blood is mainly composed of plasma and RBC's. That is the reason why Goldsmith, in [71], [74], studied blood flow through the flow of RBC suspensions only and why, in this chapter, we consider suspensions of identical mono-dispersed particles only. It should be noted that Goldsmith's work, even though of a certain age now, is considered as the reference for this application,

since he carried out a very careful and thorough investigation.

As mentioned previously in last chapter, RBC's have a very high internal fluid viscosity (1000 times more viscous than the plasma) and a very low surface tension: nearly zero. Ion protein pumps ensure that an important depletion of the inside compared to the plasma and together with restriction of constant interfacial surface area, provide the RBC's with their typical bi-concave shape as well as their deformability. Indeed, RBC's with inefficient ionic pumps return to a spherical shape and do not deform (like an inflated football). It should be noted that the precise deformability of RBC's is also influenced by the viscoelatic property of their membrane. Goldsmith studies did not take this into account since they involved 'ghost red cells' (red blood cells which have had all of their cytoplasmic contents removed so that only their outer cytoplasmic membrane remains), serving as a model for whole blood. RBC's are consequently said to behave like like deflated footballs, containing a viscous oil: they are slowly but highly deformable ([19]).

Goldsmith showed through this thorough study that the behaviour of RBC's at low Reynolds Number (less than unity) and high volume fraction is similar in many ways to that of suspensions of deformable spheres, discs and rods ([71], [23]). However, he also observed that the mesoscopic flow of solid particle was qualitatively different than the mesoscopic flow of deformable particles [71], [74], [23]. This is widely taken to mean that deformability plays a crucial role in overall flow field at this scale and that the exact shape of the particles in suspension is not of prime importance. Goldsmith also showed that the influence of the the shape of the particles in suspension was significant only at low volume fraction (through the different equilibrium position of a single particle and similar velocity profiles of high volume fraction of suspensions in long straight tubes) [73], [72].

In summary, the following results highlight the need for our N-component LB model, again, given that blood flow and deformable particle transport are key, targeted applications of this thesis, since:

- deformability cannot be overlooked, even at high volume fraction,
- the exact shape of the particles is only significant at low volume fraction,
- no other current numerical model can actually simulate efficiently both high

volume fraction and deformability.

In order to validate our N-component model, we compare the response of our new model to the velocity profiles obtained experimentally by Goldsmith and their dependance on the different parameters.

5.2 Configuration and definitions

5.2.1 Flow regime and flow configuration

Goldsmith's experiments were carried under a microscope in transparent suspensions of red cell ghosts, tracking the particles in flow through tubes having radii of 32 to 80 μm, at Reynolds numbers from 10^{-3} to 0.3, and volume concentration from 0.1 to 0.9. The cells' diameter was typically 6 μm [74].

A quantitative one-to-one comparison of Goldsmith's work would not be practical with our LB N-component flow since we do not represent exactly the same objects (Goldsmith considers ghost RBC's while we consider liquid droplets). We therefore studied, quantitatively, the influence of the same parameters as Goldsmith (volume fraction, flow rate and deformability) and extracted the qualitative trends to make appropriate, valid comparisons.

We used a two dimensional straight channel, the typical size of the simulations was 250×100 lattice nodes. We used mid-link bounce back to impose top and bottom walls and periodic boundary conditions to close the simulation left and right. The particles' typical size was 8 lattice nodes in diameter, providing Goldsmith's particle diameter to channel's width ratio. We considered that a length to width aspect ratio of 2.5 was sufficient to smear out the effect of the periodic boundary conditions. A uniformly impressed body-force was used to impose the pressure gradient, which is a good approximation at low Reynolds number when there is only a small difference of density between the particles and the surrounding fluid. The explicit density difference between the RBC's and the plasma (about 1%) was not modeled. Results were obtained from steady state, typically after 10^5 time steps.

In comparison to Goldsmith's experimental configuration, we matched:

- the surrounding fluid's Reynolds number,
- the relative diameters of the particles (cells) to the width of the tube,
- the volume fraction of the particles to the surrounding fluid.

We used a random arrangement of identical mono-dispersed droplets as initial configuration, in order to minimise periodic boundary and artificial alignment effects. The velocity profile was initiated as a longitudinally uniform parabola. We could not match Goldsmith's concentration factor up to 0.9 by volume, since a random initial arrangement of the particles needed to be retained and it was found that a volume fraction of 0.6 was as high as we could obtain with the time available. Note that this upper bound on concentration reflects only the initialisation of our simulation alone: the core algorithm could run with much higher concentration (see the application on sedimenting immiscible droplets of next chapter).
We used the N-component model described in the previous chapter, together with the λ correction described in chapter 3.

5.2.2 Definitions

Goldsmith's arguments on the role of deformability are based on the comparisons of the 'blunting' of measured velocity profiles obtained with different particles in suspension. He compared velocity profiles qualitatively only and did not provide any quantitative definition for the blunting. In this study, we define the blunting of a measured velocity profile quantitatively as its departure from pure parabola. We measure this departure as the mean departure (at 0.25% and 0.75% of the width of the channel) to the fitted (6^{th} order polynomial) length averaged velocity profile, normalised to its maximum velocity, to the corresponding normalised parabola (see also figure 5.1):

$$\beta \equiv \frac{\bar{v}(\bar{y}=0.25)+\bar{v}(\bar{y}=0.75)}{2\times 0.75}, \tag{5.1}$$

in which, 0.75 is the height of such a normalised parabola. With this definition, a flat velocity profile is characterised by $\beta = 1.33$ and a parabolic velocity profile by $\beta = 1.00$. This definition minimises the error due to the asymmetry of the velocity

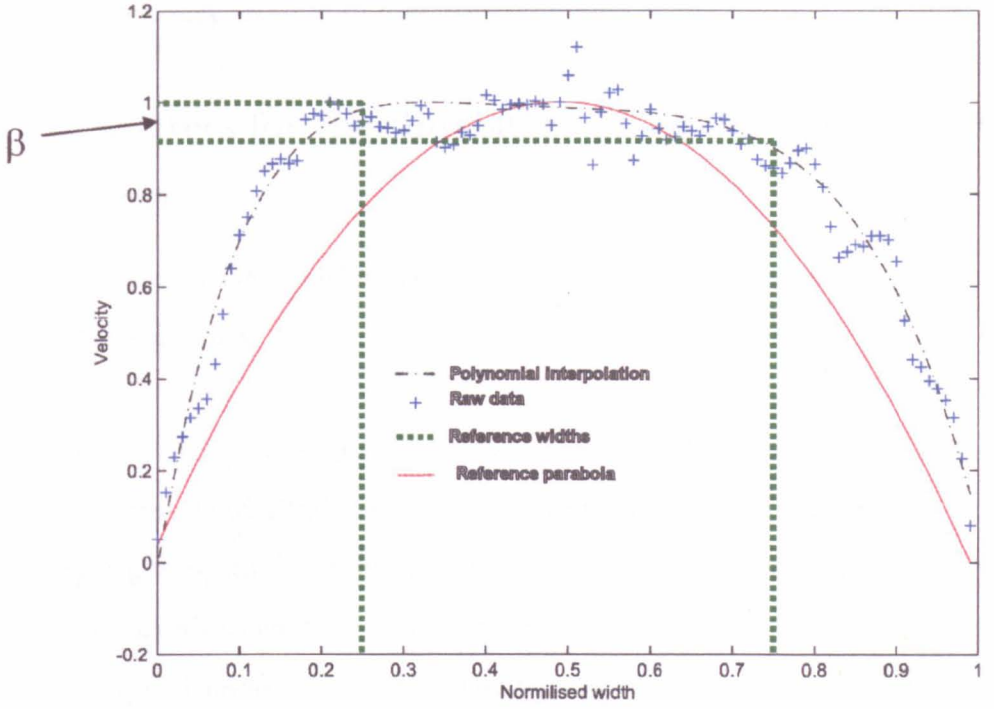

Figure 5.1: Schematic representation of the definition of the blunting β of the velocity profiles.

profile due to asymmetries in the suspension axial concentration and local flow. Other definitions are used:

- Φ: volume fraction of the suspension.
- superscript 'D' denotes any droplet's fluid and superscript 'S' denotes the surrounding fluid.
- σ^D is the surface tension parameter of the droplets in suspension. It is important to note that Σ is the same for all the droplets of the suspension ($\sigma^{SD} = \Sigma$).
- Γ is the body force parameter, used to mimic a pressure difference in the simulation. Since the flow rate of the simulation is linearly related to Γ, Γ is taken as a measure of the flow rate.
- $\Psi = \nu^D/\nu^S$: ratio of the droplets viscosity (ν^D) to the surrounding fluid's viscosity (ν^S).
- R_{drop}: radius of the droplet. Note that through this study, all the droplets have the same radius, since Goldsmith studied suspensions of mono-dispersed

particles (typically, R_{drop}=8 l.u.).

5.2.3 Parameters for the simulation of solid and deformable particles

Drops' viscosity and surface tension were the two free parameter remaining to vary the droplet's deformability.

For the solid drop study, the droplets' viscosity was set to be 40 times greater than the surrounding fluid's (Ψ=40, $\omega^S = 1.8$) and their surface tension was set to the highest value giving stable simulations and relatively low micro-currents activity (recall that too high a surface tension can cause a large micro-current activity, overwhelming the hydrodynamical flow which can causes the simulation go unstable, see chapter 3). We took typically $\sigma^D = 0.001$.

For the study of deformable drops, the droplets' viscosity was the same as the surrounding fluid's ($\Psi = 1$) and σ^D was reduced to a small value, ensuring however that the droplets do not break-up in the achieved local shear with the highest flow rate. Typically, we had $\sigma^D = 0.0001$.

In both studies, we tuned the surface tension matrix $\sigma^{\alpha\beta}$ so that the droplets in the suspension exhibit a biological, cell-like behaviour: the surrounding fluid is encouraged to wet each droplet at all time (typically, $\sigma^{DD} = 10\,\sigma^{SD}$). We also tuned the wall-wetting parameters of each droplet to be negative (to dry the walls) whilst the surrounding fluid wall wetting was tuned to be positive (to wet the wall). We had typically $\sigma^S_{wall} = 0.002$ and $\sigma^D_{wall} = -0.002$.

5.3 Simulations of solid/deformable droplets

Goldsmith observed experimentally different dependencies of β over Γ, R_d and Φ for solid and deformable suspended particles [71], [72], [23]. We propose to assess the response of our N-component model against the same parameters, and to demonstrate

in this way the capabilities and correct hydrodynamics of our model.

5.3.1 Solid particles

In the case of *solid particles*, Goldsmith showed that β depends solely on the particles' volume fraction (Φ) and relative size to the channel (R_d) [23].

We used the parameters described in section 5.2.1.

Figure 5.2 shows the expected increase in β with increasing Φ (which is qualitatively in accord with Goldsmith's experimental results).

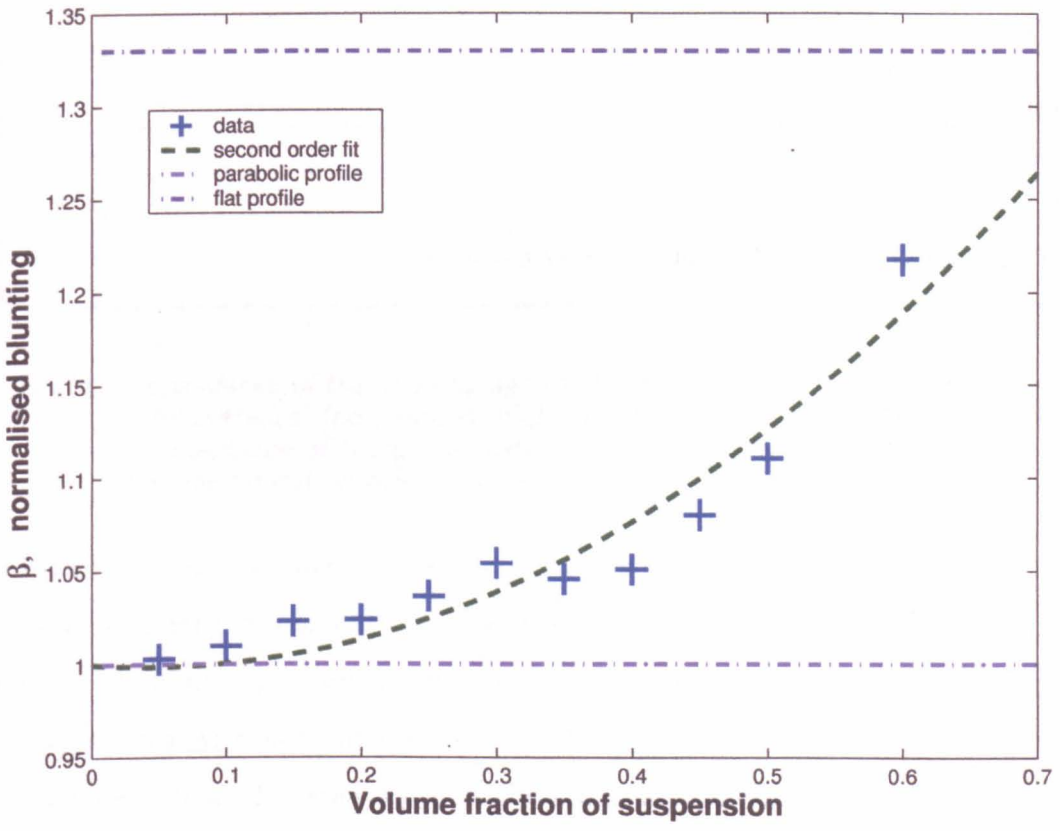

Figure 5.2: Dependance of the blunting against the volume fraction of the suspension. Case of solid particles (i.e. viscous, high surface tension drops). The expected increase of β against Φ is recovered.

We observed however a small dependance of β against Γ (Goldsmith observed no dependance), as figure 5.3 shows.

This implies that the set of parameters used to model solid particles with the droplets described in section 5.2.3 are not sufficient to obtain really solid particles.

We could increase the solidity of the 'particles' (drops) in suspension by increasing Σ^D and/or Ψ but this would tend to make the flow more noisy (because increased

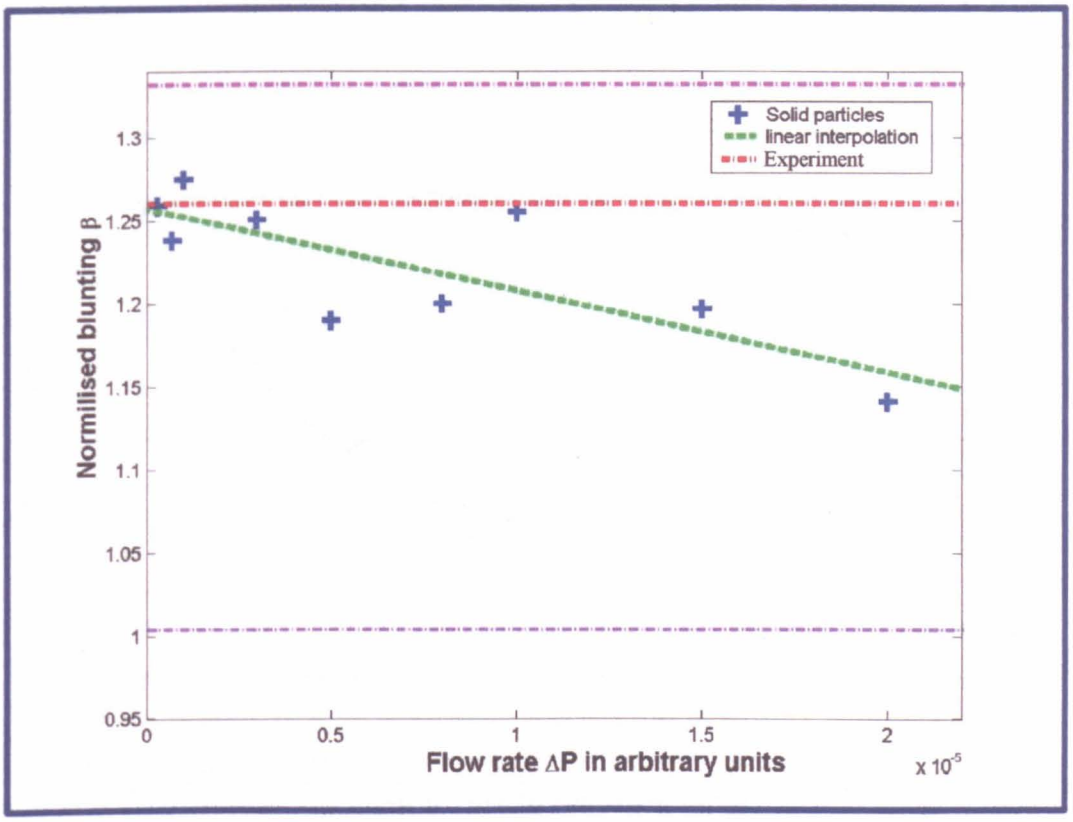

Figure 5.3: Dependance of the blunting against the flow rate of the suspension. Case of 'solid particles' (i.e. viscous, high surface tension drops). The model shows a dependance of β against with the 'solidest' particles achievable, showing that the limitation of this model.

micro-currents) and ultimately lead to unstable simulations. This effectively defines the boundary of our current model for application to the modeling of rigid particles. It should, however, be noted that this limitation is not surprising since the very essence of this technique is to model droplets (deformable particles), not solid particles. If solid particles have to be modeled, our LB based technique allows the concurrent implementation of a (say) Ladd type method [113] (which is more appropriate for this task).

5.3.2 Deformable particles

In the case of deformable particles, Goldsmith found that β depends on the flow rate (recall that β was independent of the flow rate for solid particles) [71], [72], [23]. We used the parameters described in section 5.2.3 to assess this dependance. Figure 5.4 shows the expected decrease of β with increasing Γ.

This last set of results, we suggest, validates qualitatively at least, the overall hy-

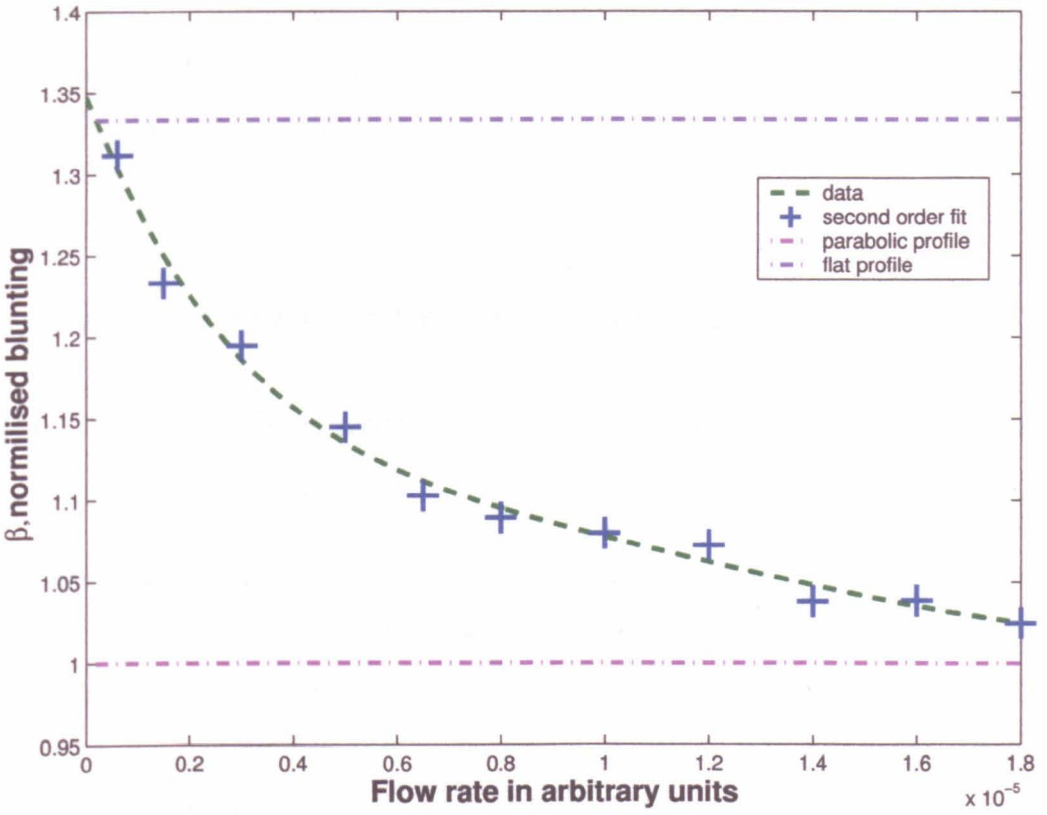

Figure 5.4: Dependance of the blunting against the flow rate of the suspension. Case of deformable particles. The expected decrease of β against is recovered.

drodynamics of our new N-component model.

5.3.3 Conclusion on the blunting results

We found that our model gives good agreement against experimental observations of Goldsmith for 'rigid' and deformable particles and identified that purely 'solid' particle behaviour could not be achieved, even with the λ method. In the remainder of this thesis, we will consequently refer to 'rigid' rather than 'solid' particles. We also note that our model is not ideally designed to represent solid particles, represented by droplets anyway (it would be pointless to disable to great advantage of this technique to model deformability over many others). More careful optimisation of the model (reduction of the micro-currents) will increase the stability of the model and improve the flow field allowing higher surface tension and more 'rigid' droplets (see next chapter). This new technique however allows the implementation of models for simulating real solid particles (such as the Ladd approach [113]).

This study has identified that tuning the surface tension and viscosity ratio could be used to give suspended particles a rigid or deformable behaviour. The next section consequently investigates the behaviour of suspensions in between these two extremes cases.

5.4 In between solid and deformable droplets

5.4.1 Flow regime and configuration and droplet's parameters

In this section, we assess the 'solidity' of suspended particles with hydrodynamical parameters (surface tension and viscosity) between the two extreme case seen previously (solid and deformable), from the point of view of the properties of the overall liquid.

We use the observations of last section: β for a suspension of solid particles does not vary with Γ while β for a suspension of deformable particles does. We use the same simulation configuration as previously (see section 5.2.1). Γ is set to the maximum value that allowed the previous study of the solid particle regime to remain in the constant β regime, as figure 5.5 schematically illustrates.

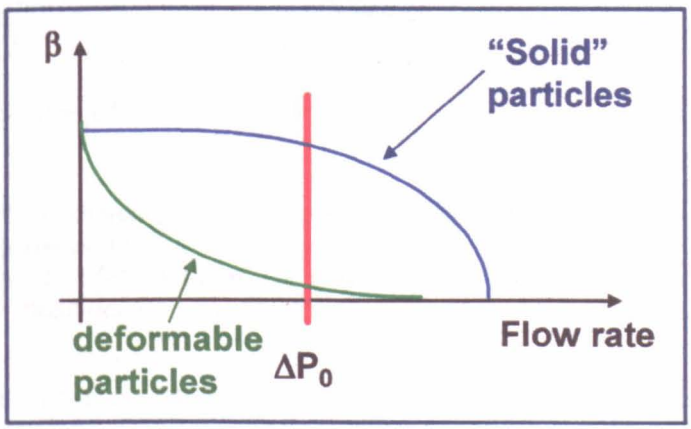

Figure 5.5: Schematic representation of the variation of β for rigid and deformable drops in solution with our simulation against the flow rate. At $\triangle P_0$, solid particles exhibit a maximum β while deformable particles exhibit a minimum β. β can therefore be taken as a direct measure of deformability of the particles.

At Γ_0, stiff particles therefore give a maximum β (1.33) while very deformable par-

ticles return a minimum β (1.00). Measuring β for different σ^D and Ψ gives a quantitative measure of the deformability of the particles in the suspension in terms of a property of the suspension as a whole.

5.4.2 Measurements

Figure 5.6 shows the response of β with different values of Σ and Ψ for the suspended particles.

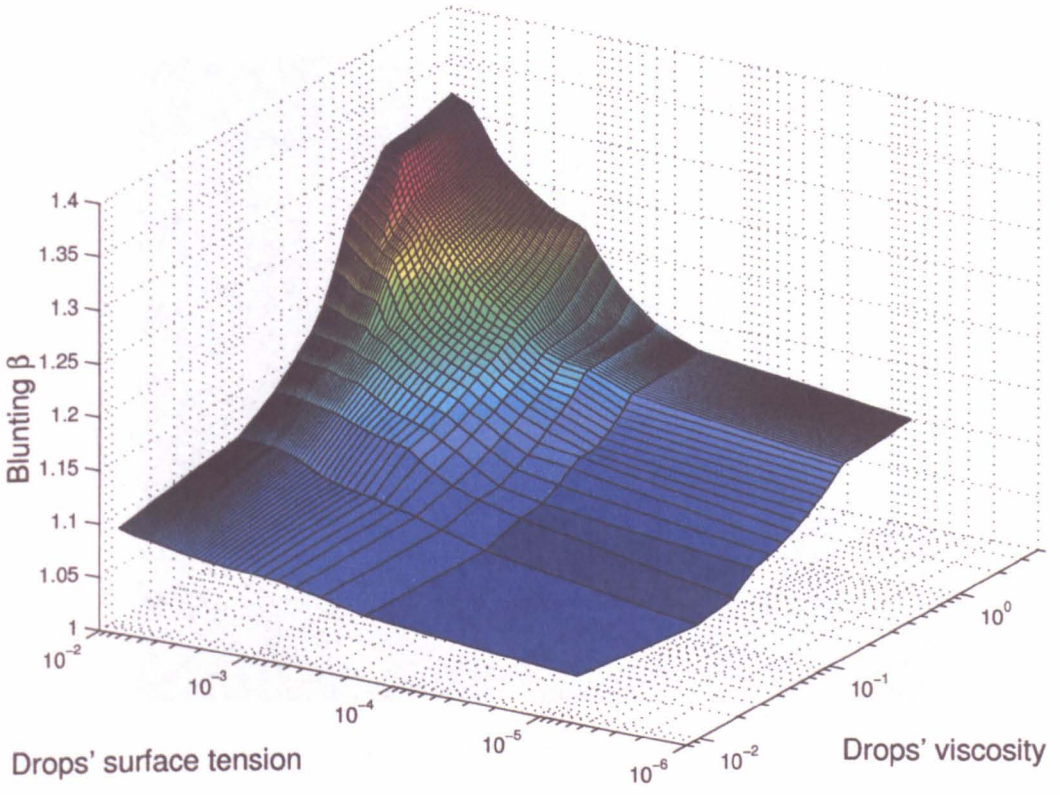

Figure 5.6: Surface showing the β response of the suspension with our N-component model depending on the droplet's surface tension and viscosity. Expectingly, the most solid particles are found at highest viscosity and surface tension while most deformable are found at low viscosity and surface tension.

It should be noted that we removed approximately 10% of visibly aberrant values of β when the interpolation of the fitted profile picked-up the noise of the profile, and returned a value of β that was clearly not representative. This happened mostly at low deformability, since the flow is highly *interface dominated*, and is therefore subjected to moderate micro-currents, increasing the noise and biasing the averaging and subsequent interpolations (see equation 5.1).

5.4.3 Results

As expected, the higher the viscosity and surface tension of the droplet, the higher their rigidity. This surface provides a calibration of the solidity of the suspended particles as a function of their surface tension Σ and ratio of their viscosity with the surrounding fluid viscosity, Ψ. To serve this application, this surface (of figure 5.6 is represented as contour plot in which each contour represents a line of iso-deformability in the particles. See figure 5.7.

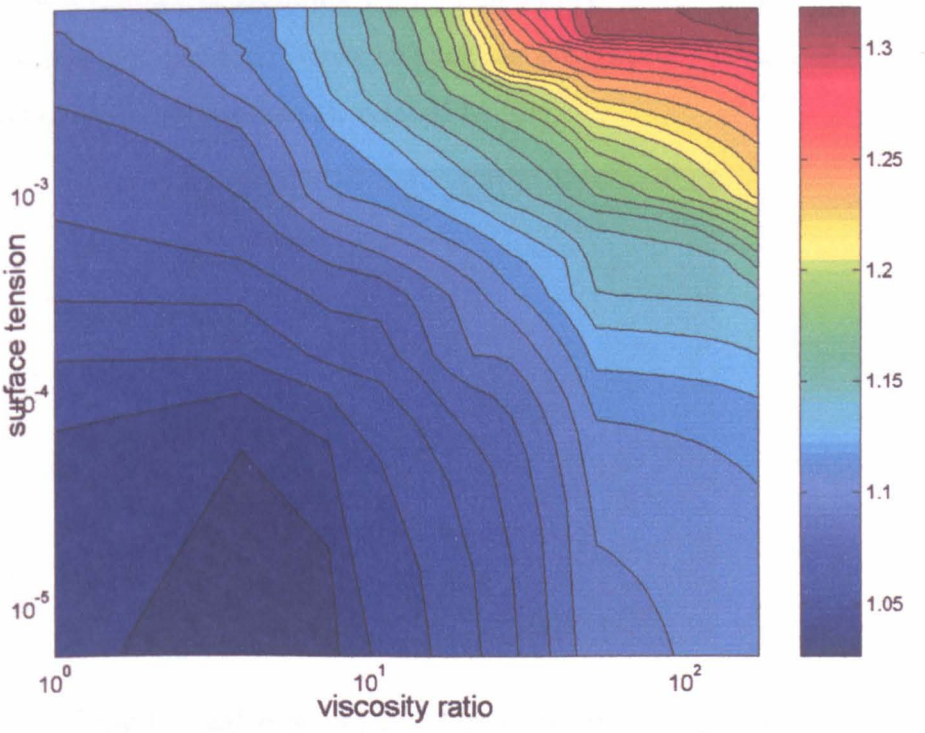

Figure 5.7: Contour plot of figure 5.6 showing sets of parameters giving identical deformability to the droplets.

The contours of figure 5.7 provide a very useful calibration of the solidity exhibited by our particles: a set of parameters can be found to give unstable simulations and through this calibration, other sets of parameters giving similar deformability can be determined immediately.

5.5 Chaining of a dense suspension

5.5.1 Experimental evidence

We observed a high degree of alignment of the particle in suspension in all of the previous simulations.

In the current literature, this phenomenon is known as *chaining*: some studies showed experimental evidence of chaining through the imaging of the flow of colloidal particles using a laser scanned confocal video [61]. Figure 5.8 shows an example of experimental evidence of chaining by Martin Frank, Doug Anderson, Jeff Morris, Denis Semwogerere, and Eric Weeks on their website (`http://www.physics.emory.edu/~weeks/lab/flowing.html`), related to [61].

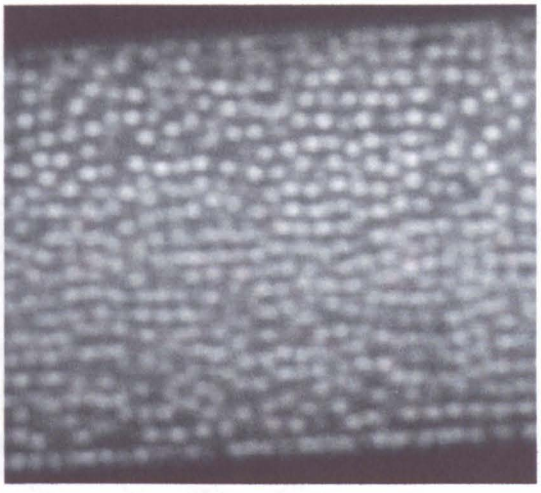

Figure 5.8: Experimental observation of colloidal particles chaining. Available on `http://www.physics.emory.edu/~weeks/lab/labpics/v02c.gif`

Molecular Dynamics simulations show that particles in a straight channel of a few particle diameter's in width exhibit analogous chaining behaviour [206], [166]. Other studies showing chaining of colloidal particles can be found in [51], [52]. Chakrabarti *et al.* [26] also note that the transition towards 'lane formation' is a general phenomenon and occurs also in systems such as dusty plasma particles [202], ions migrating with two-dimensional membranes [142], granular matter [207], [175], and collective dynamics of pedestrian zones [88], [198].

It is therefore the author's belief that this behaviour is less significant than the previous study on blunting to the validation our N-component model's overall hy-

drodynamics, since the latter observations implies that it is mainly due to packing and mechanical properties only. However, the exact arrangement of the particle within the suspension can be crucial in some studies where, for example, the suspension is made of chemically inter-reacting particles. The kinetic of these reactions obviously greatly depends on the relative arrangement of the particles.

5.5.2 Numerical evidence

In order to further study this phenomenon, we initialised randomly 560 droplets in a rectangular box. Their viscosity and surface tension were chosen so that they exhibited medium deformability ($\sigma^D = 0.0001$, $\sigma^{DD} = 0.001$, $\Psi = 20$). The simulation size was 100×250 with mid-link bounce back top and bottom and periodic boundary conditions left and right. The particles' initial diameter was 8 lattice nodes. The Reynolds number was 12.

Figure 5.9 shows the typical random initial configuration of the suspension.

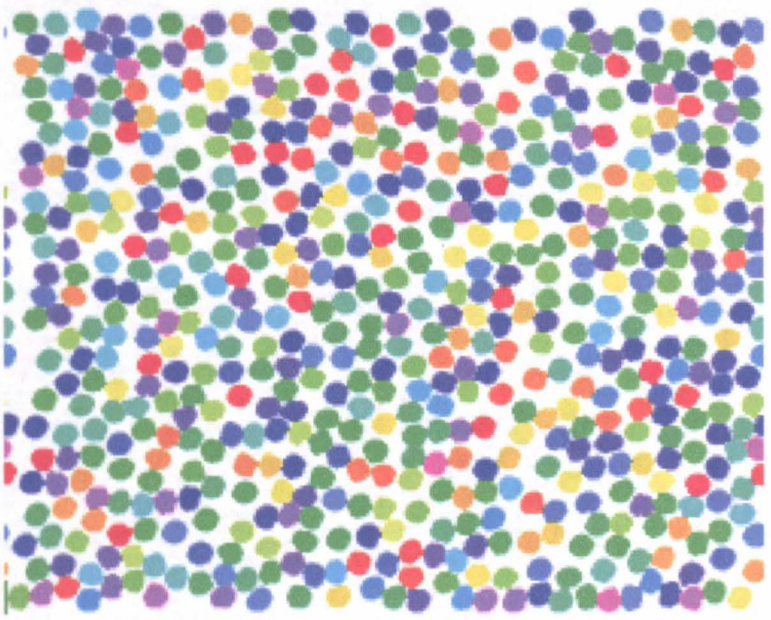

Figure 5.9: Random initial arrangement of the particles in solution for the study of chaining.

A body-force was used to impress a pressure gradient left to right ($\Gamma = 10^{-6}$). Figure 5.10 shows the time evolution of the chaining.

It is immediate from the last slide of the sequence in figure 5.10 (taken as representing a steady state) that the suspension exhibits a high degree of chaining. This chaining,

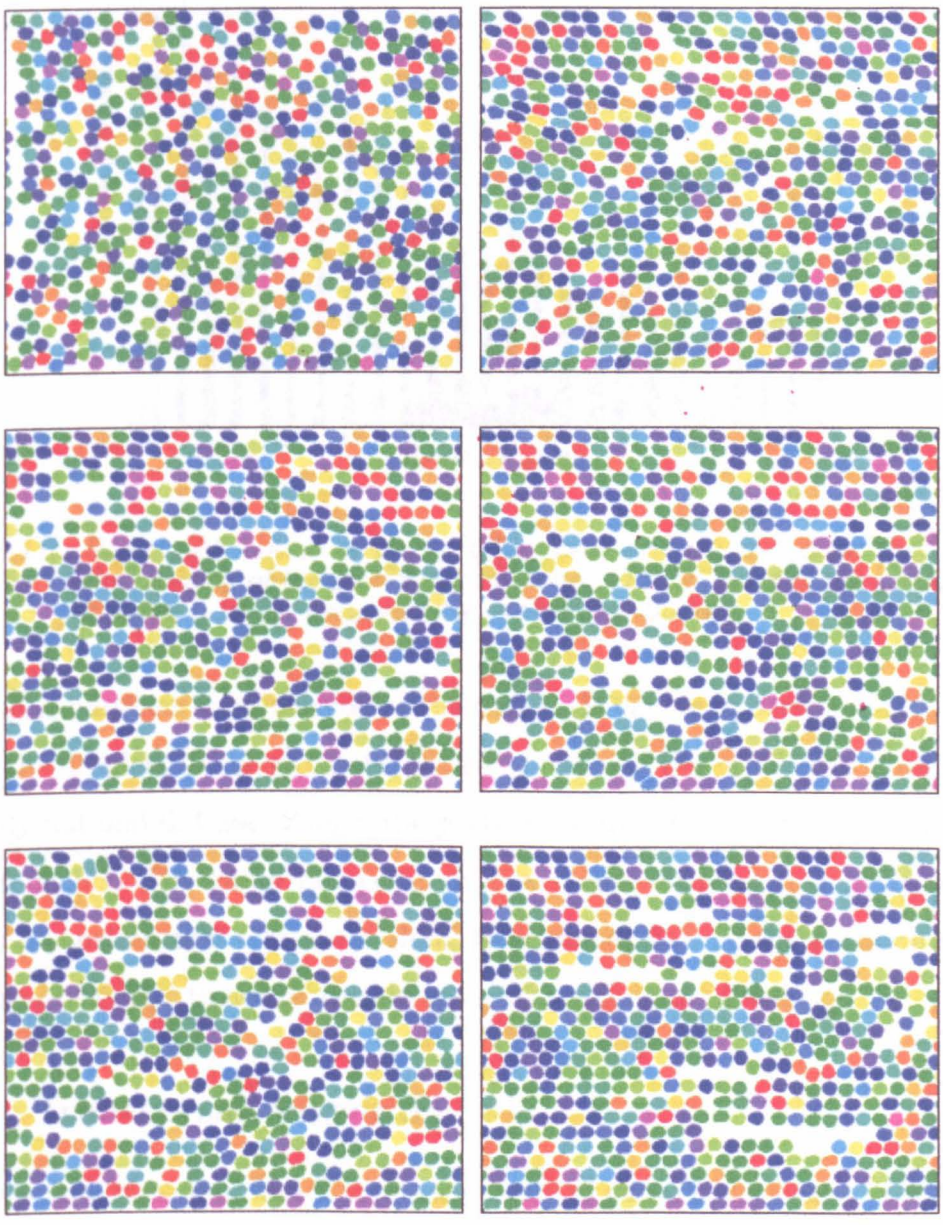

Figure 5.10: Chaining time sequence. From a random arrangement to aligned configuration.

at steady state, can be better visualised thought the distribution of the droplets across the channel, as figure 5.11 shows.

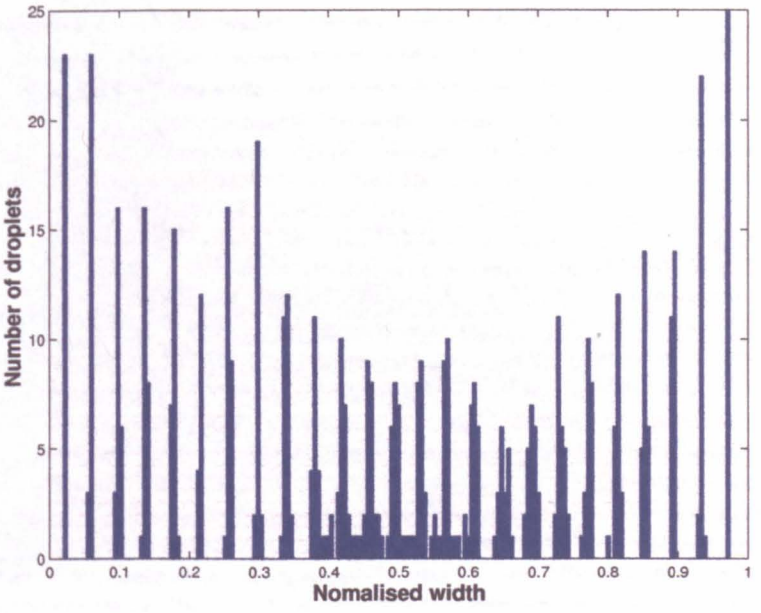

Figure 5.11: Radial distribution of the particles' centre of gravity across the capillary. The chaining of the particles is very clear. The 25 lanes of the last snapshot of figure 5.10 are clearly visible in this distribution.

Chaining of particles in suspension at the mesoscale can be understood as a compliance of the droplets to the parabolic velocity profile. If the profile was initialised as uniformly flat and did not change, the particles would not have to rearrange themselves in chains. The initial parabolic velocity profile evolving to slightly blunted, imposes a constant non zero shear along the channel, forcing the particles to rearrange 'transversally' to accommodate the radial difference of velocity.

5.5.3 Transversal migration

As we saw in last section, random arrangements of particles evolved to a configuration with a very high degree of chaining at steady state. It is therefore interesting to illustrate the mechanism leading to this final configuration. To this effect, we plot the '*path*' of each particle (the transverse component of the centre of gravity of each particle with time to be precise), see figure 5.12.

It can be seen that the rate of transverse migration (or 'hopping') of the particles decreases with time. The reason for that is two fold: (i) the particles get aligned

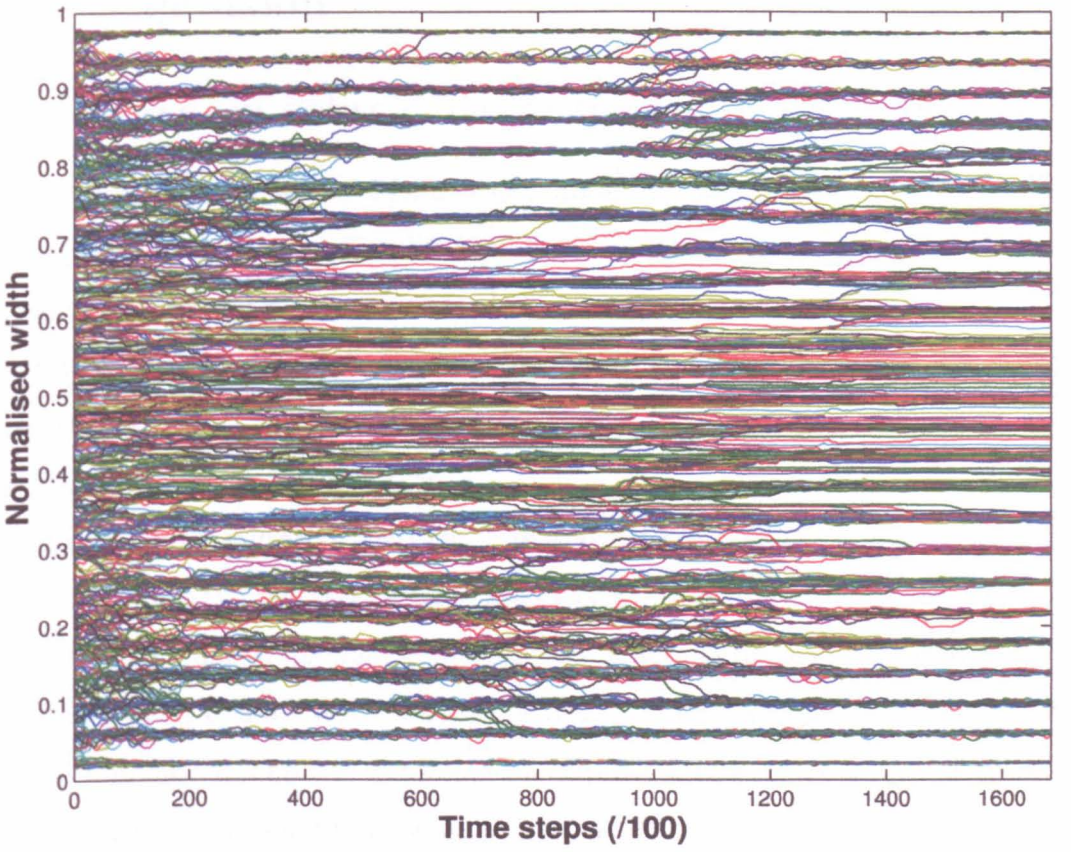

Figure 5.12: 'Path' of each droplet showing alinement at steady state. Initial transversal migration is clearly visible.

and reach a steady configuration and (ii) the velocity profile gets blunted decreasing the transversal shear between chains.

Figure 5.12 also shows that the particles along the walls align first (compared to those in the bulk). This can be understood on the hypothesis that the rate of alignment depends on the local shear rate. A higher local shear rate (like that on the sides) drives a faster rearrangement through transverse migration.

Similarly, Rennie [166] observed (experimentally) that 'low shear rates tend to increase the order and align domains in a single direction'. He also observed sliding structure in oscillatory shear [34].

5.6 Conclusion

5.6.1 *Meso-* in between *macro* and *micro*

We have demonstrated a model for a large number of non–coalescing, non–evaporating, mutually immiscible incompressible liquid drops. The model supports a large range of parameterisation e.g. supernate to drop viscosity ratio and surface tensions, and is able to recover correct bulk 'macroscopic' flows from the particular set of microscopic rules in use. This observation is particularly relevant as a vindication of our representation of lubrication forces.

So the expected qualitative features, apparent in the results in figures 3a and 3b tend to vindicate the method we have used to represent lubrication forces: the qualitatively correct nature of the variation in the macroscopic suspension flow profiles in depicted in figures 5.2 and 5.4 emerges from the microscopic rules implemented. In particular our method of enforcing an explicit layer of supernate at drop and boundary surfaces seems to be valid, at least at volume fraction $\phi = 0.6$

Where particle deformation is high one might expect large contacts between drops at high volume fraction. Accordingly, the representation of sub–lattice lubrication forces in the algorithm is one point at which further work needs to be undertaken.

5.6.2 Omitting the third dimension

The validity of the comparison of the relative behaviour of a three dimensional experiment with two dimensional numerical simulation can obviously be argued. However, it is the author's belief that the tests carried out in this chapter are very promising and do validate the qualitative accuracy of the hydrodynamic interactions of the N non-coalescing droplets of our model. More detailed validation is clearly needed to quantify the exact deformation of the droplets in suspension.

It is interesting to note that the degree of alignment of the particles in our two dimensional LB simulation was much higher than the one observed experimentally in three dimensions. The particles in two dimensions do not have to 'choose' between only two sides of a blocking particle, the third dimension provides an increased freedom. This is probably the reason why margination (transverse migration of

the cells towards the middle of the channel leaving a cell free layer next to the wall) of leukocytes (modeled as less deformable droplets with lower viscosity than the RBC's) has never been observed so far with our two dimensional model. In future, we propose to develop the model in 3D, in which case margination should be recovered.

Conclusion

An incompressible liquid drop is characterised by two parameters. Provided the degree and rate of deformation available to our 'drop' blood cells are comparable with that exhibited by actual cells under equivalent conditions (and our observations show that they are) the basic premise of the model, both microscopically and in terms of the properties of the overall effective liquid (suspension) are, we believe, sound.

Goldsmith commented on the role of ghost cells as models of erythrocytes and concluded that at high concentration, suspensions of reconstituted ghosts provide a good physical model for blood, which confirmed that exact cell's representation is less and less important as the scale gets bigger [72].

We must sound a cautionary note. The correct ratio of the viscosity of real RBC's and the viscosity of plasma (1000) could not be reached due to stability issues. However, it is the author's belief that this underestimated viscosity of the particles in suspension had no major impact on the velocity profiles and dependance of the flow upon the different parameters. It is important to note that such a viscosity ratio will not be trivial to achieve alongside the required and important forcing on the simulation (surface tension). This will be an important issue when considering the feasibility of studying leukocyte rolling with the N-component model.

Figure 5.3 showed that 'solid particle' behaviour of a suspension could not be obtained with the λ method, due to instability and micro-currents issues. The subsequent (and very recent) development of the Lishchuk method in N-component model should permit one to reach more rigid droplets' behaviour. To the author's mind, solid particle behaviour would not be reached unless further reduction of the micro-currents is achieved. There would be no point in studying solid particles mod-

eled as very rigid droplets with the N-component model since the main advantage of the model would be erased, and the programme would also be more expensive compared to using a Ladd type approach to simulate solid colloids in suspension. Rather, what one should aim at from the present work is a model which allows from a range of deformability in the drop/particle available to the method.

Chapter 6

Microfluidic and other applications

Introduction

The last chapter of this thesis assesses the possible application of our N-component LB models (enhanced binary or N-component) to microfluidics. Through this last chapter, we will see that this regime is computationally a problem for most numerical methods but that, with some further improvements, our model can be applied successfully and more importantly, efficiently to this regime. This consists of the fourth set of original results in this thesis, it will be submitted to publication shortly.

6.1 Micro-fluidic simulation case study

6.1.1 What did you say again? Micro-fluidic?

The renowned GNU online encyclopedia *Wikipedia* (http://en.wikipedia.org) defines microfluidics as '*a multidisciplinary field comprising physics, chemistry, engineering and biotechnology that studies the behavior of fluids at the microscale and mesoscale, that is, fluids at volumes thousands of times smaller than a common droplet. It also concerns the design of systems in which such small volumes of fluids will be used.*'. In other words, it refers to any flow configuration where the Reynolds number is less than unity and if there is a fluid interface, the capillarity (or Taylor) number is even smaller. Example of the technology includes inkjet printers, blood-cell-separation equipment, biochemical assays, chemical synthesis, genetic analysis.

Not surprisingly, the medical industry has shown keen interest in microfluidics' technology (from `http://www.whatis.com`).

6.1.2 A computational challenge

The microfluidics regime is acknowledged in the current literature as a computational *hard – to – get*. Reynardy *et al.* for example mentioned the difficulty of this regime when describing the VOF method in [165]: '*As in any numerical method (...) it [the VOF method] has its weaknesses, namely, for flows in which the capillary force is the dominant physical mechanism*'.

Our model, as we will see in this chapter, is not excluded from the rule, although we believe, it represents the best hope. The Gunstensen algorithm provides good starting point for the microfluidics applications and great advantages compared to other methods: very sharp interfaces, possible viscosity contrast and nodal locality (enabling differences in local hydrodynamical parameters).

6.2 Case study: 'Flow-focusing' configuration

We chose to apply our model to the 'Flow-focusing' configuration. It consists of focusing a flow (generally a binary filet) through an aperture, in the aim of obtaining very mono-dispersed droplets downstream of the aperture (see [3] for example). This technique is relatively recent (less than five years old) and is the subject of significant research efforts (see for example [64], [157], [3]).

6.2.1 Configuration

We chose to compare our model with the configuration described by Anna *et al.* in [3]. The configuration is depicted in figure 6.1.

Experimental configuration

Figure 6.1 shows the schematic flow-focusing configuration with parameters (in mm, Kg, s): $\nu^W = 10^{-6}$, $\rho^W = 10^{-6}$, $U^W = 1.25$, $\nu^O = 6 \times 10^{-6}$, $\rho^O = 10^{-6}$, $U^O = 1.67$, $\gamma^{OW} = 5 \times 10^{-3}$ (where 'O' denotes 'Oil' and 'W' water).

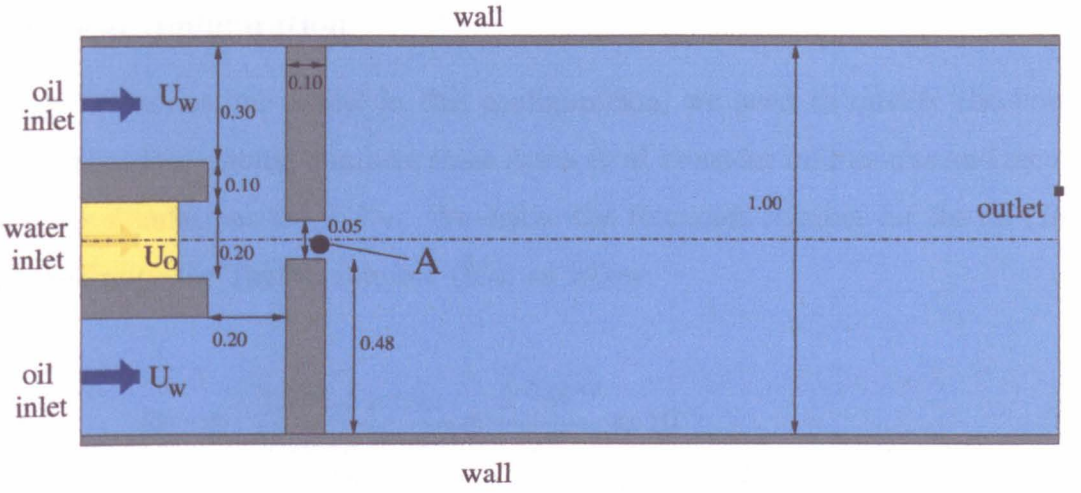

Figure 6.1: Schematic representation of the flow-focusing configuration. The lengths are in millimetres.

Keeping matters simple, the flow-focusing configuration can be understood as follows: distilled water flows into the middle channel and silicone oil (of viscosity 6 times higher than the water's) flows into the two outside channels, the two liquid phases are then forced to flow through a small orifice that is located downstream of the three channels. The outer fluid exerts pressure and viscous stresses that force the inner fluid into a narrow thread, which then breaks inside or downstream of the orifice. Water drops form in a continuous phase of oil (from [3]).

It is important to note that span 80 surfactant (Sorbitan monooleate, Aldrich) is dissolved in the oil phase at 0.67 wt % ([3]). We return to this point.

Figure 6.2 shows the time evolution of the experimental flow focussing configuration by Anna *et al.* [3].

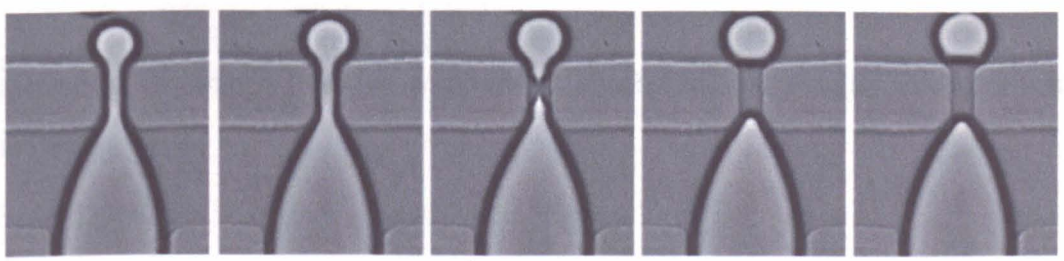

Figure 6.2: Experimental pictures of flow breakup sequences occurring inside the flow-focusing orifice (from Anna et al. *[3])*

Numerical configuration

In order to assess our model in this configuration, we need to qualify the flow in term of non-dimensional numbers since Anna *et al.* consider millimetres and seconds while our simulations are in l.u.. We define the Reynolds number for the oil (Re^O) and capillarity (or Taylor) number (Ca) as follow:

$$Re \equiv \frac{\text{Inertia forces}}{\text{Viscous forces}} \equiv \frac{U^O W^O}{\nu^O} \approx 10^{-1} \tag{6.1}$$

$$Ca \equiv \frac{\text{Viscous forces}}{\text{Surface tension forces}} \equiv \frac{\mu_O \, |U_O - U_{water}|}{\Sigma^{OW}} \approx 10^{-4} \tag{6.2}$$

We define that the aperture (see figure 6.1) should be approximately 10 lattice nodes wide to obtain sufficient. Given the lattice length for the aperture, the rest of the solid boundaries of the simulation can be determined. Next, setting the hydrodynamic parameters for one fluid sets the hydrodynamical parameters of the other fluid ($\nu^O = 6\,\nu^W$, and $U_O = 1.33\,U_W$). We therefore have two equations (Re, Ca) with three unknowns (U_O, Σ^{OW}, μ_O):

$$\begin{cases} \frac{U_O W^O}{\nu^O} = 0.25\,, \\ \frac{\mu_O \, 0.33\, U_O}{\Sigma^{OW}} = 0.8 \times 10^{-5}\,, \end{cases}$$

which leaves a free parameter. We also have the following stability and low micro-currents condition:

$$\begin{cases} \sigma^{OW} < 0.05\,, \\ 0.1 < \omega < 0.9\,. \end{cases}$$

Representative sets of possible parameters are listed below with the appropriate comments.

ω_O (lu)	U_O (lu)	σ^{OW} (lu)	Δt (hrs)	Remarks
0.1	0.0099	14.4	4.80	σ^{OW} too big
0.2	0.0029	3.7	16.1	σ^{OW} too big
0.5	0.0015	1.8	30.5	σ^{OW} too big
0.7	8×10^{-4}	0.96	49.2	σ^{OW} too big
0.9	6×10^{-4}	0.53	74.8	σ^{OW} and Δt too big
1.1	4×10^{-4}	0.30	111	σ^{OW} and Δt too big
1.3	2×10^{-4}	0.15	170	σ^{OW} and Δt too big
1.5	1×10^{-4}	0.06	274	σ^{OW} and Δt too big
1.7	9×10^{-5}	0.02	518	Δt too big
1.82	5×10^{-5}	0.007	924	Δt too big
1.9	2×10^{-5}	0.002	1737	Δt too big
1.95	1×10^{-5}	5×10^{-4}	3565	Δt too big
1.99	2×10^{-6}	2×10^{-5}	18194	Δt too big

Here ω_O is the BGK relaxation parameter of the oil in our LB simulation defining the viscosity of the fluid, U_O is the inlet velocity, σ^{OW} is the surface tension parameter of the oil/water interface and Δt is the estimated time for a 'particle' to cross the channel (from the inlet to the outlet) with our Standard PC Computational Capabilities (SPC3 hereafter, see appendix under SPC3 for more details). We restricted Δt to two days maximum.

It is immediate from this table that no set of parameters allows a stable simulation in a short execution time (it should be mentioned that we did run a stable simulation for more than a week but observed very high micro-currents, overwhelming the hydrodynamical flow). We therefore identified the surface tension as the major obstacle to address this regime, and we had to find other alternatives to allow us to impose surface tension in our model, reducing μ_a and increasing the stability of the model at high surface tension.

6.3 Necessary modifications

6.3.1 The Lishchuk's method

In 2003, Lishchuk *et al.* [127] developed a method to impose surface tension in a Gunstensen the fluid interface, and unexpectedly, found that their method had enhanced stability and greatly reduced micro-current activity μ_a (see equation 3.2) by a factor 40 compared to the standard Gunstensen model [127], corresponding to a factor 5 to the λ method. This was therefore the way forward but a non-locality property in the calculation of the curvature had been a major drawback in this application (recall that, contrary to the Lishchuk method, the λ method remains local to a node).

6.3.2 Further improvements to Lishchuk's method

We implemented the Lishchuk method, as published in [127], to a binary fluid configuration, first to assess the capability of the method. Thanks to the enhanced robustness of the Lishchuk method, the simulations were stable at the targeted 'micro-fluidic' Re and Ca, but the micro-currents were still significant. The remainder of this section describes some improvements to the binary fluid Lishchuk method, designed to address this issue.

We used the same enhancement of the colour-field definition and recolouring step as the one described for the λ method (see chapter 3). Both corrections have important effects on the Lishchuk method since colour gradients are an essential reference in the technique through the calculation of the curvature (equation 2.8).

Redefinition of the colour-field next to solid, no slip walls

Implemented as published by Lishchuk *et al.* [127], the calculated curvature and normal direction to the interface are wrong at nodes adjacent to any wall. This generates additional micro-currents up to two sites away from any wall. Recall that the curvature is defined in terms of spatial gradients of the colourfield, which is itself defined as a spatial gradient of the ρ^N function.

The simple modification described in chapter 3, section 3.3 (used for the λ method)

reduced μ_a by a factor 6 when using the Lishchuk method on drops approaching solid boundary.

Redefinition of the recolouring order

Recall that the recolouring step of the original Gunstensen model has to be corrected when the interface lies along lattice links (see section 3.3). The wrong recolouring step has a significant effect on the colour gradients and hence the surface tension step with Lishchuk algorithm (through the calculation of curvature K, identical arguments as previously in chapter 3). It ultimately results in additional micro-currents, since this error is always in the the same direction (still identical argument than in chapter 3 with the λ method, see chapter 3). We found that refining the re-colouring step reduced μ_a by a further factor 4 when using the Lishchuk method.

Time averaging of the velocities

By reducing the micro-currents significantly relative to the Lishchuk method a checker board pattern appeared and dominated the undisturbed flow (similarly when we reduced μ_a in the λ method). See figure 6.3. The simulation parameters for this data were 100×100 nodes, $\omega^S = \omega^D = 1.7$, $\sigma^{SD} = 0.01$ and the steady state was typically after 5×10^5 time steps.

In order to reduce the micro-current further, we found that a simple time average over two time step of the calculated nodal velocities used in the collide step is enough to smear out this checker board pattern, by taking a short time average:

$$\overline{\mathbf{v}} = \frac{\mathbf{v}(\mathbf{x}, t-1) + \mathbf{v}(\mathbf{x}, t)}{2}$$

where $\mathbf{v}$ is the hydrodynamical velocity calculated by equation 1.38 and $\overline{\mathbf{v}}$ is the averaged velocity used for the calculation of the Boltzmann equilibrium function (see equation 1.37). It is important to note that this averaging of velocity does not invalidate the hydrodynamics: $\overline{\mathbf{v}}$ remains a solution of the NSE.

Figure 6.4 shows the velocity field of a drop with the Lishchuk method with averaged velocities and both corrections. The simulation parameters and the scale of the vector plot were the same as those of figure 6.3.

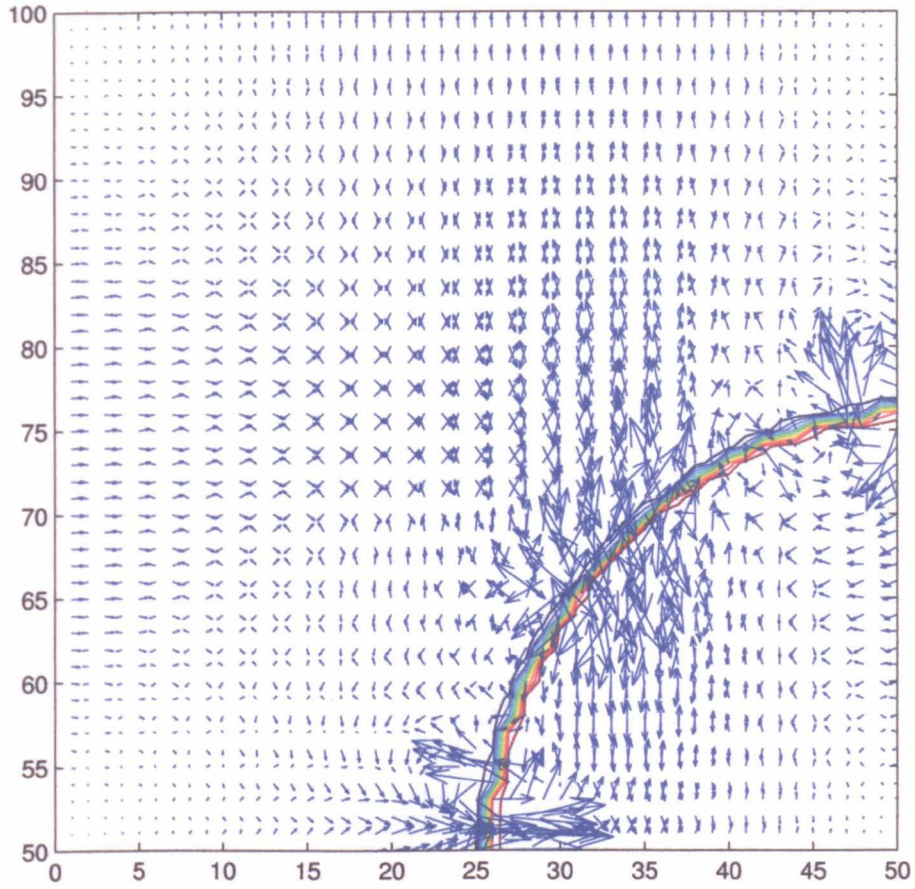

Figure 6.3: Checker board pattern of the velocity field with the enhanced Lishchuk method. It should be noted these velocities are much smaller than with the original Lishchuk method.

Using the time average of the nodal velocities reduces μ_a by a factor 18 and reduced the bulk micro-currents in proximity of the drop by, typically, a factor 30. It also concentrates the micro-currents near to the interface.

It is interesting to note that this checker board pattern exhibits some asymmetry ('jets' of velocity shown in figure 6.5(a)) but has no significant effect on the overall dynamics since (i) the droplet's centre of gravity does not vary more than $10-5\%$ and (ii) it smears out between two time steps (as figure 6.5(b) shows).

It should also be noted that this time averaging is valid as long as the hydrodynamic velocities do not vary significantly in time, or in other words, $(\mathbf{v}(\mathbf{x},t)-\mathbf{v}(\mathbf{x},t-1) << 1)$. This is obviously the case in microfluidics and capillary flow applications.

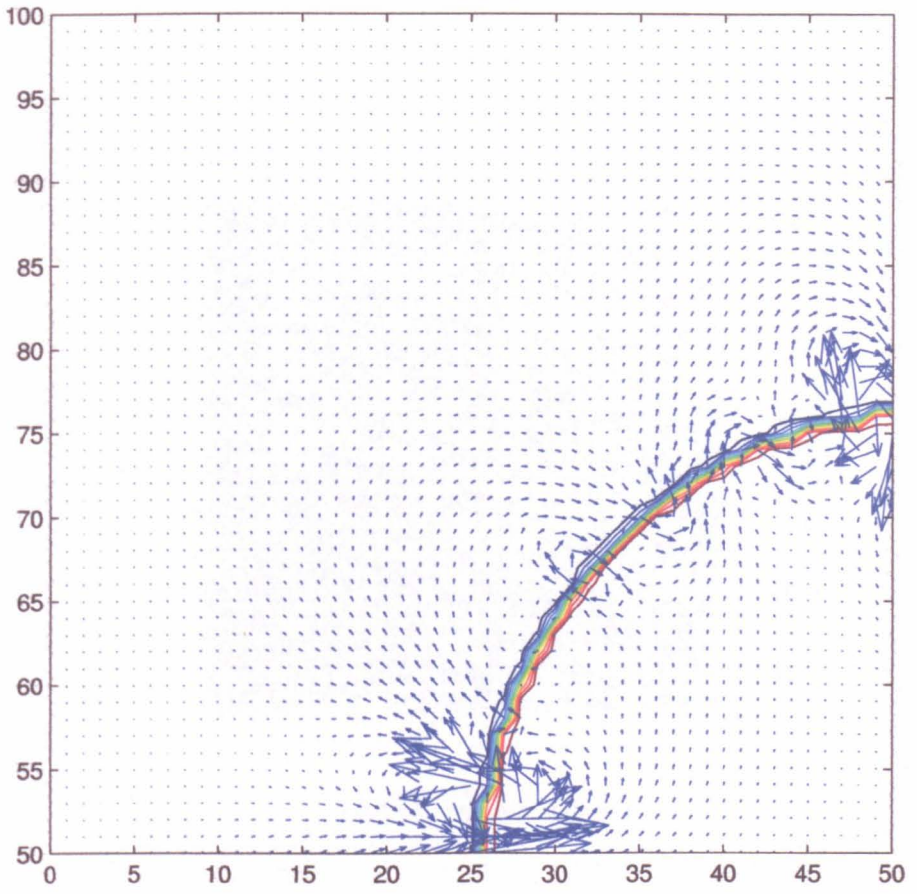

Figure 6.4: Smear out of the checker board pattern with a simple velocity time average over two time steps. The scale of the vector plot is the same that of figure 6.3.

Wall-wetting behaviour with the Lishchuk method

Similarly to the λ method, wall wetting behaviour had not been implemented with the Lishchuk method and needed, therefore, to be accomplished for our micro-fluidic and blood flow applications. The implementation of wall-wetting with the Lishchuk method follows the same approach as previously with the λ method: the Lishchuk method imposes surface tension by means of a body-force acting towards the interior of the droplet. We therefore impose wetting affinities by a body-force acting in the direction towards the inside or outside of the droplet (depending on the required wetting or drying property), directed *parallel* to the walls:

$$\Delta f_i = t_i \, \partial_\alpha(\rho^N) c_{i\alpha} \, \sigma_{wall} \, ,$$

where $\rho^N = (\rho^D - \rho^S)/\rho$ and whose gradient determines the direction of the forcing (definition of the colour-field), σ_{wall} is the wall-wetting parameter of the drop's

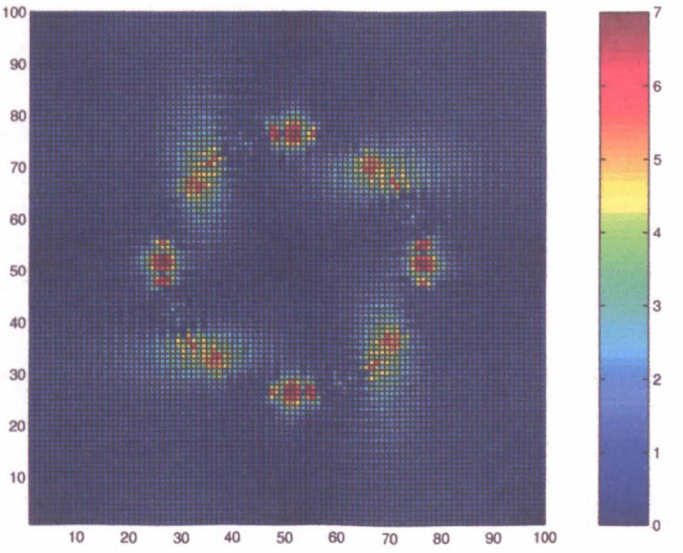

(a) Original Lishchuk method

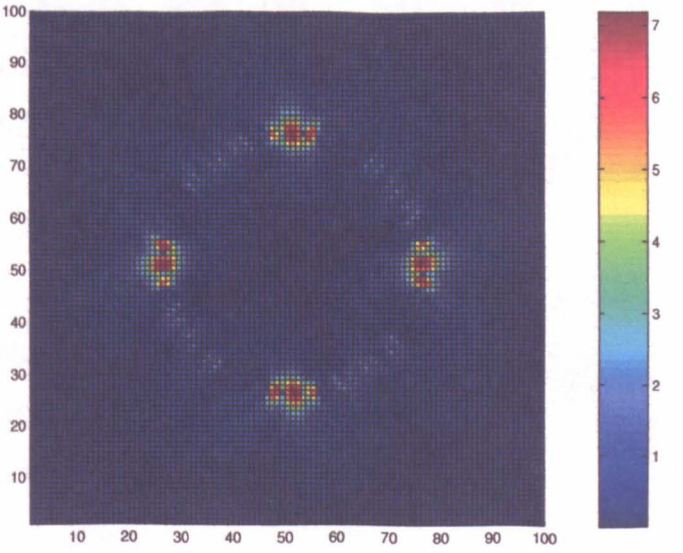

(b) Velocity averaged and corrections

Figure 6.5: Effect of the velocity average on the velocity flow. The colour represents $|\mathbf{u}(\mathbf{x})|$ *corresponding to the vector plot of figure 6.3 and 6.4. Note that the asymmetry in (a) is smeared out by the short-time averaging.*

fluid against the surrounding fluid (note that here, again, the droplet's fluid is the fluid of reference). A positive(negative) value to the wall-wetting parameter gives a wetting(drying) behaviour to the fluid.

6.3.3 Proof of concept, microfluidics simulated successfully

Flow focussing configuration

As mentioned previously, the aim of this chapter is to simulate the flow-focusing configuration. This objective required few improvements to the existing model. We reduced μ_a for the Lishchuk method by, typically, a factor 40 and 80 when an interface is in contact to a wall. Figure 6.6 shows the time evolution of a simulation addressing the flow-focusing configuration of Anna *et al.* [3].

The simulation parameters for this data were 100×40 nodes, $\omega^O = 0.1$, $\omega^W = 0.7$, $\sigma^{OW} = 0.1$, $U_O = 0.002$, $U_W = 0.004$ (in l.u.). The time interval between images is 1000 time steps. This sequence required approximately 20 minutes on our SPC3.

Note that the simulation of figure 6.6 was a test of capabilty of our enhanced binary N-component model, rather than an attempt for a one-to-one comparison of the flow-focusing configuration of Anna *et al.*, since the latter used surfactant to interrupt the coalescence of the droplets downstream of the aperture (the droplets in Anna *et al.* 'jam' downstream the of aperture) and that our binary model cannot model more than two different fluids. It should also be noted that the parameters we used were slightly different from those of Anna *et al.*. Our set of parameters were purposely pushing the simulation more to assess the model's robustness (see below).

This simulation was half the length and width of the targeted simulation of Anna *et al.* [3], the surface tension was purposely chosen to be larger (recall that the stability of the model decreases with increasing surface tension), leading to proportionally bigger droplets. The wetting property was tuned down so that the droplets wet the aperture to assess the wetting property of the model. We also altered the ratio of the water/oil flow rate to give well separated droplets since this model (so far), does not allow the definition of more than two fluids.

This simulation, despite not being a one-to-one comparison with the experimental set-up, does demonstrate that our binary model can address the flow focussing

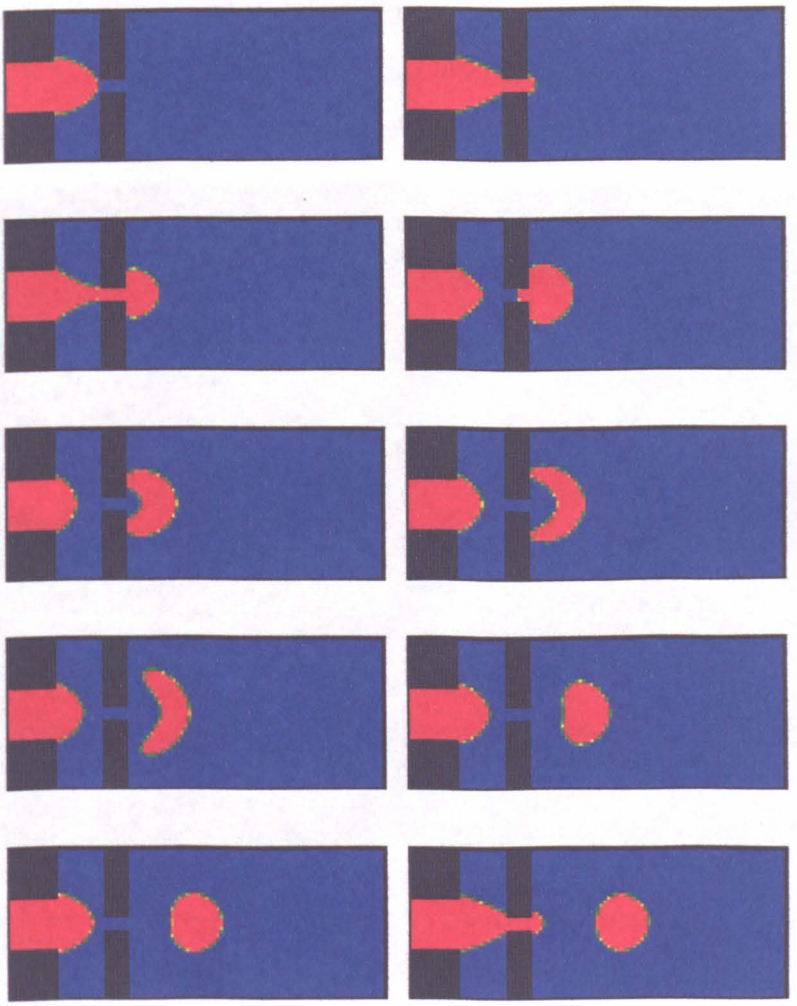

Figure 6.6: Proof of capability of the improved Lishchuk method, seen now to be able to tackle microfluidics applications efficiently. This sequence required only 20 minutes on our SPC3.

configuration successfully.

Mono-dispersed micro-droplets device

To serve as further validation of the applicability of our binary model to the microfluidics regime, we applied our model to a binary fluid microfluidics configuration, found on the website of D. Weitz's laboratory from the division of Engineering and Applied Sciences at Harvard University ([212]). Figure 6.7 shows schematically this configuration. It is similar to the flow-focusing configuration of Anna *et al.* but has the advantage for our binary model better to separate the droplets downstream.

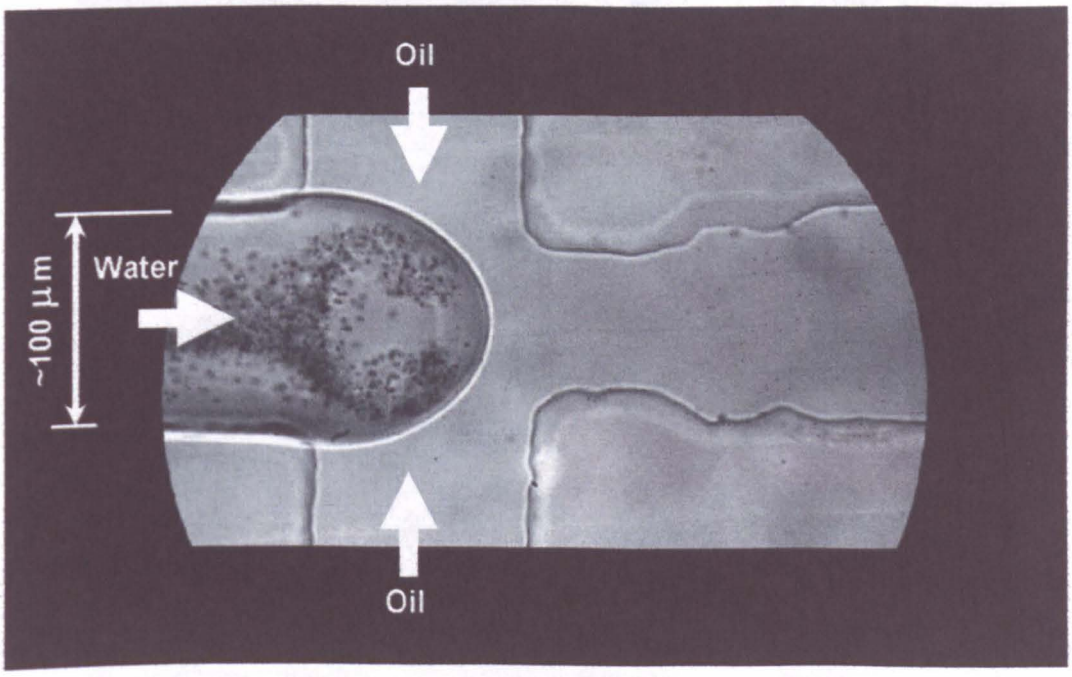

Figure 6.7: Schematic representation of the D. Weitz's configuration. Image taken from [212]

It should be noted that a lack of explicit parameters for this configuration did not allow the author to match confidently the parameters 'one-to-one'. However, through trial and error and with similar parameters as the previous flow-focusing configuration, we obtained very convincing one-to-one comparison, as figure 6.8 shows. The simulation parameters for this data were 150×100 nodes, $\omega^O = 0.1$, $\omega^W = 0.7$, $\sigma^{OW} = 0.1$, $U_O = 0.002$, $U_W = 0.005$. The time interval between images is 1000 time steps. This sequence required approximately 20 minutes on our SPC3. We also obtained the two vortices obtained experimentally by D. Weitz's group

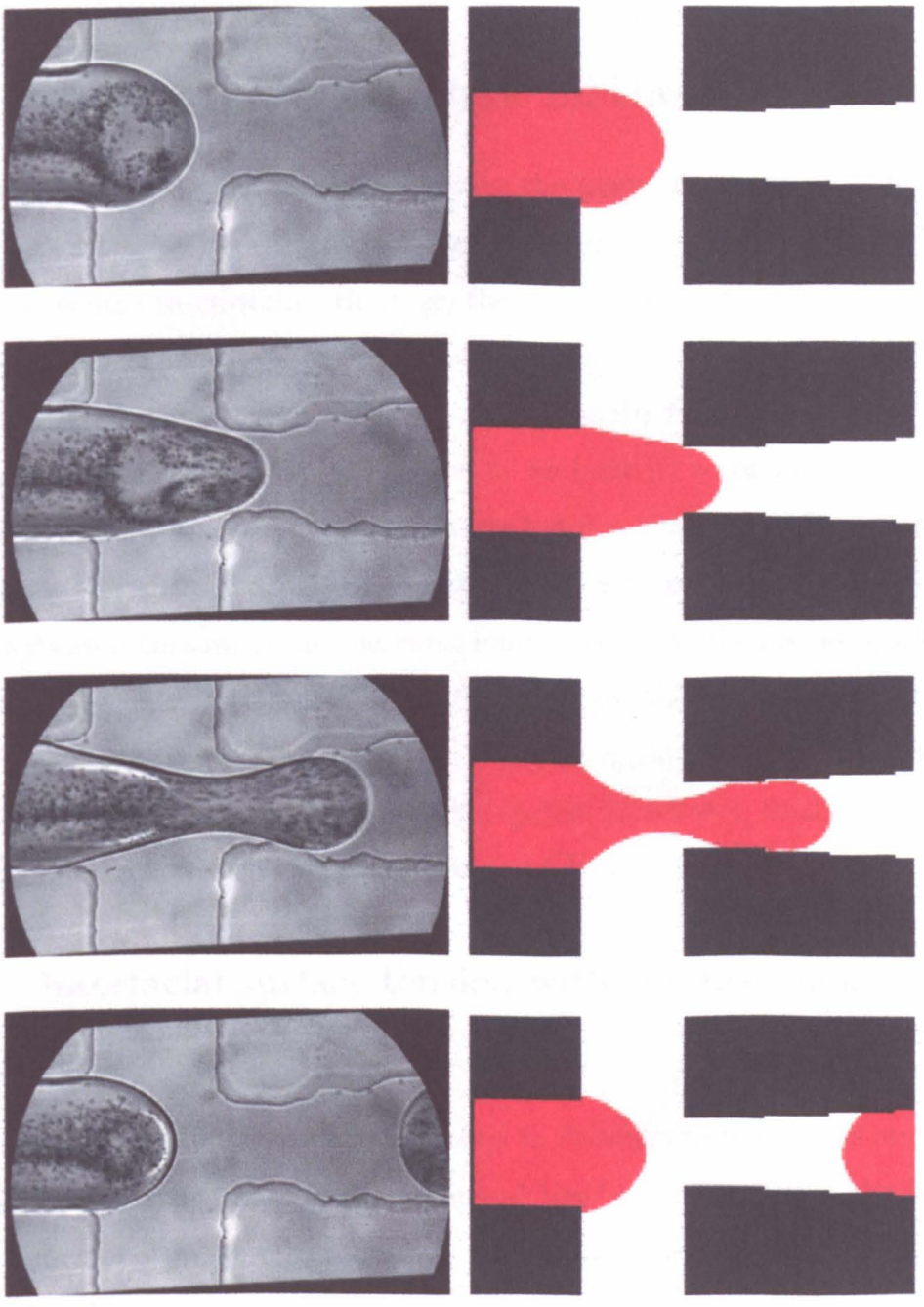

(g) Experimental picture *(h)* Numerical simulation

Figure 6.8: Further proof of capability of the improved Lishchuk method against another microfluidics device: one of the Weitz's lab's configuration.

[212] (visualised by colloidal tracers), as figure 6.9 shows. This simulation further validated the capability and correct hydrodynamics of our binary model in the microfluidics regime.

6.4 N-component Lishchuk method

We saw in previous sections how to improve the Lishchuk method for the binary model and that these improvements made the technique capable of simulating microfluidics devices successfully. However, the full results of Anna *et al.* [3] require non coalescence of the droplets downstream of the aperture (as mentioned previously, they reported the use of surfactant to limit coalescence). See figure 6.10.
It is important to realise that, at this point, we have (i) a complicated, local, N-component model with reduced micro-currents but it is unable to tackle microfluidics applications efficiently and (ii) the improved Lishchuk method (a different model, also complicated because of the numerous improvements to the method), which, on the other hand, is able to tackle efficiently the microfluidics regime but is unable to avoid coalescence between droplets. The remainder of this chapter explains, therefore, how to merge these two models together to achieve, finally, the realistic simulation of the flow focussing configuration of Anna *et al.*.

6.4.1 Interfacial surface tension with the Lishchuk method

New concepts

The implementation of the Lishchuk method in N-component is not as straightforward as the implementation of the λ method has been. Recall that the Lishchuk method imposes a pressure step through the interface by the mean of a body force applied as follows:

$$\triangle f_i = \sigma \, t_i \, K \, c_{i\alpha} \, \partial_\alpha (\frac{\rho^r - \rho^b}{2\,\rho}).$$

The main idea of this method is, therefore, to apply a body force on the interface, pointing *from* the surrounding fluid *to* the inside of the droplet. In the binary case, defining a fluid as the droplet's fluid set by default the surrounding fluid (the other fluid). However, in the N-component model, the very concept of a binary interface

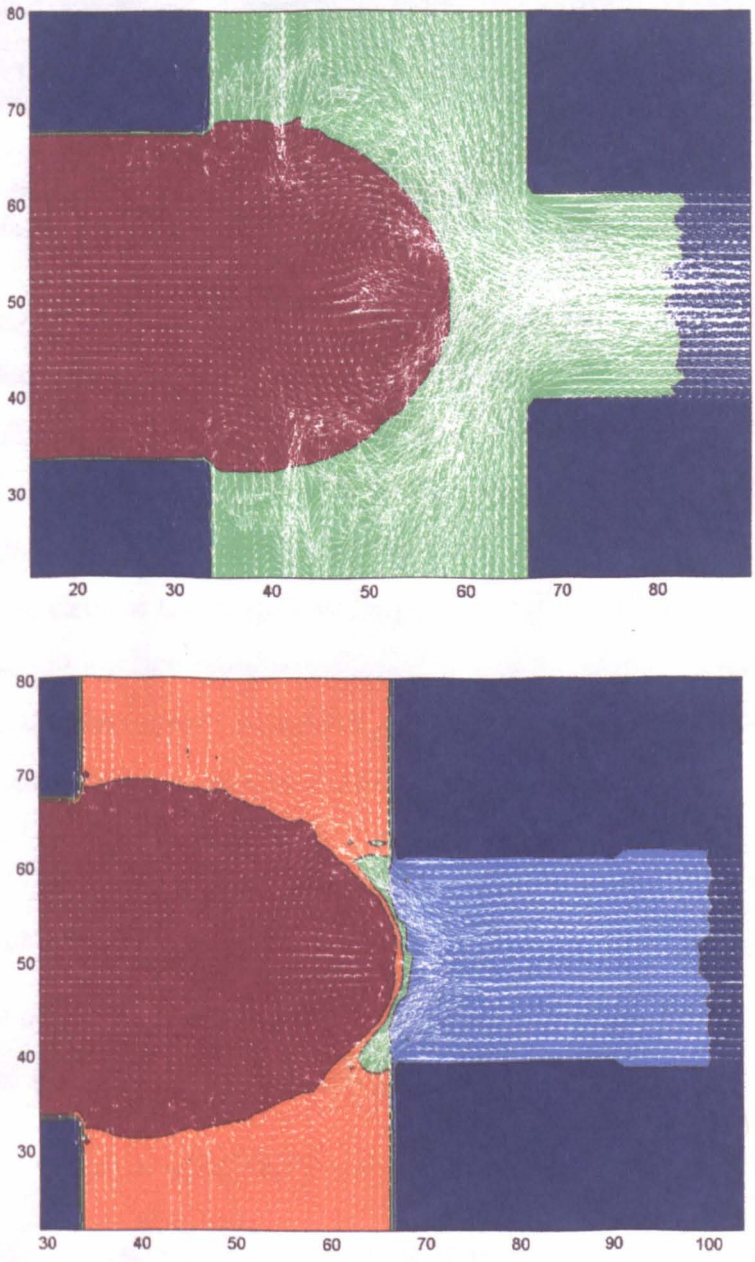

Figure 6.9: Qualitatively identical pair of recirculations as those obtained experimentally.

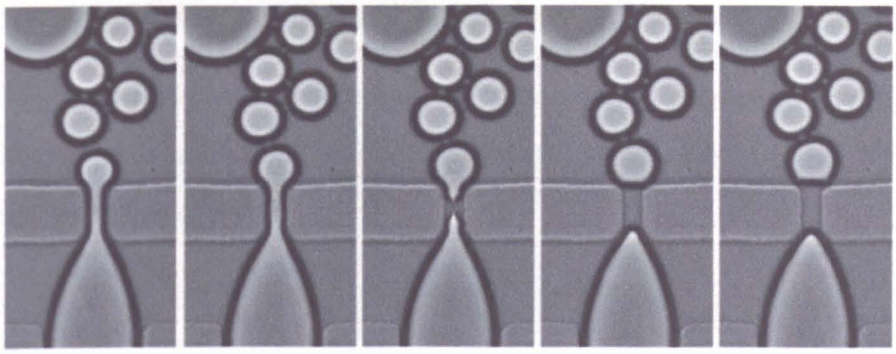

Figure 6.10: Experimental images from Anna et al. *[3] showing non-coalescence of droplets downstream of the aperture of the flow-focusing configuration.*

has to be generalised, not to apply between two fluids (as previously), but to apply between droplet's fluid α and *any other fluid* (written as $\overline{\alpha}$). Consequently, in this method we will refer to the interface of fluid α rather than the interface $\alpha\beta$ (note that α can denote any droplet as well as the surrounding fluid). It follows that the binary Lishchuk method contains in fact *two* interfaces: the interface of the red fluid and the interface of the blue fluid (happening to lie on the same position at all time), and only *one* surface tension is applied to this interface, the surrounding fluid has no surface tension (since, by definition, a supernate in a suspension of droplets fills the voids and does not tend to form a large bubble).

Calculation of the curvature

First of all, we generalise the definition of the local curvature $K(\mathbf{x})$ to the curvature of the interface of fluid α, in two dimensions:

$$K^{\alpha}(\mathbf{x}) = n_x^{\alpha}\, n_y^{\alpha}(\partial_x n_y^{\alpha} + \partial_y n_x^{\alpha}) - n_x^{\alpha 2}\partial_x n_x^{\alpha} - n_x^{\alpha 2}\partial_y n_y^{\alpha}$$

where n_x^{α} and n_y^{α} are the x and y component of the interface normal of the interface of fluid α (of the fluid α). There is still not a valid argument why this interface normal (n_{β}^{α}) could not be represented again by the colour-field (P_{β}^{α}), defined as a vector pointing towards the fluid α's interior, normal to its surface (interface $\alpha\overline{\alpha}$):

$$P_{\beta}^{\alpha}(\mathbf{x}) = \sum_i (\rho^{\alpha}(\mathbf{x} + \mathbf{c_i}) - \rho^{\overline{\alpha}}(\mathbf{x} + \mathbf{c_i}))\, c_{i\beta}\,.$$

Surface tension vector

We generalise the Lishchuk surface tension parameter σ to a column vector surface tension, with N_D elements for the N_D droplets of the simulation (where $N{=}N_D{+}1$, 1 for the surrounding fluid):

$$\sigma^{\alpha} = [\Gamma^1; \Gamma^2; \Gamma^3; ...; \Gamma^{N_D}]^T$$

A great difference with the λ method has to be noted here: the λ method surface tension $N \times N$ matrix is now a column vector of the N_D. This originates from the required assumption that the Lishchuk method considers fluids as entities rather than interfaces as figure 6.11 shows.

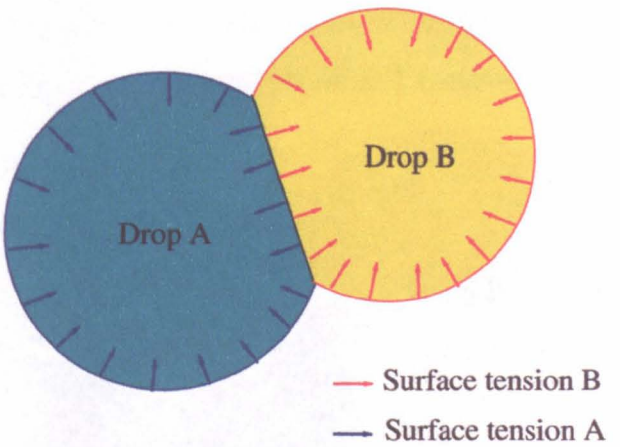

Figure 6.11: Schematic representation of the Lishchuk surface tension method in N-component. The surface tension parameter is the same over the whole fluid's interface, irrespectively of the particular fluid in contact.

This surface tension column vector is therefore less realistic than the $N \times N$ matrix surface tension in the λ method. This provides an unexpected advantage to the λ method over the Lishchuk method (despite its higher micro-currents). In some configurations, where the explicit surface tension of each couple of fluid in the simulation has to be resolved,the λ method remains the only alternative.

In addition, where the $N \times N$ matrix $(\sigma^{\alpha\beta})$ controls the liquid-wetting in the λ method, additional steps have to be implemented in the Lishchuk method to consider liquid-wetting properties (see next section).

This generalised Lishchuk method provides however identical perturbations as its binary counterpart in identical configurations, and its associated micro-currents'

activity has been measured to be identical to that of the enhanced binary Lishchuk method.

6.4.2 wettings method in the Lishchuk method

Lishchuk method liquid-wetting

As mentioned previously, the liquid surface tension cannot be impressed by the surface tension matrix σ^{α} providing droplet α with a range of surface tensions. A similar step is added to impose liquid-wetting: applying a body force towards the 'outside' of the surrounding fluid, typically towards the interface of the droplets in contact (see figure 6.12). This encourages the surrounding fluid to migrate between the two droplets and ensure good lubrication of the supernate. It provides the same macroscopical behaviour as the more physical λ method.

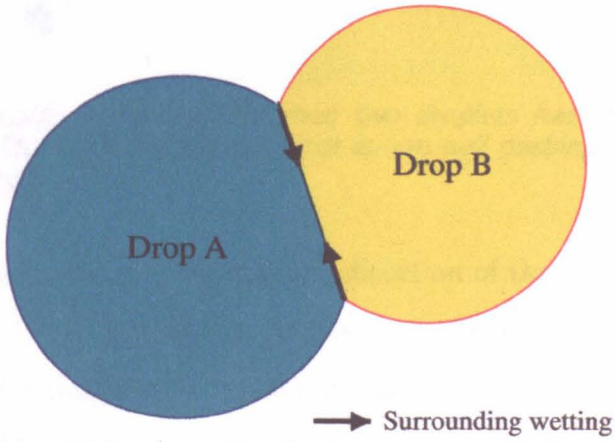

Figure 6.12: Schematic representation of the liquid wetting in the N-component Lishchuk surface tension method. Supernate wetting is impressed by a body-force acting normally to the surrounding fluid's interface, and is therefore less physical than the set of surface tensions $\sigma^{\alpha\beta}$ of the N-component λ method.

We add the following perturbation after the collide step:

$$\triangle f_i = -\sigma^S \, t_i \, \rho^S \, \hat{P}^S_{\alpha} \, c_{i\alpha}$$

where the subscript S denotes the surrounding fluid, σ^s is the surrounding fluid's liquid wetting towards other droplets (corresponding to $\sigma^{S\alpha}$ in the λ method), and $\hat{P}^S_{\alpha}$ is the normalised colour-field vector of the surrounding fluid (giving the direction of the forcing). The minus sign denotes that the surrounding liquid tends to wet

other droplets (biological cell like behaviour).

This method produced very good results for the lubrication of two droplets of similar size but to induce non-physical behaviour for a suspension of highly polydisperse droplets, or when droplets lose their integrity by breaking up. When a smaller droplet comes into contact with a bigger droplet, the very difference of radii of the two droplets induces the colour-field of the surrounding fluid to point towards the bigger droplet, while it should point parallel to the interface of both droplets. See figure 6.13.

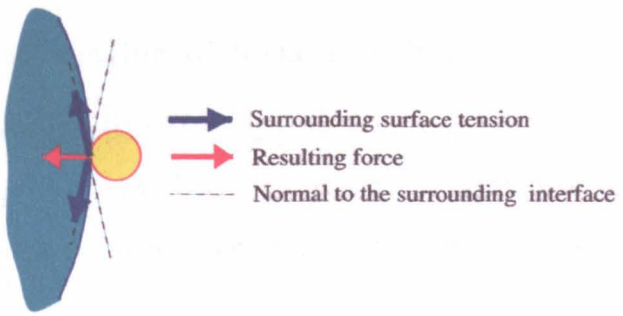

Figure 6.13: Schematic representation when two droplets have significantly different sizes. The resultant normal force is non null pushing the smaller drop into the bigger.

This leads to an unphysical net force in the direction of the bigger droplet from the smaller droplet (by symmetry arguments, the same force is acting on the other side of the small droplet, balancing the net force) and drives the smaller droplet into the bigger one. It should however be noted that this occurs only when the two droplets are of significantly different sizes (typically more than a factor 10 in diameter) and is insignificant for most of the applications of this thesis, which considerers mono-dispersed droplets only (blood flow or microfluidics). An alternative representation will therefore be required if this model is applied to highly polydispersed suspension.

Spontaneous liquid-wetting behaviour of the Lishchuk method

In this test, two rectangular 'droplets', initialised in contact, have identical surface tensions ($\gamma^{D_1} = \gamma^{D_2}$), and the surface tension of the surrounding fluid is set to be zero ($\gamma^S = 0$). The simulation parameters for this data were 200×100 nodes, $\omega^S = \omega^D = 1.7$, $\sigma^{SD} = 0.01$, $\sigma^{DD} = 0$ and the steady state was typically after 10^6 time steps. Figure 6.14 shows the initial and steady state of this test. Note the

significant difference with the spontaneous liquid behaviour of the λ method.
The spontaneous repulsion between two droplets can be understood by imagining that each droplet of the Lishchuk method is a separate entity as far as the surface tension is concerned (unlike with the λ method). Recall that the curvature of the interface of fluid α is calculated as the curvature of the interface of fluid α with any other fluid (other droplet or surrounding fluid). This leads to an important value of the curvature at the diagonals of the initial droplets, until each droplet has an equal curvature throughout its interface.

N-component wall wetting with the Lishchuk method

Recall that the wetting with the binary Lishchuk method is impressed by imposing a body-force acting parallel to the wall, from the drop to the surrounding fluid (the sign of the body-force coefficient sets the wetting/drying behaviour):

$$\triangle f_i = -\sigma_{wall}\, t_i\, \partial_\alpha \rho^N c_{i\alpha}\,, \tag{6.3}$$

where σ_{wall} is the wall wetting parameter. Generalising the wall wetting step to the N-component algorithm is straight forward from equation 6.3, and reads, for fluid β:

$$\triangle f_i = -\sigma^{\beta}_{wall}\, t_i\, \partial_\alpha \rho^{N\beta} c_{i\alpha}\,, \tag{6.4}$$

where $\rho^{N\beta}$ is the generalised ρ^N function defined as:

$$\rho^{N\beta} = \frac{\rho^{\beta} - \rho^{\overline{\beta}}}{2\,\rho}\,,$$

and σ^{β}_{wall} is the generalised wall wetting parameter for the β fluid, against the surrounding fluid.

6.4.3 Conclusion and applications of the different spontaneous liquid-wetting of both surface tension methods

Both methods have shown significantly different spontaneous liquid wetting behaviour. Along with the stability issues discussed in previous chapters, different spontaneous behaviour is actually great advantage for the stability of the simulation. For example, if the simulation of sticky aggregates is required, the λ method

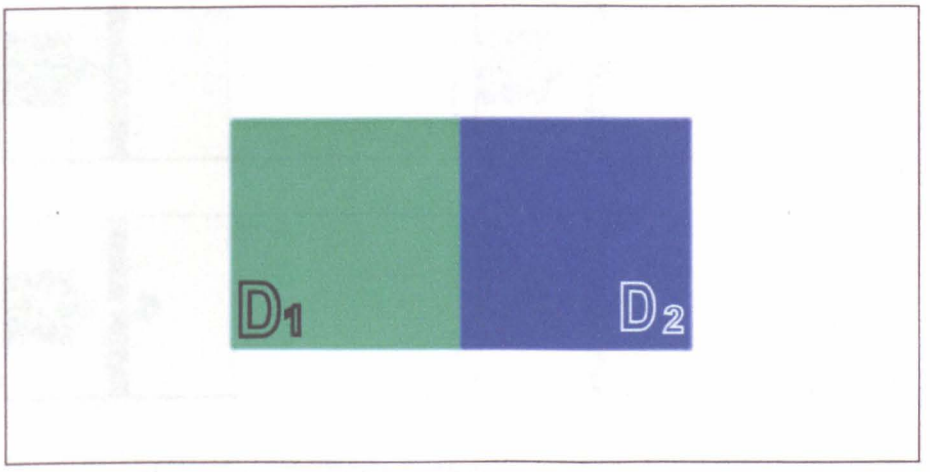

(a) Initial configuration

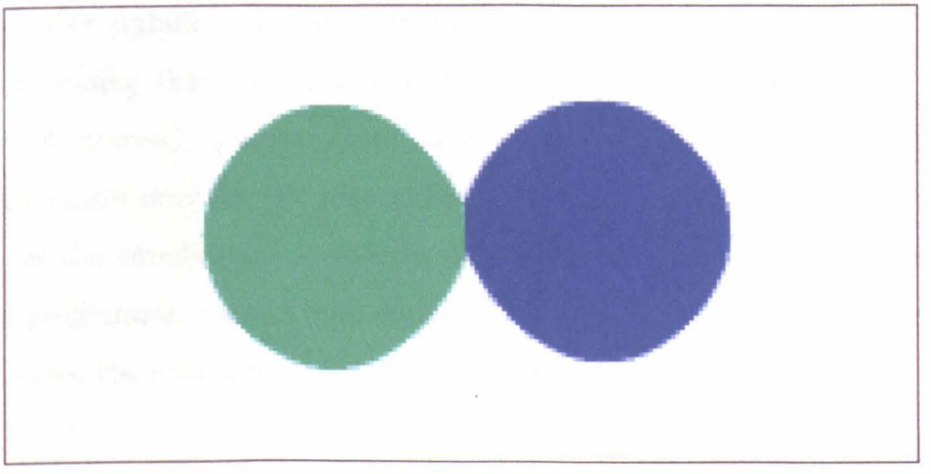

(b) Steady state

Figure 6.14: Spontaneous drying of two droplets in the N-phase Lishchuk method. Note the significant difference with the spontaneous liquid behaviour of the λ method.

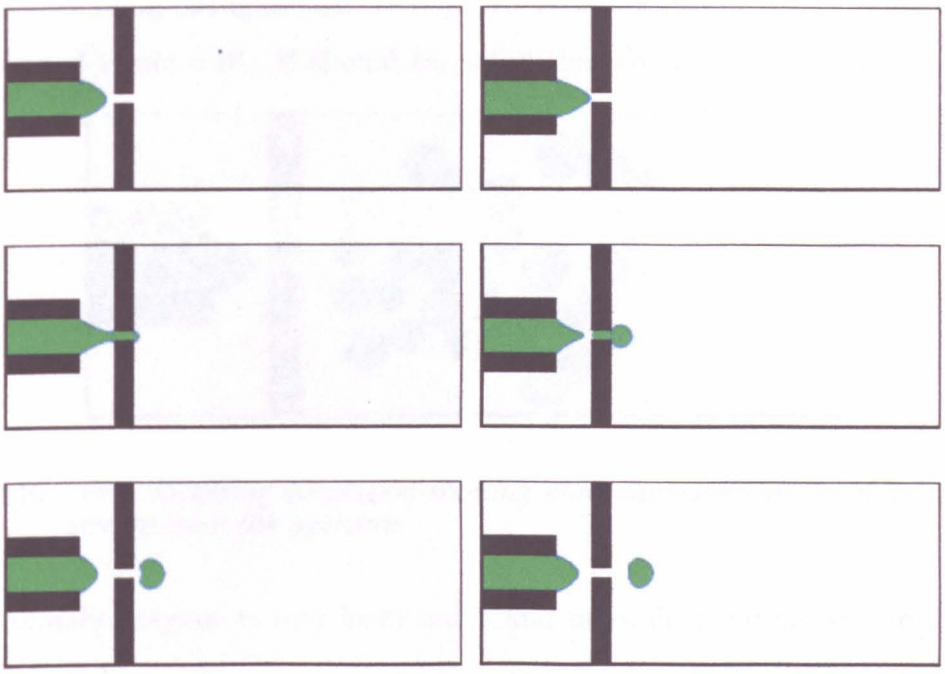

Figure 6.15: Flow-focusing simulation with our novel Lishchuk N-component algorithm. It looks qualitatively at least, very similar to the experimental snapshots by Anna et al. *of figure 6.2.*

provides better stability, since less forcing (if any) has to be impressed on the simulation (providing that the micro-currents do not overcome the flow at the sort of regime of interest). On the other hand, to model vesicles like blood cells, the Lishchuk method provides the required anti-sticking behaviour between the different cells in the simulation. It is even possible to implement both techniques in the same programme, should both spontaneous behaviours be needed for different droplets, since the core algorithms are exactly compatible.

6.4.4 Proof of capability: simulation

Figure 6.15 shows the development of the water flow breaking up in the flow focusing configuration, simulated by our novel enhanced N-component Lishchuk algorithm. The simulation parameters for this data were 250×100 nodes, $\omega^W = 0.1$, $\omega^O = 0.5$, $\sigma^{SD} = 0.1$, the time interval between the images is 500 times steps. This sequence took 30 mins on our SPC3.

Figure 6.16 shows the explicit non-coalescence of the droplets downstream of the aperture, demonstrating that our new model can address, the main specifications

of the flow focusing configuration. It required 10 hours on our SPC3 to acquire the 28 droplets of figure 6.16. It should be noted that the breaking up of droplets in

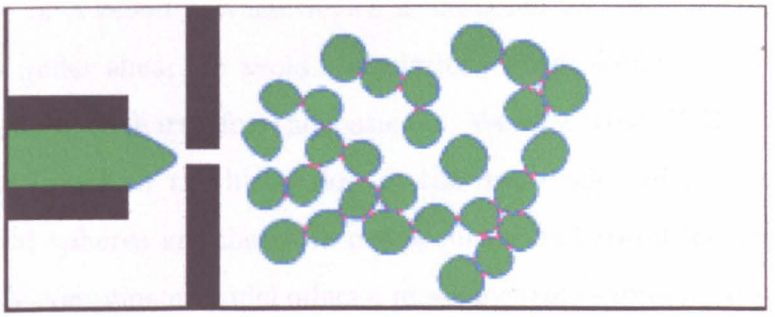

Figure 6.16: Flow-focussing simulation showing non-coalescence of the droplet downstream from the aperture.

the microfluidics regime is very fashionable and more illustrations and studies can be found in [126], [213], [188], [150], [210], [189] (review articles), [187], [204], [54] (droplets in microfluidics devices).

The results in this chapter demonstrate that our model can tackle this configuration and very efficiently, which as far as the author is aware, no other model can. Our model has, therefore, great advantages over most other models and has already been the subject of great interest from other research laboratories and industries.

6.5 Other applications, proofs of concept

This last section shows the application of our N-component model to other configurations than microfluidics related applications, and demonstrates its capabilities for heavily interface-dominated flows.

6.5.1 Rayleigh-Taylor Instability with N-component fluids

There are many medical and scientific developments that have been and are being developed to minimise the amount of blood lost in a particular surgery, and to make best use of a patients own blood. A technique that is being used successfully is called Post-Operative Blood Salvage and Reinfusion. Although in many surgeries the majority of the bleeding happens during the actual surgery, in some types of surgery it continues after the operation has been completed. A recent technology

has been developed that allows this blood to be collected and returned to patients. To express it simply, the blood is cleaned, decontaminated, and usable.
The chamber of a blood salvage device is designed so that the blood it contains is constantly under shear, to avoid coagulation, which could lead to the machine's damage or potential harm for the patient. We saw that RBC's deformation is an important factor for the blood flow at the mesoscale,and simulations modeling RBC's as solid spheres are therefore not accurate and could incorrectly validate a design. Our N-component model offers a more accurate representation as figure 6.17 demonstrates.

Simulation

260 non-coalescing droplets were initialised on the top of the simulation and subjected to a step of gravitational force acting towards the bottom of the simulation. The simulation parameters for this data were 200×200 nodes, $\omega^S = 1.8$, $\omega^D = 1.0$, $\sigma^{SD} = 0.01$, $\sigma^{DD} = 0.01$ and $g = 10^{-4}$. The simulation required 5 hours on our SPC3, which makes it very accessible. This simulation can also be seen as the modeling of the Rayleigh-Taylor instability with deformable particles, similarly to Pan *et al.* who used the Direct Numerical Simulation technique to model the Rayleigh-Taylor instability with solid particles [153].

6.5.2 Stenosed capillary

Motivation

Preproliferative (or Background) diabetic retinopathy is primarily a disease of retinal blood vessels. The earliest vessel closures in diabetic retinopathy are usually the capillaries. These small vessels are critical to the health of the retina, since they are needed to deliver oxygen and nutrients to the area and to carry away carbon dioxide and other waste products. The source of this capillary closure is not completely understood and theories include: (i) clumping of blood cells or other blood elements, (ii) abnormality or damage to the endothelium (the cells lining the inner wall of the capillary), (iii) swelling of an abnormally permeable vessel wall and (iv) compression of the capillary by surrounding retinal swelling [37].

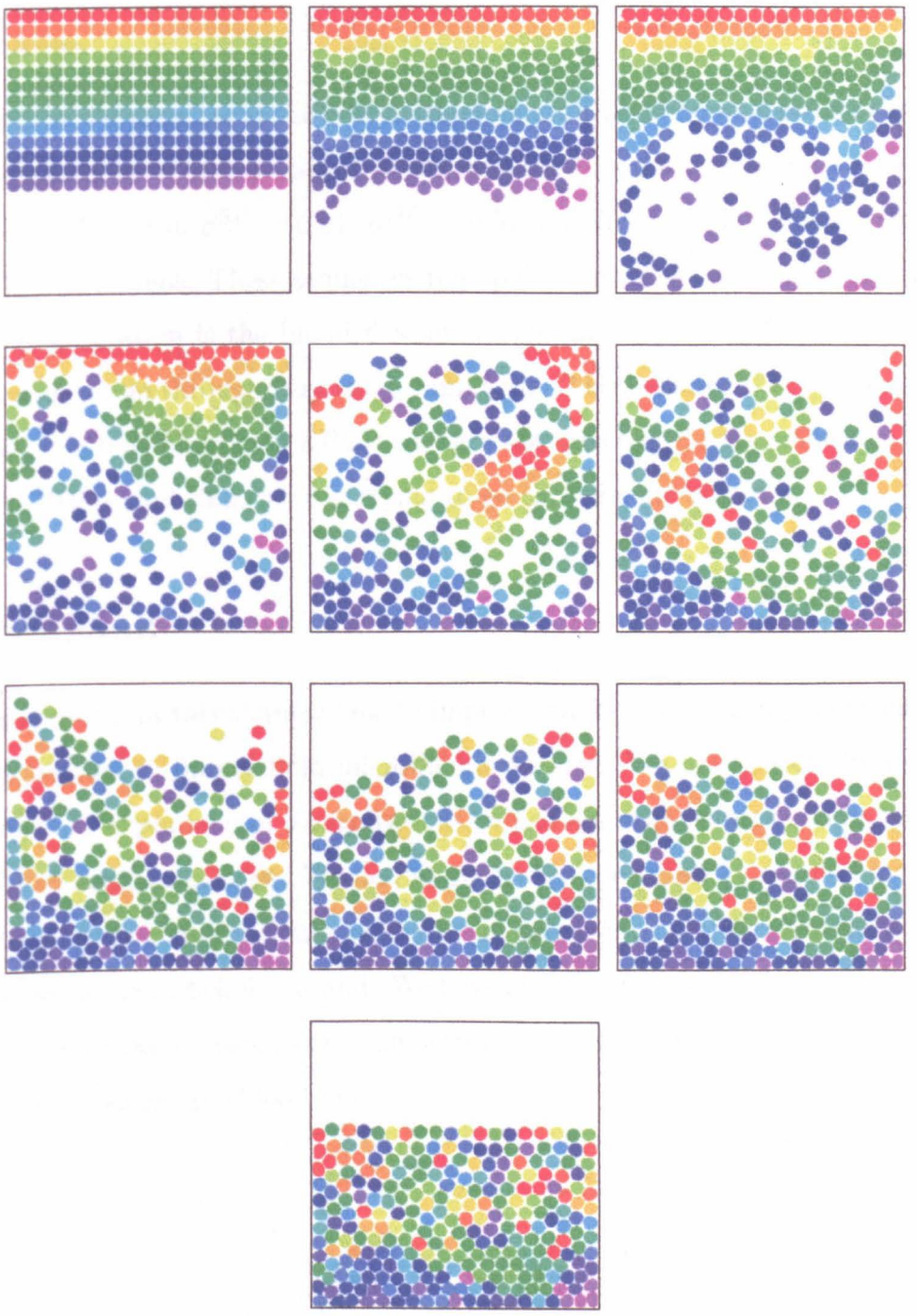

Figure 6.17: Flow of deformable droplets subjected to gravity. This simulation demonstrates the capability of our N-component model in the area of blood salvage or the simulation of the Rayleigh-Taylor instability with deformable particles. The deformation and interactions of the drops in apparent through the simulation.

This last example illustrates the capability of our novel N-component model, to address this issue. See figure 6.18.

Simulation

We initialise the droplets at the inlet of the simulation and impose a pressure gradient via a body-force. The simulation parameters for this data were 500×100 nodes, $\omega^S = 1.8$, $\omega^D = 1.0$, $\sigma^{SD} = 0.01$, $\sigma^{DD} = 0.01$ and $Re = 1$. The images are taken every 200 time steps. These sequences required 30 minutes each on our SPC3.
Another application is the blood flow in the spleen, where RBC's have to deform significantly to go through very small capillaries. This consists of a very simple and efficient design to filter aged RBC's who are not able to deform as much as healthy (young) RBC's and simply burst trying to go through the blockage.

Conclusion

We have shown in this chapter how to improve further our N-component model for the application to binary fluid microfluidic systems. We have successfully applied our model to experimental configurations, which are acknowledged to be computationally difficult to address. We had to generalise the Lishchuk method for surface tension to our N-component model and found unexpected properties of the λ method compared to the Lishchuk method. We have also demonstrated the capability of the model in some dense suspension configurations and made a (successful) first attempt to simulate mesoscopic blood flow.

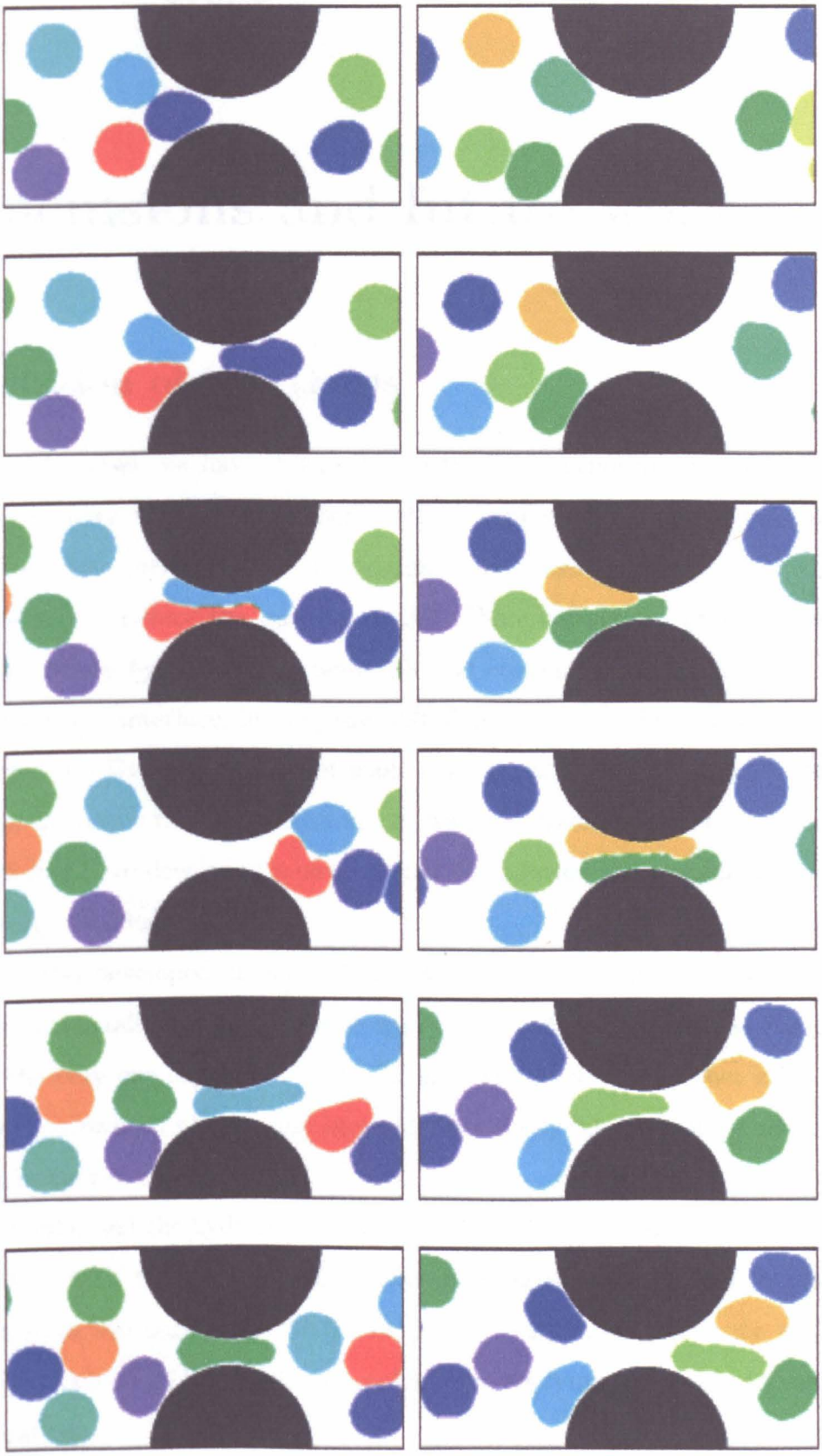

Figure 6.18: *Blood capillary with a significant blockage. This situation happens in retinal capillaries of diabetics. This could also represent the very small capillaries of the spleen where RBC's have to deform significantly to pass the constriction.*

Conclusions and future work

Conclusion of this thesis

During this thesis, we have designed a method to purposely decrease the micro-currents activity in the Gunstensen method applied to a Gunstensen interfacial algorithm. Few corrections to the original Gunstensen algorithm have also been implemented to reduce the micro-currents. These corrections reduced the micro-currents activity by a order of magnitude and concentrated their velocity fluctuation around the interface, leaving the bulk fluids 'neater'. This also improved the circularity of a Gunstensen droplet while relaxing to equilibrium. Since blood flow has been the prime target application, the walls' interactions could not be set aside. We therefore have developed a new method of imposing wall-wetting and obtained convincing behaviour.

We have also developed an algorithm enabling the efficient simulation of a large number of mutually non-coalescing droplets. This method is, as far as the author is aware, the only one capable of such efficiency and have already met great interest by other (renowned) physics and biological university laboratories as well as world leading industrial companies.

We have validated the hydrodynamics of our N-component model by comparing our simulations with well established experimental results. We have also provided a calibration of the parameters of the droplets in suspension (viscosity and surface tension), which could be found very useful when applying this model to engineering configurations.

We have generalised and improved the Lishchuk surface tension method for the Gunstensen algorithm and obtained an even greater reduction of the micro-currents, and we were capable of simulating convincingly binary fluid micro-fluidic devices. This

application has also found great interest from very well established groups.
We managed to retain the advantage of the Gunstensen method over most other numerical methods for multi-phase: the method remains very adaptable, as the core algorithm does not impose a lot of constraints on the user, who is free to add new physics to the algorithm (or even to change the evolution equation).
It is the author's belief that this new model will find numerous very fruitful applications, in a very wide range of applications.

General future work

As mentioned many times in this thesis already, the prime target application of this project was the mesoscale modeling of blood flow and the flow of other deformable bodies in suspension. We certainly have made significant progresses in this direction, and achieved what no other model could efficiently simulate. However, within the blood flow application, the exact biconcave shape of the RBC is very important to recover, for example in the study of the formation of rouleaux (RBC cloths), margination or leukocyte rolling. The whole of this thesis was only concerned with two dimensions, but the third dimension has always been in sight. To demonstrate this, we have successfully extended the Lishchuk algorithm to three dimensions and simulated a cubic droplet relaxing into a spherical sphere. Every step of the final algorithm is, theoretically, generalisable to three dimensions. We have measured (as it could be deduced from our test on efficiency), that going to three dimensions still scales linearly with the number of nodes (note however that some tricks had to be applied for the recolouring to remain efficient).
To improve the efficiency of the model even further, some future work might attempt to implement a dynamical allocation of colour and density, to reduce the number of fluids declared but not used on a node. This could reduce, considerably, the time and memory requirements (up to half, to the author's opinion).
Some other future work could also be done to consolidate the validation of the hydrodynamics of the N-component model, since some issues over lubrication still remain unaddressed. This could ultimately provide some insight on the detailed mechanism of margination in blood capillaries, which remains only superficially

understood at the present day.

The author's future work

The author will develop further this model as a Postdoctoral fellow of Harvard Medical School, at the Steel Laboratory (Boston, Massachusetts, USA) for the investigation of cancer growth. This project will consist in investigating the possibility that blood flow can be a factor in cancer growth.

The author's future work is to generalise the N-component Lishchuk method in 3D and implement restrictions of constant surface area for the RBC's needed at the micro-capillary scale.

Appendix A

List of Symbols/Abreviations

A.1 Abbreviations

BE: Boltzmann Equation

BGK: Bhatnagar–Gross–Krook model

CFD: Computational Fluid Dynamics

CSF: Continuous surface force (method)

CSS: Continuous surface stress (method)

D2Q9: LB 2 dimensions 9 velocity geometry

FC: front capturing

FT: Front tracking

HVAC: Heat ventilation and air conditioning

ll: long/diagonal links

l.u.: Lattice unit

LB: Lattice Boltzmann.

LBE: Lattice Boltzmann Equation.

LBGK: Lattice Bhatnagar–Gross–Krook method.

LBM: Lattice Boltzmann Method

LSM: Level set method

NSE: Navier Stokes Equation

sl: short/transverdal links

SPC3: Standard PC Computational Capability. In our lab: Intel Pentium Zeon 2.4 GHz with 2.0 Gb of RAM

VOF: Volume of fluid (method)

A.2 Greek symbols

α_i: Momentum density associated with the colour α in the direction i.

$\overline{\alpha}$: Any fluid other than fluid α

$\overline{\alpha}_i$: Complement momentum density to the colour α. We have $\overline{\alpha}_i = f_i - \alpha_i$.

β: Blunting of the velocity profiles

$\delta^{\alpha}(\mathbf{x}, i, n)$: boolean function equal to 1 if the colour label lb(x,i,n) is α and 0 otherwise

ϵ: Knudsen number.

Δt: Estimated time for a particle to cross the flow focusing configuration longitudinally.

Γ: Body force parameter used when inducing an inlet/outlet pressure difference.

γ: Microscopic surface tension parameter

γ^{OW}: Oil-Water surface tension

$\gamma_{\alpha\beta}$: Surface tension between fluid α and β

λ: Modulation of the surface tension parameter for long and short links

λ_0: Value of λ giving the most reduced μ_a and the most isotropic drop. We found that $\lambda_0 = 2.1415$

μ: Shear viscosity

μ_a: micro-currents activity

ν: Kinematic viscosity

ν^O: Oil viscosity in the Flow-focusing configuration

ν^W: Water viscosity in the Flow-focusing configuration

ν^D: Drops' viscosity

ν^S: Surrounding fluid's viscosity

ν_C: Collision rate in the BGK collision operator

Ω: Collision operator in the BE.

ω^α: BGK relaxation parameter of fluid α

ω^O: BGK relaxation parameter of the Oil in the flow focusing configuration

ω_e: Effective BGK relaxation parameter

Φ: volume fraction of suspension to surrounding fluid

Ψ: ratio of the droplet viscosity and the surrounding fluid's viscosity

ρ: Fluid density

ρ^α: Nodal density of fluid α

$\widehat{\rho^{\overline{\alpha}}}$: nodal fluid density without fluid α

ρ^B: Nodal density of blue fluid

ρ^O: Oil density in the Flow-focusing configuration

ρ^R: Nodal density of red fluid

ρ^W: Water density in the Flow-focusing configuration

Σ: macroscopic surface tension defined by the Laplace's law

σ: surface tension parameter

σ^{α}_{wall}: Wall wetting parameter of fluid α

σ^{DD}: Drop's liquid wetting parameter with each other

σ^{OW}: Oil-Water surface tension parameter

σ^{SD}: Surrounding-Drop liquid wetting parameter

σ^{D}: Drops' surface tension parameter

σ^{D}_{wall}: Drop wall-wetting parameter

σ^{S}_{wall}: Surrounding fluid wall-wetting parameter

$\sigma'_{\alpha\beta}$ **(with** $\alpha \neq \beta$**)**: Shear stress tensor (non diagonal elements of $\sigma_{\alpha\beta}$.

$\sigma_{\alpha\beta}$: Stress tensor

σ''_{α}: Normal stress tensor

σ^{B}_{wall}: Blue fluid wall wetting parameter

σ^{R}_{wall}: Red fluid wall wetting parameter

σ_i: Link dependant surface tension parameter

τ_C: Collision time of the BGK collision operator

$\theta_{P\alpha}$: angle of the colour-field $\mathbf{P}^{\alpha}$

θ_c: Contact angle

θ_i: Angle of link i

θ_P: Colour-field angle of the red-blue interface

$\theta_W(\mathbf{x})$: Angle of the wall at x

A.3 Latin symbols

A: Aperture of the Flow-focusing configuration

A_L: Local anisotropy of the drop

A_T: Total anisotropy of a drop

b_i: Momentum distribution of the Blue fluid in direction i

BB_{mid}: boolean array defining the simulation boundary in the mid-link bounce back method

BB_{on}: Boolean array defining the simulation boundary in the on-link bounce back method

D: droplet

$f(\mathbf{v})$: Density of probability associated to the velocity $\mathbf{v}$.

f^{eq}: LB Maxwell-Boltzmann distribution function.

f^n: n^{th} order component of velocity distribution f

f^e: Boltzmann-Maxwell equilibrium distribution function

f_i: Colourblind momentum distribution, in direction i

f_n: n-body velocity distribution

g: gravitational field parameter

K: curvature of the interface

lb: Colour map identifying the colour of each density

m: Mass of the fluid particle

N: total number of fluid in the simulation

N_{mol}: Total number of molecules in V

N_Q: maximum of fluids allowed at any site

$N_T(\mathbf{x})$: number of different fluids at $\mathbf{x}$

O: Oil in the Flow-focusing configuration

O_{re}: Order of recolouring

P: Fluid's static pressure, or thermodynamic pressure, or hydrostatic pressure.

P_β^α: β component of the colour-field of colour α

P^α: colour-field of colour α

$\widehat{P}_\alpha^S$: α component of the surrounding colour field

Q: Arbitrary quantity conserved in binary collisions

R_{drop}: Initial radius of the drop

r_i: Momentum distribution of the Red fluid in direction i

$\overline{Ra}$: Averaged radius of the drop

Re^{oil}: Oil Reynolds number at the inlet

S: Surrounding fluid

$S_{\alpha\beta}$: Strain rate tensor

T_α: Table of priorities for the recolouring process of colour α

T_B: Table of priorities for the recolouring process of the blue colour

t_i: lattice dependent weights of f^{eq}

T_R: Table of priorities for the recolouring process of the red colour

U^O: Mid-line oil inlet velocity

U^W: Mid-line water inlet velocity

W: Water in the Flow-focusing configuration

W^W: Width of the water inlet in l.u.

A.4 Vectors

A: Total body-force acting on a fluid element.

$\mathbf{c_i}$: LB link velocity associated with the geometry

F: External body-force acting on the fluid

n: normal to the interface

P: Colourblind colour field

$\mathbf{P}^\alpha$: colour field of colour α

$\mathbf{q}^\alpha$ colour flux of colour α

u(x): Macroscopic velocity of the fluid at **x**.

v: Microscopic velocity of a fluid's particle

V: Volume control fluid

$\overline{\mathbf{v}}$: Short time averaging of the velocity **v** designed to smear out the checker board pattern

W(x): Wall direct with respect to the node at **x**

$\mathbf{x}_{gra}$: Coordinate of the centre of gravity of a droplet

$\mathbf{x}_{mixed}$: Coordinate of mixed nodes

Bibliography

[1] M. B. ABBOT and D. R. BASCO. *An introduction to computational fluid dynamics.* Addison Wesley, 1989. ISBN: 0582013658.

[2] J. D. ANDERSON. *Computational Fluid Dynamics: The basics with applications.* McGraw-Hill International Series in Mechanical Engineering, 1995.

[3] S. L. ANNA, N. BONTOUX and H. A. STONE. *Formation of dispersions using flow-focusing in microchannels.* Appl. Phys. Lett., **82**, (2003) pages 364–366.

[4] L. ANTIGA, B. ENE-IORDACHE, A. REMUZZI and M. NEGRI. *Personalized Blood Flow Simulations.* Fluent NEWS, Fall 2003, page 23.

[5] S. V. APTE, K. MAHESH and T. LUNDGREN. *A Eulerian-Lagrangian model to simulate two-phase particulate flows.* Annual Research Briefs, Center for Turbulence Research, Stanford University, **1**, (2003) pages 161–171.

[6] G. K. BATCHELOR. *An introduction to fluid dynamics.* Cambridge University Press, 1967.

[7] M. BELLET. *Implementation of surface tension with wall adhesion effects in a three-dimensional finite element model for fluid flow.* Commun. Numer. Meth. Eng., **17**, (2001) pages 563–579.

[8] B. BERTHIER, R. BOUZERAR and C. LEGALLAIS. *Blood flow patterns in an anatomically realistic coronaryvessel: influence of three different reconstruction methods.* J. of Biomech., **35**, (2002) pages 1347–1356.

[9] P. BHATNAGAR, P. E. GROSS and M. K. KROOK. *A Model for Collision Processes in Gases. I. Small Amplitude Processes in Charged and Neutral One-Component Systems.* Phys. Rev., **94**, (1954) pages 511–.

[10] A. V. BOBYLEV. *The Chapman-Enskog and Grad methods for solving the Boltzmann equation.* Soviet Physics-Doklady, **27**, (1982) pages 29–31.

[11] L. BOLTZMANN. *Lectures on Gas theory.* Berkeley: University of California Press, 1964. Translated by S. G. Brush from 'Vorlesungen über Gastheorie' (1896-98).

[12] M. BORN and H. S. GREEN. *A General Kinetic Theory of Liquids.* Cambdridge University Press, 1949.

[13] K. BORYCZKO, W. DZWINEL and D. A. YUEN. *Dynamical clustering of red blood cells in capillary vessels.* J. Mol. Modeling, **9**, (2003) pages 16–33.

[14] K. BORYCZKO, W. DZWINEL and D. A. YUEN. *Modeling Fibrin Polymerization in Blood Flow with Discrete-Particles. In press 2004.* Comp. Mod. and Prog. in Biomed.

[15] A. BOURLIOUX. *A coupled level-set volume-of-fluid algorithm for tracking material interfaces.* 6th International Synosium On Computational Fluid Dynamics, **1**, (1995) pages 15–22.

[16] J. U. BRACKBILL, D. B. KOTHE and C. ZEMACH. *A Continuum Method for Modeling Surface Tension.* J. Comput. Phys., **100**, (1992) pages 335–.

[17] A. J. BRIANT, A. J. WAGNER and J. M. YEOMANS. *Lattice Boltzmann simulations of contact line motion. I. Liquid-gas systems.* Phys. Rev. E, **69**, (2004) pages 031602–.

[18] A. J. BRIANT and J. M. YEOMANS. *Lattice Boltzmann simulations of contact line motion. II. Binary fluids.* Phys. Rev. E, **69**, (2004) pages 031603–.

[19] F. BROCHARD and J. F. LENNON. *Une bulle dégonflée : le globule rouge.* La Recherche, **75**, (1977) pages 174–177.

[20] J. M. BROOKE, P. V. COVENEY, J. HARTING, S. JHA, S. M. PICKLES, R. L. PINNING and A. R. PORTER. *Computational Steering in RealityGrid.* Proceedings of the UK e-Science All Hands Meeting 2003, published online. URL: `http://www.nesc.ac.uk/events/ahm2003/AHMCD/pdf/179.pdf`.

[21] S. G. BRUSH. *Statistical Physics and the Atomic Theory of Matter, from Boyle and Newton to Landau and Onsager.* Princeton Series in physics, Princeton University Press, 1983.

[22] J. M. BUICK, J. A. COSGROVE, S. J. TONGE, M. W. COLLINS, J. GOMATAM, A. J. MULHOLLAND and B. A. STEVES. *The Lattice Boltzmann Equation for Modelling Arterial Flows: Review and Application.* Biomed. and Pharmacotherapy, **56**, (2002) pages 345–346.

[23] C. G. CARO, T. J. PEDELEY, R. C. SCHROTER and W. A. SEED. *The Mechanics of the Circulation.* Oxford Medical Publications, 1998.

[24] A. R. CARRILLO, J. E. WEST, D. A. HORNER and J. F. PETERS. *Interactive Large-Scale Soil Modeling Using Distributed High Performance Computing Environments.* The Int. J. of High Perf. Comp. App., **13**, (1999) pages 33–48.

[25] J. R. CEBRAL, P. J. YIM, R. LÖHNER, O. SOTO and P. L. CHOYKE. *Blood Flow Modeling in Carotid Arteries with Computational Fluid Dynamics and MR Imaging.* Academic Radiology, **9**, (2002) pages 1286–1299.

[26] J. CHAKRABARTI, J. DZUBIELLA and H. LOWEN. *Reentrance effect in the lane formation of driven colloids. In press 2004.* Phys. Rev. E.

[27] Y. CHANG, T. HOU, B. MERRIMAN and S. OSHER. *A level set formulation of eulerian interface capturing methods for incompressible fluid flows.* J. Comput. Phys., **124**, (1996) pages 449–464.

[28] S. CHAPMAN and T. COWLING. *The Mathematical Theory of Non-Uniform Gases.* Cambridge University Press, 3rd edition, 1990.

[29] H. CHEN. *Discrete Boltzmann systems and fluid flows.* J. Comput. Phys., **7**, (1993) pages 632–.

[30] H. CHEN, S. CHEN and W. H. MATTHAEUS. *Recovery of the Navier-Stokes equations using a lattice-gas Boltzmann approach.* Phys. Rev. A, **45**, (1992) pages R5339–R5342.

[31] S. CHEN and G. D. DOOLEN. *Lattice Boltzmann method for fluid flows.* J. Fluid Mech., **30**, (1998) pages 329–.

[32] J. CHIN and P. V. COVENEY. *Towards tractable toolkits for the Grid: a plea for lightweight, usable middleware.* UK e-Science Technical Report, number UKeS-2004-01.

[33] J. CHIN, J. HARTING, S. JHA, P. V. COVENEY, A. R. PORTER and S. M. PICKLES. *Steering in computational science: mesoscale modelling and simulation.* Contemporary Phys., 44, (2003) pages 417–434.

[34] S. M. CLARKE and A. R. RENNIE. *Structures of Spherical Particles Dispersed in Density Matched Media Under Oscillatory Shear.* Progress in Colloid and Interface Sci., **104**, (1997) pages 180–182.

[35] P. W. CLEARY. *Axial transport in dry ball mills.* Third International conference on CFD in the minerals and process industries, **1**, (2003) pages 651–656.

[36] P. W. CLEARY, B. F. C. LAURENT and J. BRIDGWATER. *DEM prediction of flow patterns and mixing rates in a ploughshare mixer.* Proc. of World Congress on Particle Technology 4, Fully refereed proceedings as CD-ROM ISBN 085 825 7947, paper 715.

[37] A. V. CLINIC. *Nonproliferative Diabetic Retinopathy.* URL: `http://www.avclinic.com/nonproliferative.htm`.

[38] J. CORTIAL. *Two-phase flow in reduced gravity.* Rapport de stage d'option scientifique, Ecole Polytechnique, 2002. URL: `http://www.imprimerie.polytechnique.fr/Rapports/Files/cortial.pdf`.

[39] A. V. COWARD, Y. RENARDY, M. RENARDY and J. R. RICHARDS. *Temporal evolution of periodic disturbances in two-layer Couette flow.* J. Comput. Phys., **132**, (1997) pages 346–.

[40] J. P. CRAVEN. *Secondary Electron Imaging of liquid droplets on Insulating surfaces in the Environemental SEM.* Ph.D. thesis, Cavendish Laboratory, University of Cambridge, 2002.

[41] A. CRISTEA and V. SOFONEA. *Reduction of spurious velocity in finite difference lattice Boltzmann models for liquid - vapor systems.* Int. J. Mod. Phys. C, **14**, (2003) pages 1251–1266.

[42] B. CROUSE, S. KUEHNER, M. KRAFCZYK, E. RANK and C. VAN TREECK. *Indoor air flow analysis based on lattice Boltzmann methods.* Int. J. Energy and Buildings, **34**, (2002) pages 941–949.

[43] B. CROUSE, E. RANK, M. KRAFZYK and J. TOLKE. *A LB-Based approach for adaptative flow simulations.* Int. J. Mod. Phys., **17**, (2003) pages 109–112.

[44] S. F. DALY and M. A. HOPKINS. *Estimating Forces on an Ice Control Structure using DEM.* Proc. of 11th Workshop on the Hydraulics of Ice Covered Rivers. Published on CD-ROM by the Committee on River Ice Processes and the Environment, Canadian Geophysical Union-Hydrology Section, Ottawa, Canada., **1**.

[45] J.-C. DESPLAT, I. PAGONABARRAGA and P. BLADON. *LUDWIG: A parallel Lattice-Boltzmann code for complex fluids.* Comp. Phys. Comm., **134**, (2001) pages 273–290.

[46] M. M. DUPIN, I. HALLIDAY and C. M. CARE. *Multi-component lattice Boltzmann equation for mesoscale blood flow.* J. Phys. A, **36**, (2003) pages 8517–8534.

[47] M. M. DUPIN, I. H. HALLIDAY and C. M. CARE. *A lattice Boltzmann model of flow blunting.* Phil. Trans. Roy. Soc. Lond. A, **362**, (2004) pages 1755–1761.

[48] M. M. DUPIN, I. H. HALLIDAY and C. M. CARE. *A many-component Lattice Boltzmann equation simulation for transport of deformable particles.* Phil. Trans. Roy. Soc. Lond. A, **362**, (2004) pages 1885–1914.

[49] A. DUPUIS and J. M. YEOMANS. *Mesoscopic modelling of droplets on heterogeneous surfaces. In press 2004.* Future Generation of Comp. Syst.

[50] A. DUPUIS and J. M. YEOMANS. *Mesoscopic modelling of droplets on topologically patterned substrates, to be presented at the ICCS 2004 conference*, 2004. URL: `http://xxx.lanl.gov/abs/cond-mat/0401150`.

[51] J. DZUBIELLA, G. P. HOFFMANN and H. LÖWEN. *Lane formation in colloidal mixtures driven by an external field.* Phys. Rev. E, **65**, (2002) pages 021402–.

[52] J. DZUBIELLA, H. LÖWEN and C. N. LIKOS. *Depletion Forces in Nonequilibrium.* Phys. Rev. Lett., **91**, (2003) pages 248–301.

[53] W. DZWINEL, K. BORYCZKO and D. A. YUEN. *A discrete-particle model of blood dynamics in capillary vessels.* J. Colloid and Interface Sci., **258**, (2003) pages 163–173.

[54] E. E. GRASLAND-MONGRAIN, D. R. LINK and D. A. WEITZ. *Droplet coalescence in microfluidic devices*, July 2003. Magister Repport, Magistère Inter-Universitaire de Chimie, Ecole Normale Supérieure, Paris and Experimental Soft Condensed Matter Group Department of Engineering and Applied Sciences Department of Physics, Harvard University, Cambridge.

[55] C. D. EGGLETON and A. S. POPEL. *Large deformation of red blood cell ghosts in a simple shear flow.* Phys. of Fluids, **10**, (1998) pages 1834–1845.

[56] EXA-COORPORATION. *Exa coorporation website.* URL: `http://www.exa.com/`.

[57] T. E. FABER. *Fluid Dynamics for Physicists.* Cambridge University Press, 2nd edition, 1997.

[58] Z. G. FENG and E. MICHAELIDES. *Fluid-particle interaction and resuspension in sinple Shear Flow.* J. Hydrol. Eng., **129**, (2003) pages 985–994.

[59] Z.-G. FENG and E. E. MICHAELIDES. *Equilibrium position for a particle in a horizontal shear flow.* Int. J. Multip. Flow, **29**, (2003) pages 943–957.

[60] N. D. FILIPOVIC. *MedCFD website*, 2004. URL: `http://www.csk.kg.ac.yu/csk_eng/content.php`.

[61] M. FRANK, D. ANDERSON, E. R. WEEKS and J. F. MORRIS. *Particle migration in pressure-driven flow of a Brownian suspension.* J. Fluid Mech., **493**, (2003) pages 363–378.

[62] U. FRISH, B. HASSLACHER and Y. POMEAU. *Lattice gas automata for the Navier-Stokes equations.* Phys. Rev. Lett., **56**, (1986) pages 1505–.

[63] B. FRYXELL, E. MULLER and D. ARNETT. Astrophys. J., **367**, (1991) pages 619–.

[64] A. M. GANAN-CALVO. Phys. Rev. Lett., **80**, (1998) pages 285–288.

[65] I. GINZBURG and P. M. ADLER. *Boundary flow condition analysis for the three-dimensional lattice Boltzmann model.* J. Phys. II France, **4**, (1994) pages 191–214.

[66] I. GINZBURG and D. D'HUMIÈRES. *Local second order boundary methods for lattice Boltzmann models.* J. Stat. Phys., **84**, (1996) pages 927–971.

[67] I. GINZBURG and K. STEINER. *A free surface lattice-Boltzmann method for modelling the filling of expanding cavities by Bingham Fluids.* Phil. Trans. Roy. Soc. Lond. A, **360**, (2002) pages 453–466.

[68] I. GINZBURG and K. STEINER. *Lattice Boltzmann model for the free-suface flow and its application to filling process in casting.* J. Comput. Phys., **185**, (2003) pages 61–99.

[69] I. GINZBURG and G. WITTUM. *Two-Phase Flows on Interface Refined Grids Modeled with VOF, Staggered Finite Volumes, and Spline Interpolants.* J. Comput. Phys., **166**, (2001) pages 302–335.

[70] R. GLOWINSKI, T.-W. PAN and D. JOSEPH. *Modeling Rayleigh-Taylor Instability of a Sedimenting Suspension Arising in Direct Numerical Simulation.* UMSI 99/158, University of Minnesota Supercomputing Institute Research Report, September 1999.

[71] H. L. GOLDSMITH. *Microscopic flow properties of red cells.* Federation Proceedings, **26**, (1967) pages 1813–1820.

[72] H. L. GOLDSMITH. *Red cells motions and wall interactions in tube flow.* Federation Proceedings, **30**, (1971) pages 1578–1588.

[73] H. L. GOLDSMITH and T. KARINO. *Microscopic Considerations: the motions of individual particles.* Annals New York Academy of Sciences, **283**, (1977) pages 241–255.

[74] H. L. GOLDSMITH and J. C. MARLOW. *Flow behavior of erythrocytes. II. Particle motions in concentrated suspensions of ghost cells.* J. Coll. Interface Sci., **71**, (1979) pages 383–407.

[75] N. GONZLEZ-SEGREDO and P. V. COVENEY. *Coarsening dynamics of ternary amphiphilic fluids and the self-assembly of the gyroid and sponge mesophases: lattice-Boltzmann simulations, In press 2004.* Phys. Rev. E.

[76] N. GONZLEZ-SEGREDO and P. V. COVENEY. *Self-assembly of the gyroid cubic mesophase: lattice-Boltzmann simulations.* Europhysics Letters, **65**, (2004) pages 795–801.

[77] J. R. GRAHAM. *AY 202: Astrophysical Gas Dynamics*, 2002. URL: `http://astron.berkeley.edu/~jrg/ay202/lectures.html`.

[78] D. GRUNAU, S. CHEN and K. EGGERT. *A lattice Boltzmann model for multiphase fluid flows.* Phys. Rev. A, **5**, (1993) pages 2557–2562.

[79] A. K. GUNSTENSEN and D. H. ROTHMAN. *Microscopic modeling of immiscible fluids in three dimensions by a lattice Boltzmann method.* Europhysics Letters, **18**, (1992) pages 157–161.

[80] A. K. GUNSTENSEN, D. H. ROTHMAN, S. ZALESKI and G. ZANNETI. *Lattice Boltzmann model of immiscible fluids.* Phys. Rev. A, **43**, (1991) pages 4320–4327.

[81] E. GUYON, J. P. HULIN, L. PETIT and C. D. MITESCU. *Physical hydrodynamics.* Oxford University Press, 2001.

[82] I. HALLIDAY, S. P. THOMPSON and C. M. CARE. *Macroscopic surface tension in a lattice Bhatnagar-Gross-Krook model of two immiscible fluids.* Phys. Rev. E, **57**, (1998) pages 514–523.

[83] J. HARTING, M. VENTUROLI and P. V. COVENEY. *Large-scale grid-enabled lattice-Boltzmann simulations of complex fluid flow in porous media and under shear, In press 2004.* Phil. Trans. Roy. Soc. Lond. A.

[84] X. HE, S. CHEN and R. ZHANG. *A lattice Boltzmann Scheme for incompressible Multiphase Flow and Its Application in Simulation of Rayleigh-Taylor Instability.* J. Comput. Phys., **152**, (1999) pages 642–663.

[85] X. HE and L. S. LUO. *A priori derivation of the lattice Boltzmann equation.* Phys. Rev. E, **55**, (1997) pages R6333–R6336.

[86] X. HE and L. S. LUO. *Theory of the lattice Boltzmann method: From the Boltzmann equation to the lattice Boltzmann equation.* Phys. Rev. E, **46**, (1997) pages 6811–6817.

[87] X. HE, Q. ZOU, L. S. LUO and M. DEMBO. *Analytic solutions of simple flow and analysis of noslip boundary conditions for the lattice Boltzmann BGK model.* J. Stat. Phys., **87**, (1997) pages 115–136.

[88] D. HELBING, P. MOLNÄR, I. J. FARKAS and K. BOLAY. *Self-organizing pedestrian movement.* Environment and Planning B: Planning and Design, **28**, (2001) pages 361–383.

[89] M. HIRABAYASHI, M. OHTA, D. A. RÜFENACHT and B. CHOPARD. *Characterization of flow reduction in an aneurysm due to a porous stent.* Phys. Rev. E, **68**, (2003) pages 021918–.

[90] M. HIRABAYASHI, M. OHTA, D. A. RÜFENACHT and B. CHOPARD. *Lattice Boltzmann Analysis of the Flow Reduction Mechanism in Stented Cerebral Aneurisms for the Endovascular Treatment.* Int. Conf. Comp. Sci. 2003, LCNS, **2657**, (2003) pages 1044–1053.

[91] M. HIRABAYASHI, M. OHTA, D. A. RÜFENACHT and B. CHOPARD. *A lattice Boltzmann study of blood flow in stented aneurism. In Press 2004.* Future Generation of Comp. Syst.

[92] C. HIRT. *VOF - What's in a Name.* Technical report, Flow Science Inc. website, 2004. URL: `http://www.flow3d.com`.

[93] C. HIRT and B. NICHOLS. *Volume of Fluid (VOF) Method for the Dynamics of free Boundaries.* J. Comput. Phys., **39**, (1981) pages 201–225.

[94] C. W. HIRT. *Simulating the Wetting and Drying of Shallow Flows*, 2002. Flow Science Technical Note, FSI-00-TN54 URL: `http://www.flow3d.com/pdfs/TN54.pdf`.

[95] S. HOU, X. SHAN, Q. ZOU, G. D. DOOLEN and W. E. SOLL. *Evaluation of Two Latice Boltzmann Models for Multiphase Flows.* J. Comput. Phys., **138**, (1997) pages 695–713.

[96] T. INAMURO, N. KONISHI and F. OGINO. *A Galilean invarient model of the lattice Boltzmann method for multiphase flows using free-energy approach.* Comp. Phys. Com., **129**, (2000) pages 32–45.

[97] T. INAMURO, R. MIYAHARA and F. OGINO. *Lattice Boltzmann simulations of drop deformation and breakup in simple shear flow*, chapter N. Satofuka (Ed.), pages 499–504. Computational Fluid Dynamics 2000. Springer-Verlag, Berlin, 2001; .

[98] T. INAMURO, T. OGATA and F. OGINO. *Numerical simulation of bubble flows by the lattice Boltzmann method. In press 2004.* Future Generation of Comp. Syst.

[99] T. INAMURO, T. OGATA, S. TAJIMA and N. KONISHI. *A lattice Boltzmann method for incompressible two-phase flows with large density differences. In press 2004.* J. Comput. Phys.

[100] T. INAMURO, R. TOMITA and F. OGINO. *Lattice Boltzmann simulation of drop deformation and breakup in shear flows.* Int. J. Mod. Phys. B, **17**, (2002) pages 21–26.

[101] T. INAMURO, M. YOSHINO, H. INOUE, R. MIZUNO and F. OGINO. *A lattice Boltzmann Method for a Binary Miscible Fluid Mixture and Its Application to a Heat-Transfer Problem.* J. Comput. Phys., **179**, (2002) pages 201–215.

[102] S. JAKSCH. *Facettierung dreidimensionaler Gebiete und Gittergenerierung unter Verwendung von Octree-Datenstrukturen.* Diploma thesis, Lehrstul für Bauinformatik, Technische Universität München, 2001.

[103] L. JIANZHONG, S. XING and Y. ZHENJIANG. *Effects of the aspect ratio on the sedimentation of a fiber in Newtonian fluids.* Aerosol Sci., **34**, (2003) pages 909–921.

[104] Y. KATO, K. KONO, T. SETA, D. MARTINEZ and S. CHEN. *Amadeus project and microscopic simulation of boiling two phase flow by the Lattice-Boltzmann method.* Int. J. Mod. Phys. C, **8**, (1997) page 843858.

[105] D. KEHRWALD. *Numerical Analysis of Immiscible Lattice BGK.* Ph.D. thesis, Abteilung Strömung in Komplexen Strukturen, Fraunhofer-Institut für Techno- und Wirtschaftsmathematik, Kaiserslautern, Germany, 2003.

[106] D. KEHRWALD. *Towards a consistency proof for immiscible lattice BGK.* Proc. Appl. Math. Mech., **3**, (2003) pages 80–83.

[107] V. M. KENDON, M. CATES, I. PAGONABARRAGA, J.-C. DESPLAT and P. BLADON. *Inertial effects in three dimensional spinodal decomposition of a symmetric binary fluid mixture: A lattice Boltzmann study.* J. Fluid Mech., **440**, (2001) pages 147–.

[108] D. B. KOTHE, M. W. WILLIAMS and E. G. PUCKETT. *Accuracy and convergence of continuum surface tension models, in Fluid Dynamics at Interfaces.* edited by W. Shyy and R. Narayanan, Cambridge Univ. Press, 1998.

[109] M. KRAFCZYK, M. CERROLAZA, M. SCHULZ and E. RANK. *Analysis of 3D transient blood flow passing through an artifficial aortic valve by Lattice Boltzmann methods.* J. of Biomech., **31**, (1998) pages 453–462.

[110] M. KRAFCZYK, J. TÖLKE, E. RANK and M. SCHULZ. *Two-dimensional simulation of fluidstructure interaction using lattice-Boltzmann methods.* Comp. and Structures, **79**, (2001) pages 2031–2037.

[111] S. KUEHNER, M. KRAFCZYK and E. RANK. *Some aspects of Virtual Reality based computational steering of indoor air flow computation.* Proceedings of Roomvent 2002, 8th International Conference on Air Distribution in Rooms.

[112] S. KUEHNER, M. KRAFCZYK and J. TOELKE. *Towards interactive comfort optimization of Indoor Flows using Virtual Reality based analysis of Large-Eddy simulation results.* ICCCBE-IX, The 9th International Conference on Computing in Civil and Building Engineering, Proceedings, Taipei, Taiwan. ISBN 986-80000-0-7.

[113] A. J. C. LADD. *Numerical simulations of particulate suspensions via a discretized Boltzmann equation. Part 1. Theoretical foundation.* J. Fluid Mech., **271**, (1994) pages 285–309.

[114] A. J. C. LADD. *Numerical simulations of particulate suspensions via a discretized Boltzmann equation. Part 2. Numerical results.* J. Fluid Mech., **271**, (1994) pages 311–339.

[115] B. LAFAURIE, C. NARDONE, R. SCARDOVELLI, S. ZALESKI and G. ZANETTI. *Modelling merging and fragmentation in multiphase flows with SURFER.* J. Comput. Phys., **113**, (1994) pages 134–147.

[116] L. D. LANDAU and E. M. LIFSHITZ. *Course in Theoretical Physics Vol 6: Fluid Mechanics.* Butterworth-Heinemann, 2nd edition, 1995.

[117] K. LANGAAS. *Viscous coupling and two-phase flow in porous media.* Proceedings from the 6th European Conference on the Mathematics of Oil Recovery, Peebles, UK, 8-11 September 1998).

[118] K. LANGAAS and Y. M. YEOMANS. *Lattice-Boltzmann simulations of a binary fluid with different phase viscosities and its application to fingering in two dimensions.* Euro. Phys. J. B, **15**, (2000) pages 133–141.

[119] J. C.-M. LEE and D. E. DISCHER. *Deformation-Enhanced Fluctuations in the Red Cell Skeleton with Theoretical Relations to Elasticity, Connectivity, and Spectrin Unfolding.* Biophys. J., **81**, (2001) pages 3178–3192.

[120] K. W. LEE and X. Y. XU. *Modelling of flow and wall behaviour in a mildly stenosed tube.* Med. Eng. and Phys., **24**, (2002) pages 575–586.

[121] G. LENORMAND, A. RICHERT, J. SIMON, S. HNON and F. GALLET. *Direct measurement of the area expansion and shear moduli of the human red blood cell membrane skeleton.* Biophys. J., **81**, (2001) pages 43–56.

[122] J. LÉOPOLDÈS, A. DUPUIS, G. D. BUCKNALL and J. M. YEOMANS. *Jetting Micron-Scale Droplets onto Chemically Heteroneous Surfaces.* Langmuir, **19**, (2003) pages 9818–9822.

[123] D. LEVERMORE. *History of Kinetic Theory*, 2002. URL: `http://www.math.umd.edu/~lvrmr/History/Irreversibility.html`.

[124] H. LI, H. FANG, Z. LIN, S. XU and S. CHEN. *Lattice Boltzmann simulation on particle suspensions in a two-dimensional symmetric stenotic artery.* Phys. Rev. E, **69**, (2004) pages 031919–.

[125] R. L. LIBOFF. *Kinetic Theory.* Springer Verlag, 3rd edition, 2003.

[126] D. R. LINK, S. L. ANNA, D. A. WEITZ and H. A. STONE. *Geometrically Mediated Breakup of Drops in Microfluidic Devices.* Phys. Rev. Lett., **92**, (2004) pages 054503–.

[127] S. V. LISHCHUK, C. M. CARE and I. HALLIDAY. *Lattice Boltzmann algorithm for surface tension with greatly reduced micro-currents.* Phys. Rev. E, **67**, (2003) pages 036701–.

[128] Y. LIU, Y. LAI, A. NAGARAJ, B. KANE, A. HAMILTON, R. GREENE, D. D. MCPHERSON and K. B. CHANDRAN. *Pulsatile flow simulation in arterial vascular segments with intravascular ultrasound images.* Med. Eng. and Phys., **23**, (2001) pages 583–595.

[129] E. W. LLEWELLIN. *Multiphase Lattice Boltzmann approaches to modelling the dynamics of volcanic eruptions.* Geophys. Research Abstracts, Euro. Geophys. Soc., **5**, (2003) pages 01498–.

[130] L. S. LUO. *Unified theory of lattice Boltzmann models for nonideal gases.* Phys. Rev. Lett., **81**, (1998) pages 1618–1621.

[131] L. S. LUO. *Theory of the lattice Boltzmann method: lattice Boltzmann models for non ideal gases.* Phys. Rev. E, **62**, (2000) pages 4982–4996.

[132] L. S. LUO and S. S. GIRIMAJI. *Lattice Boltzmann model for binary mixtures.* Phys. Rev. E, **66**, (2002) pages 035301–.

[133] L. S. LUO and S. S. GIRIMAJI. *Theory of the lattice Boltzmann method: two-fluid model for binary mixtures.* Phys. Rev. E, **67**, (2003) pages 036302–.

[134] I. MARSHALL, S. ZHAO, P. PAPATHANASOPOULOU, P. HOSKINS and X. Y. XU. *MRI and CFD studies of pulsatile flow in healthy and stenosed carotid bifurcation models.* J. of Biomech., **37**, (2004) pages 679–687.

[135] N. S. MARTYS and H. CHEN. *Simulation of multicomponent fluids in complex three-dimensional geometries by the lattice Boltzmann method.* Phys. Rev. E, **53**, (1996) pages 743–750.

[136] K. MAYES, G. RILEY, R. W. FORD, M. LUJAN and T. L. FREEMAN. *The Design of a Performance Steering System for Component-Based Grid Applications*, chapter In Performance Analysis and Grid Computing, pages 111–127. Kluwer Academic Publishers, v. getov, m. gerndt, a. hoisie, a. maloney, b. miller, edition, 2003; .

[137] G. MCNAMARA and G. ZANETTI. *Use of the Boltzmann equation to simulate lattice gas automata.* Phys. Rev. Lett., **61**, (1988) pages 2332–.

[138] R. MEI, L. S. LUO and W. SHYY. *An accurate curved boundary treatment in the lattice Boltzmann method.* J. Comput. Phys., **155**, (1999) pages 307–330.

[139] R. MEI, W. SHYY, D. YU and L. S. LUO. *Lattice Boltzmann method for 3-D flows with curved boundaries.* J. Comput. Phys., **161**, (2000) pages 680–699.

[140] C. MIGLIORINI, Y. H. QIAN, H. CHEN, E. B. BROWN, R. K. JAIN and M. L. L. *Red Blood Cells Augment Leukocyte Rolling in a Virtual Blood Vessel.* Biophys. J., **83**, (2002) pages 1834–1841.

[141] J. A. MOORE, D. A. STEINMAN, D. W. HOLDSWORTH and C. R. ETHIER. *Accuracy of computational hemodynamics in complex arterial geometries reconstructed from magnetic resonance imaging.* Annals of Biomed. Eng., **27**, (1999) pages 32–41.

[142] R. R. NETZ. *Conduction and diffusion in two-dimensional electrolytes.* Europhysics Letters, **63**, (2003) pages 616–.

[143] N. Q. NGUYEN and A. J. C. LADD. *Lubrification corrections for lattice-Boltzmann simulations of particles suspensions.* Phys. Rev. E, **66**, (2002) pages 046708–.

[144] B. D. NICHOLS and C. W. HIRT. *Method for Calculating Multidimensional, Transient Free Surface Flows Past Bodies.* Proc. First Intern. Conf. Num. Ship Hydrodynamics, 1, (1975) pages 20–23.

[145] H. NIIMURA. *Verification of Multi-component Lattice-Boltzmann method.* Int. J. Mod. Phys. B, **17**, (2003) pages 157–160.

[146] R. R. NOURGALIEV, T. N. DINH and B. R. SEHGAL. *On lattice Boltzmann modeling of phase transition in an isothermal non-ideal fluid.* Nucl. Eng. and Design, **211**, (2002) pages 153–171.

[147] P. OLLA. *Simplified Model for Red Cell Dynamics in Small Blood Vessels.* Phys. Rev. Lett., **82**, (1999) pages 453–456.

[148] W. R. OSBORN, E. ORLANDINI, M. R. SWIFT, J. M. YEOMANS and J. R. BANAVAR. *Lattice Boltzmann study of hydrodynamic spinodal decomposition.* Phys. Rev. Lett., **75**, (2000) pages 4031–4034.

[149] S. OSHER and J. A. SETHIAN. *Front propagating with curvature dependent speed: algorithms based on Hamiltonian-Jacobi Formulations.* J. Comput. Phys., **79**, (1988) pages 12–49.

[150] J. OUELLETTE. *A New Wave of Microfluidic Devices.* The Industrial Physicist, Aug-Sep., **1**, (2003) pages 14–17.

[151] C. PAN, M. HILPERT and C. T. MILLER. *Lattice-Boltzmann simulation of two-phase flow in porous media.* Water Resour. Res., **40**, (2004) pages W01501–.

[152] C. PAN, J. F. PRINS and C. T. MILLER. *A high-performance lattice Boltzmann implementation to model flow in porous media.* Comp. Phys. Comm., **158**, (2004) pages 89–105.

[153] T. W. PAN, D. JOSEPH and R. GLOWINSKI. *Modeling Rayleigh-Taylor instability of a sedimenting suspension of several thousand circular particles in direct numerical simulation.* J. Fluid Mech., **434**, (2001) pages 23–37.

[154] T. W. PAN, D. D. JOSEPH, R. BAI, R. GLOWINSKI and V. SARIN. *Fluidization of 1204 spheres: simulation and experiment.* J. Fluid Mech., **451**, (2002) page 2002.

[155] N. PATANKAR, T. KO, H. G. CHOI and D. D. JOSEPH. *A correlation for the lift-off of many particles in plane Poiseuille flows of Newtonian fluids.* J. Fluid Mech., **445**, (2001) pages 55–76.

[156] N. A. PATANKAR and D. D. JOSEPH. *Modeling and numerical simulation of particulate flows by the Eulerian-Lagrangian approach.* Int. J. Multip. Flow, **27**, (2001) pages 1659–1685.

[157] M. PEREZ-SABORID and A. M. GANAN-CALVO. *A novel pneumatic technique to generate steady capillary microjets.* Journal of Aerosol Science, **30**, (1999) pages 117–125.

[158] C. S. PESKIN and D. M. MCQUEEN. *A three-dimensional computational method for blood flow in the heart.* J. Comput. Phys., **81**, (1989) pages 372–.

[159] S. POPINET and S. ZALESKI. *A front-tracking algorithm for accurate representation of surface tension.* Int. J. Numer. Meth. Fluids, **30**, (1999) pages 775–793.

[160] C. POZRIKIDIS. *Modeling and Simulation of Capsules and Biological Cells.* Chapman and Hall, crc press edition, 2003.

[161] C. POZRIKIDIS. *Numerical Simulation of the Flow-Induced Deformation of Red Blood Cells.* Annals of Biomed. Eng., **31**, (2003) pages 1194–1205.

[162] Y. H. QIAN, D. D'HUMIÈRES and P. LALLEMAND. *Lattice BGK models for Navier-Stokes equation.* Europhysics Letters, **17**, (1992) pages 479–484.

[163] REALITY-GRID. *Reality Grid: Moving the bottleneck out of the hardware and into the human mind*, 2004. URL: `http://www.realitygrid.org/`.

[164] L. E. REICHL. *A Modern Course in Statistical Physics.* Edward Arnold Publishing, 1980.

[165] Y. RENARDY and M. RENARDY. *PROST: a parabolic reconstruction of surface tension for the Volume-of-Fluid method.* J. Comput. Phys., **183**, (2002) pages 400–421.

[166] A. R. RENNIE. *Structure and Alignment in Concentrated Colloidal Dispersions under Flow.* Fundamentals and Applications to Industrial Processing, **8**, (1999) pages 139–150.

[167] W. J. RIDER and D. B. KOTHE. *Reconstructing volume tracking.* J. Comput. Phys., **141**, (1998) pages 112–.

[168] D. H. ROTHMAN and J. M. KELLER. *Immiscible cellular-automaton fluids.* J. Stat. Phys., **52**, (1988) pages 1119–1127.

[169] D. H. ROTHMAN and S. ZALESKI. *Lattice-gas models of phase separations: interfaces, phase transitions.* Rev. Mod. Phys., **66**, (1994) pages 1417–.

[170] D. H. ROTHMAN and S. ZALESKI. *Lattice-gas Automata Dynamics - Simple model for Complex Hydrodynamics.* Cambridge University Press, 1997.

[171] J. S. ROWLINSON and B. WIDOM. *Molecular Theory of Capillarity.* Dover Publications, 2003.

[172] K. SANKARANARAYANAN, I. G. KEVREKIDIS, S. S., J. LU and G. TRYGGVASON. *A comparative study of lattice Boltzmann and front-tracking finite-difference methods for bubble simulations.* Int. J. Multip. Flow, **29**, (2003) pages 109–116.

[173] K. SANKARANARAYANAN, X. SHAN, I. KEVREKIDIS and S. SUNDARESAN. *Analysis of drag and virtual mass forces in bubbly suspensions using an implicit formulation of the lattice Boltzmann method.* J. Fluid Mech., **452**, (2002) pages 61–96.

[174] K. SANKARANARAYANAN and S. SUNDARESAN. *Lift force in bubbly suspensions.* Chem. Eng. Sci., **57**, (2002) pages 3521–3542.

[175] S. B. SANTRA, S. SCHWARZER and H. HERRMANN. *Fluid-induced particle-size segregation in sheared granular assemblies.* Phys. Rev. E, **54**, (1996) pages 5066–5072.

[176] R. SCARDOVELLI and S. ZALESKI. *Direct numerical simulation of free surface and interfacial flow.* Annu. Rev. Fluid Mech., **31**, (1999) pages 567–.

[177] M. SCHELKLE, M. RIEBER and A. FROHN. *Comparison of lattice Boltzmann and Navier-Stokes simulations of three-dimensional free surface flows*, volume FED-VOL. 256 of *Proceedings of the ASME*, page Book No. H01072. 1996; .

[178] J. A. SETHIAN. *Level Set Methods: An Act of Violence - Evolving Interfaces in Geometry, Fluid Mechanics, Computer Vision and Materials Sciences.* URL `citeseer.ist.psu.edu/235087.html`.

[179] J. A. SETHIAN. *Curvature and the evolution of fronts.* Commun. in Math. Phys., **101**, (1985) pages 487–499.

[180] J. A. SETHIAN. *Fast Marching Methods and Level Set Methods*, 1999. URL `http://math.berkeley.edu/~sethian/level\_set.html`.

[181] E. SHALMAN, M. ROSENFELD, E. DGANY and S. EINAV. *Numerical modeling of the flow in stenosed coronary artery. The relationship between main hemodynamic parameters.* Comp. in Bio. and Med., **32**, (2002) pages 329–344.

[182] X. SHAN and H. CHEN. *Lattice Boltzmann model for simulating flows with multiple phases and components.* Phys. Rev. E, **47**, (1993) pages 1815–1819.

[183] X. SHAN and H. CHEN. *Simulation of non-ideal gases and liquid-gas phase transisions by the lattice Boltzmann equation.* Phys. Rev. E, **49**, (1994) pages 2941–2948.

[184] X. SHAN and G. D. DOOLEN. *Multicomponent lattice Boltzmann model with interparticle interaction.* J. Stat. Phys., **81**, (1995) pages 379–393.

[185] X. SHAN and G. D. DOOLEN. *Diffusion in a multi-component lattice Boltzmann equation model.* Phys. Rev. E, **54**, (1996) pages 3614–3620.

[186] T. G. SITHARAM. *Numerical simulation of particulate materials using discrete element modelling.* Current Sci., **78**, (2000) pages 876–.

[187] H. SONG, J. D. TICE and R. F. ISMAGILOV. *A Microfluidic System for Controlling Reaction Networks in Time.* Angew. Chem. Int. Ed., **42**, (2003) pages 768–772.

[188] H. A. STONE and S. KIM. *Microfluidics: Basic Issues, Applications, and Challenges.* A. I. Ch. E. Journal, **47**, (2001) pages 12–50.

[189] H. A. STONE, A. D. STROOCK and A. AJDARI. *Engineering flows in small devices: Microfluidics Toward a Lab-on-a-Chip.* Annu. Rev. Fluid Mech., **36**, (2004) pages 381–411.

[190] S. SUCCI. *The lattice Boltzman Equation for Fluid Dynamics and Beyond.* Oxford Science Publications, 2001.

[191] C. SUN, C. MIGLIORINI and L. L. MUNN. *Red Blood Cells Initiate Leukocyte Rolling in Postcapillary Expansions: a Lattice-Boltzmann Analysis.* Biophys. J., **85**, (2003) pages 208–222.

[192] M. SUSSMAN. *A second order coupled level set and volume-of-fluid method for computing growth and collapse of vapor bubbles.* J. Comput. Phys., **187**, (2003) pages 110–136.

[193] M. SUSSMAN, P. SMEREKA and S. OSHER. *A level set approach for computing solutions to incompressible two-phase flow.* J. Comput. Phys., **114**, (1994) pages 146–159.

[194] M. R. SWIFT, E. ORLANDINI, W. R. OSBORN and J. M. YEOMANS. *Lattice Boltzmann simulations of liquid-gas and binary fluid systems.* Phys. Rev. E, **54**, (1996) pages 5041–5052.

[195] M. R. SWIFT, W. R. OSBORN and J. M. YEOMANS. *Lattice Boltzmann simulations of non-ideal fluids.* Phys. Rev. Lett., **75**, (1995) pages 830–833.

[196] K. TAKAHASHI. *Modeling of Surface Tension in Fluidic MEMS Using the Level-Set Method.* Technical Proceedings of the 2003 Nanotechnology Conference and Trade Show, **1**, (2003) pages 182–185.

[197] C. A. TAYLOR, T. J. R. HUGHES and C. K. ZARINS. *Finite element modeling of blood flow in arteries.* Comp. Meth. App. Mech. Eng., **158**, (1998) pages 155–196.

[198] K. TEKNOMO, Y. TAKEYAMA and H. INAMURA. *Microscopic Pedestrian Simulation Model to Evaluate "Lane-Like Segregation of Pedestrian Crossing".* Proceedings of Infrastructure Planning Conference, Kouchi, Japan, **24**, (2001) pages 1–6.

[199] H. N. V. TEMPERLEY and D. H. TREVENA. *Liquids and their properties. A Molecular and Macroscopic Treatise with Application.* Ellis Horwood: London, 1978.

[200] S. TENG, Y. CHEN and H. OHASHI. *Lattice Boltzmann simulation of multiphase fluid flows through the total variation dimishing with artificial compression scheme.* Int. J. of Heat and Fluid Flow, **21**, (2000) pages 112–121.

[201] C. THEODOROPOULOS, K. SANKARANARAYANAN, S. SUNDARESAN and I. KEVREKIDIS. *Coarse bifurcation studies of bubble flow lattice Boltzmann simulations.* Chem. Eng. Sci., **59**, (2004) pages 2357–2362.

[202] H. M. THOMAS, D. GOLDBECK, T. HAGL, A. IVLEV, U. KONOPKA, G. E. MORLL, H. ROTHERMEL, R. SUTTERLIN and M. ZUZIC. *Complex Plasmas under Microgravity Conditions: Parabolic Flights.* Physica Scripta, **T89**, (2001) pages 16–20.

[203] S. P. THOMPSON, I. HALLIDAY and C. M. CARE. *Mesoscopic hydrodynamics of diphasic lattice Bhatnagar Gross Krook fluid interfaces.* Phys. Chem. Chem. Phys., **1**, (1999) pages 2183–2190.

[204] T. THORSEN, F. H. ROBERTS, R. W. Arnold and S. R. QUAKE. *Dynamic Pattern Formation in a Vesicle-Generating Microfluidic Device.* Phys. Rev. Lett., **86**, (2001) pages 4163–4166.

[205] J. TÖLKE, M. KRAFCZYK, M. SCHULZ and E. RANK. *Lattice Boltzmann simulation of binary fluid flow through porous media.* Phil. Trans. Roy. Soc. Lond. A, **360**, (2002) pages 535–545.

[206] K. P. TRAVIS, B. D. TODD and D. J. EVANS. *Departure from Navier-Stokes hydrodynamics in confined liquids.* Phys. Rev. E, **55**, (1997) pages 4288–4295.

[207] P. VALIVETI and D. R. KOCH. *The inhomogeneous structure of a bidisperse sedimenting gas-solid suspension.* Phys. Fluids, **11**, (1999) pages 32–83.

[208] A. VARDY. *Fluid Principles.* McGraw-Hill International Series in Civil Engineering, 1990.

[209] P. F. VELASQUEZ, D. O. GÓMEZ, G. M. DUBNER, G. GIMÉNEZ DE CASTRO and A. COSTA. *Study of the Rayleigh-Taylor instability in Tycho's supernova remnant.* Astron. Astrophys., **334**, (1998) pages 1060–1067.

[210] E. VERPOORTE and N. F. DE ROOIJ. *Microfluidics Meets MEMS.* Proceedings of the IEEE, **91**.

[211] A. J. WAGNER. *The origin of spurious velocities in lattice Boltzmann.* Int. J. Mod. Phys. B, **17**, (2003) pages 193–196.

[212] D. A. WEITZ. *Experimental solf Condensed matter Group.* URL: `http://www.deas.harvard.edu/projects/weitzlab/research/Microfluidics/Microfluidic.html`.

[213] G. M. WHITESIDES and A. D. STROOCK. *Flexible methods for microfluidics.* Physics Today, **1**, (2001) pages 42–49.

[214] WORLD-HEALTH-ORGANISATION. *Reducing risks, promoting healthy life.* W. H. O. Pub., 2002.

[215] Z. YANG, B. PALM and B. R. SEHGAL. *Numerical simulation of bubbly two-phase flow in a narrow channel.* Int. J. Heat & Mass Transfert, **45**, (2001) pages 1579–1602.

[216] T. YOUNG. *An essay on the cohesion of fuids.* Phil. Trans. Roy. Soc. Lond. A, **95**, (1805) pages 65–87.

INSTITUTE OF PHYSICS PUBLISHING JOURNAL OF PHYSICS A: MATHEMATICAL AND GENERAL

J. Phys. A: Math. Gen. 36 (2003) 8517–8534 PII: S0305-4470(03)58720-0

Multi-component lattice Boltzmann equation for mesoscale blood flow

M M Dupin, I Halliday and C M Care

Materials Research Institute, Sheffield Hallam University, Howard Street, S1 1WB, UK

Received 20 January 2003, in final form 3 June 2003
Published 23 July 2003
Online at stacks.iop.org/JPhysA/36/8517

Abstract

We present an improved lattice Boltzmann model of multi-component flow which permits practical, hydrodynamic modelling of multiple immiscible fluids. The model is robust and significantly reduces the interface anisotropy and micro-currents, which are artefacts observed in many schemes. Our new scheme is used on a particular regime of blood flow: that of the veinule mesoscale, where it is necessary to resolve significant numbers of deformable, interacting cells, which we model as incompressible liquid drops. We demonstrate the model's ability to recover the complex flow phenomena typical of the veinule scale.

PACS numbers: 02.70.–c, 47.11.+j

1. Introduction

Over the last decade, a range of lattice Boltzmann (lB) methods have been developed as mesoscopic models of isotropic [1] and anisotropic [2] fluids. The lB method shows particular promise when applied to complex flow at low Reynolds number [3] and especially to multi-fluid systems. A range of techniques have been developed to model fluid interfaces (e.g., [4–6]), with perhaps the Shan–Chen approach [7] being the most popular. More details can be found in reviews by Benzi *et al* [8] and Chen *et al* [9]. It is our objective here to demonstrate that a multi-component lB provides a basis for one particular model of veinule-scale flows. In section 2 we outline this 'explicit' model of mesoscale blood flow, in which we resolve deformable, advected blood cells as incompressible drops of many immiscible liquids.

It should be noted that even in mesoscale hydrodynamics the boundary between two immiscible fluids should have no structure or thickness. Surface tension is activated in lB by a number of methods which are *microscopically* physical. As a result, the emergent *continuum* interface suffers from unwanted artefacts: (i) small but spurious velocities, or *micro-currents*, and (ii) a finite thickness.

Key lB interface models are able to capture the kinematics of phase separation [5]. However, where hydrodynamics *alone* defines the problem narrow interfaces are desirable,

simply from the point of view of computational resources. This is especially true when the interfaces are intimate and the geometry is complex. Here we wish to simulate many immiscible, interacting drops. Computational considerations restrict the size of each. For hydrodynamic behaviour, graded interfaces of (say) width 6 lattice units on drops practically restricted to radius 20 lattice units are unphysical. Fortunately, in the hydrodynamic regime, simpler lB interface models [4] which produce a sharp interface (typically 2–3 lattice units) are as valid as any other lB method [10]. The basic technique of Gunstensen and Rothmann [4] is, moreover, the method most readily amenable to the algorithmic developments designed to accommodate mutually immiscible species (section 3.3).

To be precise, we base the work reported here on a version [6] of the interfacial model due originally to Gunstensen and Rothmann [4]. The use of a Gunstensen/Rothmann-type lB model is further justified by its ability to sustain a significant difference in kinematic viscosity between the separated liquids at low *Re*. The basic method is described in section 3.1 and refined in section 3.2, reducing both the anisotropy of the interface and the intensity of the micro-currents. The generalization of this model to any number of mutually immiscible species is then presented in section 3.3.

In section 4 we present quantitative results which demonstrate the improvements in the surface tension algorithm and results which demonstrate its ability to realize veinule-scale blood flow.

We present our conclusions in section 5.

2. Model for mesoscale blood flow

Blood flow has been studied for many years. The majority of studies deal with visco-elastic flow in vessels with a diameter more than two orders of magnitude greater than that of a red blood cell (RBC). Here blood is considered to be a homogeneous, non-Newtonian liquid (see Quarteroni [12]). There is also work on microscopic flows, where single cells are modelled explicitly (see below). In this case, the flow is recovered from low *Re* multi-component hydrodynamics in which the interface-mediated physics is of primary importance. Certain mesoscale calculations have 'resolved' cells by assuming that blood components advect along the streamlines of the corresponding undisturbed flow. Whilst limiting, this assumption is probably reasonable for small, rigid cells. However, when cells are of a size comparable with the vessel, explicit deformations and interactions cannot be neglected. A full understanding of such processes requires explicit modelling of a high volume fraction of deformable, and interacting, particles [11].

Microcirculation flows, in small veins or veinules, are characterized by significant numbers of strongly interacting cells, which require explicit resolution. Capillary length scales have flow dominated by plasma-advected RBCs and the crucial properties of constant RBC surface area and preferred membrane curvature are undoubtedly of central importance. But at the veinule scale there are a range of important phenomena, in which explicit models of deformable cells should be used, and where one expects membrane curvature to be less important than the volume exclusion effects associated with high cell numbers. We briefly discuss some examples of such situations:

(1) In veinules, white blood cells (WBCs) can concentrate near the walls. *Margination* can promote WBC function. Margination is affected by flow rate, WBC to RBC ratio and *haematocrit*, the latter being the percentage volume of solids in plasma, typically 37%. The mechanism which drives the RBC to migrate towards the centre of the vessel may be RBC aggregation, and associated volume exclusion effects, or it may also be their greater

deformability. Calculations have considered single solid cells but there are no results in the interface-dominated regime treating significant numbers of deformable particles.

(2) Empirically, haematocrit is found to be the principal determinant of blood viscosity. The investigation of haematocrit dependence of viscosity becomes possible only with an explicit model.

(3) Margination near a microcirculation junction causes plasma-rich blood in any side vessel [13]. This effect, known as plasma skimming, clearly requires explicit resolution of blood components and flow geometry.

Clearly, it would be valuable to have a model capable of resolving flow constitution, geometry, differential deformability (RBC versus WBC) and particle size distributions. So, for the type of applications outlined above, we propose an incompressible liquid drop model. Such a model must automatically capture the constraint of constant cell volume and allow for differential deformability. The constraint of constant cell surface area is assumed to be less important. In summary, we represent veinule-scale blood as a heterogeneous *liquid* consisting of a wetting, ambient plasma component and a number of intimate, approximately solid and mutually immiscible drops. The drops may have different sizes, viscosities and surface tensions for different applications.

Despite success over a range of applications, conventional computational fluid dynamics (CFD) is unsuited to model such flows as we propose here. However, lB offers a practical vehicle for our drop model of the veinule microcirculation. The multi-component lattice Boltzmann (lB) method has been used for flows containing separated liquids. However, to simulate the situations outlined in (1)–(3) above, one must have a means of interrupting coalescence/evaporation between drops. For, note, RBCs accrete at low shear into 'rouleaux' but certainly do not amalgamate like drops of oil in water. Therefore, to adapt lB for the veinule microcirculation it is necessary to devise a practical algorithm with controlled liquid drop coalescence. This is discussed in section 3.

To demonstrate its worth in situations such as (1)–(3), our model must work sensibly with many suspended drops, all of a size comparable to that of the veinule, all showing deformation. Using the N-phase lB (section 3), we simulate, in section 4, a dense suspension of relatively viscous, neutrally buoyant deformable cells. The cells are assumed to be advecting through an asymmetrically expanding duct at a Reynolds number—a situation representative of physiological flows. Crucially, the balance between inertial and surface tension forces (capillarity or Taylor number) is controlled so as to allow clear deformation in all parts of the flow.

3. Development of the lB model

We outline an lB model of multi-component flow for $\gg 2$ mutually immiscible species, designed to provide a vehicle for the modelling requirements outlined in section 2. For the reasons discussed in section 1, our liquid–liquid interface is generated by a version of the Gunstensen and Rothmann lB algorithm [4]. We further demonstrate that this interface has, for hydrodynamic applications, properties matching those of more popular lB interfaces [7].

As a basis we adopt the two-dimensional, 9-velocity LBGK model (denoted by $D2Q9$, with the $Q = 9$ velocities depicted in figure 1), which has a single scalar collision parameter. This was pioneered by Qian and d'Humières [18] and analysed in detail by Hou *et al* [15]. The lB model fluid is weakly compressible but for the envisaged range of Re, compressibility errors should be very small.

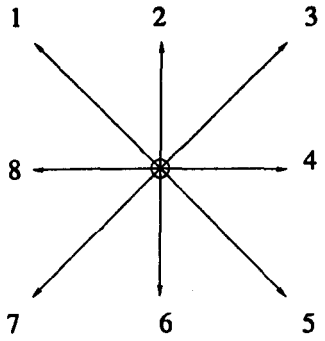

Figure 1. The D2Q9 lattice basis or velocity set used for our basic single relaxation time LBGK model.

3.1. An lB interface

We first consider two immiscible liquids. Our model currently applies to fluids with the same physical density. For small Re, the effect of gravity on differential drop buoyancy may be approximated through a body force, an approach which is exact only at $Re = 0$. However, buoyancy effects will not be of primary importance in the target blood flow application though they may be significant in other adaptations of our model. Hence we consider body forces in this subsection.

Vectors of the lattice basis are denoted as $\mathbf{c}_i$ with indexing given in figure 1. The collision, propagation and forcing of a D2Q9 LBGK algorithm is written as

$$f_i(\mathbf{r} + \mathbf{c}_i\delta_t, t + \delta_t) = f_i(\mathbf{r}, t) + \frac{1}{\tau}\left(f_i^{(0)}(\rho, \rho\mathbf{v}, t) - f_i(\mathbf{r}, t)\right) + F_i \tag{1}$$

where δ_t represents the time step, τ controls the molecular viscosity of the lattice fluid through

$$\nu = \left(\frac{2\tau - 1}{6}\right) \tag{2}$$

(units of the time step, δ_t) and the constant, F_i, represents a spatially *uniform* body force density which includes (i) parameter g, which differs for the two fluids and approximates the effects of buoyancy [17], and (ii) a term which represents an applied constant pressure gradient, G. The overall forcing, F_i, is thus

$$F_i = 3Gt_p\rho c_{ix} + 3gt_p\rho c_{iy} \tag{3}$$

where the weights, t_p, are defined below.

The macroscopic density and momenta of the two fluids are obtained from the moments

$$\rho = \sum_i f_i \qquad \rho\mathbf{v} = \sum_i f_i\mathbf{c}_i \tag{4}$$

and the equilibrium distribution function, $f_i^{(0)}$, is

$$f_i^{(0)}(\rho, \mathbf{v}) = t_p\rho\left[1 + \frac{\mathbf{v}\cdot\mathbf{c}_i}{c_s^2} - \frac{|\mathbf{v}|^2}{2c_s^2} + \frac{(\mathbf{v}\cdot\mathbf{c}_i)^2}{2c_s^4}\right] \tag{5}$$

with weights $t_p = 4/9, 1/9, 1/36$ for link index $i = 0$, i even, i odd, respectively (labelling of figure 1). $c_s = 1/\sqrt{3}$ is the velocity of sound for the D2Q9 model. The form of the equilibrium distribution function, (5), ensures that

$$\rho = \sum_i f_i^{(0)} \qquad \rho\mathbf{v} = \sum_i f_i^{(0)}\mathbf{c}_i \tag{6}$$

and also recovers the non-viscous components of the momentum–flux tensor through

$$\Pi^{(0)}_{\alpha\beta} = \sum_i f_i^{(0)} c_{i\alpha} c_{i\beta} = \frac{1}{3}\rho\delta_{\alpha\beta} + \rho v_\alpha v_\beta. \tag{7}$$

For a more detailed derivation of this basic algorithm see Zou *et al* [15].

Gunstensen and Rothmann [4] were the first to introduce multi-component behaviour into lB through the action of new rules added to a model similar to that outlined above. These new rules give a spontaneous interface between immiscible, *colour*-differentiated fluids, represented by momentum densities $R_i(\mathbf{r}, t)$ and $B_i(\mathbf{r}, t)$, as outlined in the next few paragraphs.

$R_i(\mathbf{r}, t)$ and $B_i(\mathbf{r}, t)$ are summed at each lattice node to define a conserved red density $\rho_R(\mathbf{r}, t)$ and a conserved blue density $\rho_B(\mathbf{r}, t)$, with $\rho(\mathbf{r}, t) = \rho_B(\mathbf{r}, t) + \rho_B(\mathbf{r}, t)$. $R_i(\mathbf{r}, t)$ and $B_i(\mathbf{r}, t)$ evolve as follows.

The overall, *colour-blind*, momentum density,

$$f_i(\mathbf{r}, t) = R_i(\mathbf{r}, t) + B_i(\mathbf{r}, t) \tag{8}$$

is used to calculate an overall density and velocity. These quantities are interpreted as the total density and velocity of the red and blue fluids at position $\mathbf{r}$, time t. A colour-blind equilibrium $f_i^{(0)}$ is then defined using equation (5). Collision of the multi-component fluid is performed in three steps: (i) a colour-blind collision using equations (5) and (1), (ii) a perturbation which introduces interfacial tension and (iii) a re-allocation of colour (*re-colouring*) which introduces component segregation.

Surface tension is introduced by inserting a small (nominally $O(\delta_t^2)$ [6]) mass and momentum conserving perturbation, Δf_i, to the post-collision $f_i(\mathbf{r}, t)$ prior to re-colouring:

$$\Delta f_i(\mathbf{r}, t) = \sigma C(\mathbf{r}, t) \cos(2(\theta_f(\mathbf{r}) - \theta_i)). \tag{9}$$

Here, the parameter σ controls the strength of the effective surface tension, angle θ_i is the angular orientation of lattice link i (figure 1) and $\theta_f(\mathbf{r}, t)$ is the direction of the colour gradient:

$$\mathbf{f}(\mathbf{r}, t) = \sum_{ij} (R_j(\mathbf{r} + \mathbf{c}_i, t) - B_j(\mathbf{r} + \mathbf{c}_i, t))\mathbf{c}_i \tag{10}$$

which is taken as an approximation to an interface normal at the boundaries between the two fluids. $C(\mathbf{r}, t)$ is a *concentration factor*:

$$C(\mathbf{r}, t) = 1 - \left| \frac{\rho_R(\mathbf{r}, t) - \rho_B(\mathbf{r}, t)}{\rho_R(\mathbf{r}, t) + \rho_B(\mathbf{r}, t)} \right| \tag{11}$$

which limits activation of surface tension to multi-coloured nodes [6].

Colour is de-mixed by re-allocating colour densities $\rho_R(\mathbf{r}, t)$ and $\rho_B(\mathbf{r}, t)$ over the post-collision 'receptacle' $f_i(\mathbf{r}, t)$ so as to maximize the work done by colour flux:

$$\mathbf{q}(\mathbf{r}, t) = \sum_i (R_i(\mathbf{r}, t) - B_i(\mathbf{r}, t))\mathbf{c}_i \tag{12}$$

against the colour gradient (10).

Different relaxation parameters τ can be applied to the separated liquids, to give them different kinematic viscosities. In the mixing/segregating region an effective relaxation parameter τ_{eff} is used, which, through identity (2), gives the appropriate mean viscosity for the fluids mixing at the interface:

$$\nu_{\text{eff}} = \frac{1}{6}(2\tau_{\text{eff}} - 1) = \left(\frac{\rho_R}{\rho_R + \rho_B}\right)\nu_R + \left(\frac{\rho_B}{\rho_R + \rho_B}\right)\nu_B. \tag{13}$$

Segregation and surface tension is thus produced in any region of the lattice where colours mix. Such a region corresponds to a fluid–fluid interface, with essentially correct continuum length scale properties [6]. Finally, it is important, for present applications, to note that the interfacial region is relatively narrow.

3.2. An lB interface with reduced micro-currents

It is possible to improve the properties of the emergent interface described in section 3.1. For given values of σ and τ, macroscopic interfacial tension in the 'diphasic' model (section 3.1) can be calculated for two interface orientations [16]. Surface tension for an lB interface parallel to the short link direction (even i, figure 1) is, to first order in product $\sigma\tau$ [16],

$$\Sigma_s = \frac{4\sigma\tau}{3}. \tag{14}$$

For an interface parallel to a long link direction (odd i, figure 1), we have a surface tension

$$\Sigma_l = \frac{4\sigma\tau}{\sqrt{2}}. \tag{15}$$

This difference holds a clue to the minimization of the micro-current.

The form of the perturbation we choose in equation (9) allows one to set surface tensions Σ_s and Σ_l independently. That is, perturbations applied to the odd i and even i $f_i(\mathbf{r}, t)$, will separately control Σ_l and Σ_s. This may be seen, for example, by considering an interface oriented parallel to the long links (odd i, figure 1). The value of perturbation (9), for all even i value $f_i(\mathbf{r}, t)$, is zero. Hence, all even i value $f_i(\mathbf{r}, t)$ are ignorable when considering Σ_l. An equivalent argument follows for Σ_s. Accordingly, we set Σ_s and Σ_l independently, using different perturbation parameters, σ and $\lambda\sigma$, to perturb even i and odd i value $f_i(\mathbf{r}, t)$. By adjusting λ, the closed interface bounding a red drop can be characterized by a single, uniform macroscopic surface tension. Dividing equations (14) and (15), we can estimate a value of λ to first order in the product $\sigma\tau$ [16]:

$$\lambda = \frac{3}{\sqrt{2}} \approx 2.15. \tag{16}$$

Ensuring that interfacial tension is uniform has other beneficial effects besides making a static drop more isotropic (circular). The interfacial micro-current field associated with a drop placed centrally on a lattice, bounded with no-slip walls, represents a solution of the Navier–Stokes equations with boundary conditions determined by the walls and by the velocities induced near to the interface by the segregating flux of the interfacial perturbation. The qualitative features of the micro-current flow field may be predicted by considering the directions in which the segregating flux has its maxima and minima. Hence, by smoothing the variation of this quantity with angular position, we also smooth the imbalance responsible for driving a micro-current. Accordingly, adjusting the ratio 16 should improve drop isotropy and minimize the micro-current activity, as measured by the velocity residual:

$$m = \sum_{\mathbf{r}} v(\mathbf{r}, t). \tag{17}$$

3.3. N immiscible fluids in lB: coalescence and wetting

Sections 3.1 and 3.2 introduce our lB model of a binary liquid. Here we generalize that model to a mixture of N immiscible liquids which must not coalesce or evaporate and which must have controlled wetting properties.

Hence, there are certain essential requirements in the N-colour extension. To regulate evaporation masses of individual drops each need to be conserved. Over 10^6 lattice updates, our interface algorithm in section 3.2 conserved the mass of a drop to better than $2.0 \times 10^{-3}\%$. Interruption of coalescence is just as crucial to model blood cells. The latter is quantified, for this algorithm, below. To avoid the need to consider cells' interaction with the veinule wall, we choose to prevent all drops from wetting the solid boundaries.

Our generalization to N immiscible components assigns each fluid a 'colour' superscript, $\alpha = 0, 1, 2, 3, \ldots, (N-1)$. Fluids with different values of α can have different properties, e.g., collision parameters, τ_α. Now, for N different species, multi-component lB quickly demands unviable amounts of computer storage, as N increases. But for relatively small, non-evaporating, 'sharp', drops, these arrays for N primary quantities $f_i^\alpha(\mathbf{r}, t)$ will be very sparse. Moreover, a natural question arises around the validity of attempting to represent, on lattice nodes with Q links or velocities (see figure 1), more than Q different colours or species.

To address storage, we track only N_Q ($<Q \ll N$) dominant species at any node. Note also that the particular N_Q colours, or immiscible components, vary between nodes. We are thus considering colour *difference*, as opposed to absolute colour, which is the source of the principal reduction in the requisite storage. The sharp interfaces from our Gunstensen-type interface method mean minimal mixing and a reduction in the number of different colours found on a node. In practice we take $N_Q = 5$. This value is found to be adequate for even the most intimate mono-disperse multi-component flows. But, note, this choice reflects the geometry and number of components (colours/drops) in our particular application.

Before further detailing our method, we acknowledge that, to guide species segregation, a lattice map of absolute colour is needed. However, for such a map, sufficient information can be stored in a four-dimensional array of integer type, with a subscript set $\{x, y, i, N_Q\}$ to identify, for lattice position $\{x, y\}$, direction i, the colours ($\leqslant N_Q$ in number) present their integer superscript, α. By recording N_Q species at each node, the dominant-type real storage requirements, on the primary quantity $f_i^\alpha(\mathbf{r}, t)$, for a total of N_0 drops (or immiscible components), is reduced by a factor N_Q/N_0, in fact to levels comparable with the diphasic model (below).

Controlling coalescence amounts to dealing consistently with all possible mixed node states, with a generalized perturbing and re-colouring processes, designed to eliminate mixing between all species. This requirement may still be stated as a need to maximize the work done by a generalized colour flux against a generalized colour gradient.

The diphasic colour gradient (section 3.1) must be generalized. We continue to assume that colour gradient defines an interface normal [20], and generalize it, based upon section 3.1. We define an interfacial colour gradient between any pair of de-mixing immiscible components, denoted by α and β, relative to the vector

$$\mathbf{I}_{\alpha\beta}(\mathbf{r}) = \sum_i \sum_j \left(f_j^\alpha(\mathbf{r}+\mathbf{c}_i) - f_j^\beta(\mathbf{r}+\mathbf{c}_i)\right)\mathbf{c}_i \tag{18}$$

which, we emphasize again, is assumed to be normal to the local (α, β) interface. This colour gradient is used to perturb the 'colour-blind', total:

$$f_i(\mathbf{r}, t) = \sum_{\alpha=0}^{N_Q-1} f_i^\alpha(\mathbf{r}, t)$$

with a surface tension inducing perturbation. Note that this summation is on α: the corresponding summation of i gives the total density of fluid α on the node:

$$\rho_\alpha(\mathbf{r}, t) = \sum_{i=0}^{Q} f_i^\alpha(\mathbf{r}, t).$$

For the interface between components α and β we use a generalized perturbation after section 9:

$$\Delta f_i^{\alpha\beta}(\mathbf{r}, t) = \sigma_{\alpha\beta} C_{\alpha\beta}(\mathbf{r}, t) \cos(2(\theta_l(\mathbf{r}) - \theta_i)) \tag{19}$$

in which there is no summation on repeated subscripts, $\sigma_{\alpha\beta}$ is a surface tension parameter for the $\alpha\beta$ interface, θ_l is the polar angle of the field in equation (18) and

$$C_{\alpha\beta}(\mathbf{r}, t) = 1 - \left| \frac{\rho_\alpha(\mathbf{r}, t) - \rho_\beta(\mathbf{r}, t)}{\rho_\alpha(\mathbf{r}, t) + \rho_\beta(\mathbf{r}, t)} \right| \tag{20}$$

is the concentration factor for the (α, β) fluid pair, after equation (11). For a D2Q9 lattice, $\sigma_{\alpha\beta}$ is modulated by the factor λ (section 3.1), so that $\sigma_{\alpha\beta}$ becomes

$$\sigma_{\alpha\beta}^i = \begin{cases} \lambda\sigma_{\alpha\beta} & i \text{ even} \\ \sigma_{\alpha\beta} & i \text{ odd.} \end{cases}$$

The perturbations described in equation (19) are superposed for each of the $\leqslant {}_2P_Q$ fluid pairs (α, β) on a mixed node. This yields an effective perturbation to the colour-blind $f_i(\mathbf{r}, t)$:

$$\Delta f_i(\mathbf{r}, t) = \sum_{(\alpha\beta)} \Delta f_i^{\alpha\beta}(\mathbf{r}, t)$$

in which the summation is taken over all pairs (α, β) of fluids present (see below).

We now define an 'average' colour gradient which points towards component α and away from the total of all other components present at the node at $\mathbf{r}$:

$$\begin{aligned} \mathbf{f}^\alpha(\mathbf{r}) &= \sum_i \sum_j \left[f_j^\alpha(\mathbf{r} + \mathbf{c}_i) - \sum_{\beta \neq \alpha} f_j^\beta(\mathbf{r} + \mathbf{c}_i) \right] \mathbf{c}_i \\ &= \sum_i \sum_j \left[2 f_j^\alpha(\mathbf{r} + \mathbf{c}_i) - f_j(\mathbf{r} + \mathbf{c}_i) \right] \mathbf{c}_i. \end{aligned} \tag{21}$$

The same calculation is repeated for each fluid component present at the node, position $\mathbf{r}$. The appropriate colour gradient $\mathbf{f}^\alpha(\mathbf{r})$ (equation (21)) is used to re-colour for component α within each node in the same way as for a binary fluid.

The process defined above opposes the inter-diffusion of all different components. Note that to calculate the colour gradient (21) requires knowledge of the absolute colour, not just the relative amounts of the different colours present in a local environment. We also note that the sum on α of these individual fields is a measure of the local gradient in the total fluid density and is therefore zero only in a uniform fluid.

In order to achieve full colour separation, the order of the re-allocation of more than two colours to receptacle f_i is significant. Different ordering in the re-colouring process can clearly result in small differences in the post-collision post-segregated state. Careful observation shows that these differences are small but not without consequence. They are, for example, probably linked to the residual micro-current activity. In order to produce optimum segregation (sharp interface), the minority species at a node is given *priority* allocation to its favoured direction. Failure to adopt this scheme results in a relatively large loss of information about the location of minority species, resulting in increased drop evaporation.

Target flow applications are, by intention, heavily interface dominated. Recall, for our effectively mono-disperse systems here, a maximum of five drops in proximity were allowed (again, simple packing considerations mean this value will increase with increasing polydispersity). Five immiscible drops or de-mixing fluids lead to ${}_2P_5 = 10$ *possible* local interfaces. This factor 'amplifies' the computational overhead attending the increase in the total length of interface as N (drop number) increases, as assessed in table 1 (see below).

Table 1. The dependence of the memory of the algorithm and execution speed (times) upon N, number of immiscible drops (fluids), based upon a 100 lattice updates on a 200 × 200 square lattice. The drop size varies (decreases) as N increases.

N	2	10	100	1000
Time (min)	7	8	9	11
Memory (Mb)	64	64	64	64

Table 2. The dependence of the memory of the algorithm and execution speed (times) upon N, number of immiscible drops (fluids), based upon a 100 lattice updates on a 200 × 200 square lattice. The drop size remains fixed as N increases, hence the constrained range of parameter N.

$N = N_Q$	2	3	4	5	6	7	8	9
Time (min)	1.1	1.5	1.8	2.1	2.3	2.6	3.0	3.4
Memory (Mb)	10	12	14	16	18	20	22	25

We now proceed to consider the wetting properties of our algorithm. To bound a mixture of suspended drops in an internal flow we must consider the relative wetting properties of the liquids, and we now describe a means of controlling continuum-scale inter-component and wall-wetting properties.

Consider a mixture of fluids close to a boundary. Differential wetting is achieved using a perturbation process similar to that used for liquid–liquid wetting. Accordingly, the wall-wetting perturbation for a fluid α is taken to be

$$\Delta f_i^\alpha(\mathbf{r}, t) = \rho^\alpha(\mathbf{r}) \cos(2(\theta_w(\mathbf{r}) - \theta_i))\sigma_{\alpha|\text{wall}} \tag{22}$$

where $\rho^\alpha(\mathbf{r})$ is the wall-nodal density of the fluid α, $\theta_w(\mathbf{r})$ is the orientation of of the wall normal and $\sigma_{\alpha|\text{wall}}$ is a parameter controlling the 'wetting surface tension' of the fluid α. By setting different values of $\sigma_{\alpha|\text{wall}}$, the different components present at a boundary may each be differently inclined to wet. Different components therefore compete to wet the boundary, which is the essence of the underlying physical process. The perturbations described in equation (22) are repeated (superposed) for each fluid α on a mixed wall node.

Results of wall-wetting simulations are presented in section 4. These show the change in shape of a drop at a wall as a result of variation in the wetting parameter. The wall perturbation process is found correctly to control the wetting at the boundary, and this leads to a wide range of possible applications. For the present, we wish simply to ensure that the 'plasma' preferentially wets the boundary, thereby denying adhesion of the red blood cell drops and maintaining an explicitly resolved layer of plasma at the boundary. Thin films of incompressible liquid at low Re (the 'lubrication regime') can sustain large hydrostatic pressures. An explicitly resolved layer of plasma also avoids the need to postulate the sub-lattice 'lubrication force' associated with narrow contacts in the lubrication regime. We note that white-cell adhesion could also be easily incorporated using the methods just described.

Tables 1 and 2 summarize the performance of our algorithm executed on a Silicon Graphics Origin 300 500 MHz IP35 (CPU: MIPS R14000) workstation. Table 1 shows the dependence of the memory requirements of the algorithm and execution time upon N, number of immiscible drops (fluids), based upon a 100 lattice updates on a 200 × 200 lattice, with the drop size decreasing as N increases, note. The information in table 1, which assumes a maximum of five colours or immiscible components per node *for all values of* N, emphasizes that the total memory requirement is tied to the choice of N_Q (=5, recall), number of 'recognized components' and therefore it does not scale with N. The execution time increases in proportion to the total length of all interfaces, although this is not apparent in the data of table 1, because of the particular way that the drop size is reduced as N is increased, (to assist packing).

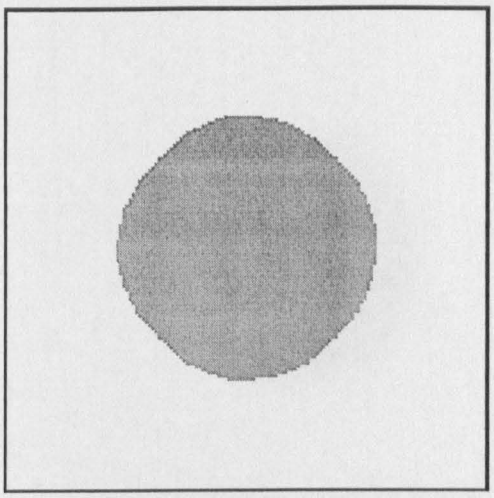

a(i)

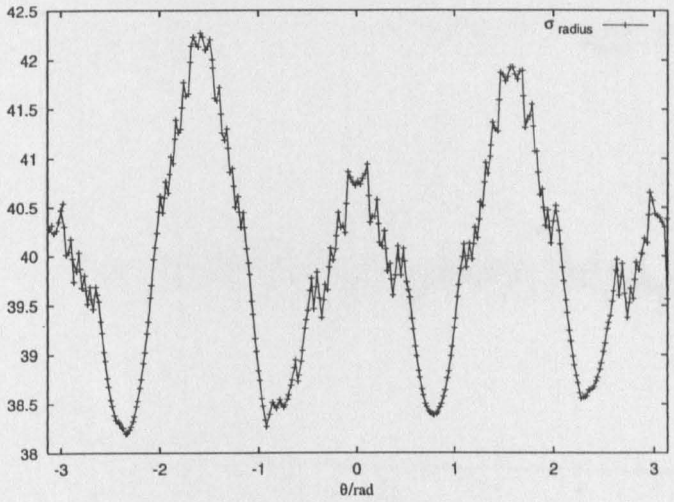

a(ii)

Figure 2. Results performed on a 150 × 150 lattice with drops initialized to radius 40 lattice units. The images *a*(i), *b*(i) and *c*(i) show the shape of the interface for the different values of λ: λ = 1.0 (too small), λ = 2.1 (close to optimum) and λ = 4.0 (too big). The corresponding plots *a*(ii), *b*(ii) and *c*(ii) show drop radius as a function of angular position in the interface. The optimum value of the parameter λ occurs close to the predicted value (2.15) obtained from equation (16).

Table 2 shows the dependence of the memory of the algorithm and execution time upon $N = N_Q$, based upon a 100 lattice updates on a smaller 100 × 100 lattice, now with the drop size fixed as N increases over a smaller range. Unsurprisingly, given these conditions, the execution times and memory requirements in table 2 both increase in proportion to $N = N_Q$.

4. Validation and application of the lB model

In this section we first describe the validation of the improved lB interface followed by simulation results typical of the veinule-scale microcirculation. In respect of the latter, we

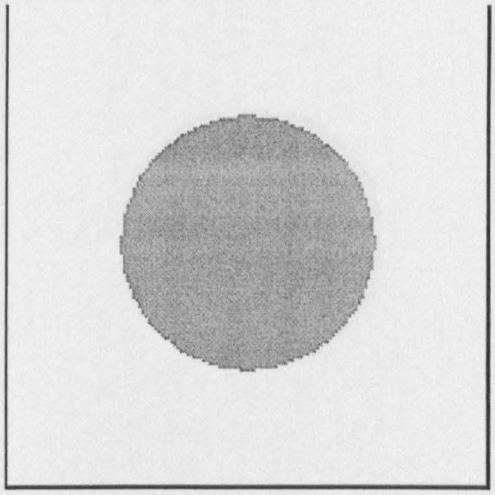

b(i)

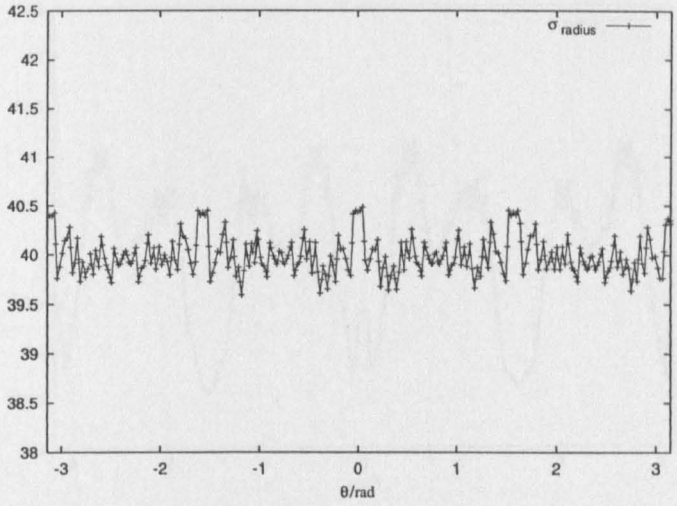

b(ii)

Figure 2. (Continued.)

consider (i) single advecting, deforming drops, (ii) control of coalescence and (iii) many immiscible, deformable drops.

Note that the contact angle for three components α, β and γ in contact may be compared with its value from Young's equation:

$$\cos(\theta_e) = \frac{\gamma_{\alpha\gamma}}{\gamma_{\alpha\beta} + \gamma_{\beta\gamma}} \tag{23}$$

in which $\gamma_{\alpha\beta}$ is the macroscopic $\alpha\beta$ surface tension, proportional to $\sigma_{\alpha\beta}$.

4.1. Drop interface

Simulations reported here refer to a lattice fluid nominally at rest, initialized to an equilibrium state of uniform density $\rho = 1.80$ on a 150×150 lattice with a drop of initial radius 40 lattice units. Evolution was performed to steady state. The interface and lattice collision parameters

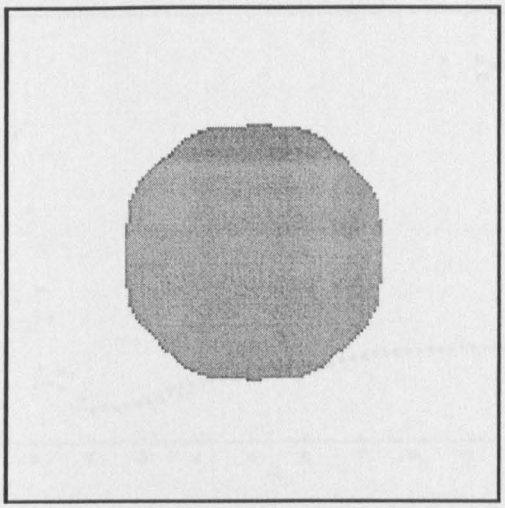

c(i)

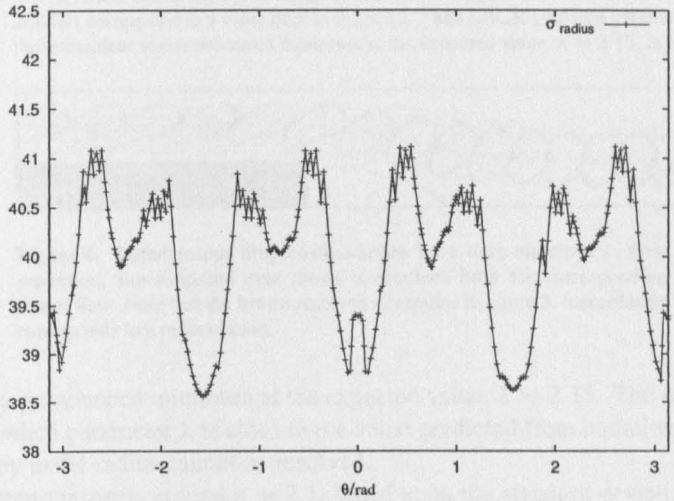

c(ii)

Figure 2. (Continued.)

were 0.0075 and 1.7, respectively. Micro-current activity and isotropy were assessed at each time step by the scalar lattice summation of the velocity residual (equation (17)). This quantity was used to identify the steady state and the results were obtained for a wide range of ratio parameter λ.

Drop isotropy is measured in graphs of the drop radius (distance from the centre of mass to multi-coloured sites in the interface) as a function of angular position. Figures 2*a*(i), *b*(i) and *c*(i) depict the position of the interface for $\lambda = 1.0$ (too small), $\lambda = 2.1$ (close to optimum) and $\lambda = 4.0$ (too big) and the corresponding plots *a*(ii), *b*(ii) and *c*(ii) represent drop radius with angular position. The increased range and resolution of λ shown in figure 3 confirms the trend. Figure 3 shows two sets of data, each normalized to its value at parameter $\lambda = 2.15$. The first set (circles) shows the standard deviation of the drop radius, the second (triangles) shows the micro-current activity measured by the parameter m (equation (17)). Both series

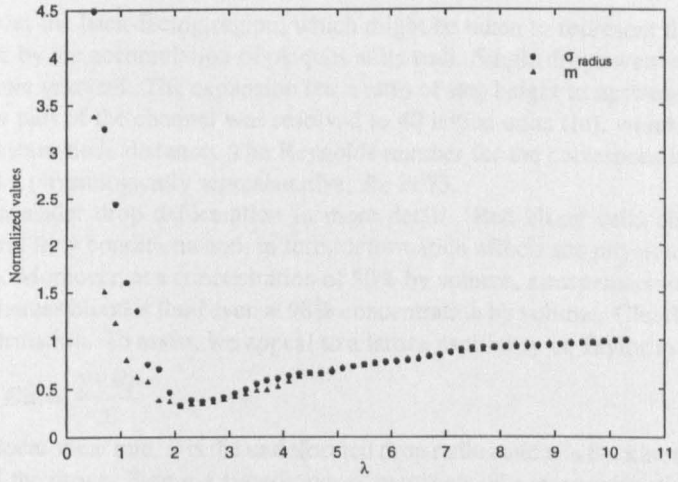

Figure 3. The standard deviation of a drop radius (circles) normalized to its value at parameter $\lambda = 2.15$ and the micro-current activity m (triangles) again normalized to their value at $\lambda = 2.15$. All data correspond to a value of $\sigma = 7.5 \times 10^{-3}$ and LBGK collision parameter $1/\tau = 1.7$. Note the coincident and pronounced minimum at the expected value, $\lambda \approx 2.15$, in both series of data.

Figure 4. Instantaneous drop configurations for a drop entrained in flow past an asymmetric expansion, superimposed over shows streamlines from the corresponding undisrupted (single phase) flow. Note that the lowest resolved streamline in figure 3, immediately to the left of the step corresponds to a recirculation.

of data show a pronounced minimum at the expected value, $\lambda = 2.15$. The optimum circular shape occurs when parameter λ is close to the value predicted from equation (16) and in this case anisotropy in the radius cannot be resolved.

Careful measurements around $\lambda = 2.1$, based upon the standard deviation of the radius, reveal weak dependence of optimum λ upon the value of LBGK relaxation parameter τ. This is understandable, since the theory behind equation (16) is only first order in product $\tau\sigma$ [16].

4.2. Deforming, advecting drop

For definiteness, we take an asymmetrically expanding duct. A number of detailed, physiologically relevant questions arise around this geometry (figure 4), e.g., for given Re, what size of drop can become trapped in any feature corresponding to a primary vortex of the undisturbed flow? Our aim here is to demonstrate the potential of our lB simulation in such problems.

In the results presented here, the effects of gravity are ignored. Although the effects of gravity are not important in most mesoscale blood flow applications, it is still possible to approximate the influence of gravity by the use of different constants g in the evolution (equations (1) and (3)). Flow was forced by a constant body force, G (equation (3)), applied uniformly to both fluids. The step was simulated as adjacent front-facing and back-facing steps in a channel with periodic boundary conditions in the horizontal direction. Figure 4 shows

results only from the back-facing region, which might be taken to represent the occlusion of a vessel caused by the accumulation of plaques at its wall. Single drops were entrained by an effective pressure gradient. The expansion has a ratio of step height to upstream throat of 1/3 and the narrow part of the channel was resolved to 40 lattice units (lu), which are defined to be the shortest inter-node distance. The Reynolds number for the corresponding undisturbed flow was set at a physiologically representative, $Re = 73$.

We now consider drop deformation in more detail. Red blood cells change shape in response to local flow conditions and, in turn, deformation affects the physiological function of the red cells. Moreover, at a concentration of 50% by volume, a suspension of solid spheres cannot flow, whereas blood is fluid even at 98% concentration by volume. Clearly it is essential to capture deformation. To assist, we appeal to a lattice capillarity or Taylor number:

$$Ca = \frac{\gamma \nu R \rho}{\Sigma} \tag{24}$$

where γ is the local shear rate, R is the undeformed drop radius and ν is the kinematic viscosity of the liquid of the drops. Figure 4 superimposes snapshots of a reasonably deformable drop over the streamlines of the corresponding undisturbed flow. The Taylor number was set at $Ca = 0.04$ and the initial radius 7 lu. This choice of Ca was made in order to produce a drop deformation similar to that photographed for a red blood cell deforming in a hydrodynamic focusing experiment [19].

By adjusting the collision parameter of the drop fluid in the range $0.4 < \tau < 1.99$, it is possible to obtain a drop/fluid viscosity ratio up to approximately 300. However, for all our results, this viscosity ratio is set to be 7, which is approximately the correct ratio for the viscosity of the internal fluid of red blood cells by comparison with the surrounding plasma. These arguments clearly ignore the effects of the elastic properties of the cell membrane which we have assumed to be less important in the class of flows we consider. Note also that the lowest value of resolved streamline in figure 4 is actually recirculating.

4.3. Many deforming, advecting drops: blood flow

In high volume fraction flows, drops can come close to the simulation boundary. To avoid the need to postulate sub-lattice lubrication forces, we always encourage an explicit layer of plasma fluid to remain between drops and the boundary. We need to ensure preferential wetting of the boundary by the plasma fluid and this requires control over contact angle. Before proceeding to consider applications and results for veinule-scale simulation, we must therefore verify the wetting behaviour of our lB algorithm.

To demonstrate our liquid–liquid wetting algorithm (section 3.3), figure 5 shows typical results obtained for three static, immiscible fluids on a lattice, dimension 150×50, reciprocal collision parameter $1/\tau = 1.7$. This data was obtained by assigning a range of different values to the respective surface tensions. A circular arc has been fitted through the set of mixed nodal densities to obtain the interface fit and hence θ_e. Each of the interfacial points in figure 5 lies <10th lu from the fitted circle. Results in figure 5 are in excellent agreement with the expected values; the difference between the measured and expected contact angles (equation (23)) evaluates to <2%.

In respect of liquid-boundary wetting, simulation results achieve the similar degree of agreement. However, the shapes of the drops at a solid surface (figures 6) are not so circular; the fit shows an average of ≈0.5 lu between the fit and the interpolated interface. This discrepancy is due to the cumulative effect of the micro-current at the simulation walls, which drives very small circulations sufficient to disturb the drops in a rest simulation. However, these effects are small and normally overwhelmed by flow.

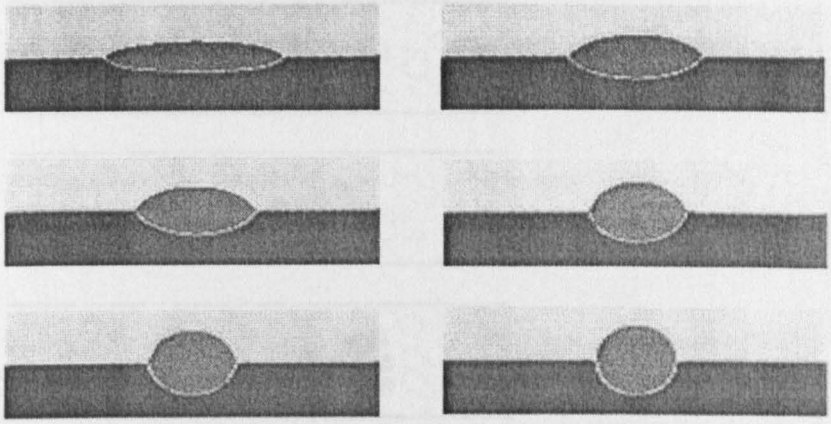

Figure 5. Results obtained for three immiscible fluids at three different relative surface tensions, chosen so as to vary the resulting contact angle. Data shown derive from a simulation of 10^5 time steps, on a lattice, dimension 150×50, again with collision parameter $1/\tau = 1.7$ (all fluids). Measured contact angle values may be compared with the theoretical values given by Young's equation.

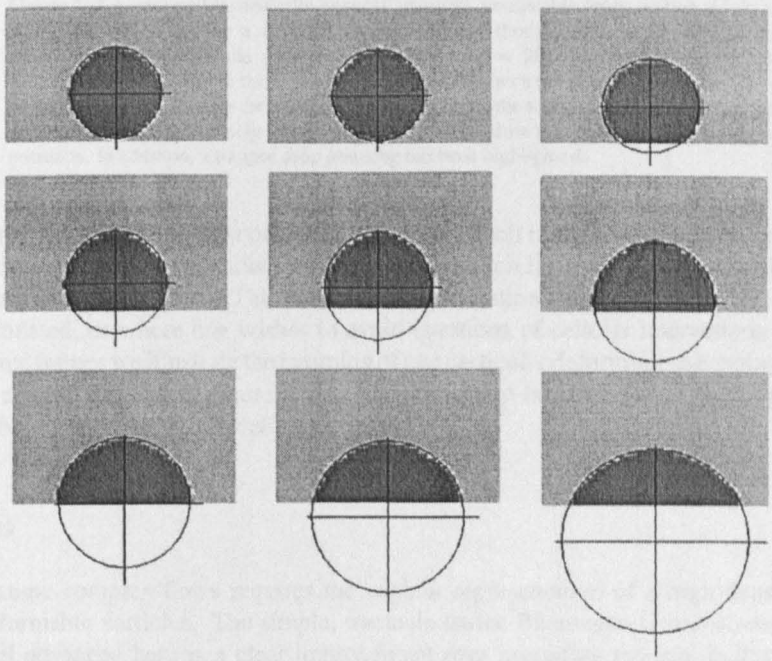

Figure 6. Results obtained for a fluid in contact with a boundary, with increasing wall wetting in 'reading order'. The collision operator in use was again $1/\tau = 1.7$ and the assumed steady state at 10^5 steps. System size was 100×80.

The results shown in figure 7 represent the flow which our model is aiming to recover. Sixty incompressible, neutrally buoyant, mutually immiscible drops of identical internal viscosity and surface tension were initialized on a lattice of size 220×50 and forced by a uniform pressure gradient. This internal geometry is broadly characteristic of the veinule

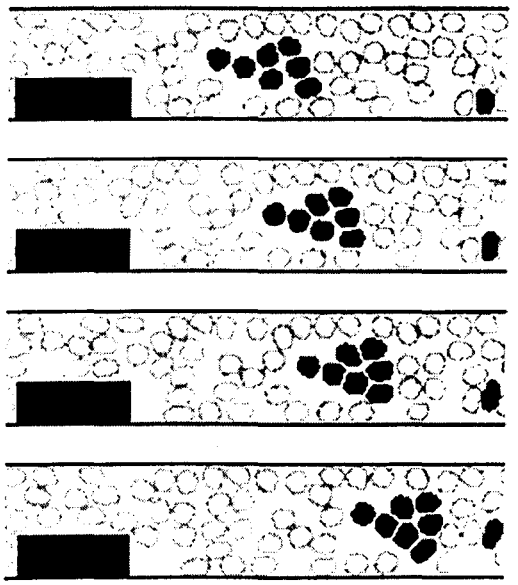

Figure 7. Incompressible, neutrally buoyant, identical, immiscible drops, initialized on a lattice, 220 × 50, and forced by a uniform pressure gradient (body force), in an internal geometry characteristic of the veinule microcirculation (here $Re = 20$). Periodic boundary conditions were in force left to right in this simulation. The figure shows a developing time sequence of drops, in most cases showing only the interface of each drop with the surrounding fluid; however, a cluster of drops has been completely shaded in black so as to allow the reader to track their respective positions. In addition, a trapped drop *jamming* has been highlighted.

microcirculation. Periodic boundary conditions were applied left to right. The ambient plasma fluid was set strongly to wet the boundary wall. Thus, an explicit layer of fluid was maintained between all drops and the boundary. This is a necessary precaution where no lubrication forces have been postulated, or where one wishes to avoid questions of cellular interactions at the wall. In four time frames we illustrate the jamming of one particular deforming–advecting drop (shaded grey) and the dispersion of an initially compact group (shaded black). Throughout, the role of deformation in the drops/cells is clear.

5. Conclusions

The study of some complex flows requires the explicit representation of a high density of suspended, deformable particles. The simple, tractable lattice Bhatnagar–Gross–Krook (lB) interface model advanced here is a clear improvement over preceding models, built on the basic Gunstensen algorithm [4] (figures 2 and 3). It has application to situations where it is necessary to recover only hydrodynamics of separated components. The micro-current reduction from this algorithm alone is important in opening up low Re, high Ca (*microfluidic* or surface tension dominated) flows to lB, for it is in this regime that the lB micro-current field is comparable to that of the simulated flow.

In veinule blood flow, inertial forces are more important and Ca is larger. Our application, in figure 4, demonstrates the considerable potential for modelling the advection of deformable particles. In figure 4 the drop appears to deform considerably. As an aside it follows, quite closely, a streamline of the corresponding undisturbed flow, but with considerable deformation.

That no corresponding statement seems possible when considering multiple drops, at high concentration (figure 7), is unsurprising.

With the addition of control over coalescence (evaporation) (section 3.3), our lB method also has applications to any flow containing deformable particles which can be modelled as drops, the results of figures 5 and 6, culminating in figure 7, demonstrate its ability to provide explicit information on the location of the drops and the interdependence of their motions.

Figure 7 strongly supports our controlled-coalescence lB model as the vehicle of that representation of the 'veinule' mesoscale of blood flow in which a high volume fraction of strongly interacting, advecting and deforming cells, confined by vessels of diameter comparable to the cell diameter, are modelled as non-coalescing liquid drops (section 2). The results of simulations show real potential. In figure 7 it is tempting to identify (a) 'plug flow' of drops, giving plasma-rich regions, with positive implications for the modelling of plasma skimming, (b) trapping in the primary recirculation and notably (c) the role of deformation. All these features are promising for the applications outlined in section 2. We stress that to regulate coalescence whilst controlling interfacial tension and internal drop viscosity (and hence effective particle deformability) is key in this underlying model.

The lB scheme described in this paper should be of considerable use in modelling the microcirculation. As a next step, with a simple pipe geometry, our lB model might be used quantitatively to investigate the 'phase transitions' and variations in viscosity associated with haematocrit. In this challenging application one would need, for example, explicitly to calibrate parametrization for the different fluids (to represent red, white cells, platelets, etc). However, we believe that the results presented here make the necessary investment of effort worthwhile.

References

[1] Succi S 2001 *The Lattice Boltzmann Equation for Fluid Mechanics and Beyond* (Clarendon Press) and references therein

[2] Care C M, Halliday I and Good K 2000 Lattice Boltzmann Nemato-dynamics *J. Phys. Condens. Matter* **12** 665

[3] Koponen A 1998 Simulations of fluid flow in porous media by lattice gas and lattice Boltzmann methods *PhD thesis* University of Jyvakyla, Finland

[4] Gunstensen A K, Rothman D H, Zaleski S and Zanetti G 1991 Lattice Boltzmann model of immiscible fluids *Phys. Rev.* A **43** 4320

[5] Swift M R, Osborn W R and Yeomans J M 1995 Lattice Boltzmann simulation of non-ideal fluids *Phys. Rev. Lett.* **75** 830

[6] Thompson S P, Halliday I and Care C M 1999 Mesoscopic hydrodynamics of diphasic lattice Bhatnagar–Gross–Krook fluid interfaces *Phys. Chem. Chem. Phys.* **1** 2183

[7] Shan X W and Chen H D 1994 Simulation of nonideal gases and liquid–gas phase transitions by the lattice Boltzmann equation *Phys. Rev.* E **49** 2941

[8] Benzi R, Succi S and Vergassola M 1992 The lattice-Boltzmann equation—theory and applications *Phys. Rep.* **3** 145

[9] Chen S and Doolen G D 1998 Lattice Boltzmann method for fluid flows *Ann. Rev. Fluid Mech.* **30** 329

[10] Do-Quang M, Aurell E and Vergassola M An inventory of lattice Boltzmann models of multiphase flows *Internal Report* Webpage www.psci.kth.se/Activities/Reports

[11] Damiano E R, Westheider J, Tozeren A and Ley K 1996 Variation in the velocity, deformation, and adhesion energy density of leukocytes rolling within venules *Circ. Res.* **79** 1122

[12] Quarteroni A 2001 *SIAM News* July/August **9**

[13] Caro C G, Pedeley T J, Schroter R C and Seed W A 1978 *The Mechanics of the Circulation* (Oxford: Oxford Medical Publications)

[14] Zou Q and He X Y 1997 On pressure and velocity boundary conditions for the lattice Boltzmann BGK model *Phys. Fluids* **96** 1591

[15] Zou Q, Hou S, Chen S and Doolen G D 1995 Analytical solutions of the lattice Boltzmann BGK model *J. Stat. Phys.* **81** 319

[16] Halliday I, Care C M and Thompson S P 1998 Macroscopic surface tension in a lattice Bhatnagar–Gross–Krook model of two immiscible fluids *Phys. Rev.* E **57** 514
[17] Halliday I, Hammond L A, Care C M, Good K and Stevens A 2001 Lattice Boltzmann equation hydrodynamics *Phys. Rev.* E **64** 011208
[18] Qian Y H, d'Humières D and Lallemand P 1992 Lattice BGK models for the Navier–Stokes equation *Europhys. Lett.* **17** 479
[19] Kachel V *et al* Webpage www.cyto.purdue/flowcyt/educate/ee520
[20] Dupin M M, Halliday I and Care C M (in preparation)

10.1098/rsta.2004.1403

THE ROYAL SOCIETY

A lattice Boltzmann model of flow blunting

BY M. M. DUPIN, I. HALLIDAY AND C. M. CARE

Materials Research Institute, Sheffield Hallam University, Howard Street, Sheffield S1 1WB, UK (mriih@exchange.shu.ac.uk)

Published online 3 June 2004

We review our recent multi-component lattice Boltzmann equation method for the simulation of a large number of mutually immiscible liquid species and then apply it to the simulation of dense volume fraction suspensions of deformable particles in internal geometry. In particular, we illustrate the scope of our method by applying it to the simulation of pipe flows containing a high volume fraction of monodisperse suspended, deformable particles. The particles are modelled as immiscible, relatively viscous liquid drops. We modify the 'solidity' of the particles by modifying their viscosity and surface tension and demonstrate the effect of the solidity upon the blunting of the velocity profile.

Keywords: lattice Boltzmann; multi-phase flow; blunting; particle solidity

1. Introduction

The lattice Boltzmann (LB) method shows real promise when applied to complex multi-component flow at low Reynolds number and a range of LB techniques have been developed to model fluid interfaces (e.g. Gunstensen *et al.* 1991; Thompson *et al.* 1999), with perhaps the Shan–Chen approach (Shan & Chen 1994) being the most popular. Here we consider two-dimensional simulations of mutually immiscible, and interacting, drops. The development of a method which is computationally efficient for $N \gg 2$ drops is a prime consideration of this work.

We base this work on an interfacial model, due originally to Gunstensen *et al.* (1991), with improved interface isotropy and reduced micro-current activity (Dupin *et al.* 2003). Where hydrodynamics alone defines a continuum case study, the Gunstensen interface algorithm is desirable, simply from the point of view of computational memory resources. From the many-component point of view, it provides a sharp interface necessary to obtain an efficient method in execution time and memory requirements, by reducing the number of nodes containing more than one colour (mixed nodes).

In § 2*a*, we outline a binary model, with some recent improvements, and in § 2*b*, we generalize to N immiscible fluids. In § 3, we consider how the 'solidity' of incompressible liquid drops, used to model a dense deformable particulate suspension, may be assessed by profile blunting (Dupin *et al.* 2004).

One contribution of 21 to a Theme 'Connecting scales: micro, meso and macro processes'.

2. General model

Our basic model is the two-dimensional nine-velocities (denoted D2Q9) weakly compressible LBGK (lattice Bhatnagar–Gross–Kross) model (Succi 2001), which has a single scalar collision parameter. In our multi-component version, segregation and surface tension are produced in any region of the lattice where colours mix by additional local (microscopic) rules. Such a region defines a fluid–fluid interface with essentially correct macroscopic (continuum-length-scale) properties (Thompson *et al.* 1999).

(*a*) *The two-phase model*

Since target flows are heavily interface dominated, the surface tension of our incompressible droplets is of prime consideration. It is activated by perturbing the post-collided densities $f_i(\boldsymbol{r},t)$ of any mixed node as follows:

$$\Delta f_i(\boldsymbol{r},t) = \lambda_i \sigma C(\boldsymbol{r},t)\cos(2(\theta_f(\boldsymbol{r}) - \theta_i)), \tag{2.1}$$

where λ_i is a modulation parameter ensuring good isotropy of the interface and reduced micro-current flow (see Dupin *et al.* (2003) for more details). λ_i takes a value of $\sqrt{3}/2$ for the short links and unity for the long links (cf. the D2Q9 model). C is a concentration factor which limits activation of surface tension to multicoloured nodes. θ_f is the direction of the local colour gradient, being the normal to the local interface as a good approximation. θ_i is the direction of the ith link.

Colour segregation is ensured by numerically reallocating colour in the colour-blind post-collided f_i so as to maximize the work done by the colour flux against the colour gradient (Gunstensen *et al.* 1991).

(*b*) *The N-phase model*

We now consider the generalization of the diphasic model in (§ 2 *a*) to a mixture of N immiscible liquids in which mutual coalescence and evaporation is completely suppressed.

Our generalization to N immiscible components assigns each fluid a 'colour' superscript, $\Gamma = 0, 1, 2, 3, \ldots, (N-1)$. Fluids with different values of Γ can have different properties, e.g. collision parameters τ_Γ and, accordingly, viscosity ν_Γ. Now, for N different species, multi-component LB quickly demands impractical amounts of computer storage, as N increases. However, for non-evaporating fluids forming 'sharp' interface drops the arrays for N hydrodynamic quantities ($f_i^\Gamma(\boldsymbol{r},t)$, $\rho^\alpha(\boldsymbol{r},t)$), are very sparse, hence the use of the Gunstensen-type interface.

Consequently, to minimize storage, we record only N_c, with $N_c < Q \ll N$, species at any node, which gives considerable reduction in the required storage. The sharp interfaces from our Gunstensen-type interface method mean minimal mixing and a reduction in the number of different colours found on a node, as well as a reduction in the total number of mixed nodes. In practice we take $N_c = 5$. This value is found to be adequate for even the most intimately monodisperse multi-component flows. Note, however, that the number of colours, or immiscible components, varies between nodes and in time.

In our generalization to N different fluids, we assign each local hydrodynamic density ($f_i(\boldsymbol{r},t)$) a superscript α ($0 \leqslant \alpha < N_c$), which is used to identify the fluids

associated with the node. Clearly, the identification of particular fluids within a node must refer to the lattice map of absolute colour, $l(\boldsymbol{r}, i, \alpha)$. However, for such a map sufficient information can be stored in a four-dimensional array of integer type. Both l and the hydrodynamic densities f now have a subscript set $\{x, y, i, \alpha\}$ to identify, for lattice position $\{x, y\}$, direction i, the colours present at the node. We note that these two quantities propagate jointly along the lattice.

By recording at most N_c species at each node, the storage and time requirements are reduced by a factor N_c/N, to levels comparable with the diphasic model (see § 2 *a*).

In the N-phase model, as in the diphasic model, collision is performed in three steps: mixed fluid collision, perturbation and colour reallocation. The collision of the mixed fluid's momentum densities,

$$f_i(\boldsymbol{r}, t) = \sum_{\alpha=0}^{N_c-1} f_i^{\alpha}(\boldsymbol{r}, t), \tag{2.2}$$

is performed on the mixed fluid, exactly after Zou *et al.* (1995), with an effective relaxation parameter giving, at a mixed node, the effective viscosity

$$\nu(\boldsymbol{r}, t) = \frac{1}{\rho(\boldsymbol{r}, t)} \sum_{\alpha=0}^{N_c-1} \rho^{\alpha}(\boldsymbol{r}, t)\nu^{\alpha},$$

where ν_α defines the chosen kinematic viscosity of any component α present at $\boldsymbol{r}$ which relates to a particular ν^{Γ} through the colour map $l(\boldsymbol{r}, i, \alpha)$, and

$$\rho(\boldsymbol{r}, t) = \sum_{\alpha=0}^{N_c-1} \rho^{\alpha}(\boldsymbol{r}, t), \qquad \rho^{\alpha}(\boldsymbol{r}, t) = \sum_{i=0}^{Q-1} f_i^{\alpha}(\boldsymbol{r}, t).$$

Controlling coalescence amounts to dealing consistently with all possible colour pairs at every mixed node, in order to eliminate any mixing between species after propagation. This requirement may still be stated as a need to maximize the work done by a generalized colour flux against a generalized colour gradient (following Gunstensen *et al.* 1991). Accordingly, the diphasic colour gradient is generalized to any pair of fluids α and β at a node.

We may define a colour gradient at the interface between fluid α and fluid β by what we assume to be its local normal:

$$\boldsymbol{I}_{\alpha\beta}(\boldsymbol{r}) = \sum_i (\rho^{\alpha}(\boldsymbol{r} + \boldsymbol{c}_i) - \rho^{\beta}(\boldsymbol{r} + \boldsymbol{c}_i))\boldsymbol{c}_i. \tag{2.3}$$

This colour gradient is used to perturb the mixed fluid's momentum densities (equation (2.2)). For the interface between two components α and β we use a generalized perturbation after equations (2.1):

$$\Delta f_i(\boldsymbol{r}, t) = \sum_{(\alpha,\beta)} \Delta f_i^{\alpha,\beta}(\boldsymbol{r}, t) = \sum_{(\alpha,\beta)} \sigma_{\alpha\beta}\lambda_i C_{\alpha\beta}(\boldsymbol{r}, t) cos(2(\theta_f(\boldsymbol{r}) - \theta_i)), \tag{2.4}$$

in which there is no summation on repeated subscripts, but the summation is taken on all possible pairs α, β. $\sigma_{\alpha\beta}$ is a surface tension parameter for the interface between

fluid α and fluid β and

$$C_{\alpha\beta}(\boldsymbol{r},t) = 1 - \left|\frac{\rho_\alpha(\boldsymbol{r},t) - \rho_\beta(\boldsymbol{r},t)}{\rho_\alpha(\boldsymbol{r},t) + \rho_\beta(\boldsymbol{r},t)}\right| \tag{2.5}$$

is the concentration factor for the α, β fluid pair, after the diphasic model of § 2 *a*. λ_i is the modulating factor introduced in § 2 *a*. We now define an 'average' colour gradient which points towards component α and away from the total of all other components present at the node at position $\boldsymbol{r}$:

$$\boldsymbol{f}^\alpha(\boldsymbol{r}) = \sum_i [2\rho^\alpha(\boldsymbol{r}+\boldsymbol{c}_i) - \rho(\boldsymbol{r}+\boldsymbol{c}_i)]\boldsymbol{c}_i. \tag{2.6}$$

The same calculations ((2.4) and (2.5)) are repeated for each pair of fluid components α, β present at the node, position $\boldsymbol{r}$. To avoid coalescence, the appropriate colour gradient $\boldsymbol{f}^\alpha(\boldsymbol{r})$ (equation (2.6)) is used to recolour component α within each node, essentially in the same way as for a binary fluid but with the order in which components α are treated being significant. Note that to calculate the colour gradient (2.6) requires knowledge of the absolute colour, not just the relative amounts of the different colours present in a local environment.

It is crucial to note that we have shown that execution time and memory requirements scale linearly with the simulation size (total number of nodes) and N_c but are almost independent of N (Dupin *et al.* 2003).

3. Simulations

As an initial step, to avoid the need to postulate sublattice lubrication forces associated with thin layers of fluid, we manipulate wetting to ensure that a resolved layer of ambient liquid always remains between drops and any boundary. We therefore need to ensure preferential wetting of the boundary and suspended drops by the ambient fluid. This was achieved for the simulations here in the manner described in Dupin *et al.* (2003). The correct hydrodynamics recovered in Dupin *et al.* (2004) (also depicted in §§ 3 *a* and 3 *b*) tend to support this assumption for a volume fraction of particle, Φ, up to 0.6 at least. Targeted flows are, by intention, heavily interface dominated. We investigate the blunting of the flow profile, β (see below), of a suspension of N particles at a volume fraction Φ of viscosity ratio (droplets/surrounding) Λ, surface tension σ, in a straight channel. We employed the well-established mid-link bounce-back method (Succi 2001) top and bottom. Periodic boundary conditions were applied left and right. The flow rate is quantified by the pressure gradient ΔP/length along the channel. By inspection, our blunted profiles have noticeable departure from parabolic profiles. We measure averaged departure, at normalized cross-duct distance $\bar{y} = 0.25$ and $\bar{y} = 0.75$, by defining the blunting β:

$$\beta \equiv \frac{\bar{v}(\bar{y}=0.25) + \bar{v}(\bar{y}=0.75)}{2 \times 0.75}, \tag{3.1}$$

in which 0.75 is the height of a normalized parabola. With this definition, a flat velocity profile is characterized by $\beta = 1.33$ and a parabolic velocity profile by $\beta = 1.00$.

(*a*) *Rigid particles*

It has been found experimentally that for rigid suspended particles, the velocity profile is determined *solely* by the suspension concentration and the relative particle size (Caro *et al.* 1998). We considered that immiscible incompressible drops with $\Lambda = 50$ and high surface tension represented solid particles over that range of flow rates (specified by ΔP) for which the expected invariance in bulk flow parameter β was observed. Note, however, that, by increasing ΔP without bound, small changes in β occur (Dupin *et al.* 2004), showing the limits of the solid-particle behaviour of our droplets at high forcing.

(*b*) *Flexible particles*

For immiscible liquid drops (i.e. flexible particle suspensions) with $\Lambda = 1$ and smaller σ on the other hand, we observed the expected decrease of β upon increasing ΔP (Dupin *et al.* 2004; Caro *et al.* 1998).

(*c*) *Simulation results: rigid or flexible particles?*

It is appropriate to test our method by using it to resolve the changes that occur between deformable- and solid-particle-based bulk suspension behaviour, using parameters Λ and σ. We consider dense suspensions $\Phi = 0.6$ in order to ensure $\beta \to 1.33$ (solid-particle bulk behaviour, § 3 *a* above). With large Λ and σ, we limit ΔP to lie within the constant-β 'solid-particle' regime (§ 3 *a*). For small Λ and σ, the choice of ΔP should allow $\beta \to 1.00$ (deformable suspension bulk behaviour) to be observable (§ 3 *b*). Figure 1 shows the contours of the departure of β from a parabola as a function of Λ and σ. The data of this figure were compiled using the method outlined at the start of this section.

The simulation size was 250×100, the ambient fluid had a relaxation parameter $\omega = 1.7$, and the particle relaxation parameter varied between 0.1 and 1.9 in increments of 0.2 (giving viscosity ratios from 0.3 to 110). The surface tension varied (14 different values) from its maximum value (giving stable simulations in this configuration with $\sigma \leqslant 0.006$) down by three orders of magnitude. Values of β were calculated at steady state, typically after 5×10^5 iterations. The surface is an interpolation of the fitted measurements. The measured values of β departed typically from this interpolated surface by 10% (standard deviation from the data and the interpolated curve). This scattering is due to the noise on the measured velocity profile, from which β is extracted.

As we saw previously, one can relate blunting dependence to solidity. With the set of parameters of figure 1, it provides a calibration of the 'solidity' of the suspended particles upon parameters σ and Λ (through the measured value of β). In terms of elaborating a possible empirical rule, it is interesting to note that curves of β as a function of Λ, parametrized by σ, appear to be self-similar. The curves are similar in turn to self-similar curves of β as a function of σ, parametrized by Λ. It is worth noticing that figure 1 confirms the droplet behaviour that one would expect: the droplet's 'solidity' (here measured by β) increases with increasing viscosity ratio (Λ) and with increasing droplet surface tension (σ).

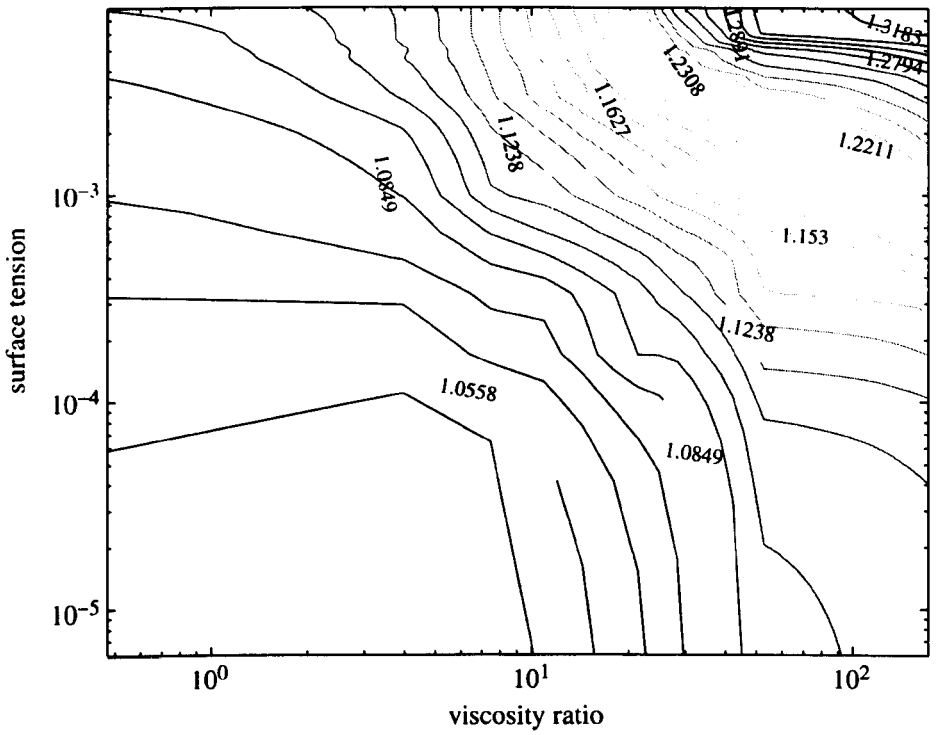

Figure 1. Blunting β contours for the flow of droplets in suspension as a function of their surface tension and viscosity (the surface from which these contours have been taken is an interpolation of the values of β calculated from fitted velocity profiles). The pure parabolic profile corresponds to $\beta = 1.0$ and the plug flat profile to $\beta = 1.33$.

4. Conclusion

In conclusion, we have demonstrated a model for large numbers of non-coalescing, non-evaporating, mutually immiscible incompressible liquid drops. From the results here (figure 1), the model supports a large range of parametrization, e.g. ambient fluid to drop viscosity ratio and surface tensions, and is able to recover correct bulk 'macroscopic' flows from the particular set of microscopic rules in use. This observation is particularly relevant as a vindication of our representation of lubrication forces. With the help of this new lattice Boltzmann scheme, we have been able to *microscopically* parametrize dense suspensions of immiscible drops by relative viscosity and surface tension to produce *macroscopic* effects on bulk channel flows which, qualitatively at least, encompass the range of behaviour from solid suspensions to suspensions of deformable particles. In addition to the latter, this calibration provides crucial information for future investigations where one might need to model solid particles at a given flow rate. This opens unique possibilities for investigation, where deformability cannot be ignored when simulating advecting suspensions.

Where particle deformation is high, one might expect close contacts between drops at high volume fraction. Accordingly, the representation of sublattice lubrication forces in the algorithm is the first point at which work needs to be undertaken.

References

Caro, C. G., Pedeley, T. J., Schroter, R. C. & Seed, W. A. 1998 *The mechanics of the circulation.* Oxford Medical Publications.

Dupin, M. M., Halliday, I. & Care, C. M. 2003 Multi-component lattice Boltzmann equation for mesoscale blood flow. *J. Phys.* A **36**, 8517–8534.

Dupin, M. M., Halliday, I. & Care, C. M. 2004 Multi-component lattice Boltzmann equation. (Submitted.)

Gunstensen, A. K., Rothman, D. H., Zaleski, S. & Zanetti, G. 1991 Lattice Boltzmann model of immiscible fluids. *Phys. Rev.* A **43**, 4320–4327.

Shan, X. W. & Chen, H. D. 1994 Simulation of non-ideal gases and liquid–gas phase transitions by the lattice Boltzmann equation. *Phys. Rev.* E **49**(4), 2941–2948.

Succi, S. 2001 *The lattice Boltzmann equation.* Oxford: Clarendon.

Thompson, S. P., Halliday, I. & Care, C. M. 1999 Mesoscopic hydrodynamics of diphasic lattice Bhatnagar–Gross–Krook fluid interfaces. *Phys. Chem. Chem. Phys.* **1**, 2183–2190.

Zou, Q., Hou, S., Chen, S. & Doolen, G. D. 1995 Analytical solutions of the lattice Boltzmann BGK model. *J. Stat. Phys.* **81**, 319–334.

10.1098/rsta.2004.1422

THE ROYAL SOCIETY

A many-component lattice Boltzmann equation simulation for transport of deformable particles

BY M. M. DUPIN, T. J. SPENCER, I. HALLIDAY AND C. M. CARE

Materials Research Institute, Sheffield Hallam University, Howard Street, Sheffield S1 1WB, UK (mriih@exchange.shu.ac.uk)

Published online 16 July 2004

We review the analysis of single and N-component lattice Boltzmann methods for fluid flow simulation. Results are presented for the emergent pressure field of a single phase incompressible liquid flowing over a backward-facing step, at moderate Reynolds Number, which is compared with the experimental data of Denham & Patrick (1974 *Trans. IChE* **52**, 361–367). We then access the potential of the N-component method for transport of high volume fraction suspensions of deformable particles in pressure-driven flow. The latter are modelled as incompressible, closely packed liquid drops. We demonstrate the technique by investigating the particles' transverse migration in a uniform shear ('lift'), and profile blunting and chaining.

Keywords: lattice Boltzmann; N-component flow; blunting; pressure-driven flow

1. Introduction

The expanding literature on the lattice Boltzmann method (hereafter LBM) may be classified into general model development (use) in simple (complex) geometry, turbulence, thermohydrodynamics and complex, N-component fluids. Simple geometries are used for quantitative comparisons or qualitative tests of new schemes. Typical of the latter, Hou *et al.* (1995) and Hou (1995) compare LBM and computational fluid dynamics (hereafter CFD) results for lid-driven cavity flow for a range of Reynolds numbers $10 \leqslant Re \leqslant 10^5$. Other geometries include backward-facing steps and arrays of cylinders (Qian *et al.* 1996; He & Luo 1997*a*; Chen *et al.* 1997), for both creeping and vortex shedding. Several informative reviews can be found (see, for example, Wagner 1994; Higuera & Luo 1989; Mei *et al.* 2000). Relative ease of boundary implementation makes LBM well suited for complex geometries. Typical of this application is work by He & Doolen (1997*a*, *b*), who also use an irregular lattice and an interpolation system. In porous media, the LBM's application to the problem of the emergence of macroscopic transport coefficients from microscopic dynamics has demonstrated its mesoscale credentials. Darcy's law has been confirmed in LBM schemes by Succi *et al.* (1989), Cali *et al.* (1992) and Ferreol & Rothman (1995). Fundamental LBM development is now a large area of research encompassing boundary models, numerical stability (Reider & Sterling 1995), non-uniform grids (He & Doolen 1997*a*, *b*; Filippova & Hänel 1998; Tölke *et al.* 1998) and spurious dynamics (Qian & Zhou

One contribution of 12 to a Theme 'Discrete-element modelling: methods and applications in the environmental sciences'.

1998). Several turbulence models are currently available (Martinez *et al.* 1994; Succi *et al.* 1991; Hou *et al.* 1996) and these may be coupled with thermohydrodynamic models (see below). Further afield, LBM models for the Schrödinger equation are under development (Succi 2002; Boghosian & Taylor 1997).

LBMs for fluids with an energy mode were initially developed by Alexander *et al.* (1993), to model monotonic gases. Subsequent improvements (Chen *et al.* 1994) have produced a model which agrees well with analytical results for Couette and Poiseuille flows. However, these thermohydrodynamic LBM models only allow small temperature variations, due to their limited stability arising from the lack of an H-theorem.

Simulating complex fluids is a strength of the LBM. Colloids have been considered with algorithmic generalizations to represent suspended particles (Ladd 1994), and other LBM models include magnetohydrodynamics (Chen *et al.* 1991), bubble growth (Yang *et al.* 2001) and granular flows (Luo *et al.* 1997). Most importantly for this work, two-phase fluids with spontaneous interface formation have been developed to model immiscible fluids (Swift *et al.* 1995; Gunstensen *et al.* 1991; Shan & Chen 1994; Halliday *et al.* 1998; Lishchuk *et al.* 2003), and, for N immiscible components ($N \gg 2$) by Dupin *et al.* (2003). It is on this area that we shall now concentrate.

Currently, LBM models fluid mixtures using two strategies, broadly termed 'bottom up' and 'top down'. On one hand, top-down strategies are adopted when appropriate behaviour may be postulated for the model: the system considered (often mesoscale) has an interface with a known equilibrium state. Free-energy LBM interface models (Swift *et al.* 1995) capture the kinematics and hydrodynamics of phase separation, for example. On the other hand, bottom-up strategies are adopted where hydrodynamics alone defines a continuum problem (as in the present work), or where, for very complicated systems, an equilibrium state of the interface is not known. In the latter case simpler LBM interface algorithms are equally valid (Do-Quang *et al.* 2000) and desirable from several points of view: computational efficiency (Dupin *et al.* 2003), their ability to embed additional physics directly and their ability to produce a sharp fluid–fluid interface which impacts minimally on the continuum length-scales of the application. A range of techniques has been developed to model such fluid interfaces with, perhaps, the Shan & Chen (1994) approach being the most popular. More details can be found in reviews by Benzi *et al.* (1992) and Chen & Doolen (1998).

In continuum hydrodynamics, the boundary between immiscible fluids should have no structure. However, surface tension in the (*mesoscale*) LBM is activated by methods which are *microscopic* and as a consequence, the emergent LBM interface has artefacts: small but spurious velocities or micro-currents and a finite thickness. It should be noted that another scheme for imposing surface tension by Lishchuk *et al.* (2003) has a greatly reduced micro-current activity. Here we aim to illustrate the potential of the two-dimensional N-component LBM applied to the transport of high-volume-fraction suspensions of deformable particles in internal pressure-driven flow. We model the latter particles as mutually immiscible, relatively viscous drops of incompressible liquid.

The paper is essentially divided into three further parts. We firstly review the core LBM method (§ 2). Secondly, we present an appropriate generalization, inserting practical immiscibility between a large number of drop species, in § 3. Finally, in § 4, we validate pressure-driven single-component flow with experimental evidence and

proceed to consider N-component problems such as transverse migration on single, deformable drops in a linear shear and the transport of dense suspensions. For the experienced reader, all new results/analysis are to be found there.

2. The Lattice Boltzmann equation for single-component fluids

There are several approaches to the modelling of fluid systems. Microscopic approaches ($<10^{-9}$ m) include molecular dynamics (MD) and non-equilibrium molecular dynamics (NEMD), mesoscale approaches ($<10^{-6}$ m) include lattice gas cellular automaton (LGCA) and lattice Boltzmann and macroscopic approaches ($>10^{-9}$ m) include the broad family of traditional CFD. This section proposes briefly to set the LBM into context and length-scale. For more detail the reader is directed to excellent, comprehensive reviews by Succi (2001), Chen & Doolen (1998) and Luo (2000).

(*a*) *Practical context of the lattice Boltzmann simulation*

At the microscopic scale, MD and NEMD (Goodfellow 1991; Allen & Tildesley 1997) solve numerically the Newtonian equations of motion for a set of explicitly modelled molecules. Both of these techniques show great potential but are impractical for continuum systems: current computer ability limits simulations to only $\sim 10^5$ molecules, *far* short of continuum scales. To bridge the gap, mesoscale methods like dissipative particle dynamics (DPD), Stokesian and Brownian dynamics and LGCA and LBM have evolved.

DPD simulation (Groot & Warren 1997; Español 2002) was originally developed by Hoogerbrugge & Koelman (1992) to avoid the lattice artefacts of LGCA (§ 2 *e*), while accessing hydrodynamic time- and space-scales. In DPD, point-like 'particles' move and interact with each other through prescribed conservative, repulsive, dissipative and stochastic forces whose amplitudes are governed by a fluctuation-dissipation theorem. These particles represent a population of molecules moving coherently. DPD is effectively a coarse graining of MD to a hydrodynamic mesoscale which can accommodate additional microphysics (possibly in the form of potentials) in the interest of multi-phase flows, colloids, and polymers. However, like MD, DPD is computationally expensive. Moreover, problems remain regarding its equation of state, diffusion coefficients and length-scale separations.

The LBM (Chen & Doolen 1998; Succi 2001) uses a discretized Boltzmann equation (§ 2 *g*) with fully discretized space, time and therefore velocity. Distributed groups of particles (hereafter densities) with the same discrete velocity move along links of a lattice and are redistributed at nodes, according to local collision rules. This locality brings decisive advantages to LBM: it is massively parallelizable, complex geometries are made trivial, and additional physics can be included.

In fact the LBM can be used, as in this paper, at continuum scales. However, by far the most popular single-component continuum-scale method remains CFD (Anderson 1995; Conner & Brebbia 1976).

(*b*) *Hydrodynamics of the lattice Boltzmann method*

We shall see that the macroscopic dynamics describing a standard LBM is a weakly compressible form of the Navier–Stokes (Landau & Lifshitz 1995) and continuity

equations

$$\partial_t(\rho) + \partial_\beta(\rho u_\beta) = 0, \tag{2.1}$$

$$\partial_t(\rho u_\alpha) + \partial_\beta(\rho u_\alpha u_\beta) = -\partial_\alpha P + \partial_\beta(2\nu\rho S_{\alpha\beta}) + \rho a_\alpha, \tag{2.2}$$

where a_α is a uniform acceleration acting on the lattice fluid, ν its kinematic viscosity, P the lattice fluid pressure, ρ the lattice fluid's density, $S_{\alpha\beta} = \frac{1}{2}(\partial_\beta u_\alpha + \partial_\alpha u_\beta)$ the rate of strain tensor and $\boldsymbol{u}$ the lattice fluid's velocity (see equation (2.20) for the definition of ρ and $\boldsymbol{u}$). The LBM has an ideal gas equation of state,

$$P = c_s^2 \rho, \tag{2.3}$$

where c_s^2 is the speed of sound squared. Equations (2.1) and 2.2 have solutions parametrized by a single dimensionless number, based on a characteristic lattice velocity U_0, lattice dimension L_0 and the LBM's kinematic viscosity ν: the lattice Reynolds number

$$Re = \frac{U_0 L_0}{\nu}, \tag{2.4}$$

which quantity may be directly compared with the Reynolds number of the flow under study. Note that, for LBM, the speed of sound c_s is only $O(1)$, which induces some problems for high-Re applications of the standard LBM.

(c) *Theoretical foundations of the lattice Boltzmann method*

The earliest example of LBM (*ca.* 1988) was essentially an attempt to address statistical noise inherent in LGCA (Succi 2001). Subsequently, the essential theoretical basis of the LBM has been shown to derive from non-equilibrium statistical mechanics (Succi 2001, 2002) so its theoretical analysis has two distinct routes. One, heuristic, follows LBM's advent from LGCA's, the other a formal discretization of the exact Boltzmann transport equation (He & Luo 1997*b*; Abe 1966). We detail the former here.

Boltzmann made stringent assumptions (Liboff *et al.* 2003) to close the description of dilute systems obtained from kinetic theory. For dilute systems the macroscopic observables of interest only depend on one- or two-body distributions, so the $6N$ variables were reduced to just $M = 1, 2$. The Boltzmann equation

$$\partial_t f + \boldsymbol{v} \cdot \partial_{\boldsymbol{x}} f + \boldsymbol{a} \cdot \partial_{\boldsymbol{v}} f = C_2\{f_2\} \tag{2.5}$$

then follows, where $f = f_1(\boldsymbol{x}, \boldsymbol{v}, t)$ is the one-body distribution representing the probability density of finding a particle at position $\boldsymbol{x}$, with particle velocity $\boldsymbol{v}$ at time t. f_2 is a two-body distribution (see below) and C_2 is the two-body-collision operator. It should be noted that, for dense systems, the validity of this reduction is less clear and, at the time of writing, there are attempts to formulate lattice BBGKY equations (after Bogolyubov, Born, Green, Kirkwood and Yvon), which may be better adapted to the simulation of denser fluids. The left-hand side of equation (2.5) represents the free steaming of particles in phase space; the collision operator, $C_2\{f_2\}$, henceforth denoted $C(f, f)$, on the right, represents the effects of collisions. In the dilute-gas limit (where binary collisions alone are significant) the gas is considered to be subjected to molecular chaos (molecules entering a binary collision have uncorrelated motion):

$$f_2(\boldsymbol{x}_1, \boldsymbol{v}_1, \boldsymbol{x}_2, \boldsymbol{v}_2, t) = f(\boldsymbol{x}_1, \boldsymbol{v}_1, t) f(\boldsymbol{x}_2, \boldsymbol{v}_2, t). \tag{2.6}$$

This allowed Boltzmann to write down an integral expression for the $C_2\{f_2\}$ (Liboff *et al.* 2003). In fact He & Luo (1997*a*) have shown that one particular LBE algorithm may be obtained by a systematic discretization of equation (2.5).

(*d*) *Solving the Boltzmann equation: Chapman–Enskøg analysis*

The Chapman–Enskøg procedure is used to solve the Boltzmann equation (2.5) by means of recursive perturbation techniques (Chapman & Cowling 1970). A variant of this method might be better known as 'successive approximation', 'multi-scale expansion' or 'Hilbert expansion'. It is used to obtain the behaviour of hydrodynamic modes in the LBM, although crucially, it may miss other, kinetic, modes. The expansion is parametrized by a small dimensionless Knudsen number, Kn, introduced into the collision term of the Boltzmann equation (2.5) without the forcing term (Liboff *et al.* 2003):

$$\partial_t f + v_\alpha \partial_\alpha f = \frac{1}{\varepsilon} C(f,f), \quad \varepsilon \equiv Kn = \frac{l}{L}. \tag{2.7}$$

The distribution function $f(\boldsymbol{x},\boldsymbol{v},t)$ and time derivative are then expanded in terms of ε as

$$f = \sum_{n=0}^{\infty} \varepsilon^n f^{(n)}, \qquad \partial_t = \sum_{n=0}^{\infty} \varepsilon^n \partial_{t_n}, \tag{2.8}$$

with the constraints that 'moments' of the *equilibrium distribution* $f^{(0)}$,

$$f^{(0)} = f^{(\mathrm{eq})} = \frac{\rho}{(2\pi RT)^{D/2}} \exp\left\{ -\frac{(\boldsymbol{v}-\boldsymbol{u})^2}{2RT} \right\}, \tag{2.9}$$

alone determine the hydrodynamic quantities

$$\left.\begin{aligned} \int f^{(0)} \begin{bmatrix} 1 \\ \boldsymbol{v} \\ \frac{1}{2}(\boldsymbol{v}-\boldsymbol{u})^2 \end{bmatrix} \mathrm{d}\boldsymbol{v} &= \rho \begin{bmatrix} 1 \\ \boldsymbol{u} \\ e \end{bmatrix} \\ \int \varepsilon^{(n)} f^{(n)} \begin{bmatrix} 1 \\ \boldsymbol{v} \\ \frac{1}{2}(\boldsymbol{v}-\boldsymbol{u})^2 \end{bmatrix} \mathrm{d}\boldsymbol{v} &= 0, \quad n > 0, \end{aligned}\right\} \tag{2.10}$$

where e is the energy and $\boldsymbol{u}$ is the macroscopic fluid velocity. Importantly, higher-order non-equilibrium parts ($f^{(n)}$, $n > 0$) do not contribute to the hydrodynamic observable. Note, the space/time variation of $f^{(0)}$ is purely implicit, through, for example, $f^{(0)} = f^{(0)}(\rho, \boldsymbol{u}, T)$. The collision term is also expanded in terms of ε,

$$C(f,f) = \sum_{n=0}^{\infty} \varepsilon^n C^{(n)}, \qquad C^{(n)} = \sum_{k+l=n} C(f^{(k)}, f^{(l)}), \tag{2.11}$$

and solutions to the Boltzmann equation may now be obtained by equating powers of ε in the expanded equation, obtained from equations (2.7)–(2.11), then solving each order of this recursion hierarchically:

$$\left.\begin{aligned} O(\varepsilon^{-1}): &\quad C(f^{(0)}, f^{(0)}) = 0, \\ O(\varepsilon^{0}): &\quad \partial_t f^{(0)} + v_\alpha \partial_\alpha f^{(0)} = 2C(f^{(0)}, f^{(1)}) \\ &\quad \vdots \end{aligned}\right\} \tag{2.12}$$

By solving to $O(\varepsilon^{-1})$, the equilibrium distribution $f^{(0)}$ is found to be the Maxwell–Boltzmann distribution (Chapman & Cowling 1970). Given this, the $O(\varepsilon^0)$ equation can, in principle, yield $f^{(1)}$, and so on through increasing orders of ε.

Hydrodynamic equations are extracted by evaluating moments of the Boltzmann equation with normal solutions (Liboff *et al.* 2003):

$$\int (\partial_t f + v_\alpha \partial_\alpha f - C(f,f))\,\mathrm{d}\boldsymbol{v} \begin{bmatrix} 1 \\ \boldsymbol{v} \\ \frac{1}{2}(\boldsymbol{v}-\boldsymbol{u}) \end{bmatrix} = 0. \tag{2.13}$$

The above equations will give the Euler equation (Landau & Lifshitz 1995) for $f = f^{(0)}$ and the Navier–Stokes equations (2.2) for $f = f^{(0)} + f^{(1)}$ (Liboff *et al.* 2003).

The Chapman–Enskøg procedure is, unsurprisingly, key to extracting the hydrodynamic equations of the LBM and will be used in detail in § 2 *h*. An important approximation of the Bhatnagar–Gross–Krook (BGK) collision operator (Bhatnagar *et al.* 1954) greatly simplifies solution. The BGK Boltzmann equation is

$$\partial_t f + v_\alpha \partial_\alpha f = -\frac{1}{\tau}(f - f^{(0)}), \tag{2.14}$$

and now the first-order solution $f^{(1)}$ is easily obtained, from equation (2.12), as

$$f^{(1)} = -\tau(\partial_t f^{(0)} + v_\alpha \partial_\alpha f^{(0)}). \tag{2.15}$$

(*e*) *Lattice gas cellular automata*

It is instructive to look at the construction of lattice gas cellular automata (LGCA) models, as these are parents to the LBM and operate in a similar vein.

Cellular automata (CA) (von Neumann 1966) and MD for gases (Broadwell 1964) were merged to gave rise to the first LGCA. Mono-energetic molecules are confined to move/interact on a lattice and updated by CA rules. Space, velocity and time are all discretized. The first LGCA model (the HPP model) with deterministic rules that reproduce fluid dynamic-like features was introduced by Hardy, de Pazzis and Pomeau (Hardy *et al.* 1973, 1976). This was superseded by the FHP model (proposed by Frisch, Hasslacher and Pomeau (Frisch *et al.* 1986; Wolfram 1986)), which was the first LGCA model shown to map onto the Navier–Stokes equations (2.2). It has discrete velocity and position space and discrete collision rules (Frisch *et al.* 1986), represented in essence in figure 1, which shows two sequential lattice states.

Notwithstanding, evolution of the LGCA models is very simple and consists of two main repeated steps: collision and streaming (see figure 1), the time-order of which is irrelevant. Collisions are very simple but must conserve particle number, momenta and energy (only). Evolution is represented by a lattice-species Boltzmann equation

$$n_i(\boldsymbol{x} + \boldsymbol{c}_i, t+1) - n_i(\boldsymbol{x}, t) = C_i(n_1, n_2, \dots), \tag{2.16}$$

where $n_i(\boldsymbol{x}, t)$ is the number $\in \{0,1\}$ of particles with particle velocity $\boldsymbol{c}_i$, $n_i \in \{0,1\}$; the subscripts i and j denote discrete velocities $i, j \in \{1, 2, \dots, b\}$, b is the size of the lattice velocity basis and $\boldsymbol{c}_i$ is a 'Boolean' function of the n_i values which expresses the possible collisions.

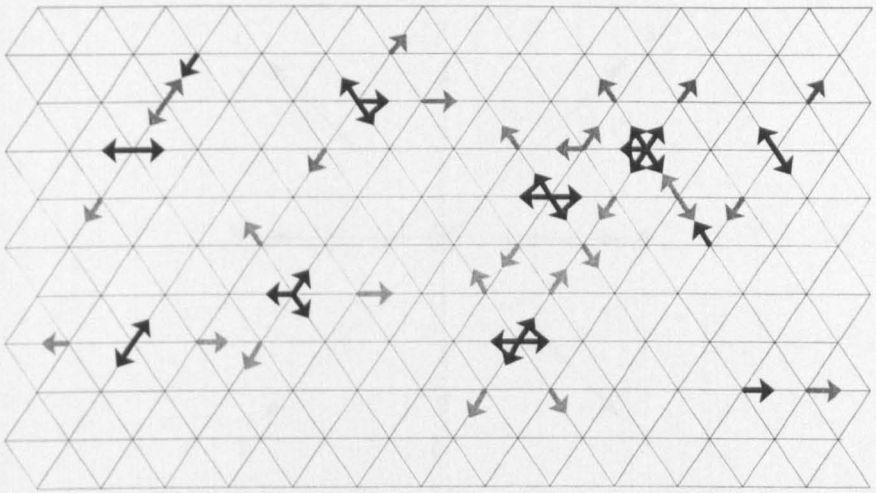

Figure 1. Lattice structure and evolution of the FHP-I LGA model. Solid (hollow) arrows represent particles with the velocities corresponding to time t ($t+$). Hollow arrows therefore represent post collision, post propagation evolution.

The LGCA may be viewed as a maximally discretized MD model. Variants with increased stability on more complicated lattices have been developed: essentially, all give the same general hydrodynamic equations but with different values for, e.g., the speed of sound squared c_s^2 and lattice fluid viscosities ν and η. The key advantages of LGCAs are their unconditional stability, optimal use of computer memory, and localization, allowing for massive parallelization and dedicated computers. In fact it has been shown that isothermal LGCA models admit both a local and global H-theorem (Frisch *et al.* 1986), confirming the unconditional stability—a decisive advantage in the computation of turbulence. Further information on LGCA and its applications may be found in Succi (2001), Wolfram (1986), He *et al.* (1997*a*), McNamara & Zanetti (1988), D'Humières *et al.* (1989), Rothmann & Zaleski (1994) and Benzi *et al.* (1992).

LGCA simulation has now been largely superseded by the LBM, for the above advantages are accompanied by a number of limitations. Certainly, early models were limited to relatively low Reynolds numbers (see equation (2.4)) due to high momentum diffusivity (viscosity ν) and the LGCA's lack of Galilean invariance.

(*f*) *Lattice Boltzmann models*

McNamara & Zanetti (1988) realized that equation (2.16) can be re-expressed as a Boltzmann equation for LGCA ensemble averages. Defining

$$f_i(\boldsymbol{x}, t) \equiv \langle n_i(\boldsymbol{x}, t) \rangle, \quad 0 \leqslant f_i \leqslant 1, \ i = 1, \ldots, b, \tag{2.17}$$

where $f_i(\boldsymbol{x}, t)$ are real continuous functions representing the probability distribution of finding particles with discrete velocities and space. Their evolution may be expressed after equation (2.16) as

$$f_i(\boldsymbol{x} + \boldsymbol{c}_i, t + 1) - f_i(\boldsymbol{x}, t) = \Delta_i(f_0, f_1, f_2, \ldots), \tag{2.18}$$

the collision term $\Delta_i(f_i)$ being essentially the C_i of the LGCA but with the ensemble averages f_i replacing the n_i (Frisch *et al.* 1986). In fact, there are several variants of the lattice Boltzmann method (e.g. Succi 2002); we shall focus on the simplest.

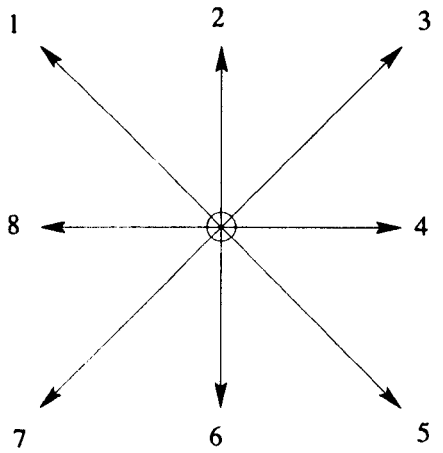

Figure 2. The D2Q9 model lattice structure showing a regular repeating structure with nine distributions located at each lattice node.

(g) *Lattice BGK (LBGK) models*

It was Qian *et al.* (1992) and Chen *et al.* (1992) who realized that Δ_i in (2.17) could be further simplified by assuming a singe relaxation time τ:

$$f_i(\boldsymbol{x}+\delta \boldsymbol{c}_i, t+\delta) = f_i(\boldsymbol{x}, t) - \frac{1}{\tau}(f_i(\boldsymbol{x}, t) - f_i^{(\mathrm{eq})}) + F_i, \quad 0 \leqslant \frac{1}{\tau} \leqslant 2, \tag{2.19}$$

in which we have added a 'forcing term', F_i, to which we shall return, taking $F_i = 0$ for the moment. Note that equation (2.19) has a relaxation form.

Equation (2.19) and its appropriate equilibrium distribution function (see below) together comprise the so-called LBGK model. Setting $\tau = 1$ in equation (2.19), the momentum densities, f_i, relax immediately to local equilibrium $f_i^{(\mathrm{eq})}$, on the scale of the propagation length $\delta c_{i\alpha}$, which is determined by the time-of-flight parameter δ. With $c_{i\alpha} = O(1)$ it is natural to associate the duration δ with the mean free path, or Knudsen number. In other words, we take $\delta = \varepsilon$ (see equation (2.7)) for the purposes of extracting the model's dynamics.

When LBM is used for two-dimensional fluid dynamics simulations, the LBGK model is the one most commonly used and, in particular, the one with nine velocities in two dimensions (D2Q9). Section 2*h* details an analysis for extracting its hydrodynamics. The shortcomings of the LBGK models include spurious invariant quantities when $1/\tau$ reaches its limits, and round-off errors which can cause instability, due to floating point algebra. At present no local or global H-theorem for LBM models has been found (Succi 2002). However, it is anticipated that this will change in the near future. This will allow the stability boundaries for these methods to be determined.

(h) *Hydrodynamics of the LBGK method*

Our method of manipulating the macroscopic dynamics differs from that of others (e.g. Hou *et al.* 1995) in that, for adaptability, it treats the role of the lattice in a general way. However, we focus on the slow, hydrodynamic modes in the usual way, by using a Chapman–Enskøg analysis to develop the LBGK evolution equation, (2.19). The requirements on $f_i^{(n>0)}$ are as discussed previously, but we have an additional

requirement that the second moment of $f_i^{(1)}$ relates directly to the viscous stress $\Pi_{\alpha\beta}^{(1)}(x_\alpha, t)$:

$$\left.\begin{aligned} \sum_i f_i^{(\mathrm{eq})} \begin{bmatrix} 1 \\ c_{i\alpha} \\ c_{i\alpha}c_{i\beta} \end{bmatrix} &= \begin{bmatrix} \rho(\boldsymbol{x},t) \\ \rho u_\alpha(\boldsymbol{x},t) \\ \Pi_{\alpha\beta}^{(0)}(\boldsymbol{x},t) \end{bmatrix}, \\ \sum_i f_i^{(n)} \begin{bmatrix} 1 \\ c_{i\alpha} \\ c_{i\alpha}c_{i\beta} \end{bmatrix} &= \begin{bmatrix} 0 \\ 0 \\ \Pi_{\alpha\beta}^{(n)}(\boldsymbol{x},t) \end{bmatrix}, \quad n > 0. \end{aligned}\right\} \tag{2.20}$$

In fact LBGK equilibrium $f_i^{(\mathrm{eq})}$ approximates a uniformly translating Maxwell–Boltzmann distribution in the peculiar velocity $(c_{i\alpha} - u_\alpha)$:

$$\left.\begin{aligned} f_i^{(\mathrm{eq})} &= \frac{\rho}{(2\pi RT)^{D/2}} \exp\left\{ -\frac{(c_{i\alpha}-u_\alpha)^2}{2RT} \right\} = \rho t_i \exp\left\{ \frac{u_\alpha c_{i\alpha}}{RT} \right\} \exp\left\{ -\frac{u^2}{2RT} \right\}, \\ t_i &\equiv \exp\left\{ \frac{c_{i\alpha}c_{i\alpha}}{RT} \right\} \frac{1}{(2\pi RT)^{D/2}}, \end{aligned}\right\} \tag{2.21}$$

by making a Taylor expansion to $O(u^2)$ in equation (2.21):

$$f_i^{(\mathrm{eq})} = \rho t_i \left(1 + \frac{c_{i\alpha}u_\alpha}{RT} + \frac{c_{i\alpha}c_{i\beta}u_\alpha u_\beta}{2(RT)^2} - \frac{u^2}{2RT} \right).$$

For isothermal flows R and T are constant and we therefore may simplify $f_i^{(\mathrm{eq})}$:

$$f_i^{(\mathrm{eq})} = t_i(A + Bc_{i\alpha}u_\alpha + Cc_{i\alpha}c_{i\beta}u_\alpha u_\beta + Du^2), \tag{2.22}$$

in which t_i, A, B, C and D are taken as constants yet to be determined (not all of which are independent). This form of the equilibrium distribution is less general than that of Hou *et al.* (1995), because it is predicated, from the outset, on a uniformly translating Maxwell–Boltzmann. However, any attempt to depart significantly from that form (i.e. that of equation (2.22)) quickly leads to instabilities. In the limit of small Re, an increased freedom of choice around the coefficients in equation (2.22) is a means of embedding different physical effects. Our discrete velocity set $\boldsymbol{c}_i$ is that of the most popular in the literature, classified D2Q9 (two dimensions and nine discrete velocities; see figure 2). Here we derive parameters for D2Q9, though it is trivial to adapt this derivation to fit any of the models listed at the end of this section.

To close the equilibrium distribution $f_i^{(\mathrm{eq})}$ of our D2Q9 model (and effectively determine the whole of the model's dynamics) we Taylor expand the left-hand side of the LBGK evolution equation (2.19) to second order in $\delta = \varepsilon$ as

$$\varepsilon[\partial_t + c_{i\alpha}\partial_\alpha]f_i + \tfrac{1}{2}\varepsilon^2[\partial_t + c_{i\alpha}\partial_\alpha]^2 f_i + O(\varepsilon^3) = -\frac{1}{\tau}(f_i - f_i^{(\mathrm{eq})}). \tag{2.23}$$

The terms of $O(\varepsilon)$ already correspond to the Boltzmann transport equation (2.14). We now substitute the Knudsen number ε-expansions of equations (2.8) (for f_i about equilibrium $f_i^{(\mathrm{eq})}$ and for the time derivative ∂_t about ∂_{t_0}) into equation (2.23) and retain terms to $O(\varepsilon^2)$. Separating orders of ε, we have, at $O(\varepsilon)$,

$$(\partial_{t_0} + c_{i\alpha}\partial_\alpha) f_i^{(0)} = -\frac{1}{\tau} f_i^{(1)}, \tag{2.24}$$

and, at $O(\varepsilon^2)$, using the result at $O(\varepsilon)$ in equation (2.24),

$$\partial_{t_1} f_i^{(0)} + (\partial_{t_0} + c_{i\alpha}\partial_\alpha)\left(1 - \frac{1}{2\tau}\right) f_i^{(1)} = -\frac{1}{\tau} f_i^{(2)}. \tag{2.25}$$

We proceed to tune the discrete moments of equations (2.24) and (2.25) onto hydrodynamic behaviour. Summing equation (2.20) on link index i:

$$\partial_{t_0} \sum_i f_i^{(0)} + \partial_\alpha \sum_i c_{i\alpha} f_i^{(0)} = -\frac{1}{\tau} \sum_i f_i^{(1)},$$

from which it is evident that the model's macroscopic dynamics are described by the continuity equation on its shortest time scales t_0:

$$\partial_{t_0} \rho + \partial_\alpha \rho u_\alpha = 0. \tag{2.26}$$

The first moment of equation (2.24) is obtained by multiplying it by $c_{i\alpha}$ prior to summing on i:

$$\partial_{t_0} \sum_i c_{i\alpha} f_i^{(0)} + \partial_\beta \sum_i c_{i\alpha} c_{i\beta} f_i^{(0)} = -\frac{1}{\tau} \sum_i c_{i\alpha} f_i^{(1)}.$$

Hence, we obtain an Euler equation for the momentum,

$$\partial_{t_0} \rho u_\alpha + \partial_\beta \Pi_{\alpha\beta}^{(0)} = 0, \tag{2.27}$$

where $\Pi_{\alpha\beta}^{(0)}$ is that defined in equation (2.20). To extract the longer-time dissipative modes it is necessary to proceed to longer times. Take moments in the $O(\varepsilon^2)$ equation (2.25) and use the identities given by equation (2.20). The zeroth moment immediately yields

$$\partial_{t_1} \rho = 0, \tag{2.28}$$

and, using equations (2.20), its first moment (with $c_{i\alpha}$) yields

$$\left(1 - \frac{1}{2\tau}\right) \partial_\beta \Pi_{\alpha\beta}^{(1)} + \partial_{t_1} \rho u_\alpha = 0. \tag{2.29}$$

The Chapman–Enskøg expansions need to be recombined, in the case of equations (2.27), (2.29) to give the Navier–Stokes equation. To obtain the desired result from this the process we clearly need to control the form $\Pi_{\alpha\beta}^{(0)}$ and $\Pi_{\alpha\beta}^{(1)}$. This is best achieved by expressing the latter directly in terms of the parameters t_i, A, B, C and D of $f_i^{(\mathrm{eq})}$, resulting in expressions which contain 'tensors' such as $\sum_i t_i c_{i\alpha} c_{i\beta}$, for it is possible to show that $\Pi_{\alpha\beta}^{(0)}$ and $\Pi_{\alpha\beta}^{(1)}$ take appropriate form when such tensors are isotropic.

After Wolfram (1986) and C. M. Care (2003, personal communication), we seek

(i) a set of isotropic tensors E^n with order $O(n)$ of the discrete velocity basis ($c_{i\alpha}$, figure 2),

(ii) the appropriate weight of link i, t_i.

The latter tensors appear in the expressions for $\Pi^{(0)}_{\alpha\beta}$ and $\Pi^{(1)}_{\alpha\beta}$. We define and evaluate the following tensors:

$$\left.\begin{aligned}
E^{(0)} &\equiv \sum_i t_i = t_0 + 4t_1 + 4t_2,\\
E^{(1)}_{\alpha} &\equiv \sum_i t_i c_{i\alpha} = 0,\\
E^{(2)}_{\alpha\beta} &\equiv \sum_i t_i c_{i\alpha} c_{i\beta} = (2t_1 + 4t_2)\delta_{\alpha\beta},\\
E^{(3)}_{\alpha\beta\gamma} &\equiv \sum_i t_i c_{i\alpha} c_{i\beta} c_{i\gamma} = 0,\\
E^{(4)}_{\alpha\beta\gamma\delta} &\equiv \sum_i t_i c_{i\alpha} c_{i\beta} c_{i\gamma} c_{i\theta} = (2t_1 - 8t_2)\delta_{\alpha\beta\gamma\theta} + 4t_2(\delta_{\alpha\beta}\delta_{\gamma\theta} + \delta_{\alpha\gamma}\delta_{\beta\theta} + \delta_{\alpha\theta}\delta_{\beta\gamma}),
\end{aligned}\right\} \tag{2.30}$$

as may be checked by direct computation, using the D2Q9 basis. Note that odd-order tensors $E^{(2n+1)}$ are zero. Only fourth-order tensors are necessary for hydrodynamics. Wolfram shows that the $E^n_{\alpha\ldots}$ will be isotropic if

$$E^{2n+1}_{\alpha\cdots} = 0, \qquad E^{2n}_{\alpha\cdots} = T^{2n}\Delta^{2n}_{\alpha\cdots}, \tag{2.31}$$

where tensor $\Delta^{2n}_{\alpha\ldots}$ is defined as (Wolfram 1986)

$$\Delta^0 = 1, \qquad \Delta^2_{\alpha\beta} = \delta_{\alpha\beta}, \qquad \Delta^4_{\alpha\beta\gamma\theta} = \delta_{\alpha\beta}\delta_{\gamma\theta} + \delta_{\alpha\gamma}\delta_{\beta\theta} + \delta_{\alpha\theta}\delta_{\beta\gamma}. \tag{2.32}$$

Comparing equations (2.32) and definitions (2.30), we obtain

$$T^0 = t_0 + 4t_1 + 4t_2, \qquad T^2 = 2t_1 + 4t_2, \qquad T^4 = 4t_2, \qquad t_2 = \tfrac{1}{4}t_1. \tag{2.33}$$

With equations (2.33), we return to the task of manipulating the emerging macroscopic equations into an appropriate form. We evaluate the requisite moments of the equilibrium distribution (equation (2.20)) by inserting the form of $f^{(\mathrm{eq})}_i$ (2.22) and using equations (2.33). For example, the moment $\sum_i f^{(0)}_i = \rho$ gives

$$-\rho + A\sum_i t_i + Bu_\alpha \sum_i t_i c_{i\alpha} + Cu_\alpha u_\beta \sum_i t_i c_{i\alpha} c_{i\beta} + Du_\alpha u_\alpha \sum_i t_i = 0, \tag{2.34}$$

which, on substituting for the tensors from equation (2.22), yields

$$-\rho + AT^0 + Cu^2T^2 + Du^2T^0 = 0 \tag{2.35}$$

after a little algebra. Similarly, the first moment

$$\sum_i f^{(0)}_i c_{i\gamma} = \rho u_\gamma$$

and the 'momentum flux' moment

$$\sum_i f^{(0)}_i c_{i\gamma} c_{i\theta} = P\delta_{\gamma\theta} + \rho u_\gamma u_\theta,$$

give, respectively,

$$\left.\begin{aligned}
-\rho u_\gamma + Bu_\gamma T^2 &= 0,\\
-P\delta_{\gamma\theta} - \rho u_\gamma u_\theta + AT^2\delta_{\gamma\theta} + T^4Cu^2\delta_{\gamma\theta} + 2T^4Cu_\gamma u_\theta + Du^2T^2\delta_{\gamma\theta} &= 0.
\end{aligned}\right\} \tag{2.36}$$

Noting that the equations (2.34)–(2.36) must be true for all ρ, u_α, we obtain the following six equations:

$$\left.\begin{aligned} -\rho + AT^0 &= 0, & CT^2 + DT^0 &= 0, & -\rho + BT^2 &= 0, \\ -P + AT^2 &= 0, & 2CT^4 - \rho &= 0, & CT^4 + DT^2 &= 0, \end{aligned}\right\} \tag{2.37}$$

and, recalling that $A = \rho$, we have a closed system of simultaneous equations with a non-trivial solution:

$$\left.\begin{aligned} A &= \rho, & T^0 &= 1, & t_0 &= \tfrac{4}{9}, \\ B &= 3\rho, & T^2 &= \tfrac{1}{3}, & t_1 &= \tfrac{1}{9}, \\ C &= \tfrac{9}{2}\rho, & T^4 &= \tfrac{1}{9}, & t_2 &= \tfrac{1}{36}, \\ D &= -\tfrac{3}{2}\rho, & P &= \tfrac{1}{3}\rho. \end{aligned}\right\} \tag{2.38}$$

We may identify the $\frac{1}{3}$ in the equation of state as the speed of sound squared (c_s^2), in terms of which the equilibrium is often written

$$f_i^{(\mathrm{eq})} = \rho t_i \left(1 + \frac{c_{i\alpha}u_\alpha}{c_s^2} + \frac{c_{i\alpha}c_{i\beta}u_\alpha u_\beta}{2c_s^4} - \frac{u^2}{2c_s^2}\right). \tag{2.39}$$

Finally, we demonstrate an appropriate form for 'viscous stress' moment $\Pi_{\alpha\beta}^{(1)}$. We need an expression for $f_i^{(1)}$, obtained by rearranging equation (2.24) as

$$\left.\begin{aligned} \Pi_{\gamma\theta}^{(1)} &= \sum_i c_{i\gamma}c_{i\theta}f_i^{(1)} \\ &= -\tau \sum_i c_{i\gamma}c_{i\theta}(\partial_{t_0} + c_{i\lambda}\partial_\lambda) f_i^{(\mathrm{eq})} \\ &= -\tau[-c_s^2 u_\gamma \partial_\theta \rho - c_s^2 u_\theta \partial_\gamma \rho - \partial_\lambda \rho u_\gamma u_\theta u_\lambda + \partial_\lambda \rho u_\gamma c_s^2 \delta_{\lambda\theta} + \partial_\lambda \rho u_\theta c_s^2 \delta_{\gamma\lambda}], \end{aligned}\right\} \tag{2.40}$$

where identity $[\partial_{t_0}\rho u_\gamma u_\theta = -c_s^2 u_\gamma \partial_\theta \rho - c_s^2 u_\theta \partial_\gamma \rho - \partial_\lambda \rho u_\gamma u_\theta u_\lambda]$ and the continuity equation have been used.

We recombine the four Chapman–Enskøg moment expansions. First the $O(\varepsilon^1)$ and $O(\varepsilon^2)$ continuity equations (2.26), (2.28):

$$(\varepsilon\partial_{t_0} + \varepsilon^2\partial_{t_1})\rho + \varepsilon\partial_\alpha \rho u_\alpha = 0 \quad \Rightarrow \quad \partial_t \rho + \partial_\alpha \rho u_\alpha = 0. \tag{2.41}$$

Combining the '$c_{i\alpha}$ moment' $O(\varepsilon^1)$ and $O(\varepsilon^2)$ (equations (2.27) and (2.29)) gives

$$\partial_t \rho u_\alpha + \partial_\beta \rho u_\alpha u_\beta = -\partial_\alpha c_s^2 \rho + \varepsilon \tfrac{1}{2} c_s^2 (2\tau - 1)\partial_\beta 2\rho S_{\alpha\beta} - (\tau - \tfrac{1}{2})\partial_\beta \partial_\gamma \rho u_\alpha u_\beta u_\gamma,$$

where $S_{\alpha\beta} = \frac{1}{2}(\partial_\alpha u_\beta + \partial_\beta u_\alpha)$ is the rate of strain. Defining the viscosity as

$$\nu \equiv \tfrac{1}{2}\varepsilon c_s^2 (2\tau - 1), \tag{2.42}$$

we note an ideal-gas equation of state, with c_s^2 only of the order of 1. Retaining terms to $O(u^2)$,

$$\partial_t \rho u_\alpha + \partial_\beta \rho u_\alpha u_\beta = -\partial_\alpha P + \partial_\beta (2\nu \rho S_{\alpha\beta}). \tag{2.43}$$

Equations (2.41) and (2.43) are a weakly compressible form of the Navier–Stokes and continuity equations. The procedure by which they have been derived may be applied

Table 1. *LBGK lattice parameters for a selection of commonly used models indicating the lattice shape, velocity directions and equilibrium distribution weights*

model	unit cell	t_0 0	t_1 1	t_2 $\sqrt{2}$	t_3 $\sqrt{3}$	t_4 2	c_s^2	order of isotropy
D1Q3	line	$\frac{2}{3}$	$\frac{1}{6}$	0	0	0	$\frac{1}{3}$	4
D1Q5	line	$\frac{1}{2}$	$\frac{1}{6}$	0	0	$\frac{1}{12}$	1	6
D2Q7	hexagonal	$\frac{1}{2}$	$\frac{1}{12}$	0	0	0	$\frac{1}{4}$	4
D2Q9	square	$\frac{4}{9}$	$\frac{1}{9}$	$\frac{1}{36}$	0	0	$\frac{1}{3}$	4
D2Q13	hexagonal	$\frac{11}{25}$	$\frac{9}{100}$	0	$\frac{1}{300}$	0	$\frac{3}{10}$	6
D3Q15	cubic	$\frac{2}{9}$	$\frac{1}{9}$	0	$\frac{1}{72}$	0	$\frac{1}{3}$	4
D3Q19	cubic	$\frac{1}{3}$	$\frac{1}{18}$	$\frac{1}{36}$	0	0	$\frac{1}{3}$	4
D3Q27	cubic	$\frac{8}{27}$	$\frac{2}{27}$	$\frac{1}{54}$	$\frac{1}{216}$	0	$\frac{1}{3}$	4
D4Q25	FCHC	$\frac{1}{3}$	0	$\frac{1}{36}$	0	0	0	4

to the other lattices summarized in terms of their velocity basis and corresponding weights (table 1). It differs from other derivations (Hou *et al.* 1996) simply in that the isotropy of lattice basis tensors is programmed-in explicitly, which is a procedural advantage when inserting additional microphysics. In considering table 1, it should be noted that the analysis of three speed models produces a sufficient number of constraints to solve the coefficients of the equilibrium distribution. However, our method is not the only path to the LBGK equilibrium. He & Luo (1997*b*) give an *a priori* derivation applicable to any lattice structure. Luo integrates the Boltzmann transport equation, via the method of characteristics, to derive the LBGK evolution equation. A Taylor expanded Maxwell–Boltzmann equilibrium distribution has its weights (t_i) and lattice calculated by a numerical integration, the number of velocities reflecting the order and choice of the polynomial used in the quadrature. Following this route leads to a number of enhanced models with flexible lattice structures (Luo 1998; Mei *et al.* 2000; He *et al.* 1997*a*), and it allows one to add physics directly from kinetic theory and the Boltzmann equation.

(*i*) *Boundaries in lattice models*

The Navier–Stokes equation is an elliptic equation: it requires the boundary velocity field to be closed to have any solution. This velocity information can be set in equivalent terms, especially at open boundaries, using, for example, pressure and flux conditions. One problem with LBM lattice closure is that the velocity distribution gives D conditions which are not necessarily sufficient to determine appropriate values for all the f_i at a boundary.

Consider first the no-slip zero velocity boundary condition. The velocity of the fluid matches that assumed for the boundary, often zero. Wolfram (1986) showed the simplest operation to reproduce a zero in velocity is the bounce-back condition. f_i which stream onto a wall site have their velocities inverted for the next streaming step. This robust process clearly inserts friction into the fluid and conserves mass but it is only first-order accurate (Kadanoff *et al.* 1989).

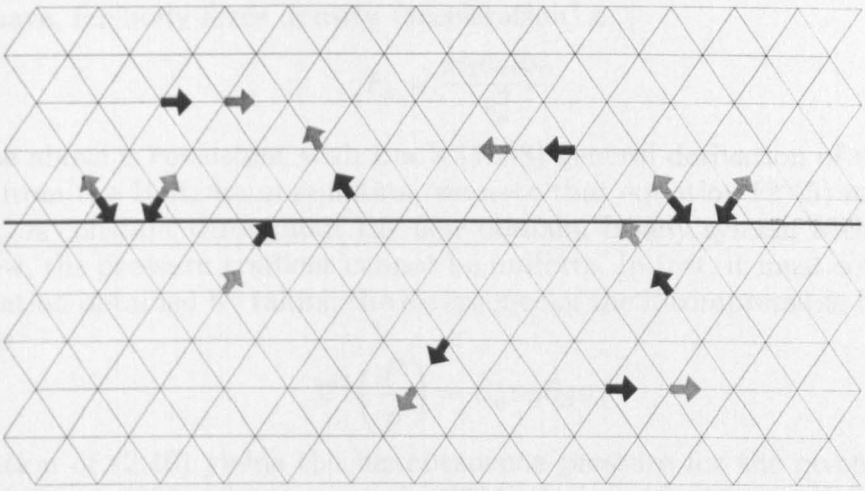

Figure 3. Simplified mid-link bounce-back method on a hexagonal lattice. The heavier line represents the wall position, note it is positioned exactly halfway between lattice nodes. Solid (hollow) arrows represent particle distribution functions at time t $(t+1)$. In one time-step the distribution function effectively travels half a link then bounces back in the reverse direction so as to introduce non-slip boundaries. Both mass and momentum are conserved. To interact with the wall, particles moving in direction i, at the end of time step t, propagate, to re-appear at the same position, moving in direction $i \oplus Q$ (addition modulo Q) at time $t+1$.

The mid-link bounce-back boundary condition retains simplicity of implementation, providing a balance between robustness and accuracy (see figure 3). The zero velocity is located a distance of exactly half a link from the lattice node on which it obtains. It is shown (He *et al.* 1997*b*; Maier *et al.* 1996; Skordos 1993) to be second-order accurate in space but first-order accurate in time, i.e. not necessarily instantaneously accurate. Note that bounce-back methods are not applicable to open boundaries or moving boundaries.

Halliday *et al.* (2002) proposed strategies for instantaneously accurate lattice closure, for plane boundaries with any known distribution of velocity. Several other sophisticated methods have been developed to overcome the closure problem, all involving velocity gradients (Skordos 1993; Noble *et al.* 1995). All the results presented here use mid-link bounce-back.

For internal pressure-driven flow, pressure and flux conditions often apply at open boundaries. LBM's inherent compressibility error (recall the $O(1)$ speed of sound) allows one to impose internal pressure gradients as gradients in density. This strategy is valid even at modest *Re* (i.e. when the pressure gradient is large). In isothermal LBM, a simple method of combating compressibility and imposing pressure boundary conditions is to approximate the pressure field to a uniform gradient, which is then represented as a body force (Halliday *et al.* 2001).

More precisely, a uniform body force or acceleration ρa_α may be used to approximate the principal part of a pressure gradient. Such an acceleration can arise in the LBM's momentum equation (§ 2*b*) from the term F_i in the lattice evolution equation (2.19). For a uniform body force in an isothermal LBGK (Halliday *et al.* 2001),

$$\sum_i F_i = 0, \qquad \sum_i F_i c_{i\alpha} = \rho a_\alpha, \tag{2.44}$$

and we have, for body force density (acceleration) a_α,

$$F_i = \frac{\rho t_i c_{i\alpha} a_\alpha}{c_s^2}. \tag{2.45}$$

While the above is consistent with Luo's (1998) general derivation of uniform accelerations from the Boltzmann equation, we note that equation (2.45) is strictly valid only if a_α is constant throughout the flow domain. In any system without unidirectional flow, the pressure gradient cannot be uniform. In fact, it must solve a Poisson-type equation obtained by taking the divergence of the incompressible Navier–Stokes equations

$$\nabla^2\left(\frac{P}{\rho}\right) = \partial_\alpha v_\beta \partial_\beta v_\alpha. \tag{2.46}$$

The solution of (2.46) yields the instantaneous pressure for the given velocity distribution (Succi 2001). Spencer *et al.* (2004) designed a 'two-part' fictitious body force. The first, conservative, part is designed to correct the pressure field after equation (2.46) (see § 4). The second, non-conservative, part is designed, after the method of Halliday *et al.* (2001), to reduce compressibility effects. For applications like those we shall consider, this conservative component closely corresponds to a uniform body force, as the results we present in § 4 will show.

(*j*) *The exactly incompressible LBGK (EILBGK) model in D2Q9*

For slowly varying flows, the problem of compressibility error may be overcome. The EILBGK model of Zou *et al.* (1995) and Lin *et al.* (1996) makes a slight change to the interpretation of the distribution function f_i in order to make the macroscopic dynamics much more incompressible, but at the expense of the accuracy of its time variation. Applications of the EILBGK are therefore restricted to steady-state solutions and to flows with slow variation (low Strouhal number). However, EILBGK allows for a more accurate treatment of pressure boundary conditions. What changes is the equilibrium distribution function and the definition of velocity (other hydrodynamic moments remain unchanged):

$$\left.\begin{aligned} f_i^{(\mathrm{eq})} &= t_i\left(\rho + \frac{c_{i\alpha}u_\alpha}{c_s^2} + \frac{c_{i\alpha}c_{i\beta}u_\alpha u_\beta}{2c_s^4} - \frac{u^2}{2c_s^2}\right), \\ c_s^2 &= \tfrac{1}{3}, \qquad t_0 = \tfrac{4}{9}, \qquad t_1 = \tfrac{1}{9}, \qquad t_2 = \tfrac{1}{36}, \end{aligned}\right\} \tag{2.47}$$

$$\sum_i f_i^{(\mathrm{eq})} \begin{bmatrix} 1 \\ c_{i\alpha} \\ c_{i\alpha}c_{i\beta} \end{bmatrix} = \begin{bmatrix} \rho(x_\alpha, t) \\ u_\alpha(x_\alpha, t) \\ \Pi^{(0)}_{\alpha\beta}(x_\alpha, t) \end{bmatrix}. \tag{2.48}$$

Using the Chapman–Enskøg analysis as in § 2 *h*, one can obtain the following dynamics:

$$\left.\begin{aligned} \partial_\alpha u_\alpha &= 0, \\ \partial_\beta u_\alpha u_\beta &= -\partial_\alpha c_s^2 \rho + \nu \partial_\beta \partial_\beta u_\alpha, \end{aligned}\right\} \tag{2.49}$$

which are the exact steady-state incompressible Navier–Stokes equations with constant density ρ_0. In this model the pressure and viscosity are given by

$$\frac{P}{\rho_0} = c_s^2 \rho, \qquad \nu = \frac{c_s^2}{2}(2\tau - 1), \tag{2.50}$$

in which ρ/ρ_0 is the effective pressure. Note that both the continuity equation and the advective term in the Navier–Stokes equations are exactly incompressible, while the form of the diffusive term is preserved at the cost of the time derivative. In general, EILBGK schemes are not able to achieve the Reynolds numbers of LBGK simulations, due to the stricter incompressibility constraints.

3. Lattice Boltzmann equation for $N \geqslant 2$ immiscible fluids

Here we consider how to insert an appropriate interface between immiscible lattice fluids which are otherwise represented by the D2Q9 model already described. We describe our generalization, to $N \gg 2$ fluids, of an existing model for binary fluids essentially after Gunstensen *et al.* (1991). Our model provides the means to deal, in the hydrodynamic regime, with a very large number of physically different, non-coalescing fluids.

For definiteness, we shall consider the velocity profile of system of stabilized, suspended drops in pressure-driven internal flow (although, of course, our algorithm can be applied more widely). Accordingly, individual drop masses need each to be conserved. In 9.0×10^5 lattice updates of our interface algorithm, the mass of a drop is conserved to better than $2.0 \times 10^{-3}\%$. For simplicity we choose to prevent all suspended/advected drops from wetting the solid boundaries.

Our generalization to N immiscible components assigns each fluid a 'colour' superscript, $\Gamma = 0, 1, 2, 3 \ldots, (N-1)$. Fluids with different values of Γ can have collision parameters τ_Γ and, therefore, different viscosity ν_Γ. Now, for N different species, the N-component LBM quickly demands impractical amounts of computer storage, as N increases. But for relatively small, non-evaporating 'sharp' drops, the storage (arrays) for N primary quantities $f_i^\Gamma(\boldsymbol{r}, t)$ will be very sparse. Moreover, a natural question arises around the value of attempting to represent, on lattice nodes with Q links (velocities), more than Q different colours or species.

To address storage, we record only $N_Q < Q \ll N$ dominant species at any node. Essentially, we deal with colour difference, as opposed to absolute colour—which generates considerable reduction in the requisite storage. The sharp interfaces from our Gunstensen–type interface method mean minimal mixing and a reduction in the number of different colours found on a node. In practice we take $N_Q = 5$. This value is found to be adequate for even the most intimate mono-disperse N-component flows. Note, however, that this choice reflects the geometry and number of components (colours/drops) in our particular application. Also note that the particular N_Q dominating colours, or immiscible components, vary between nodes and in time. We assign each colour distribution a superscript α, identifying their fluid belonging within the fluids (Γ) of the node.

To guide species segregation, a lattice map of absolute colour, label l, is needed. However, for such a map, sufficient information can be stored in a five-dimensional integer array with subscript set $\{x, y, i, \alpha\}$ to identify, for lattice position $\{x, y\}$ direction i, the n ($< N_Q$) colours present by the value of integer superscript, α. We have the following limits for the f and the associated colour label l values:

$$0 < f(x, y, i, \alpha), \qquad 0 < l(x, y, i, \alpha) < N,$$

where, for a system of size $L \times W$,

$$0 < x < L, \qquad 0 < y < W, \qquad 0 < i < Q, \qquad 0 < \alpha < N_Q.$$

By recording only a maximum of N_Q species at each node, for a total of N drops (or immiscible components), the dominant (type real) storage requirements ($f_i^\alpha(\boldsymbol{r},t)$) are reduced by a factor N_Q/N, to levels comparable with the diphasic model (Gunstensen *et al.* 1991).

In our N-phase model, collision is, as in the diphasic model, performed in three steps: mixed fluid collision, perturbation and numerical colour reallocation.

The collision step acts on the mixed fluid's distribution function f_i,

$$f_i(\boldsymbol{r},t) = \sum_{\alpha=0}^{N_Q-1} f_i^\alpha(\boldsymbol{r},t), \tag{3.1}$$

exactly after Zou *et al.* (1995), except with an effective relaxation parameter defined to give a mixed-fluid mean viscosity

$$\nu(\boldsymbol{r},t) = \frac{1}{\rho(\boldsymbol{r},t)} \sum_{\alpha=0}^{N_Q-1} \rho^\alpha(\boldsymbol{r},t)\nu^\alpha,$$

where ν_α defines the chosen kinematic viscosity of component α of the node at $\boldsymbol{r}$, which relates to a particular ν^Γ through the colour map $l(\boldsymbol{r},i,\alpha)$, and

$$\rho(\boldsymbol{r},t) = \sum_{\alpha=0}^{N_Q-1} \rho^\alpha(\boldsymbol{r},t), \qquad \rho^\alpha(\boldsymbol{r},t) \equiv \sum_{i=0}^{Q-1} f_i^\alpha(\boldsymbol{r},t).$$

Preventing coalescence amounts to dealing consistently with all possible mixed-node colour states using generalized perturbing and recolouring processes that eliminate mixing between all pairs of species, which may be stated as a need to maximize the work done by a generalized colour flux against a generalized colour gradient. Accordingly, the diphasic Gunstensen colour gradient is generalized for the interface between fluid α and fluid β, by what we assume to be its local normal (Dupin *et al.* 2003):

$$\boldsymbol{I}_{\alpha\beta}(\boldsymbol{r}) = \sum_i (\rho^\alpha(\boldsymbol{r}+\boldsymbol{c}_i) - \rho^\beta(\boldsymbol{r}+\boldsymbol{c}_i))\boldsymbol{c}_i. \tag{3.2}$$

This colour gradient is used to perturb the mixed fluids' distribution (equation (3.1)), with a surface tension inducing fluctuation. For the interface between two components α and β we use a generalized perturbation,

$$\Delta f_i^{\alpha\beta}(\boldsymbol{r},t) = \sigma_{\alpha\beta} C_{\alpha\beta}(\boldsymbol{r},t)\cos(2(\theta_f(\boldsymbol{r}) - \theta_i)), \tag{3.3}$$

in which there is no summation on repeated subscripts, $\sigma_{\alpha\beta}$ is a surface-tension parameter for the $\alpha\beta$ interface and

$$C_{\alpha\beta}(\boldsymbol{r},t) = 1 - \left|\frac{\rho_\alpha(\boldsymbol{r},t) - \rho_\beta(\boldsymbol{r},t)}{\rho_\alpha(\boldsymbol{r},t) + \rho_\beta(\boldsymbol{r},t)}\right|, \tag{3.4}$$

is the generalized *concentration factor* for the α,β fluid pair which limits the action of surface tension to multi-coloured nodes (Thompson *et al.* 1999). For a D2Q9 lattice (see figure 2), $\sigma_{\alpha\beta}$ is modulated by the factor λ_0, so that $\sigma_{\alpha\beta}$ becomes

$$\sigma_{\alpha\beta}^i = \begin{cases} \lambda_0\sigma_{\alpha\beta} & i \text{ even}, \\ \sigma_{\alpha\beta} & i \text{ odd}, \end{cases}$$

It has been found that $\lambda_0 \approx 2.12$ provides the best angular isotropy of the drop (Dupin *et al.* 2003). This maximization of the drop's isotropy ensures that radial interfacial tension is uniform, but has other beneficial effects: the micro-current flow is minimized. To confirm the value 2.12, the qualitative features of the micro-current flow field of an enclosed drop may be predicted: by considering the (angular) directions in which the perturbation (3.3) produces the minimum flow in the near-interfacial region, the factor $\lambda_0 = 3/\sqrt{2}$ is given (as shown in Dupin *et al.* (2003)).

We now define an 'average' colour gradient which points towards component α and away from the total of all other components present at the node at position $\boldsymbol{r}$:

$$\boldsymbol{f}^{\alpha}(\boldsymbol{r}) = \sum_i \sum_j \left[f_j^{\alpha}(\boldsymbol{r} + \boldsymbol{c}_i) - \sum_{\beta \neq \alpha} f_j^{\beta}(\boldsymbol{r} + \boldsymbol{c}_i) \right] \boldsymbol{c}_i$$

$$\boldsymbol{f}^{\alpha}(\boldsymbol{r}) = \sum_i [2\rho^{\alpha}(\boldsymbol{r} + \boldsymbol{c}_i) - \rho(\boldsymbol{r} + \boldsymbol{c}_i)]\boldsymbol{c}_i. \tag{3.5}$$

The same calculation is repeated for each pair of fluid components $\alpha\beta$ present at the node, position $\boldsymbol{r}$, the appropriate colour gradient $\boldsymbol{f}^{\alpha}(\boldsymbol{r})$ (equation (3.5)) being used to 're-colour' (see below) for component α within each node, essentially in the same way as for a binary fluid but with the order in which components α are treated begin significant (see below). Accordingly, the total perturbation applied to the mixed fluid at the node at position $\boldsymbol{r}$ is

$$\Delta f_i(\boldsymbol{r}, t) = \sum_{(\alpha,\beta)} \Delta f_i^{\alpha,\beta}(\boldsymbol{r}, t), \tag{3.6}$$

in which the summation is taken on all possible pairs α, β and $\Delta f_i^{\alpha,\beta}(\boldsymbol{r}, t)$ is defined in equation (3.3). Note that calculation of the colour gradient (3.5) requires knowledge of the absolute colour, not just the relative amounts of the different colours present in a local environment. The sum on α of these individual fields is a measure of the local gradient in the total fluid density and is therefore zero only in a uniform fluid.

The perturbation process produces surface-tension effects in the hydrodynamics but it does not segregate the mixed fluids. To achieve segregation, a process of 're-colouring' is used. The (conserved) masses of the individual colours present at any mixed fluid site are numerically re-allocated to the post-perturbed f_i, so as to return as much of species α as possible up the gradient $\boldsymbol{f}^{\alpha}$, defined in equation (3.5).

In order to achieve optimal colour separation, the order of the reallocation of more than two colours to receptacle f_i is significant. Different ordering in the re-colouring process can clearly result in small differences in the post-collision, post-segregated state. Careful observation shows that these differences are small but not without consequence. In order to produce optimum segregation (sharp interface), the minority species at a node is given *priority* allocation to its favoured direction. Failure to adopt this scheme results in a relatively large loss of information about the location of minority species, resulting in small but undesirable adhesion between drops in contact.

Target flow applications are, by intention, heavily interface dominated. For the effectively mono-disperse systems we shall consider here, a maximum of five drops and ambient fluid in immediate proximity was allowed (again, simple packing considerations mean this value will increase with increasing poly-dispersity). Resolving

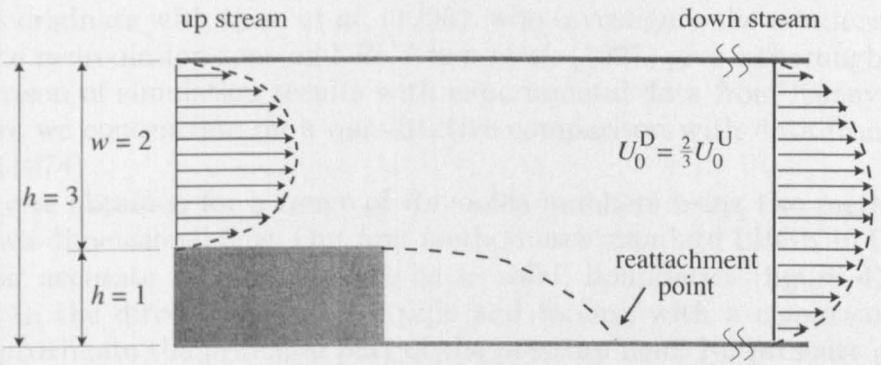

Figure 4. Geometry for a backward-facing step in channel flow with a step to channel width ratio of $\frac{1}{3}$. Both upstream and downstream of the step, flow behaves as standard Poiseuille flow. The step region introduces a recirculation zone of length L, the point of reattachment being when the x-component of the velocity changes sign. In two dimensions, the z-direction (into the plane of the paper) is infinite and so does not influence the flow.

five immiscible drops or de-mixing fluids leads to a maximum of ${}_2P_5 = 10$ *possible* local interfaces. Having selected a resolution, however, it is crucial to note that we have shown that execution-time and memory requirements scale only weakly with N, the number of components or drops (Dupin *et al.* 2003).

In high-volume-fraction flows, drops can come close to the simulation boundary and to each other. As an initial step, to avoid the need to postulate sub-lattice lubrication forces, we encourage an explicit layer of ambient liquid always to remain between drops and the boundary. We therefore need to ensure preferential wetting of the boundary and suspended drops by the ambient fluid. This was achieved for the simulations described here (Dupin *et al.* 2004). But the role of lubrication forces is quite possibly important in high-volume-fraction suspensions of deformable particles, for intimate contact is inevitable. As we shall discuss below, the applications considered in the results of figures 8–15 are designed to assist in determining this validity of this assumption.

4. Results: single and N-component pressure-driven flows

We first investigate laminar pressure-driven flow properties of a single-component fluid over a backward-facing step using two different LBM methods. Steady-state results from EILBGK simulation and from body-forced LBGK are compared with experimental data (Denham & Patrick 1974). We proceed to simulate N-component pressure-driven flow in similar internal geometries, concentrating on issues which relate to the transport of deformable particles, such as lift in a uniform shear and shear banding of a suspension.

(*a*) *Laminar flow over a backward-facing step*

The backward-facing step geometry (figure 4) produces flow separation at the step and subsequent re-attachment, which is recognized as important within industrial situations.

We consider a ratio of step height to downstream channel width of $\frac{1}{3}$, for which there exist two independent experimental investigations approximating two-dimensional flow (Denham & Patrick 1974; Kueny & Binder 1984). Other LBM

simulations originate with Qian *et al.* (1996), who investigate the relationship of the length of the recirculation zone and *Re*. Chen *et al.* (1997) give a thorough quantitative comparison of simulation results with experimental data from Kueny & Binder (1984). Here we concentrate on a quantitative comparison with data from Denham & Patrick (1974).

Results were obtained for a range of Reynolds numbers using two methods, both assuming two-dimensional flow. Our first method uses standard LBGK in D2Q9 with second-order accurate mid-link bounce-back 'solid' boundaries (figure 4), periodic boundaries in the direction along the pipe and forcing with a conservative body-force to approximate the principal part of the pressure field. No pressure gradient is set explicitly. The overall pressure field is extracted as described below. Using this method the 'pressure term' $(-c_s^2\partial_\alpha\rho)$, in the lattice Navier–Stokes equation (2.2), is regarded as a correction to a principal pressure field which is the potential function for the appropriate body force. The body force in the narrow part of the channel is $\frac{27}{8}$ times that of the wide part of the channel, based upon matching parabolic flow rates. The potential function for this conservative body-force field is

$$\Phi(x) \equiv \begin{cases} -\frac{27}{8}Gx, & x < x_0, \\ -G(x + \frac{27}{8}x_0), & L > x > x_0, \end{cases} \tag{4.1}$$

in which G is the adjustable force constant and x_0 the step length. The pressure field of the body-forced LBGK (below) is now determined by the expression $c_s^2\rho + \Phi$. Mass is strictly conserved, and pressure across the width of the inlet and outlet throats was held constant. The length of the lattice was chosen to minimize compressibility errors (which may be measured from the velocity divergence in the steady-state continuity equation

$$\partial_\alpha u_\alpha = -\frac{u_\alpha}{\rho}\partial_\alpha\rho$$

but are otherwise ignored here).

Our second method uses the exactly incompressible EILBGK model, which allows pressure and velocity boundary conditions to be applied more accurately at the inlet and outlet throats. Again non-slip boundaries are invoked using mid-link bounce back. Flow is now induced by setting discharge-matched parabolic velocity profiles at inlet and outlet and by fixing the outlet pressure while allowing the inlet pressure to develop to accord with the necessary pressure gradient (itself an observable). Because of direct link between lattice density and pressure, the total mass of this simulation increases asymptotically to a steady-state value.

Using the law of similarity, we compare body-forced LBGK and EILBGK simulations with experimental results from Denham & Patrick (1974), based on Denham's definition of *Re*:

$$Re = \frac{\bar{U}h}{\nu}, \tag{4.2}$$

in which $\bar{U}$ is the average flow velocity upstream of the step, h step height and ν the kinematic viscosity. Comparison of simulated and experimental data was made by normalizing velocities to the appropriate $\bar{U}$, distances to the step height h. For all our velocity data we note that both the body-forced LBGK and EILBGK results give very similar results for given *Re*, so velocity figures are representative of both models

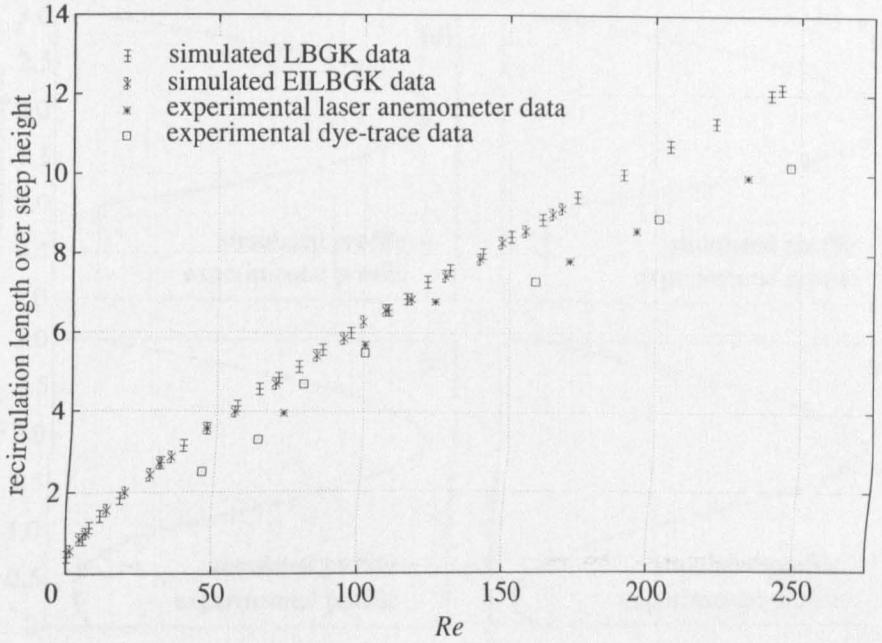

Figure 5. The recirculation length as a function of *Re* for the expansion ratio $\frac{1}{3}$. Data are compared with experimental values obtained via dye trace and laser anemometer measurements in Denham & Patrick (1974).

used. For all velocity data, flow profiles in the inlet and outlet were in good agreement compared with parabolic flow, supporting the assumption of fully developed flow. All results are analysed in their steady-state solutions, found by measuring the residual

$$R(t) = \sum_{\boldsymbol{x}} |\boldsymbol{u}(\boldsymbol{x}, t)|. \tag{4.3}$$

For the EILBGK system there is an additional condition on the total mass, which must be constant at steady state.

From stream-function data, the recirculation zone was seen to increase with increasing *Re*. The position of the vortex centre is given by the coordinates ($x_c = 0.3L_R, y_c = 0.6h$); this is in agreement with the coordinates given by Denham & Patrick (1974).

We define the recirculation length to be the distance x from the step at $y = 0$ in which a change in the x-velocity direction occurs. Figure 5 displays normalized recirculation length against *Re* for the step ratio of $\frac{1}{3}$. Note that the LBGK data provided in figure 5 are more accurate and cover a greater range of *Re* than in previous studies (Qian *et al.* 1996).

Both LBGK and EILBGK data are in good agreement. For given lattice resolution it was observed that the range of accessible *Re* for EILBGK is less than those for body-forced LBGK, owing to a more stringent incompressibility constraint. The experimental data points, taken from Denham & Patrick (1974), contain a $\pm 2\%$ tolerance for measurements of velocity. Including the tolerance limits, experimental results lie just below the simulated points, the discrepancy increasing as *Re* increases. But CFD simulations agree with our LBM models.

Velocity profiles obtained at different locations along the simulation are compared with experimental velocity profiles in figure 6. Recall that the agreement between

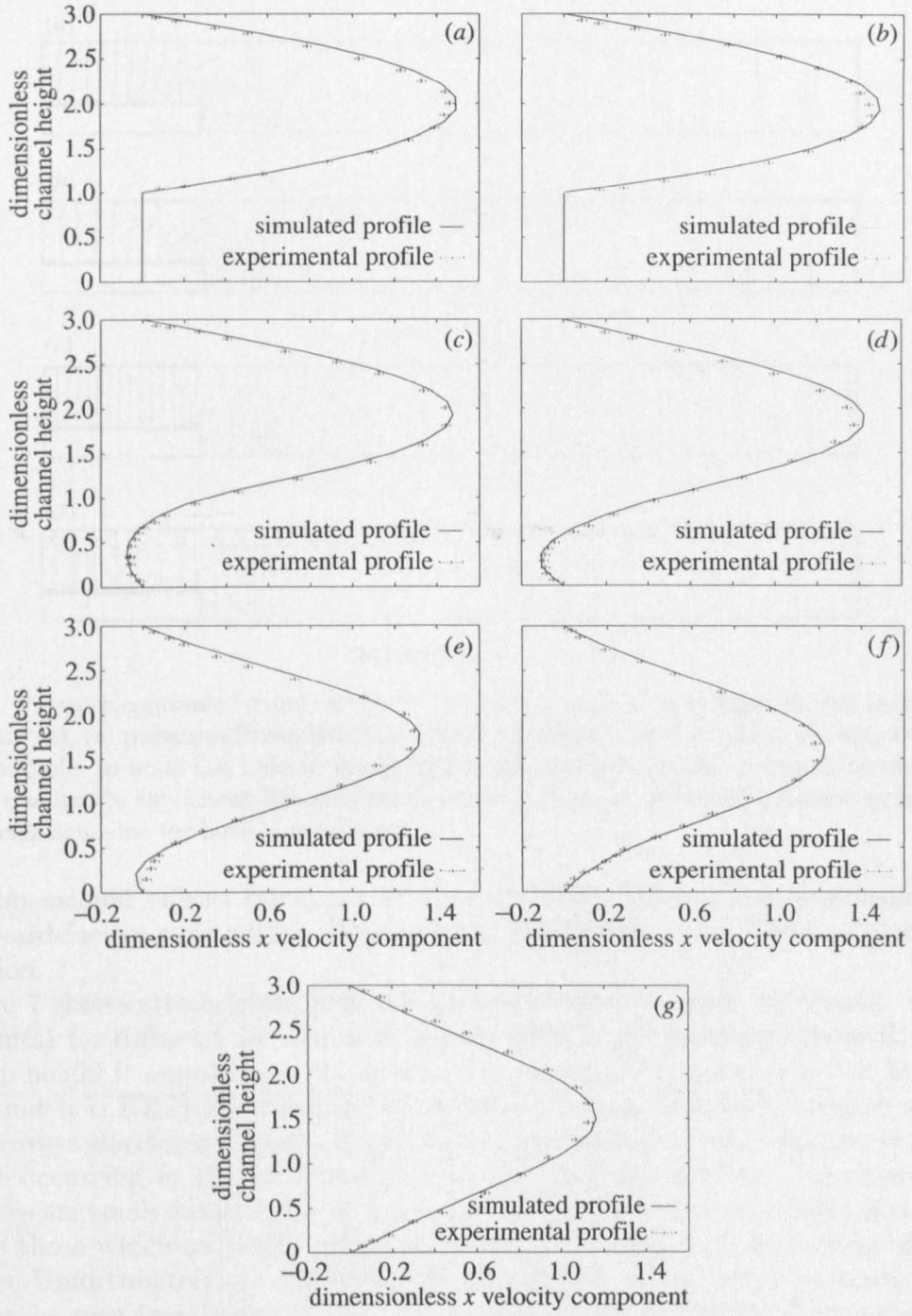

Figure 6. Comparison of simulated velocity profiles with experimental profiles obtained in Denham & Patrick (1974) in the step region at $Re = 73$ for various dimensionless distances from the step position: (*a*) −1.3, (*b*) 0.0, (*c*) 0.8, (*d*) 2.0, (*e*) 4.0, (*f*) 6.0 and (*g*) 8.0.

EILBGK and body-forced LBGK data is good and figure 6 shows only one set of simulation data, which agrees satisfactorily with experimental results at $Re = 73$. Upstream of the step, discrepancies are probably due to an inadequate development length in the experimental inlet (Denham & Patrick 1974). At higher Re, there emerge further discrepancies throughout the length of the system, probably due to

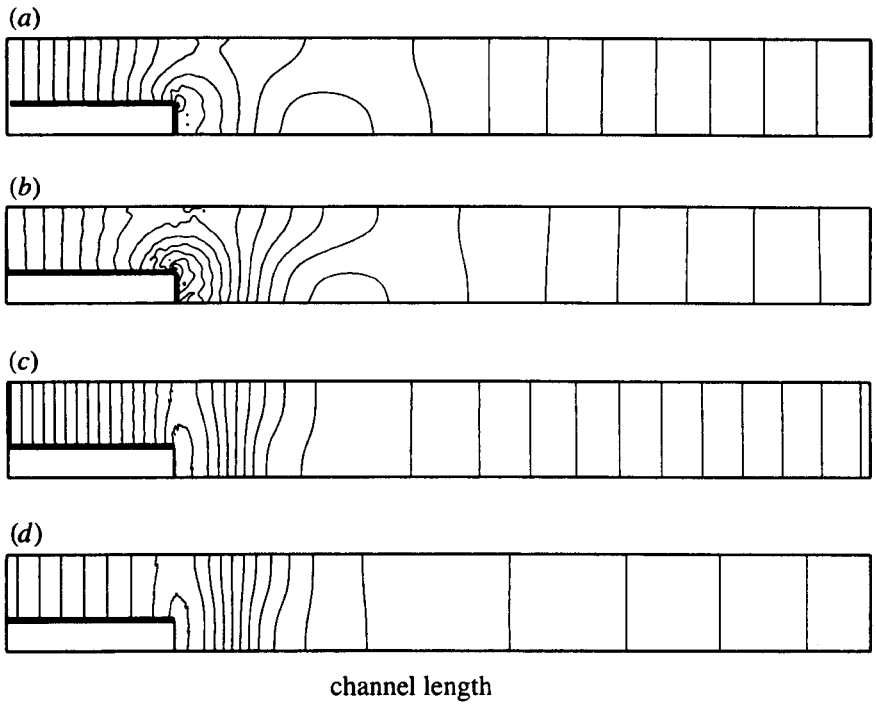

Figure 7. Pressure contours for (*a*), (*b*) $Re = 31$ and (*c*), (*d*) $Re = 174$ for (*b*), (*d*) body-forced LBGK and (*a*), (*b*) pressure-driven EILBGK. Both simulations used identical velocity boundary conditions (refer to text) but only in the EILBGK simulation does inlet pressure develop freely. There is qualitative agreement between the pressure fields (e.g. minimum pressure occurring in the recirculation zone for both simulations).

three-dimensional effects (Denham & Patrick 1974). More recent experiments on a backward-facing step with a step ratio of $\frac{1}{2}$ (Armely *et al.* 1983) support this conclusion.

Figure 7 shows steady-state pressure contours (with constant increment, in arbitrary units) for different Re, for body-forced LBGK and pressure-driven EILBGK. The step height is one-third of the width of the channel. The lattice size is 60×600. Recall that it is EILBGK which accommodates pressure boundary conditions, with inlet pressure developing freely. Qualitative agreement is good, with the minimum pressure occurring in the recirculation zone for both simulations. Notwithstanding this, there are small quantitative differences between these pressure fields of the same order as those which routinely appear between CFD solutions obtained by different methods. Unfortunately, no experimental information on the pressure exists.

As can be seen from figure 7, our two methods produce slightly different pressure contours. However, given their very different representations of a pressure field, the correspondence between the results is highly reassuring. Body-forced LBGK implementation essentially assumes a uniform gradient of pressure which is perturbed. While intuitively valid at most points in the simulation domain, this assumption is weak in the step region, where forced LBGK and EILBGK show differences.

(*b*) *Suspensions of deformable particles*

We proceed to consider pressure-driven flow of deformable particles, modelled as incompressible liquid drops, of varying volume fraction. The solid properties of our

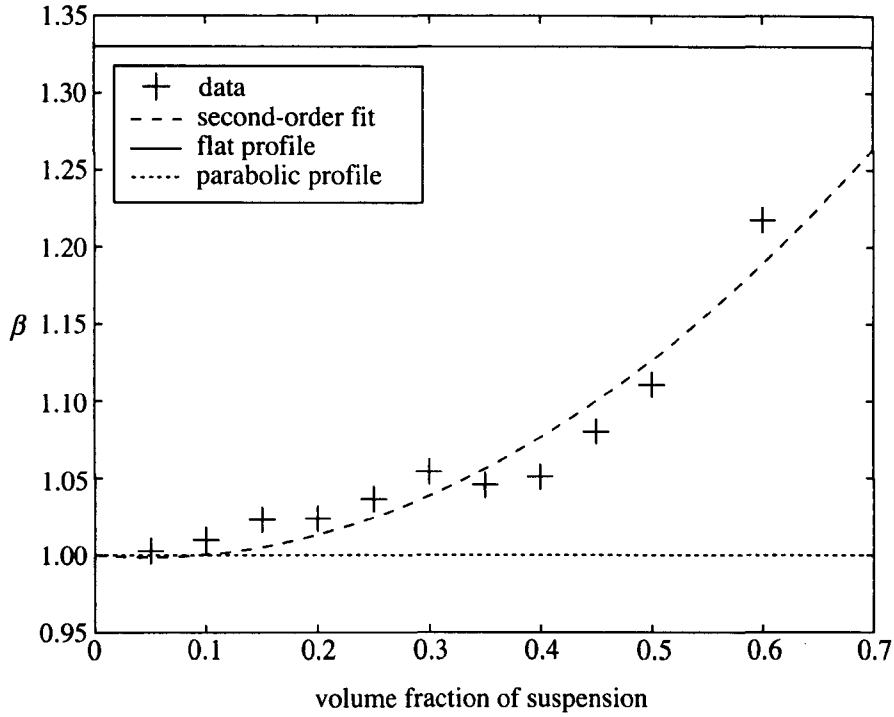

Figure 8. The increased blunting of a dense, monodisperse suspension's velocity profile with increased volume fraction ϕ, with fixed drop deformability. The latter is quantified by surface tension (parameter $\sigma = 0.01$) and viscosity ratio $\Lambda = 30$ and fixed flow rate (pressure gradient). ϕ varies over the range 0.1–0.6. The latter value is determined by packing and lubrication considerations.

particles are controlled through their interfacial tension and viscosity relative to that of the ambient fluid, Λ. The latter is parametrized by $\Lambda \leqslant 50$ and controlled as discussed in the last section. Figures 8–12 demonstrate our N-phase algorithm applied to pressure-driven duct flow of a dense suspension of neutrally buoyant drops. On inspection, our blunted profiles have noticeable departure from parabolic. We assess averaged departure, at normalized cross-duct distances $\bar{y} = 0.25$ and $\bar{y} = 0.75$ by defining a blunting β:

$$\beta \equiv \frac{\bar{v}(\bar{y} = 0.25) + \bar{v}(\bar{y} = 0.75)}{2 \times 0.75}, \tag{4.4}$$

in which 0.75 is the height of a normalized parabola. With this definition, a flat velocity profile is characterized by $\beta = 1.33$ and a parabolic velocity profile by $\beta = 1.00$.

A lattice of size 100×250 containing drops of initial radii 4 lattice units was used. Data were extracted from steady-state configuration (typically 1.0×10^5 simulation time-steps). The upper and lower dot-dashed lines in figures 8 and 9 illustrate the value of β corresponding to a flat and a parabolic velocity profile, respectively. The dashed line represents a second-order interpolation to the data. Details of each simulation are to be found in the appropriate caption.

For rigid suspended particles it is known that the velocity profile is determined solely by the suspension concentration and the relative particle size (Caro *et al.* 1998). By setting $\Lambda = 50$ (large) and increasing the volume fraction of suspended material we can obtain the expected increase in β (figure 8). We note that no significant

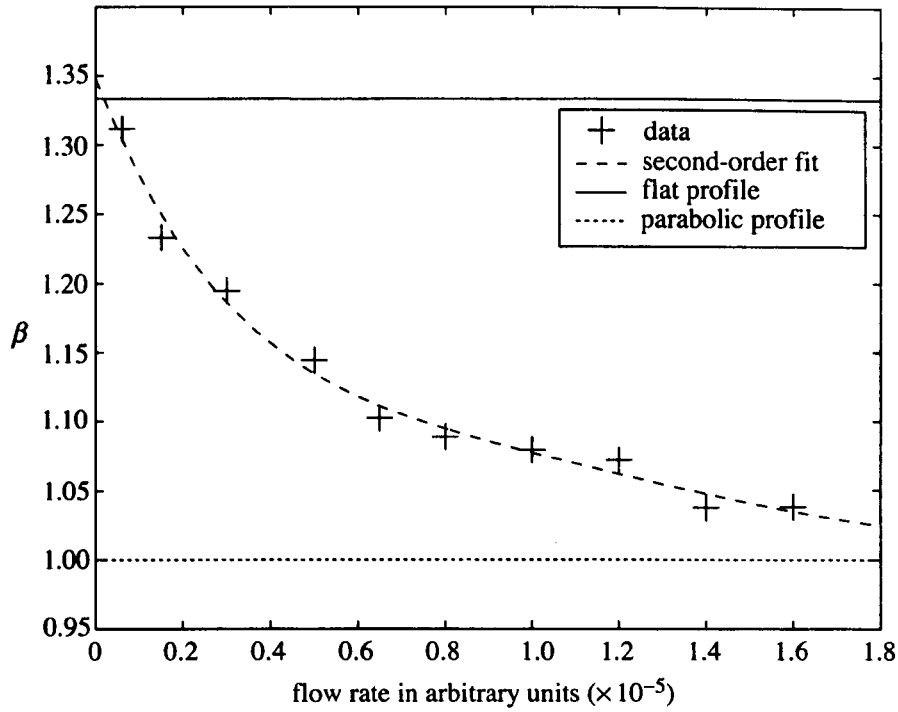

Figure 9. The decrease of blunting with increasing pressure gradient ΔP with non-constant deformability. Fixed surface tension (parameter $\sigma = 0.005$) and viscosity ratio $\Lambda = 1$.

changes in β were observed for constant volume fraction, on increasing pressure difference, as expected.

For immiscible liquid drops (i.e. flexible particle suspensions, $\Lambda = 1$), on the other hand, we observe the expected dependence of the velocity profile upon the flow rate (applied pressure gradient), with the degree of blunting decreasing as flow rate increases (Caro *et al.* 1998) (figure 9).

In both figures 8 and 9 the expected qualitative features tend to vindicate the method we have used to circumvent lubrication forces (see the last section). The qualitatively correct nature of the variation in the macroscopic suspension flow profiles emerges from the microscopic rules implemented. In particular our device of enforcing an explicit layer of ambient fluid at drop and boundary surfaces seems to be valid, at volume fraction $\phi = 0.6$ at least.

Recent experimental data confirm the shear-induced positional ordering of dense, intimate suspensions of particles and drops (Frank *et al.* 2003). Figure 10 shows the time-development of the cross-duct location of all the drop centres in an initially randomly placed suspension.

Clearly, starting from a random configuration (figure 11), and after an initial phase of transverse migration, our dense mono-disperse suspension of drops tends to flow in well-defined horizontal layers (figure 12), with occasional 'hopping', giving rise to an effective transverse diffusion of suspended drops.

(*c*) *Lift of deformable particles with linear shear*

Liquid drops deform and certainly do not transmit stresses instantaneously. To compare the properties of liquid and solid drops as components in a microscopic model of transport we consider particle lift. Particles of radius R confined in channels

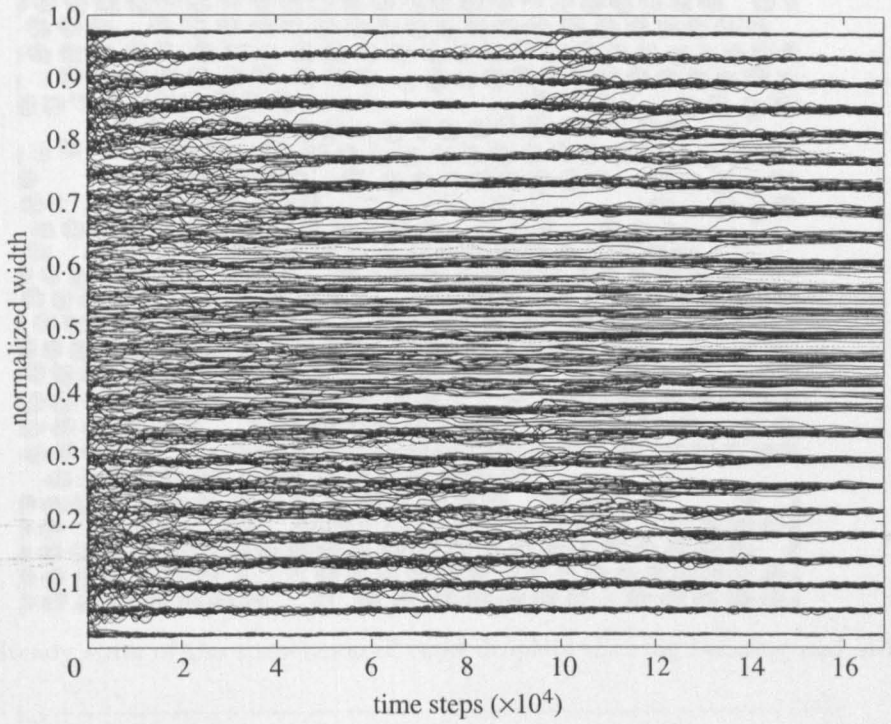

Figure 10. Trajectories of drop centres in time. Drop surface-tension parameter $\sigma = 0.005$ and viscosity ratio $\lambda = 1$. The suspended drop volume fraction was 0.6: the lattice size was 250×100 and the drop radius was 4.

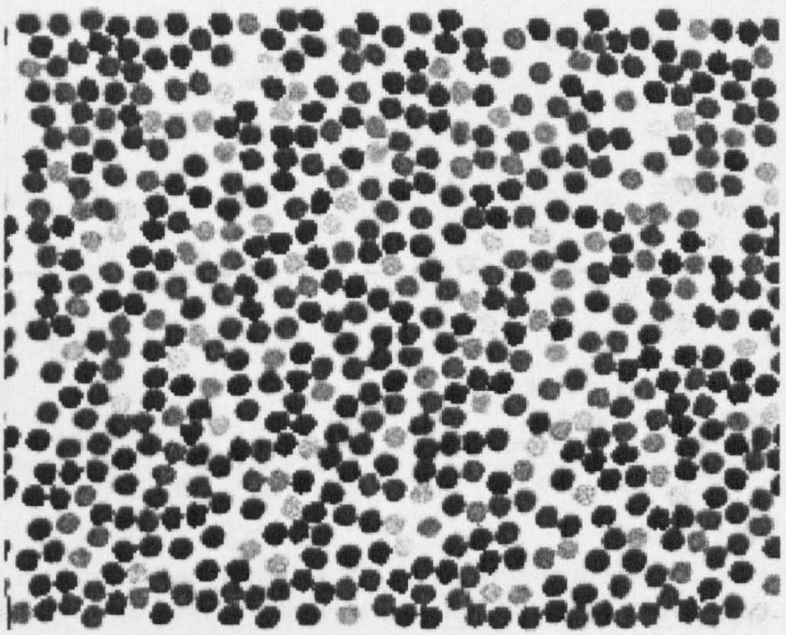

Figure 11. Random initial arrangement of the droplets.

and subject to flow (here a linear shear $\dot{\gamma}$) tend to migrate away from the wall, eventually to advect at some distance from the wall characteristic of the particle Reynolds number:

$$Re_{\mathrm{p}} = \frac{\dot{\gamma} R^2}{\nu}. \tag{4.5}$$

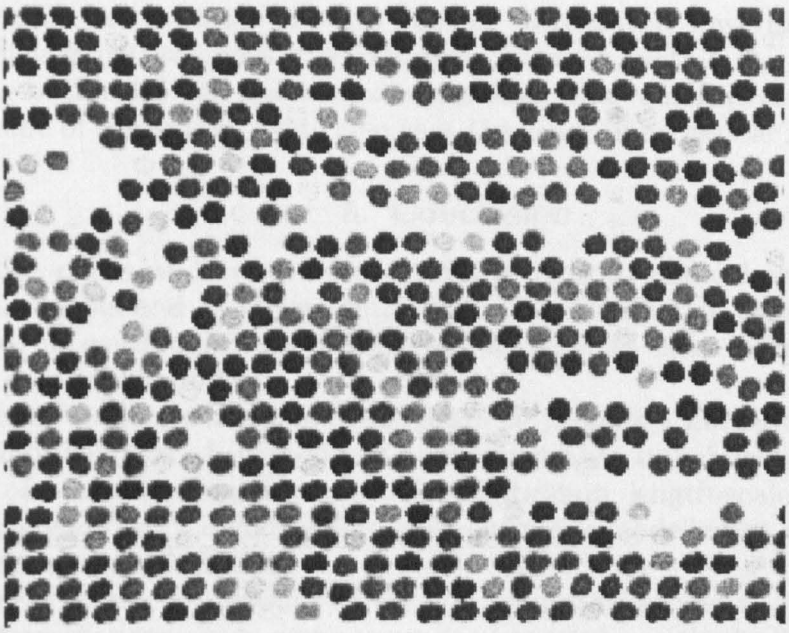

Figure 12. Steady state of the suspension of rigid droplets showing banding and ordering.

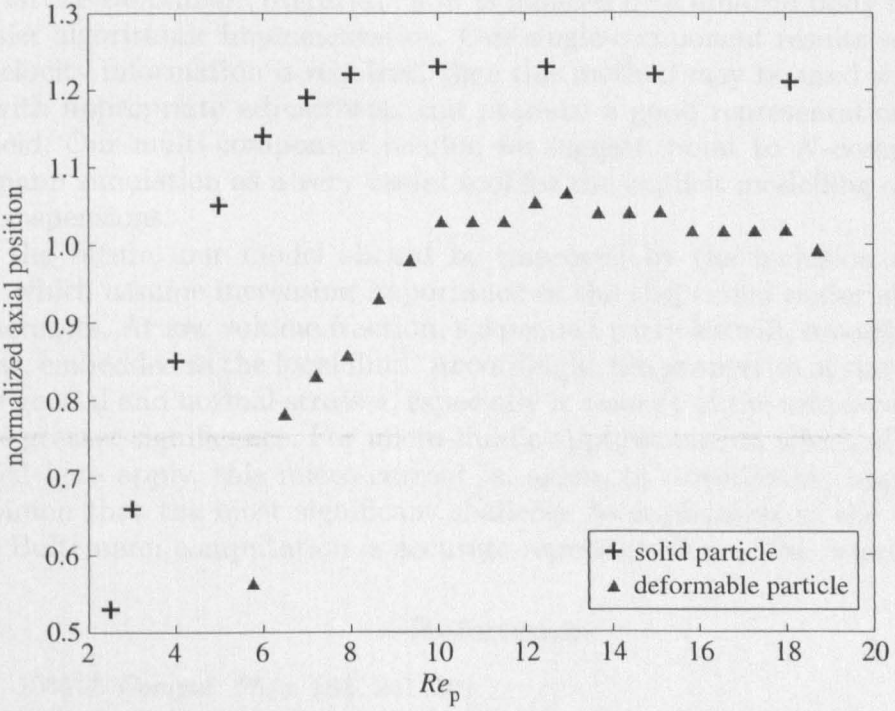

Figure 13. Steady-state elevation of a single droplet in straight channel normalized to its diameter with the particle Reynolds number.

Figure 13 shows the lift (normalized cross-duct displacement) of a neutrally buoyant deformable drop, $A = 10$, for reference, and a solid cylindrical particle of the same size, for a range of Re_p.

The latter was simulated by the LBM using the algorithm of Ladd (1994). Simulation parametrization for both solid and deformable drops is as specified in the figure caption. The geometry of both simulations was identical. As expected, there

is a some difference between the two objects—a relatively low viscosity drop has an internal flow structure and a different drag. However, within the bounds of simulation error, both solid and deformable drop data show qualitative similarities in the overall shape of the graphs. Note also that the range of accessible Re_p is appreciable.

5. Conclusion

In § 2 of this paper we have derived governing hydrodynamical equations for single-component LBMs and in § 3 we detailed the most recent N-component extension, predicated on continuum length-scale applications to large numbers of explicitly modelled deformable bodies.

The lattice Boltzmann technique appears to present a numerical scheme for the simulation of complex, N-component hydrodynamics. In particular it holds out the prospect of realistic simulations, at the continuum length-scale, of high-volume-fraction suspensions of deformable drops, currently modelled as drops of relatively viscous, incompressible fluids.

We present results for pressure-driven flow in internal geometry, demonstrating and validating an efficient single-component implementation (the backward-facing step) and an N-component extension (chaining, lift). For many engineering computations in the lattice Boltzmann literature, flow is induced by a uniform body forced method for easier algorithmic implementation. Our single-component results suggest that, if only velocity information is required, then this method may be used with confidence and, with appropriate adjustment, can produce a good representation of the pressure field. Our multi-component results, we suggest, point to N-component lattice Boltzmann simulation as a very useful tool for the explicit modelling of transport in dense suspensions.

For the future, our model should be improved by the inclusion of lubrication forces, which assume increasing importance as the suspended material volume fraction increases. At low volume fraction, suspended particles will, broadly, advect with the flow, embedded in the local fluid. Accordingly, the properties of the interface with low tangential and normal stresses, especially in respect of the micro-current activity assume greater significance. For micro-fluidic applications, to which all the methods reported here apply, this micro-current is, again, of considerable importance. It is our opinion that the most significant challenge to application of the N-component lattice Boltzmann computation is accurate representation of the interface.

References

Abe, T. 1966 *J. Comput. Phys.* **131**, 241–246.

Alexander, F. J., Chen, S. & Sterling, J. D. 1993 *Phys. Rev.* E **47**, 2249–2252.

Allen, M. P. & Tildesley, D. J. 1997 *Computer simulation of liquids.* Oxford: Clarendon.

Anderson, J. D. 1995 *Computation fluid dynamics: the basics with applications.* McGraw-Hill.

Armely, B. F., Durst, F., Pereira, J. C. F. & Schönung, B. 1983 *J. Fluid Mech.* **127**, 473–496.

Benzi, R., Succi, S. & Vergassola, M. 1992 *Phys. Rep.* **222**, 145–197.

Bhatnagar, P. E., Gross, P. E. & Krook, M. 1954 *Phys. Rev.* A **94**, 511–525.

Boghosian, B. & Taylor, W. 1997 *Int. J. Mod. Phys.* C **8**, 705–716.

Broadwell, J. E. 1964 *Phys. Fluids* **7**, 1243–1247.

Cali, A., Luo, L. S., Cancelliere, A., Benzi, R. & Gramignani, M. 1992 *Phys. Rev.* A **45**, 5771–5774.

Caro, C. G., Pedeley, T. J., Schroter, R. C. & Seed, W. A. 1998 *The mechanics of the circulation.* Oxford Medical Publications.

Chapman, S. & Cowling, T. G. 1970 *The mathematical theory of non-uniform gases*, 3rd edn. Cambridge University Press.

Chen, H., Chen, S. & Matthaeus, W. H. 1992 *Phys. Rev.* A **45**(8), 5339–5342.

Chen, S. & Doolen, G. D. 1998 *A. Rev. Fluid Mech.* **30**, 329–364.

Chen, S., Chen, H., Martinez, C. & Matthaeus, W. 1991 *Phys. Rev. Lett.* **67**(27), 3776–3779.

Chen, Y., Ohashi, H. & Akiyama, M. 1997 *JSME Int. J.* B **40**(1), 25–32.

Chen, Y., Ohashi, H. & Akiyama, M. 1994 *Phys. Rev.* E **50**(4), 2776–2783.

Conner, J. & Brebbia, C. 1976 *Finite element techniques for fluid flow.* Woburn, MA: Newnes–Butterworth.

Denham, M. K. & Patrick, M. A. 1974 *Trans. IChE* **52**, 361–367.

D'Humières, D., Lallemand, P. & Qian, Y. H. 1989 *Review of flow simulations using lattice gases.* Lecture Notes in Mathematics, vol. 1402, pp. 56–58. Springer.

Do-Quang, M., Aurell, E. & Vergassola, M. 2000 An inventory of lattice Boltzmann models of multiphase flows. Technical Report, ISSN 0348-467X. (Available at http://www.psci.kth.se/Activities/Reports/Results/R_2000_03/psci2000_03.pdf.)

Dupin, M. M., Halliday, I. & Care, C. M. 2003 Multi-component lattice Boltzmann equation for mesoscale blood flow *J. Phys.* A **36**, 8517–8534.

Dupin, M. M., Halliday, I. & Care, C. M. 2004 A lattice Boltzmann model of flow blunting. *Phil. Trans. R. Soc. Lond.* A **362**, 1755–1761.

Español, P. 2002 *SIMU Newsletter*, issue 4, ch. III, pp. 59–77. (Available at http://simu.ulb.ac.be/newsletters/N4III.pdf.)

Ferreol, B. & Rothman, D. H. 1995 *Transport Porous Media* **20**, 3–20.

Filippova, O. & Hanel, D. 1998 Grid refinement for lattice-BGK models. *J. Comput. Phys.* **147**, 219–228.

Frank, M., Anderson, D., Weeks, E. R. & Morris, J. F. 2003 *J. Fluid Mech.* **493**, 363–378.

Frisch, U., Hasslacher, B. & Pomeau, Y. 1986 *Phys. Rev. Lett.* **56**, 1505–1508.

Goodfellow, J. 1991 *Molecular dynamics.* London: Macmillan.

Groot, R. D. & Warren, P. B. 1997 *J. Chem. Phys.* **107**, 4423–4435.

Gunstensen, A. K., Rothmann, D. H., Zaleski, S. & Zanetti, G. 1991 Lattice Boltzmann model of immiscible fluids. *Phys. Rev.* A **43**(8), 4320–4327.

Halliday, I., Care, C. M. & Thompson, S. P. 1998 Macroscopic surface tension in a lattice Bhatnagar–Gross–Krook model of two immiscible fluids. *Phys. Rev.* E **57**, 514–523.

Halliday, I., Hammond, L. A., Care, C. M., Good, K. & Stevens, A. 2001 Lattice Boltzmann equation hydrodynamics. *Phys. Rev.* E **64**, 011208.

Halliday, I., Hammond, L. A. & Care, C. M. 2002 *J. Phys.* A **35**, 157–166.

Hardy, J., Pomeau, Y. & De Pazzis, O. 1973 *J. Math. Phys.* **14**, 1746–1759.

Hardy, J., De Pazzis, O. & Pomeau, Y. 1976 *Phys. Rev.* A **13**, 1949–1961.

He, X. & Doolen, G. D. 1997*a* *Phys. Rev.* E **56**, 434–440.

He, X. & Doolen, G. D. 1997*b* *J. Comput. Phys.* **134**(2), 306–315.

He, X. & Luo, L. S. 1997*a* *Phys. Rev.* E **55**(6), 6333–6336.

He, X. & Luo, L. S. 1997*b* *Phys. Rev.* E **56**(6), 6811–6817.

He, X., Zou, Q., Luo, L. S. & Dembo, M. 1997*a* *J. Stat. Phys.* **87**, 115–136.

He, X., Luo, L. S. & Dembo, M. 1997*b* *Physica* A **239**, 276–285.

Higuera, F. & Luo, L. S. 1989 *Europhys. Lett.* **8**, 517–521.

Hoogerbrugge, P. J. & Koelman, J. M. V. A. 1992 *Europhys. Lett.* **19**, 155–160.

Hou, S. 1995 PhD thesis, Kansas State University, Manhatten, KS, USA.

Hou, S., Zou, Q., Chen, S. & Doolen, G. D. A. C. 1995 *J. Comput. Phys.* **118**, 329–347.

Hou, S., Sterling, S. & Doolen, G. D. 1996 *Fields Inst. Commun.* **6**, 151–166.

Kadanoff, L. P., McNamara, G. R. & Zanetti, G. 1989 *Phys. Rev.* A **40**(8), 4527–4541.

Kueny, L. J. & Binder, G. 1984 Viscous flow over backward facing steps: an experimental investigation, analysis of laminar flow over a backward facing step. *Not. Fluid Mech.* **9**, 32–42.

Ladd, A. J. C. 1994 *J. Fluid Mech.* **271**, 311–339.

Landau, L. D. & Lifshitz, E. M. 1995 *Fluid mechanics.* Course in Theoretical Physics, 2nd edn, vol. 6. Oxford: Butterworth-Heinemann.

Liboff, R. C., Herman, J. & Liboff, R. L. 2003 *Kineic theory*, 2nd edn. Springer.

Lin, Z., Fang, H. & Tao, R. 1996 *Phys. Rev.* E **54**(6), 6323–6330.

Lishchuk, S. V., Care, C. M. & Halliday, I. 2003 *Phys. Rev.* E **67**, 036701.

Luo, L. S. 1998 *Phys. Rev. Lett.* **81**(8), 1618–1621.

Luo, L. S., Wang, J. & Qian, Y. H. 1997 *Int. J. Mod. Phys.* C **8**(4), 999–1008.

Luo, L. S. 2000 *Phys. Rev.* E **64**(4), 4982–4996.

McNamara, G. R. & Zanetti, G. 1988 *Phys. Rev. Lett.* **61**(20), 2332–2335.

Maier, R. S., Bernard, R. S. & Grunau, D. W. 1996 *Phys. Fluids* **8**(7), 1788–1801.

Martinez, D. O., Chen, S. & Matthaeus, W. H. 1994 *Phys. Plasmas* **1**, 1850–1867.

Mei, R., Shyy, S., Yu, D. & Luo, L. S. 2000 *J. Comput. Phys.* **161**, 680–699.

Noble, D. R., Georgiadis, J. G. & Buckius, R. O. 1995 *J. Stat. Phys.* **81**, 17–33.

Qian, Y. H. & Zhou, Y. 1998 *Europhys. Lett.* **42**(4), 359–364.

Qian, Y. H., D'Humières, D. & Lallemand, P. 1992 *Europhys. Lett.* **17**(6), 479–484.

Qian, Y. H., Luo, L. S., Massaioli, F. & Orszag, S. A. 1996 *Fields Inst. Commun.* **6**, 207–215.

Reider, M. B. & Sterling, J. D. 1995 *Comput. Fluids* **24**, 459–467.

Rothmann, D. H. & Zaleski, S. 1994 *Rev. Mod. Phys.* **66**(4), 1417–1479.

Shan, X. W. & Chen, H. D. 1994 *Phys. Rev.* E **49**(4), 2941–2948.

Skordos, P. A. 1993 *Phys. Rev.* E **48**(6), 4823–4842.

Spencer, T. J., Dupin, M. M., Halliday, I. & Care, C. M. 2004 An incompressible Lattice BGK scheme with enhanced stability. (In preparation.)

Succi, S. 2001 *The lattice Boltzmann equation.* Oxford: Clarendon.

Succi, S. 2002 *Phil. Trans. R. Soc. Lond.* A **360**, 429–436.

Succi, S., Foti, E. & Higuera, F. 1989 *Europhys. Lett.* **10**, 433–438.

Succi, S., Benzi, R. & Higuera, F. 1991 *Physica* D **47**, 219–230.

Swift, M. R., Osborn, W. R. & Yoemans, J. M. 1995 *Phys. Rev. Lett.* **75**(5), 830–833.

Thompson, S. P., Halliday, I. & Care, C. M. 1999 Mesoscopic hydrodynamics of diphasic lattice Bhatnagar–Gross–Krook fluid interfaces. *Phys. Chem. Chem. Phys.* **1**, 2183–2190.

Tölke, J., Krafczyk, M., Schultz, M., Rank, E. & Berrios, R. 1998 *Int. J. Mod. Phys.* C **9**, 1143–1157.

von Neumann, J. 1966 *Theory of self-reproducting automata.* University of Illinois Press.

Wagner, L. 1994 *Phys. Fluids* **6**, 3516–3518.

Wolfram, S. 1986 *Rev. Mod. Phys.* **55**, 601–644.

Yang, Z. L., Dinh, T. N., Nourgaliev, R. R. & Sehgal, B. R. 2001 *Int. J. Heat Mass Transfer* **44**, 195–206.

Zou, Q., Hou, S., Chen, S. & Doolen, G. D. 1995 Analytical solutions of the lattice Boltzmann BGK model. *J. Stat. Phys.* **81**, 319–334.